

APR 24 1983

TECHNICAL DIGEST

2

IEEE

SOLID-STATE SENSORS

Workshop

DTIC
ELECTE
DEC 16 1987
S D



Sponsored by the IEEE Electron Devices Society
and The Electrochemical Society

AD-A190 922

Best Available Copy

DISTRIBUTION STATEMENT A
Approved for public release
Distribution Unlimited

1986

Hilton Head Island, South Carolina

June 2-5

87 12 9 007

REPORT DOCUMENTATION PAGE				
1a. REPORT SECURITY CLASSIFICATION Unclassified		1b. RESTRICTIVE MARKINGS		
2a. SECURITY CLASSIFICATION AUTHORITY		3 DISTRIBUTION/AVAILABILITY OF REPORT Approved for public release; distribution unlimited.		
2b. DECLASSIFICATION/DOWNGRADING SCHEDULE		5 MONITORING ORGANIZATION REPORT NUMBER(S) ARO 24383.1-EL-CF		
4 PERFORMING ORGANIZATION REPORT NUMBER(S)		7a. NAME OF MONITORING ORGANIZATION U. S. Army Research Office		
6a. NAME OF PERFORMING ORGANIZATION NovaSensor		6b. OFFICE SYMBOL (If applicable)		7b. ADDRESS (City, State, and ZIP Code) P. O. Box 12211 Research Triangle Park, NC 27709-2211
6c. ADDRESS (City, State, and ZIP Code) 2975 Bowers Avenue Santa Clara, CA 95050		9. PROCUREMENT INSTRUMENT IDENTIFICATION NUMBER DAAL03-86-G-0161		
8a. NAME OF FUNDING/SPONSORING ORGANIZATION U. S. Army Research Office		8b. OFFICE SYMBOL (If applicable)		10. SOURCE OF FUNDING NUMBERS PROGRAM ELEMENT NO. PROJECT NO. TASK NO. WORK UNIT: ACCESSION NO.
8c. ADDRESS (City, State, and ZIP Code) P. O. Box 12211 Research Triangle Park, NC 27709-2211		11. TITLE (Include Security Classification) IEEE Sponsored Solid State Sensors Workshop		
12 PERSONAL AUTHOR(S) Kurt E. Petersen				
13a. TYPE OF REPORT Final		13b. TIME COVERED FROM 6/2/86 TO 6/1/87		14 DATE OF REPORT (Year, Month, Day) 1986
15. PAGE COUNT 121				
16. SUPPLEMENTARY NOTATION The view, opinions and/or findings contained in this report are those of the author(s) and should not be construed as an official Department of the Army position, policy, or decision, unless so designated by other documentation.				
17 COSATI CODES FIELD GROUP SUB-GROUP		18 SUBJECT TERMS (Continue on reverse if necessary and identify by block number) Solid-State Sensors, Sensors, Chemical Sensors, Thin Film Sensing Structures		
19 ABSTRACT (Continue on reverse if necessary and identify by block number) The workshop was held as scheduled. Substantial efforts by the program committee and by all of the authors and panelists insure that the program and these proceedings contain many valuable contributions to the state-of-the-art in solid-state sensors: contributions that will certainly stimulate further discussion and future research.				
20. DISTRIBUTION/AVAILABILITY OF ABSTRACT <input type="checkbox"/> UNCLASSIFIED/UNLIMITED <input type="checkbox"/> SAME AS RPT. <input type="checkbox"/> DTIC USERS		21. ABSTRACT SECURITY CLASSIFICATION Unclassified		
22a NAME OF RESPONSIBLE INDIVIDUAL		22b. TELEPHONE (Include Area Code)		22c. OFFICE SYMBOL

1986 IEEE SOLID-STATE SENSOR WORKSHOP

WELCOME

The Organizing Committee of the 1986 Solid-State Sensors Workshop is very pleased to welcome you to Hilton Head Island, South Carolina.

This Workshop is the fifth in a series of significant gatherings in the continually developing field of solid-state sensors:

- Boston in 1981,
 - Delft in 1983,
 - Hilton Head in 1984,
 - Philadelphia in 1985.
- Coming up,
- Tokyo in 1987.

Without a doubt, the most important progress during this period has been the formation and growth of a strong technical community that encompasses a broad range of interests, but shares a common commitment to research and development in solid-state sensor materials, processes, and technologies.

This workshop has been organized with the intention of maximizing technical interactions among the attendees. We encourage your active participation in the panel sessions, in the evening rump session, during the presentation of the papers themselves, and especially during the free time set aside for informal discussions with your colleagues. These multi-disciplinary interactions are one of the most stimulating aspects of current solid-state sensor research.

Substantial efforts by the program committee and by all of the authors and panelists insure that the program and these proceedings contain many valuable contributions to the state-of-the-art in solid-state sensors: contributions that will certainly stimulate further discussion and future research.

Enjoy your Workshop!

Kurt Petersen

Kurt Petersen
General Chairman



SPONSORED BY THE IEEE ELECTRON DEVICES SOCIETY

A

1986 IEEE SOLID-STATE SENSOR WORKSHOP

General Chairman:	Kurt Petersen Novasensor
Technical Program Chairman:	Richard Muller University of California
Local Arrangements Chairman:	Tom Poteat AT&T Bell Laboratories
Financial Chairman:	Joe Giachino Ford Motor Company
Technical Digest:	Dave Eddy General Motors Research
Committee Meeting Chairman:	Bob Huber University of Utah

PROGRAM COMMITTEE

Phil Barth Novasensor	Ben Hocker Honeywell
Wen Ko Case Western Reserve	Steve Senturia MIT
Ken Wise University of Michigan	Hank Wohltjen Microsensor Systems
Jay Zemel University of Pennsylvania	

ADDITIONAL SPONSORSHIP PROVIDED BY

THE ELECTROCHEMICAL SOCIETY
ARMY RESEARCH OFFICE, RESEARCH TRIANGLE PARK, NC
OFFICE OF NAVAL RESEARCH, ARLINGTON, VA

PATIO - SUNDAY, JUNE 1, 7 PM

POLYSILICON AND NEW MICROMACHINED STRUCTURES

8:15 **Welcome - K. Petersen, Conference Chairman**

8:25 **Announcements - T. Poteat, Local Arrangements Chairman**

8:30 **Characteristics of Polysilicon Layers and Their Applications
in Sensors**
 E. Obermeier, P. Kopystynski, R. Niessl
 - Fraunhofer Institute, Munich, Germany

9:10 **Design and Construction Techniques for Planar Polysilicon
Pressure Transducers with Piezoresistive Read-Out**
 H. Guckel, D.W. Burns, C.R. Rutigliano
 - University of Wisconsin

9:45 **Integrated Polysilicon Tactile Sensor**
 A.K. Oki, R.S. Muller - University of California, Berkeley

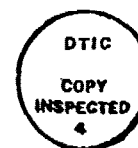
BREAK

11.00 **A Micromachined Manipulator for Submicron Positioning of Optical Fibers**
A.M. Feury, T. L. Poteat, W. S. Trimmer
Rutgers University - AT&T Bell Laboratories

LUNCH

Coffee and breakfast rolls will be available in the meeting room at 7:50 am each morning.

Light refreshments and beverages will be available at afternoon break periods.



ion For	
CRA&I	<input checked="" type="checkbox"/>
TAB	<input type="checkbox"/>
ounced	<input type="checkbox"/>
tation	
<hr/>	
<hr/>	
ution /	
<hr/>	
• Utility Codes	
<hr/>	
Avail and/or Special	

SESSION II - MONDAY, JUNE 2

CHEMICAL SENSORS I

Co-Chairmen: R. Huber, H. Wohltjen

- 1:00 **Electrical and Chemical Sensors for Biological Cell Research**
D.J. Edell, V.M. McNeil, M.G. Curley, J.H. Wolfe
- Massachusetts Institute of Technology
- 1:30 **Characterization of Proton Conducting PVA/H₃PO₄ Films**
S. Petty-Weeks, A.J. Polak - Signal Research Laboratory
- 2:00 **Pyrolyzed Organic Polymer Nitrogen Dioxide Sensor**
J.O. Colla - Johnson Controls
- 2:30 **Chemical Multisensors with Selective Encapsulation
of Ion-Selective Membranes**
F.J. Schwager, L.J. Bousse, L. Bowman, J.D. Meindl
- Stanford University
- 3:00-3:10 **BREAK**
- 3:10 **PANEL: The Future of Chemical Sensors**
Moderator: J.N. Zemel - University of Pennsylvania
Panelists: M. Thompson - University of Toronto, I. Lauks -
Integrated Ionics, J. Shultz - National Science Foundation,
H. Wohltjen - Microsensor Systems.

SESSION III - TUESDAY, JUNE 3

SENSING TECHNIQUES AND ANALYSIS

Co-Chairmen: T. Poteat, D. Eddy

- 8:00 **Fiber-Optic Sensors**
D.A. Krohn - EOTec Corporation
- 8:40 **Optical Sensing of Magnetic Fields**
M.A. Butler, S.J. Martin - Sandia National Laboratory
- 9:10 **Anomalous Emissivity from Periodic Micromachined Silicon Surfaces**
P.J. Hesketh, B. Gebhart, J.N. Zemel
- University of Pennsylvania
- 9:40 **Stress Modeling of Microdiaphragm Pressure Sensors**
P.C. Tack, H.H. Busta - Gould Electronics
- 10:10-10:25 **BREAK**
- 10:25 **Noise in Piezoresistive and Capacitive Sensors**
R.R. Spencer, B.M. Fleischer, P.W. Barth, J.B. Angell
- Stanford University
- 10:55 **Thermal Management of Integrated Microsensors**
S.B. Crary - General Motors Research Laboratories
- 11:25 **Comparison of Five Readout Techniques for an Integrated Magnetometer**
J.Lenz, K. Kawai, R. Fryer, L. Strandjord
- Honeywell Systems and Research Center
- 12:00 **LUNCH**

COOKOUT - BANQUET - TUESDAY, JUNE 3, 7PM

E

SESSION IV - WEDNESDAY, JUNE 4

SENSOR PACKAGING AND COMMERCIAL PRODUCTION

Co-Chairmen: G.B. Hocker, J. Giachino

- 8:10 **Sensors for Process Controls: Requirements for Design and Test**
W. Thompson - Bailey Controls Co.
- 8:40 **Flexible Tactile Sensing Arrays for Robotics: Architectural Robustness and Yield Considerations**
P.W. Barth, M.J. Zdeblick, Z. Kuc, P.A. Beck
- Stanford University
- 9:10 **Application-Specific Packaging for Custom Micromechanical Structures**
S. Terry, J.H. Jerman, J.W. Knutti, H.V. Allen
- Transensory Devices
- 9:40-10:00 **BREAK**
- 10:10 **Considerations in the High-Volume Production of Hybrid Pressure Sensor Modules for Automotive Applications**
R. Brown, K. Catron, W. Wright
- Delco Electronics Corporation
- 10:40 **An Integrated On-Chip Pressure Sensor for Accurate Control Applications**
J.M. Staller, W.S. Cumberledge - Motorola Inc.
- 11:10 **PANEL: Production of Sensors - Problems, Solutions, and Prospects**
Moderator: D. Eddy - General Motors Research Laboratories
Panelists: J.R. Mastroianni, Micro Switch - Honeywell,
J.W. Knutti - Transensory Devices, W.L. Thompson - Bailey Controls, K.E. Catron - Delco, J.M. Staller - Motorola.
- 12:00 **LUNCH**

SESSION V - WEDNESDAY, JUNE 4

CHEMICAL SENSORS II

Co-Chairmen: W. Ko and J. Zemel

- 1:00 **Isothermal Measurement and Thermal Desorption Using SAW Devices**
S.J. Martin, A.J. Ricco, T.E. Zipperian
- Sandia National Laboratory
- 1:30 **Thermodynamic Study of Hygroscopic Polymers Using Surface Acoustic Waves**
J.G. Brace, T.S. Sanfelippo, S.G. Joshi
Johnson Controls - Marquette University

- 2:00 **Silver Multilayers for Planar Ag/AgCl Reference Electrodes**
M. Lambrechts, J. Suls, W. Sansen
Catholic University, Leuven, Belgium
- 2:30 **The Structure and Properties of RF Reactive-Sputtered IrO_2 Films**
K.G. Kreider - US National Bureau of Standards
- 3:00 **The Response of MOS Sensors with Ultrathin Palladium Gates to Carbon Monoxide and Hydrogen**
G.J. Maclay, K.W. Jelley
- University of Illinois at Chicago

SESSION VI - WEDNESDAY JUNE 4

POSTER SESSION - 7 PM

- **Air-Loading Effects on a Capacitively Sensed, Membrane-Supported Silicon Accelerometer**
S.P. McArthur, J.W. Holm-Kennedy - University of Hawaii
- **Simulation of Diaphragm-Type IC Pressure Sensors**
H. Reimann, Y. Fathi - Sensym Inc.
- **Carrier Transport in Semiconductor Magnetic Sensors Under Locally Inverted Fields**
H.P. Baltes, W. Allegretto, A. Nathan, Y. Sugiyama
- University of Alberta - Electrotechnical Lab. Japan
- **Miniature Radiation Dosimeter for In-Vivo Radiation Measurements**
R.C. Hughes, D. Huffman, J.V. Snelling, T.E. Zipperian, A.J. Ricco, C.A. Kelsey - Sandia National Laboratories
- **Steady State and Transient Behavior of the Pd-SnO_x MIS Oxygen Sensors**
J.F. Xu, W.P. Kang, B. Lalevic, T. Poteat
- Rutgers University - AT&T Bell Laboratories
- **Joint Angle Sensor for Closed-Loop Control**
C.L. Miao, W.H. Ko - Case Western Reserve University
- **Effect of Process Conditions on Aluminum Oxide Thin Film used in pH ISFET**
A.S. Wong, P.W. Cheung
- Case Western Reserve University - University of Washington
- **A Novel Primary Air Data Quality Pressure Transducer**
Paul B. DuPuis - Honeywell Commercial Aviation Division

RUMP SESSION - WEDNESDAY, JUNE 4 - 8:30 PM

**The University-Industrial Complex
and the Future of Sensors**
Moderator: J. Giachino, Ford Motor Company



SESSION VII - THURSDAY, JUNE 5

RESONANT AND THIN-FILM SENSING STRUCTURES

Co-Chairmen: H. Wohltjen and S. Senturia

- 8:00 **Resonant Structures for Integrated Sensors**
M.A. Schmidt, R.T. Howe
- Massachusetts Institute of Technology
- 8:40 **Surface Acoustic Wave Gas Sensor Based on Film Conductivity Changes**
A. J. Ricco, S.J. Martin, T.E. Zipperian
- Sandia National Laboratories
- 9:10 **Thin-Membrane Lamb-Mode Acoustic Oscillators for Chemical Detection**
E.T. Zellers, S.W. Wenzel, R.M. White, P.J. Wicher
- University of California, Berkeley
- 9:40 **Zinc-Oxide Thin Films for Integrated-Sensor Applications**
D.L. Polla, R.S. Muller - University of California, Berkeley

10:10-10:25

BREAK

- 10:25 **Tin Oxide Microsensors on Thin-Film Membranes**
S.C. Chang, D.B. Hicks - General Electric Research Laboratory
- 10:55 **Deposition Techniques and Properties of Strain Compensated LPCVD Silicon Nitride Films**
H. Guckel, D.K. Showers, D.W. Burns, C.K. Nesler, C.R. Rutigliano
- University of Wisconsin - Johnson Controls
- 11:25 **The Use of Micromachined Structures for the Measurement of Mechanical Properties and Adhesion of Thin Films**
M. Mehregany, M.G. Allen, S.D. Senturia
- Massachusetts Institute of Technology

12:00

ADJOURN

CHARACTERISTICS OF POLYSILICON LAYERS AND THEIR APPLICATION IN SENSORS

E. Obermeier, P. Kopystynski, R. Nießl

Fraunhofer-Institut für Festkörpertechnologie, Paul-Gerhardt-Allee 42
D-8000 Muenchen 50, Germany

Abstract: The important characteristics of boron doped LPCVD polysilicon layers with regards to sensor applications are presented. Properties such as the resistivity, temperature coefficient of the resistance, gauge factor, and long term stability are described. A pressure sensor utilizing polysilicon piezoresistors with a measurement range of 1 bar and a sensitivity of roughly 11 mV/V F.S. is discussed. Finally a polysilicon temperature sensor with on chip linearization, a sensitivity of $-3.5 \times 10^{-3} \text{ K}^{-1}$ and a linearity error of less than 0.5% is described.

Introduction

Polycrystalline silicon has been an important material in integrated circuit technology for many years [1]-[4]. Growing interest has been shown recently in the utilization of polysilicon as a basic material for sensors [5]-[8]. Next to the resistivity, of particular importance for the development of sensors which operate through a change in the electrical characteristics of polysilicon are the temperature coefficient of the resistance, the strain sensitivity (gauge factor) and the long term stability of the resistors. In the following sections are described our investigations of boron doped LPCVD (low-pressure chemical vapor deposition) polysilicon structures used for the development of pressure and temperature sensors.

Characteristics of boron doped polysilicon layers

For the investigations described below polysilicon layers with a thickness of $0.5 \mu\text{m}$ were deposited using LPCVD onto oxidized silicon wafers with an oxide thickness of $0.1 \mu\text{m}$. The layers were boron doped using ion implantation and then annealed in N_2 at 950°C for 30 min. Next the layers were patterned by wet chemical etching using negative photoresist as an etch mask. Metalization is accomplished through aluminum vapor deposition and another photolithographic patterning procedure. As a final step the wafers are annealed at 470°C for 20 min in an N_2 atmosphere.

Resistivity

Figure 1 shows the resistivity of boron doped polysilicon resistors as a function of doping concentration together with the resistivity of p-doped monocrystalline silicon. From this graph it can be seen that the resistivity of polysilicon layers is always higher than that of single crystal material, even when the boron concentration is very high. At low doping concentrations the resistivity climbs rapidly, so that only the impurity concentration range shown is of interest for sensor applications as described in this paper. The solid line shows the calculated values using the carrier trapping model [9].

Temperature Coefficient

The relative resistance change of boron doped LPCVD polysilicon resistors over a temperature range from -60°C to $+160^\circ\text{C}$ is shown in Figure 2 with the implantation dose as the varying parameter. The following points can be seen:

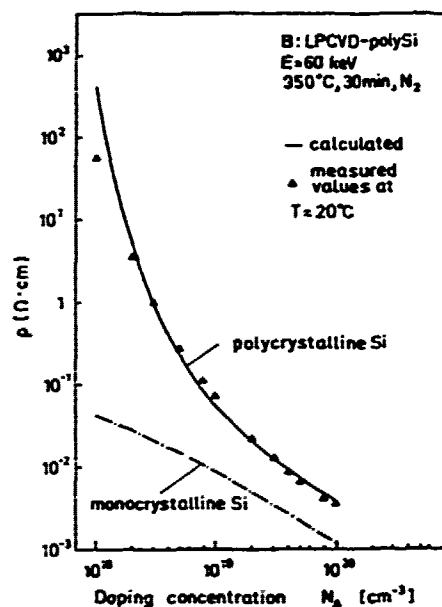


Fig. 1: Resistivity of boron doped LPCVD polysilicon as a function of doping concentration ($T=20^\circ\text{C}$).

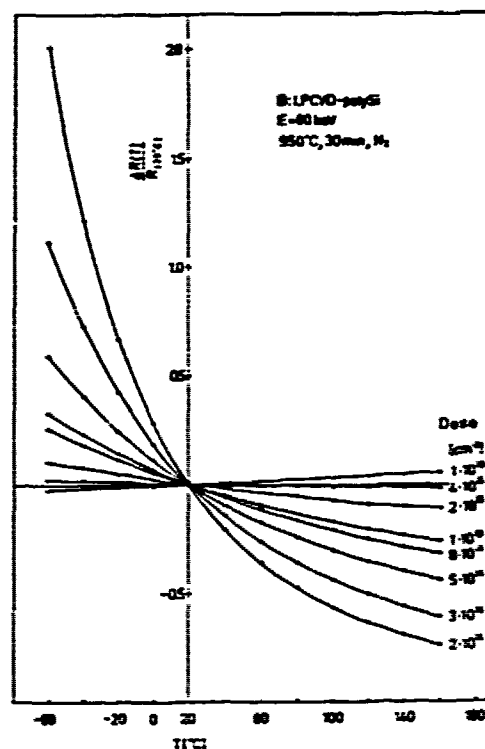


Fig. 2: Relative resistance change for boron doped LPCVD polysilicon resistors as a function of temperature.

- The resistance change with temperature is not linear.
- The temperature coefficient of the resistance may be selected over a wide range, both positive and negative, through selective doping.
- The temperature dependence increases with decreasing doping concentrations.

To determine the temperature coefficient α_R of the resistors, the curves in Fig. 2 are approximated between 0° and 40° through

$$R(T) = R_{20} \exp [\alpha_R (T - T_0)] \quad T \text{ in } ^\circ\text{C}, T_0 = 20^\circ\text{C}$$

where

$$\alpha_R = \frac{1}{R_{20}} \left. \frac{dR(T)}{dT} \right|_{T=20^\circ\text{C}}$$

is the temperature coefficient at $T = 20^\circ\text{C}$.

Figure 3 shows the change in the temperature coefficient α_R as a function of boron concentration N_A . From the figure it can be seen that the temperature coefficient of boron doped LPCVD polysilicon resistors can be negative, approach zero, or be positive depending on the doping concentration. This relationship is of particular importance for sensor applications. In comparison the temperature coefficient of monocrystalline p-doped silicon is shown in Fig. 3 as well [10].

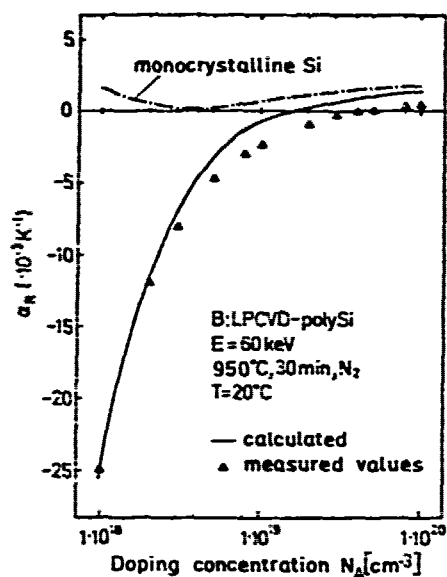


Fig. 3: Temperature coefficient of resistance for boron doped LPCVD polysilicon resistors for $T = 20^\circ\text{C}$.

Gauge factor

For the development of sensors for pressure, force, or acceleration knowledge of the strain sensitivity of polysilicon resistors expressed through the gauge factor is of particular interest. Figure 4 shows curves of the relative resistance change of boron doped polysilicon resistors, referenced to the resistance value R_0 under stress free conditions, as a function of longitudinal strain ϵ_l . The parameter varied is the implantation dose. It can be seen that the resistance decreases with compression and increases under tension. The resistance change with strain decreases with increasing doping concentration. This relationship is equivalent in principle to that of single crystal material [11]. The study was carried out through the utilization of a silicon cantilever beam structure with longitudinal and transverse polysilicon resistors.

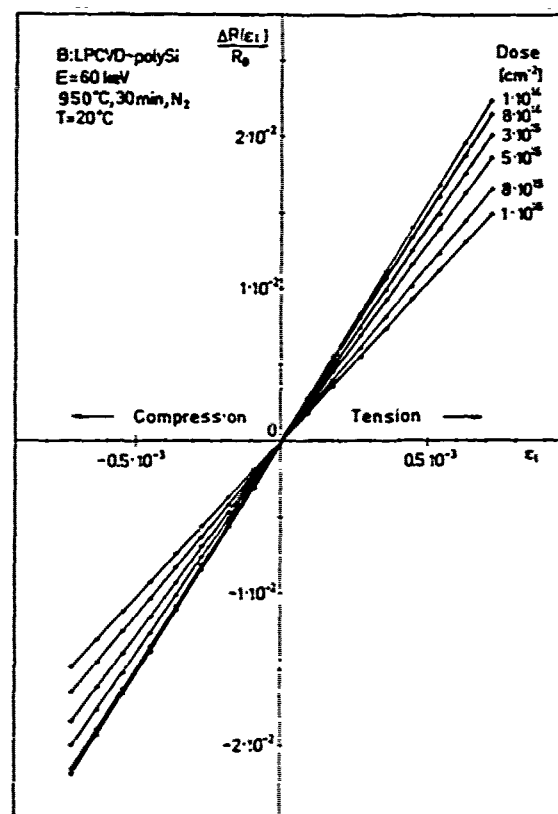


Fig. 4: Relative resistance change $(\Delta R/R_0)_l$ of boron doped polysilicon resistors as a function of the longitudinal strain ϵ_l .

Figure 5 shows the longitudinal and transverse gauge factors, G_l and G_t , as a function of the doping concentration N_A . G_l may be determined in accordance with Fig. 4 through the approximation

$$G_l = \frac{\Delta R}{R_0} \frac{1}{\epsilon_l}$$

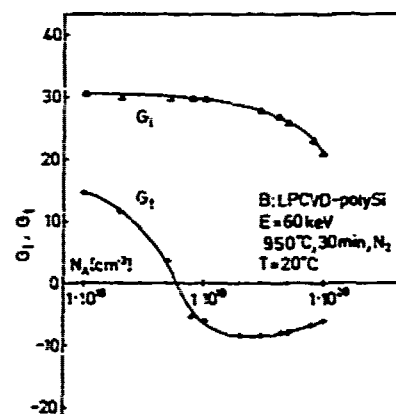


Fig. 5: Longitudinal and transverse gauge factor as a function of the doping concentration N_A of boron doped LPCVD polysilicon resistors under tension.

The maximum value of G_l in Fig. 5 is roughly 30 and is therefore roughly 15 times as large as metal strain gauges. In comparison with diffused piezoresistors this factor is however approximately 1/3 as large. The transverse gauge factor G_t displays an unusual characteristic which has not been explained up to this point in time. Due to this characteristic only the longitudinal gauge factor can be used for sensor applications.

In Figure 6 the longitudinal gauge factor is shown as a function of temperature. A linear reduction in G_l with increasing temperature can be observed. The temperature coefficient which can be determined from the curves shown can be expressed as

$$\alpha_l = \frac{1}{G_l} \left. \frac{dG_l}{dT} \right|_{T=20^\circ\text{C}}$$

and lies between $-2 \cdot 10^{-3} \text{ K}^{-1}$ and $-1 \cdot 10^{-3} \text{ K}^{-1}$. With increased doping the temperature coefficient decreases.

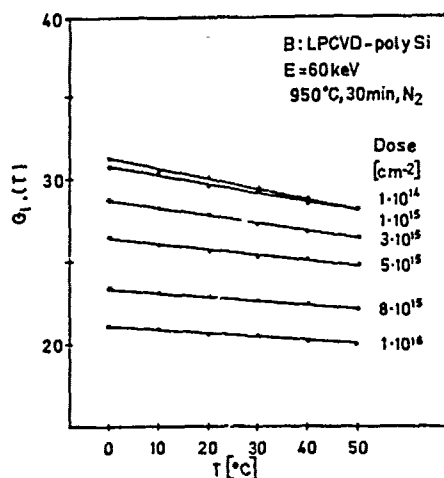


Fig. 6: Change of the longitudinal gauge factor G of boron doped LPCVD polysilicon resistors with temperature.

Longterm stability

Polysilicon resistors are capable of realizing at least as high a level of long term stability as may be expected from resistors in monocrystalline silicon since surface effects play only a secondary role in device characteristics. First results with non-passivated resistors show that at a temperature of 125°C over a time period of 1000 hours a drift of less than $5 \cdot 10^{-3}$ is obtained. It can be expected that passivation with a plasma deposited Si_3N_4 will result in a corresponding improvement in drift characteristics.

Polysilicon sensors

Pressure Sensor

Figure 7 shows the structural principle of the polysilicon pressure sensor described in this section. In this sensor the piezoresistors are no longer integrated in the single crystal silicon diaphragm, instead they are fabricated as polysilicon resistors.

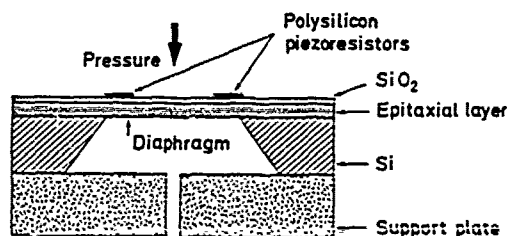


Fig. 7: Structural principle of a pressure sensor utilizing polysilicon piezoresistors.

Figure 8 shows the front and back sides of a pressure sensor chip with four polysilicon piezoresistors which are connected to a Wheatstone Bridge. The doping of the resistors was chosen to obtain the

smallest possible temperature coefficient of resistance at $N = 4.5 \cdot 10^{15}$ boron ions/ cm^2 . The resistance of the individual elements is roughly $1.8 \text{ k}\Omega$. The diaphragm fabrication is accomplished through an anisotropic etch with a $\text{KOH}/\text{H}_2\text{O}$ solution. A Si_3N_4 layer serves as an etch mask. The diaphragm dimensions are $1.5 \times 2.5 \times 0.03 \text{ mm}^3$. The fabrication of this sensor is presented in detail in [8], and [12].

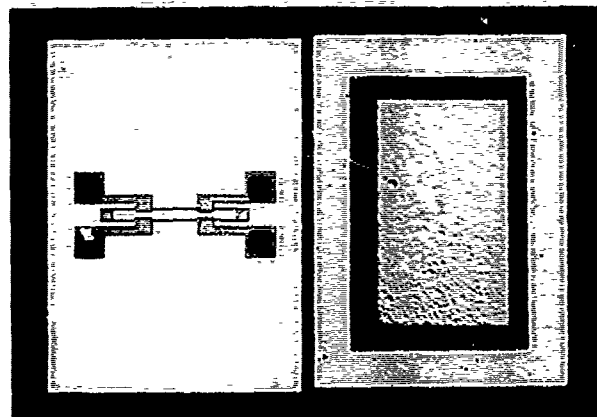


Fig. 8: Photograph of the sensor chip with polysilicon piezoresistors.

The output voltage characteristics V_o of the sensor are shown in Figure 9 as a function of pressure for the temperature range between -60°C and 200°C . At room temperature the sensor has a sensitivity of roughly 11 mV/V . The temperature coefficient of the offset voltage is $0.01\% \text{ F.S./}^\circ\text{K}$, of the sensitivity $-0.08\% \text{ F.S./}^\circ\text{K}$ and the linearity error is $\pm 0.35\%$. The temperature range given above is not meant to imply an operating temperature limit of the sensor as measurements up to 300°C have shown.

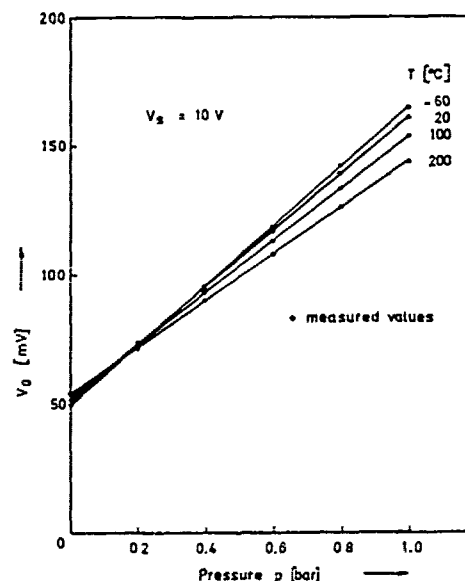


Fig. 9: Output voltage characteristics V_o of the pressure sensor as a function of pressure for temperatures between -60°C and $+200^\circ\text{C}$.

Temperature Sensor

Over a limited temperature range when linearity requirements are minimal a boron doped polysilicon resistor can be directly utilized as a temperature sensor. When however a reduced linearity error over a wider temperature range is required, the resistors temperature characteristics must be linearized. A reduced linearity error may be realized through a three point linearization method in which the actual characteristic curve of the sensor corresponds with a desi-

red line at three equidistant points [13]. The possibility of simultaneously realizing polysilicon resistors with comparatively large and very small temperature coefficients allows the placement of measurement and linearization resistors on the same chip. In this manner no external elements are needed for the linearization of the sensor characteristics.

Figure 10 shows a polysilicon temperature sensor with on-chip linearization. The resistors have varying doping concentrations and are adjusted to their specified values by laser trimming. The chip size is $1.5 \times 1.5 \text{ mm}^2$. In Figure 11 the characteristic curves of this sensor for temperatures between -40°C and $+140^\circ\text{C}$ are displayed. The sensitivity of the sensor is $-3.5 \times 10^{-3} / ^\circ\text{K}$. At room temperature the resistors have a value of $1 \text{ k}\Omega$.

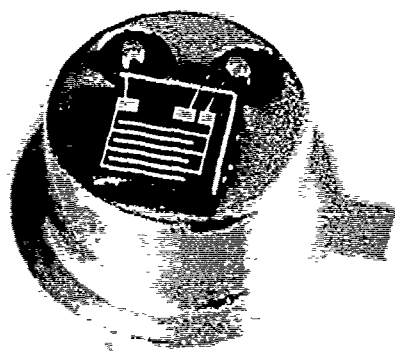


Fig. 10: Polysilicon temperature sensor with on-chip parallel linearization.

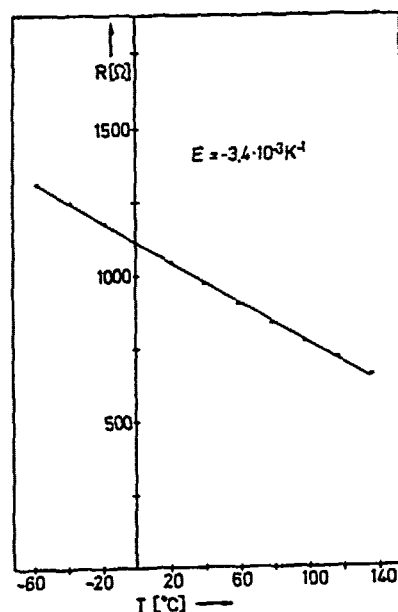


Fig. 11: Characteristic curve of the polysilicon temperature sensor shown in Figure 10.

Conclusion

From the investigations described here the following preferential characteristics for utilizing polysilicon layers as a sensor material have been determined:

- The layers may be deposited on electrically insulating substrates.
- The processing is compatible with semiconductor fabrication technology.
- Layers are easily structured.

- Junction isolation is not necessary thus allowing sensor operation over a larger temperature range.
- By varying the doping concentration the temperature coefficient of the resistor may be selected over a wide range, positive, negative, or zero.
- Polysilicon layers exhibit a comparatively large and isotropic piezoresistance effect.
- The layers are highly reproducible and exhibit homogeneous characteristics.
- Through laser trimming the resistance values can be selectively adjusted.

From these advantages the many sided application possibilities of polysilicon layers in measurement technology applications can be clearly seen. The dielectric isolation of the layers in connection with an increased operating temperature range, the possibilities for temperature compensation and the trimming capabilities are the most important advantages of polysilicon as opposed to monocrystalline silicon.

Acknowledgement

We would like to thank I. Schulz for her valuable assistance.

References

- [1] R.S. Rosler, "Low Pressure CVD Production Processes for Poly, Nitride, and Oxide," *Solid State Technol.*, vol. 20, pp. 63-70, Apr. 1977.
- [2] W. Kern, G.L. Schnable, "Low-pressure Chemical Vapor Deposition for Very Large-scale Integration Processing - A Review," *IEEE Trans. Electron Devices*, vol. ED-26, No. 4, pp. 647-657, Apr. 1979.
- [3] F. Faggin, T. Klein, "Silicon Gate Technology," *Solid-State Electr.*, vol. 13, pp. 1125-1144, 1970.
- [4] F. Masuoka, K. Ochi, M. Masuda, K. Kobayashi, and T. Kondo, "A New High Density Full CMOS SRAM Cell Using Polysilicon Interconnection Structure," in *IEDM Technical Digest*, Washington, D.C., pp. 280-283, 1985.
- [5] R.T. Howe, R.S. Muller, "Polycrystalline Silicon Micromechanical Beams," *J. Electrochem. Soc.*, vol. 130, No. 6, pp. 1420-1423, June 1983.
- [6] W. Benecke, L. Csepregi, A. Heuberger, K. Kuhl, H. Seidel, "A Frequency-selective, Piezoresistive Silicon Vibration Sensor," in *Proc. Transducers '85*, Philadelphia, pp. 105-108, 1985.
- [7] H. Guckel, D.W. Burns, "A Technology for Integrated Transducers," in *Proc. Transducers '85*, Philadelphia, pp. 90-92, 1985.
- [8] E. Obermeier, "Polysilicon Layers Lead to a New Generation of Pressure Sensors," in *Proc. Transducers '85*, Philadelphia, pp. 527-536, 1985.
- [9] N.C.C. Lu, L. Gerzberg, and J.D. Meindl, "A Quantitative Model of The Effect of Grain Size On The Resistivity of Polycrystalline Silicon Resistors," *IEEE Electron Device Lett.*, Vol. EDL-1, no. 3, pp. 38-41, 1980.
- [10] W.M. Bullis, F.H. Brewer, C.D. Kolstad and L.J. Swartzendruber, "Temperature Coefficient of Resistivity of Silicon and Germanium Near Room Temperature," *Solid-State Electr.*, vol. 11, pp. 639-646, 1968.
- [11] O.N. Tufte, E.L. Stelzer, "Piezoresistive Properties of Silicon Diffused Layers," *J. Appl. Phys.*, vol. 34, pp. 313-318, 1963.
- [12] E. Obermeier, F.v. Kienlin, "Silizium-Drucksensor für hohe Betriebstemperaturen," in *Proc. Sensor '85*, Karlsruhe, pp. 4.3-4.3.12, 1985.
- [13] A. Burke, "Linearizing Thermistors with a Single Resistor," *Electronics*, pp. 151-154, June 1981.

DESIGN AND CONSTRUCTION TECHNIQUES FOR PLANAR POLYSILICON PRESSURE TRANSDUCERS WITH PIEZORESISTIVE READ-OUT

H. Guckel, D. W. Burns and C. R. Rutigliano
Wisconsin Center for Applied Microelectronics
Department of Electrical and Computer Engineering
1415 Johnson Drive
Madison, WI 53706

We have previously reported on experimental construction techniques for planar, vacuum sealed piezoresistive pressure transducers which are fabricated from polysilicon.¹ Fabrication methods have now been finalized and involve a polysilicon diaphragm which is reactive-sealed using a low strain LPCVD silicon nitride layer.² The nitride is also used for dielectric isolation of polysilicon strain sensors which are formed from a second polysilicon film. A stable, high yield processing sequence has been achieved.

In order to make this work useful a design method is needed which converts pressure transducer specifications to device structure. The design algorithm must predict plate stresses, strains and deflections. This is complicated by the non-zero, but reproducible built-in strain field which has a first order effect on thin film plates. Virtual displacement techniques and a double trigonometric series are used to produce the necessary mechanical data for rectangular plates. The differential equation describing plate deflections w as a function of applied pressure q and stresses due to the built-in strain field N_x , N_y , and N_{xy} is³

$$\frac{\partial^4 w}{\partial x^4} + 2 \frac{\partial^4 w}{\partial x^2 \partial y^2} + \frac{\partial^4 w}{\partial y^4} = \frac{1}{D} (q + N_x \frac{\partial^2 w}{\partial x^2} + N_y \frac{\partial^2 w}{\partial y^2} + N_{xy} \frac{\partial^2 w}{\partial x \partial y})$$

If the deflection profile is known, the bending and twisting moments, and shear forces can be calculated. The boundary conditions are for the case of clamped edges. A solution of the form

$$w(x,y) = \sum_{m=1}^{\infty} \sum_{n=1}^{\infty} b_{mn} (1-(-1)^m \cos \frac{m\pi x}{a}) (1-(-1)^n \cos \frac{n\pi y}{a})$$

where the coefficients b_{mn} are given by

$$b_{mn} = \frac{3q(1-\nu^2)a^4}{\pi^4 E h^3 (3m^4 + 2m^2 n^2 + 3n^4) (1 + \frac{9(1-\nu^2)(m^2 + n^2)\epsilon_0 a^2}{\pi^2 (3m^4 + 2m^2 n^2 + 3n^4) h^2})}$$

satisfies the boundary conditions and converges to the deflected surface. The origin is located at the center of the plate. The formulation also predicts a critical built-in strain value, ϵ_0 , that will cause a plate of a given length to thickness ratio (a/h) to buckle. The algorithm produces plate dimensions to give the maximum strain sensitivity within the limits set by processing considerations. These limits include plate size due to buckling for compressive films, minimum and maximum thickness for the plate which is set by mechanical and patterning constraints, and maximum stresses before fracturing.

The built-in strain field modifies the deflections and strain sensitivity appreciably. The built-in strain is dependent on processing procedures. It can be determined and monitored during device fabrication by buckling of cofabricated doubly supported beams.⁴

The plate behavior is monitored by using polysilicon strain-sensitive resistors.⁵ The mechanical and electrical response of these devices have been studied using cantilever beam techniques. The temperature behavior, gage factor and noise figure for the resistors have been measured. The ability to produce p- and n-doped structures with opposite gage factors is of particular interest.

Resistor data and mechanical data are combined to determine resistor placement. At least two design constraints occur: a fully active bridge configuration and the need to minimize the influence of optical alignment tolerances. The design algorithm accounts for both problems. Fully active bridges are realized using n- and p- resistors on the plate. The alignment problem is reduced considerably by extending the piezoresistors slightly beyond the plate edge and with turn-around points located at the zero-strain points on the plate. Calculation of strain sensitivities must include the variation of strain with position on the piezoresistive element as well as effects of geometrical changes during loading. The algorithm has been used to design absolute pressure transducers for 15 psi, 100 psi and 500 psi. The designs are based on built-in strains of -0.05% with 2 micron polysilicon thickness. Plate dimensions of 147, 100 and 73.8 micron, respectively, have been calculated and are currently being tested in fabricated transducers. Test results for the 1 atm gages show full-scale resistance changes of 1.2% for resistor values of 47-49k Ω .

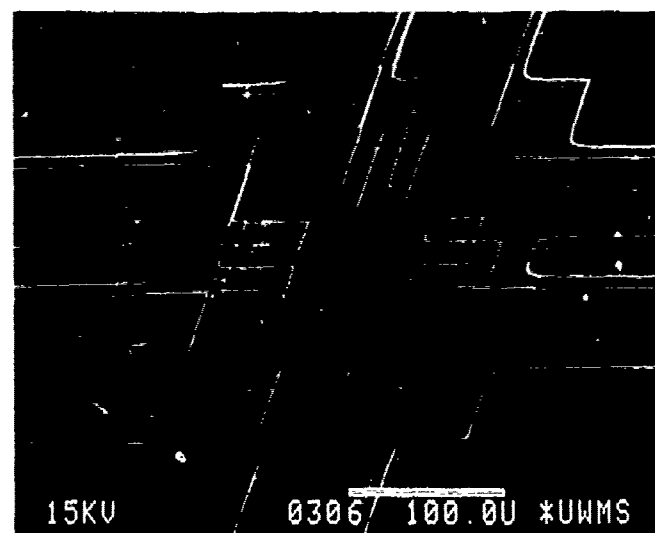


Fig. 1. An SEM of a bonded 100 psi transducer shows the serpentine piezoresistor configuration which minimizes placement error.

References

- [1] H. Guckel and D. W. Burns, "Planar Processed Polysilicon Sealed Cavities for Pressure Transducer Arrays," Technical Digest IEEE IEDM, 1984, p. 233.
- [2] H. Guckel, D. K. Showers, D. W. Burns, C. R. Rutigliano and C. G. Nesler, "Deposition Techniques and Properties of Strain Compensated LPCVD Silicon Nitride Films", this conference.
- [3] Timoshenko, Theory of Plates and Shells, Second Edition, McGraw-Hill Book Co., New York, 1959, Ch. 4.
- [4] H. Guckel, T. Randazzo and D. W. Burns, "A Simple Technique for the Determination of Mechanical Strain in Thin Films with Applications to Polysilicon," J. Appl. Phys. 57(5), 1 March 1985, p. 1671-1675.
- [5] E. Obermeier, "Polysilicon Layers Lead to a New Generation of Pressure Sensors," IEEE Transducers '85 Technical Digest, 1985 International Conference on Solid-State Sensors and Actuators, p. 430.

INTEGRATED POLYSILICON TACTILE SENSOR

A.K. Oki * and R.S. Muller

Department of Electrical Engineering and Computer Sciences
and the Center for Research on Integrated Sensors
University of California, Berkeley, California 94720

ABSTRACT

A polysilicon tactile sensor that is sensitive to tangential force has been designed, fabricated, and tested. Microfabrication of silicon is employed to create a sensor that has a linear response of 465 mV N^{-1} of tangential force over a force range of $\pm 6.25 \text{ mN}$. The minimum resolvable tangential force is $42 \text{ }\mu\text{N}$.

INTRODUCTION

The ability to sense touch is highly desirable for many robotics and manufacturing applications. In Harmon's comprehensive survey of automated tactile sensing¹, it is reported that touch sensing will become indispensable for robotic manipulation and assembly. Sensors that range from mere contact devices to highly sensitive tactile elements have been demonstrated and are commercially available for force perpendicular to surfaces. Tangential force has proven to be more difficult to detect. Previously reported tangential force sensors have depended on polymeric interfaces to transmit the force^{2,3}. Polymer tactile sensors have hysteresis problems and long recovery times that impede their use in slip-detection feedback loops which are necessary for robotic manipulators.

Polysilicon has been demonstrated to have many advantages as a material for monolithic integrated sensors. It can be precisely micromachined to create sensor structures using conventional semiconductor-fabrication techniques⁴ and its piezoresistive⁵ and pyroresistive nature⁶ allow it to be used for sensing. These qualities are exploited in this work to create a novel tactile sensor.

DEVICE FABRICATION

Fabrication was carried out using a 4-mask process in the University of California, Berkeley EECS Microelectronics Laboratory. Figure 1 shows a perspective view of the fabricated sensor which is $2.5 \text{ }\mu\text{m}$ in width by $100 \text{ }\mu\text{m}$ in length, and $1.5 \text{ }\mu\text{m}$ in height.

The starting material is a (100) 4-inch p-type silicon wafer with a resistivity of $50 \text{ }\Omega\text{cm}$. In order to simulate an MOS compatible process, a 580 nm -

thick layer of thermal silicon dioxide is grown by wet oxidation and forms the foundation for the sensor. A $1.5 \text{ }\mu\text{m}$ -thick layer of undoped LPCVD polysilicon is deposited and patterned using standard photolithographic techniques. The polysilicon is RIE plasma-etched in a Lam plasma etcher using 95 sccm CCl_4 , 80 sccm helium , and 5 sccm oxygen at 300 watts and 240 millitorr . These conditions produce an etch rate of 375 nm/min for polysilicon, 30 nm/min for silicon dioxide, and 100 nm/min for Kodak 820 photoresist. The plasma etch results in a near vertical polysilicon sidewall. The polysilicon is then thermally oxidized in steam at 915°C for 30 minutes to provide electrical isolation and act as a diffusion barrier. A second layer of undoped LPCVD polysilicon is deposited to form the piezoresistive sensing element. The wafer is annealed at 1100°C for 120 minutes in nitrogen to increase the polysilicon grain size for optimum piezoresistivity. The wafer is ion-implanted with boron at an energy of 40 keV and a dose of $1.5 \times 10^{15} \text{ cm}^{-2}$. It is then annealed in nitrogen at 1000°C for 30 minutes to activate the implant and obtain a uniform boron concentration in the polysilicon. A MOSFET polysilicon spacer technique is used to remove polysilicon from the top of the sensor and retain the polysilicon on the sidewalls. In this technique, one micrometer of positive photoresist is spun on. The planarizing properties of the photoresist result in a thinner layer over a high step than above the rest of the wafer. Etching $0.6 \text{ }\mu\text{m}$ of the photoresist in an oxygen plasma removes it from the top of the sensor and leaves $0.4 \text{ }\mu\text{m}$ over the field. The piezoresistor polysilicon is defined in an RIE plasma etch using the steps previously described. Aluminum is sputtered for the interconnect metalization, which is patterned, wet etched, and sintered at 450°C for 15 minutes in forming gas.

THEORY

The sensor, shown in Fig. 2, forms a cantilevered beam loaded by a tangential force F applied in the x -direction which causes stress σ that increases linearly to the support end of the beam.

$$\sigma = \frac{F x y}{I} \quad (1)$$

where I is the moment of inertia and y is measured from the free end. For a rectangular structure of width w and height h_b ,

$$I = \frac{h_b w^3}{12} \quad (2)$$

Substituting Eq. 2 into Eq. 1, we find

$$\sigma = \frac{12 F x y}{h_b w^3} \quad (3)$$

To find the average stress in the sensing element on the right side of Fig. 2, we integrate the stress over the piezoresistor cross-section and divide by its area.

$$\sigma_{avg} = \frac{1}{h_a w_a} \int \sigma(x, y) dA \quad (4)$$

where h_a and w_b are the height and thickness of the piezoresistor, respectively. Solving the integral and substituting the dimensions of the sensor,

$$\sigma_{avg} = 2.5 \times 10^{-3} F \text{ [N } \mu\text{m}^{-2}] \quad (5)$$

The tangential force F , applies compressive stress to the right-sensing element, and an equal magnitude of tensile stress to the left-sensing element. These elements are polysilicon piezoresistors with currents flowing transverse to the direction of the stress. Therefore, the force results in an equal and opposite change in resistance of the two polysilicon resistors.

$$\frac{\Delta R}{R} = G \sigma_{avg} E^{-1} \quad (6)$$

where G is the transverse gauge factor of the polysilicon and E is the modulus of elasticity. The transverse gauge factor for polysilicon with boron doping of $5 \times 10^{19} \text{ cm}^{-3}$, that has been annealed at 1100°C for 2 hours is -13.6. Substituting constants, the theoretical output from a half bridge, biased with 2 V, is

$$\frac{\Delta V}{F} = 465 \text{ [mV N}^{-1}] \quad (7)$$

RESULTS

The sensor output was measured using a half-bridge amplifier circuit in a static-test setup. The wafer was diced, mounted, and bonded to the top surface of a 40 pin DIP which was plugged into a breadboard mounted on an xy stage. A 2mm square chip from a silicon wafer was placed on an array of sensors. A microprobe loaded with weights was used to control the normal force on the silicon. The weights were suspended by a string running over a pulley and attached to the stage.

The sensor response to the tangential force is shown in Fig. 3. A linear output is observed as predicted in Eq. 7 for forces less than 300 mN loading an array of elements. For a single element the corresponding force was 6.25 mN. The calculated modulus of elasticity was $7.0 \times 10^{-2} \text{ N}/\mu\text{m}^2$ which is less than the bulk silicon value ($19 \times 10^{-2} \text{ N}/\mu\text{m}^2$).⁷

A time-varying force was applied to study the frequency response and hysteresis characteristics of the sensor. A piece of elastic was attached between the xy stage and a calibrated strobe wheel. The revolving wheel applies a varying tangential force to the stage. For a frequency of less than 5 Hz, the sensor response showed no hysteresis. At higher frequencies the testing setup proved inadequate.

CONCLUSIONS

Polysilicon has been used to build an integrated tactile sensor sensitive to tangential force. The device demonstrates high sensitivity to tangential force, and a linear output.

ACKNOWLEDGEMENTS: The authors thank R.M. White, D.L. Polla, G. Dairiki, and J. Goicolea for their technical support, and J. B. Camou for manuscript preparation.

This research was funded, in part, by the National Science Foundation under grant ECS-8120562 and, in part, by the State of California MICRO program.

REFERENCES

- [1] L.D. Harmon, "Automated Tactile Sensing," *The International Journal of Robotics*, vol. 1, No.2, pp 3-33, 1982.
- [2] L.S. Fan, R.S. Muller, and R.M. White. "A Mutual Capacitive Normal and Shear Sensitive Tactile Sensor," *IEDM 1984*, pp 220-221, IEEE, San Francisco, CA, December 10-12, 1984.

- [3] S. Hackwood et al., "A Torque-Sensitive Tactile Array For Robotics," *The International Journal of Robotics*, vol. 2, No. 2, pp. 46-50. Summer 1983.
- [4] R.T. Howe, "Integrated Silicon Electromechanical Vapor Sensor," *Doctoral Dissertation*, Dept. of EECS, University of California, Berkeley, CA, May 1984.
- [5] Y.C. Tai, R.S. Muller, and R.M. White, "Polysilicon Bridges For Anemometer Applications", *1985 IEEE Int. Conf. On Solid-State Sensors and Actuators*, pp.354-357, June 1985.
- [6] E. Obermeier, "Development of a New Type of Semiconductor Pressure Sensor Utilizing Polycrystalline Silicon Films," *Doctoral Dissertation*, Technical University of Munich, 1984.
- [7] R.S. Muller and T.I. Kamins, *Device Electronics For Integrated Circuits*, pp.34, 1977.

*Present Address: TRW, Advanced Microelectronic Lab, One Space Park, Redondo Beach, CA 90278

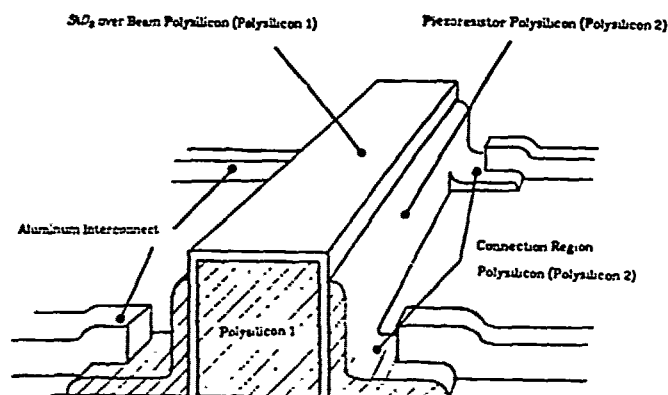


Figure 1. Perspective of the polysilicon sensor.

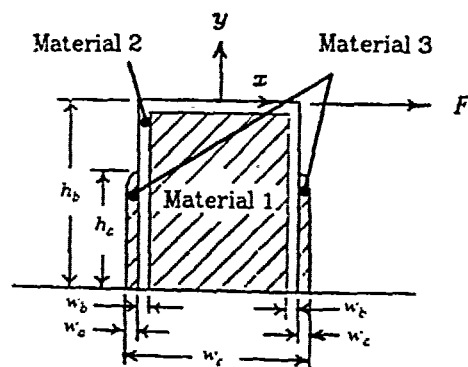


Figure 2. Cross section of the beam showing orientation of the tangential force F.

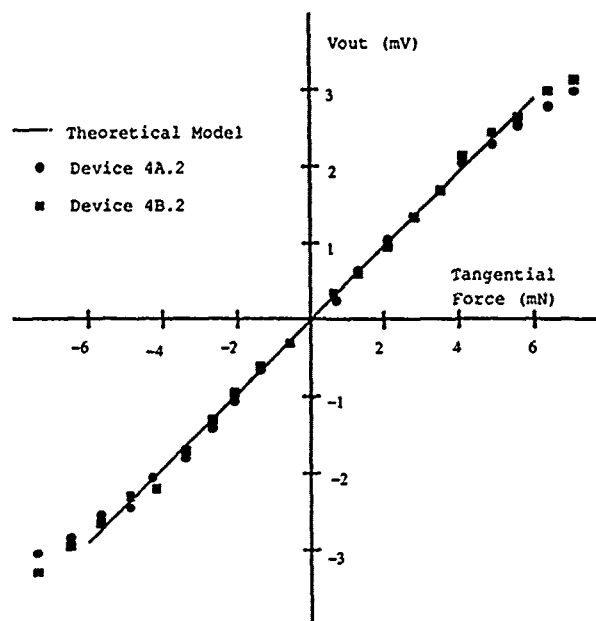


Figure 3. Half Bridge Response of Sensor To Tangential Force

A MONOLITHIC GAS FLOW SENSOR WITH POLYIMIDE AS THERMAL INSULATOR

Göran N. Stemme
Department of Solid State Electronics
Chalmers University of Technology
S-412 96 Gothenburg, Sweden

Abstract

A novel small monolithic gas flow sensor has been designed and fabricated by use of micromachining of silicon. Its operation is based on the cooling of an electrically heated mass by the gas flow, and detection of the mass's temperature by a diode. The small size, 0.4 mm by 0.3 mm by 30 μ m, of the hot part of the sensor gives a fast thermal response (50 ms). By using polyimide as a thermal insulator a high gas flow sensitivity is achieved. The shape of the sensor will present very little obstruction to the gas flow and also makes it easy to mount.

Introduction

A very common type of gas flow sensing with no moving parts is based on heat transfer by convective cooling between the sensor and the gas flow. The classical example of such a sensor is the hot-wire anemometer. However, the hot-wire anemometer has several drawbacks: It is difficult to calibrate and requires rather complicated electronics. Furthermore it is fragile and difficult to mount in the gas stream. To solve these problems, a number of gas flow sensors in silicon have been developed [1] - [5]. The silicon gas flow sensor to be presented here has several advantages over other gas flow sensors. It is extremely small. A special geometry and the small size of the sensor results in minimal disturbance of the gas flow and good measurement accuracy. The small mass provides a fast thermal response. Another advantage of this sensor is good thermal isolation between the hot part of the sensor and the supporting structure, thus increasing the sensitivity and further improving the thermal response time. The sensor has a mechanical structure that makes it easy to mount. By using standard silicon process technology, silicon micromachining and batch-fabrication it is possible to produce low cost, identical and small gas flow sensors.

Sensor design

The gas flow sensor consists of three main parts shown in Fig. 1. It has a base plate with five electrical bonding pads, which connect the sensor to external circuits. A silicon beam, extending from the base plate, protrudes through a hole in the tube wall into the gas stream in which the flow is to be measured. In order to measure the beam temperature, a temperature sensing diode is integrated on the silicon beam. At the far end of the silicon beam, four electrical conductors connect the active part of the sensor, a 0.3 mm by 0.4 mm by 30 μ m large chip, which is attached to the beam by a bridge of thermally insulating polyimide. This chip is heated electrically by dissipation in an integrated 100 ohms ion implanted resistor. An ion implanted diode similar to the one on the silicon beam is also integrated on the chip. The diode and the resistor on the chip, together with an external temperature regulator, control the chip temperature.

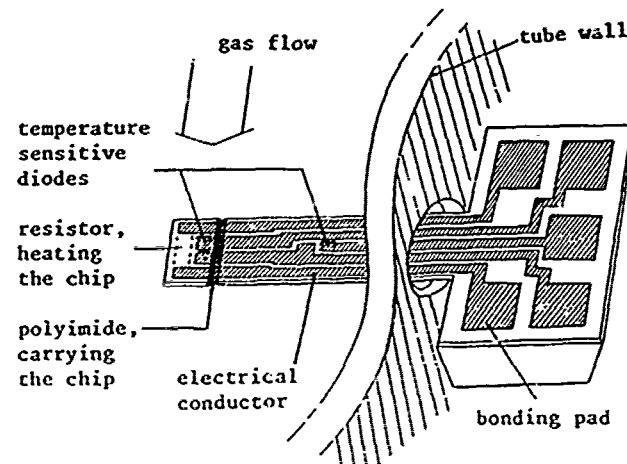


Fig. 1. The gas flow sensor with its three parts; the base plate (1.5 mm by 1.0 by 0.3 mm), the silicon beam (1.6 mm by 0.4 mm by 30 μ m) and the chip (0.4 mm by 0.3 mm by 30 μ m).

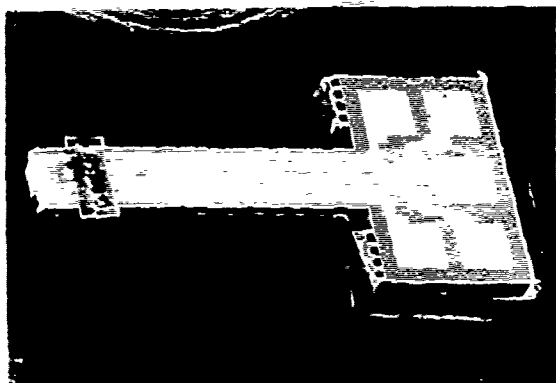
Fabrication

The micromachining was achieved by using EDP (ethylenediamine, pyrocatechol and water), an anisotropic silicon etch [6], [7].

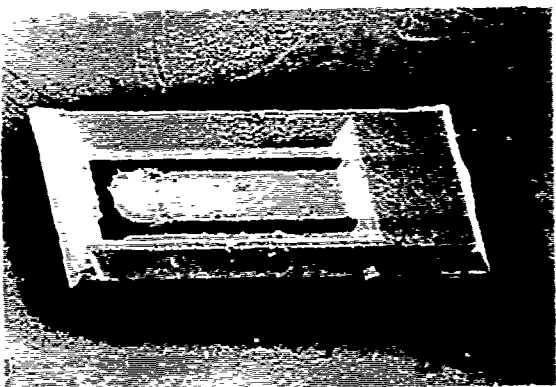
The first front side silicon etch resulted in an array of holes with different known depths shown in Fig. 3(a). These holes were used to determine the thickness of the membrane, shown in Fig. 3(b), which was etched next from the back side. The etching of the membrane was not critical and resulted in a membrane thickness of 20 - 50 μ m.

Next followed a series of standard process steps of photolithography and ion implantation forming the resistors, diodes and the ohmic substrate contacts. As an intermediate step silicon dioxide was deposited to a thickness of approximately 1 μ m on the back of the wafer. A short silicon etch on the front side finally defined the silicon beam and the active chip. A special pattern in the metal layer was used together with the convex corner etch characteristic of EDP to create the undercut channel under the four chrome-gold conductors connecting the chip to the beam. The etch uncovered the oxide deposited on the back and resulted in the chip hanging on the thin oxide membrane.

Polyimide was spun on the front of the wafer at low speed, filling the grooves and the space under the metal bridges, as illustrated in Fig. 3(d). Since the polyimide used is also a negative-working photoresist, a photolithographic step removed all polyimide except the one under (and over) the metal bridges, achieving the purpose of the polyimide, which was to join the beam to the chip and act as a thermal insulator. This is shown in Fig. 3(e).



(a)



(b)

Fig. 2. SEM photographs of the front side (a) and back side (b) of the sensor, without and with the protective silicon frame.

Finally the wafers were broken into individual components along the grooves which were etched through the wafers. The components had a frame of silicon to protect the active chip during handling. By breaking this frame it was removed as a last step before the mounting of the sensor. See Fig. 2.

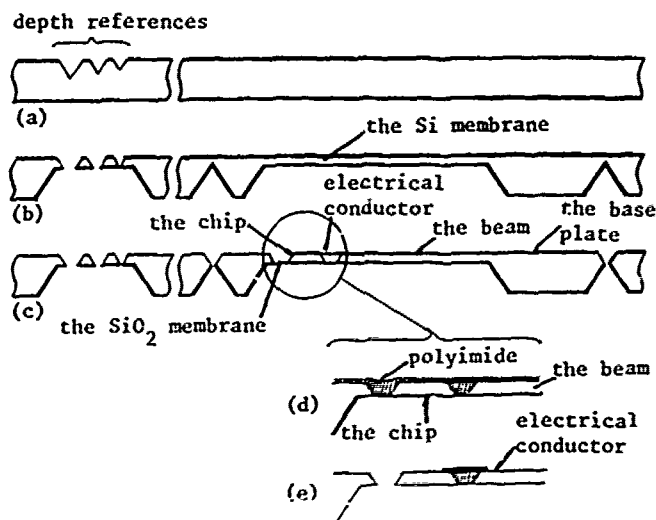


Fig. 3. A cross-sectional view of the sensor during fabrication. (a), (b) and (c) After the first, second, and third silicon etch steps. (d) Shows the sensor after polyimide application and (e) after polyimide lithography and SiO_2 membrane etch.

Measurements

Two types of sensors were used in order to investigate the improved performance of a sensor with a polyimide bridge; one type where the silicon between the beam and the chip was completely removed and replaced by polyimide, acting as supporting and insulating material, and a second type where approximately 50 % of the silicon, between the chip and the beam, was left as supporting material.

If the temperature difference between chip and flow is kept constant by using an external temperature regulator, and if it is assumed that the gas parameters (thermal conductivity, density and viscosity) are constant (true for a limited gas temperature range) then it is possible to show [8] that the input electrical power dissipation, P_e , is given by

$$P_e = C_1 v^{0.5} + P_c \quad (1)$$

where the free stream gas flow velocity, v , is in parallel with the frontside of the chip and C_1 and P_c are constants.

In Fig. 4 the power dissipation versus flow velocity has been plotted for the two types of sensors, where the chips were regulated to 100°C above gas temperature (the gas temperature was approximately 23°C). Using (1), a least square fit, regarding P_e and C_1 , to measured data was made. There is a good agreement in Fig. 4 to the square-root dependence assumed in (1).

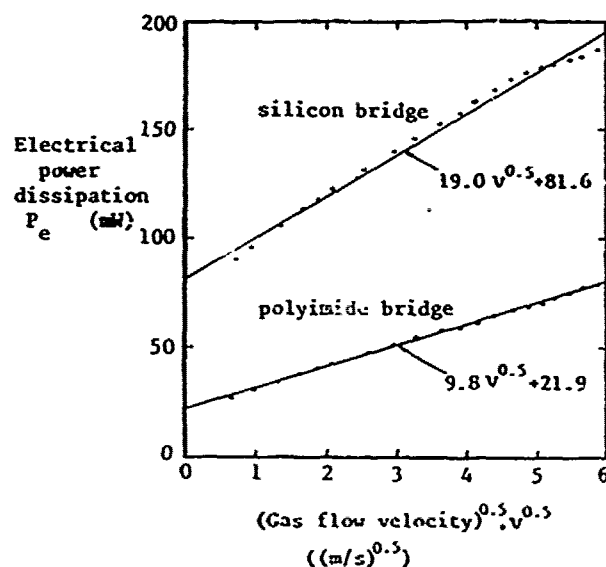


Fig. 4. Electrical power dissipation versus the square root of the gas flow velocity for the polyimide bridge sensor and the silicon bridge sensor. The least square fits to the data points are also plotted. The sensors were regulated to a temperature of 100°C above gas temperature.

Measurements of speed were also made by letting the resistor power dissipation have the form of a pulse and studying the temperature responses of the sensors. The pulse power to each sensor was adjusted to give the same temperature of approximately 100°C above gas temperature. Typical responses can be found in Fig. 5. The polyimide bridge type of sensor reached a steady-state value much faster than the silicon bridge sensor. When the pulse was applied, it took the polyimide bridge sensor 0.45 seconds to reach one degree centigrade from the steady-state value, while it took the silicon bridge sensor more than 15 seconds to reach the same temperature. The polyimide bridge sensor has a fast time constant around 50 ms.

Conclusions

A gas flow sensor, fabricated by using micromachining techniques and silicon fabrication technology has been described. It presents very little obstruction to the gas flow, has a fast thermal response, a high sensitivity, is easily mountable and can be mass produced using batch processing.

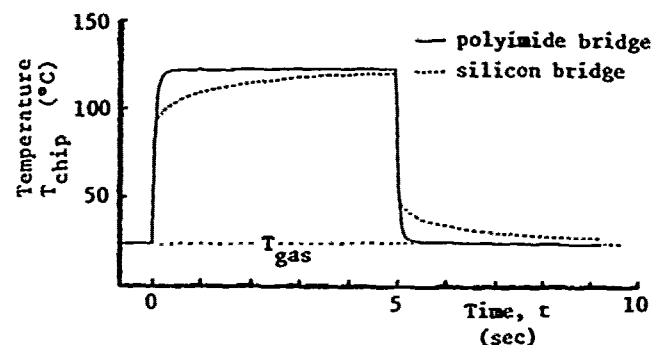


Fig. 5. Temperature responses from pulses of the electrical power dissipation for the polyimide bridge sensor and the silicon bridge sensor. The power applied in order to obtain the same temperature of 100°C above gas temperature was 130 mW and 45 mW for the silicon bridge sensor and the polyimide bridge sensor. The gas flow velocity was 1 m/s.

References

- [1] L.A. Rehn, et al., "Dual-element solid-state fluid flow sensor", 1980 Society-of-Automotive-Engineers, Inc., SAW/SP-80/458/S02.50, pp. 101 - 106.
- [2] J.H. Huysing, "Monolithic flow sensors, a survey", Proc. Vaste Stof Sensoren, Conf. University of Delft, The Netherlands, Dec., 1980, pp. 39 - 48.
- [3] A.F.P. van Putten and S. Middelhoek, "Integrated silicon anemometer", Electronics Letters, vol. 10, October 1974, pp. 425 - 426.
- [4] R.W.M. van Riet and J.H. Huysing, "Integrated direction-sensitive flowmeter", Electronics Letters, vol. 12, November 1976, pp. 647 - 648.
- [5] A.F.P. van Putten, "An integrated silicon double bridge anemometer", Sensors and Actuators, vol. 4, November 1983, pp. 387 - 396.
- [6] K.E. Bean, "Anisotropic etching of silicon", IEEE Trans. Electron Devices, vol. ED-25, October 1978, pp. 1185 - 1193.
- [7] K.E. Petersen, "Silicon as mechanical material", Proc. IEEE, vol. 70, May 1982, pp. 420 - 457.
- [8] J.R. Welty, Engineering Heat Transfer, New York: John Wiley & Sons, 1978.

A MICROMACHINED MANIPULATOR FOR SUBMICRON POSITIONING OF OPTICAL FIBERS

A. M. Feury
Dept. of EE
Rutgers University
Piscataway, N.J. 08854

T. L. Poteat
AT&T Bell Labs
Murray Hill, N.J. 07974

W. S. Trimmer
AT&T Bell Labs
Holmdel, N.J. 07733

Abstract

Described is a micromanipulator that is fabricated from IC-compatible processes and can position in x-y coordinates to submicron accuracies. The active portion uses micromachined silicon feet and piezoelectric beams. Its "stage" is a silicon wafer with CVD insulators. Applications include an optical fiber alignment device operating in a closed loop mode with positional resolution of 500 Angstroms. Other possible applications will be discussed.

Introduction

The application of optical fiber to digital communication systems has created a need for precision optical fiber connectors. That need is currently being satisfied by components that have rigid manufacturing specifications and are therefore expensive. Switching functions generally require conversion from photonic to electronic energy due to a lack of optical switches. An active connector that can position one or more optical fibers and reposition them to an alternate (nearby) site removes the requirement for manufacturing precision and it also achieves the desired switching function. The mechanical requirements on the connector components of thin, near ideal insulating layers on very flat, smooth feet are difficult (expensive) to satisfy in conventional metal systems but are easily met in IC processing facilities. Silicon parts can be batch fabricated with high accuracy, the material is strong and well characterized, electronics can be integrated into the silicon parts, and these parts lend themselves well to small mechanical systems. We believe silicon micromachining techniques can produce unique user-driven manipulators using the versatile, ubiquitous silicon.

Device Operation and Configuration

Operation of other manipulators has been previously discussed [1]. A voltage applied between conductors that are

closely spaced generates an electrostatic attraction between the conductors. This force can be on the order of pounds per square centimeter at modest voltages (~100 Volts) if the separation between the conductor plates is submicron. This spacing requirement is easily met with single crystal silicon and CVD insulators such as silicon nitride. Piezoelectric ceramics are readily available at modest cost.

We characterized an 15 mm square device by mounting an optical fiber to one foot and mounting another fiber through the substrate to form a switch. A closed-loop program allowed the fibers to be disconnected and reconnected while gathering statistics on step size and repeatability. Other configurations such as crossed-beam and L-shaped manipulators were also constructed.

Conclusion

The ability to micromachine silicon with high accuracies makes it an attractive material for manufacturing small mechanical parts. These parts do not need to be tethered to the silicon, but can be part of freely moving engines. These engines can in turn do a number of useful functions. The micromanipulator described above is useful for aligning components to high accuracies. Other possible applications for freely moving manipulators include assembly and repair of small systems. Having taken a step onto silicon, there are many intriguing possibilities.

References

- [1] G. Binnig and C. Gerber, "A Piezo Drive with Course and Fine Adjustments," IBM Tech. Disc. Bull., 22(7), 2897, 1979.

Microminiature Fluidic Amplifier

Mark J. Zdeblick

Phillip W. Barth

James B. Angell

Stanford University
Stanford, CA 94305

Abstract — A microminiature fluidic amplifier with vertical-walled features $6\text{ }\mu\text{m}$ wide and $35\text{ }\mu\text{m}$ deep has been fabricated in silicon using dry anisotropic etching. Operation was demonstrated using nitrogen as the working fluid. DC gains greater than unity were seen over a supply pressure range of 10 to 80 psi. The amplifier is intended to be used as a circuit element in integrated fluidic circuits or, together with on-board electronics, as part of a transducer system. Dry etching techniques similar to those used here offer new opportunities for the micromachining of integrated sensors and actuators.

Introduction

A fluidic amplifier operates on gasses or liquids to amplify differential pressures or flows. A number of commercial fluidic systems, including sensors for high temperature, pressure, air speed, angular rate change, and fuel flow, are currently being used in various aerospace applications[1]. These commercial devices, made from non-semiconductor materials, are at least ten times larger in linear dimension than the device to be discussed. The smaller size of this new device results in higher operating pressures, and should lead to faster responses and a higher degree of integration than is currently available. Moreover, the demonstrated ability to integrate electronic function with silicon-based fluidic devices would make possible new sensors and actuators.

The device was made by anisotropically etching a $35\text{ }\mu\text{m}$ deep trench in silicon and then sealing the trench with a brass manifold to form a capillary channel. This dry anisotropic etch is an extension of a recently developed dry etching technique developed by McVittie et al. [2] to etch depth $35\text{ }\mu\text{m}$. The process yields near-vertical walls independent of crystal orientation, as shown in SEM photographs (Figures 1 and 2). The vertical etch rate of this mixed halocarbon (SF_6 and C_2ClF_5) etchant is $0.4\text{ }\mu\text{m}/\text{min}$ when used with the Drytek RIE-100, a parallel plate reactive ion etcher system. The etch depth of $35\text{ }\mu\text{m}$ is limited by the thickness of the photoresist.

The silicon wafer was also etched in KOH from the backside to provide feed-through holes for the input and output ports. Removable brass manifolds clamped on top and bottom of the silicon wafer provided ports accessible with Tygon tubing, while a $10\text{ }\mu\text{m}$ layer of Parylene on the brass acted as gasket material.

A plan view of the wafer, shown in Figure 1, helps illustrate the operation of the device. The darker areas are the floor of the trench; the labels correspond to the different input and output ports. When the supply port is at a higher pressure than the vent, $P_s > P_v$, a laminar jet emanates from the supply's nozzle. This jet traverses the amplifier region and reaches

the output ports, where it is split into two flows by the splitter. The input control ports steer the jet. When either a small differential input pressure, $\Delta P_i = P_{i1} - P_{i2}$, or input flow, ΔF_i , is applied, the jet will be deflected toward one of the output ports, resulting in a differential output pressure & flow, ΔP_o & ΔF_o . For small variations about $\Delta P_i = 0$, the device can be modeled as $\Delta P_o = A_p * (\Delta P_i + P_{io})$, where A_p is the pressure gain of the device and P_{io} is the input offset pressure. Ideally, $P_{io} = 0$.

The device was characterized by varying the supply pressure, P_s , and resistive loads, R_L , then measuring the input and output flow rates and pressures. From these data, we were able to calculate the following: pressure gain, A_p ; flow gain, A_f ; power gain, A_w .

Results

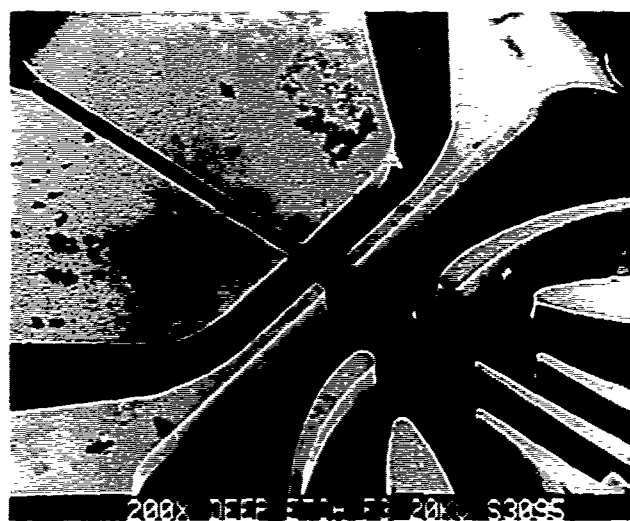
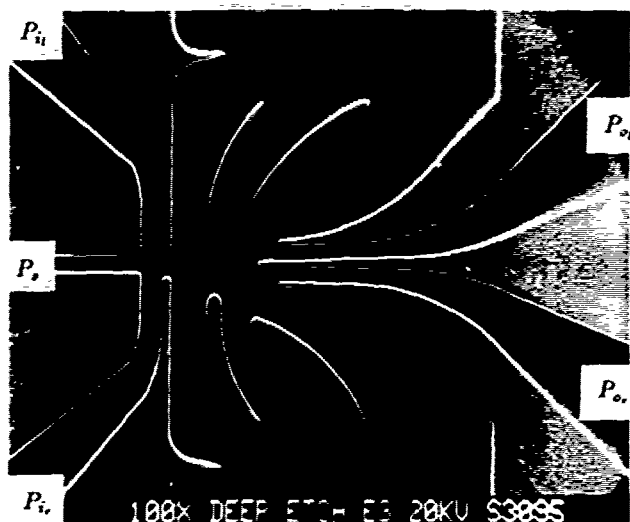
Of the four amplifiers fabricated, one has been thoroughly tested to date. This amplifier was tested by varying the capillary load resistance from 0 to $14\text{ kPa}/\text{sccm}$ and varying the supply pressures from 62 to 236 kPa (9 to 34 psi). A_p , A_f , and A_w were determined for each P_s and R_L . A_f decreases from 5.3 to 1.2 as R_L increases from 0 to $14\text{ kPa}/\text{sccm}$. Operation at $P_s = 133\text{ kPa}$ (19 psi) produced the highest flow gain at any given R_L . The pressure gain increases asymptotically from 0.1 to 2.7 as R_L increases. Again, operation at $P_s = 133\text{ kPa}$ (19 psi) produced the highest gains. (Another amplifier produced a blocked output ($F_o = 0$) pressure gain of 4.5, operating at 133 kPa.) The power gain increases from zero to a maximum of 5.9 and then declines for higher R_L . The maximum power gain was observed at $R_L \approx 4\text{ kPa}/\text{sccm}$ for most supply pressures. The A_f vs. A_p curve demonstrates some of the noise in the system. A set of smooth, parallel curves was expected; deviations are probably due to asymmetries in the load resistors.

The average flow rates in the supply, control, and output channels were also measured to determine the Reynolds number at both maximum flow and maximum power gain. The most striking observation is that the maximum output flow, F_o , is at most 31% of the supply flow, F_s , and that F_o at maximum power gain is 21% of F_s . These figures imply that most of the supply flow is going out the vents, even when the output ports vent to air. A second observation is that the Reynolds number of the supply jet is between 400 and 1300 — near the turbulent flow transition. It should be noted that since P_s is greater than twice the ambient pressure, supersonic flow at some point in the device is likely.

Conclusions and projections

This work demonstrated a 10X reduction in feature size and a 10X increase in P_s compared to 'standard' fluidic amplifiers.

¹sccm is an abbreviation for standard cubic centimeters per minute



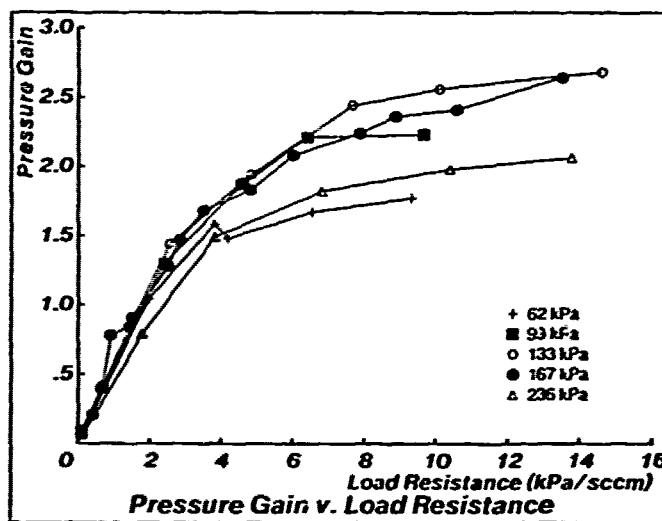
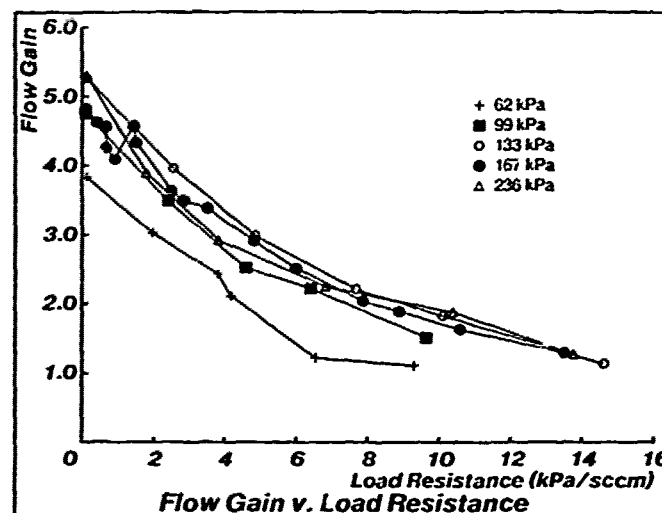
Power gain greater than one and input offset, P_{io} , less than 1% of the span of P_i were demonstrated. In addition, this work shows that dry anisotropic etching can be reliably used to produce 'vertical-walled' structures with flat bottoms. Ring oscillator structures to obtain speed data have been fabricated and are awaiting testing.

It seems likely that improvements in single stage gains are obtainable with design optimization. Integration of pressure sensors and fluidic devices on a single wafer could provide fluidic to electronic transduction with low power and high speed. Compatible fabrication processes seem feasible, but need to be developed. Future devices could take advantage of developed anodic bonding techniques [3] to reduce leakage between channels and yield 'permanent' devices. It seems feasible to pursue a level of integration for fluidic devices comparable in size and complexity to 1960's vintage electronic circuits².

²Mark J. Zdeblick is a Doctoral Candidate in the department of Electrical Engineering. His mailing address is Applied Electronics Laboratories Suite 16, Stanford University, Stanford CA, 94305.

Dr. Phillip W. Barth was with Stanford, he is now a Program Director at NovaSensor, 2975 Bowers Ave., Santa Clara, CA 95050.

Prof. James B. Angell is the Associate chairman of the Department of Electrical Engineering at Stanford. His mailing address is McCullough 162, Stanford University, Stanford, CA, 94305.



Acknowledgements

The authors would like to thank Dr. James McVittie of Stanford Integrated Circuits Laboratory for his help with the anisotropic etching technique, Martin Berdahl of Jet Propulsion Laboratories (JPL) for fabricating the brass test fixtures used to characterize the fluidic amplifier and for helpful discussions about fluidics in general, and Bill Reynolds for helpful discussions of fluid flow properties. This project was initially supported by JPL grant JPL 956888 and currently by General Motors grant GM 43-5.

References

- [1] *Garret Fluidic Systems* Garret Pneumatic systems division, PO box 52-17, Phoenix, AZ 85010.
- [2] "Anisotropic etching of Si using SF_6 with C_2ClF_5 and other mixed halocarbons," J. McVittie and C. Gonzalez, Extended abstracts, Fall Meeting, *Electrochemical Society*, Vol 84-2, p 584.
- [3] "A gas chromatography system fabricated on a silicon wafer using integrated circuit technology," Stephen Terry, Ph.D. Thesis, *Stanford University Technical Report No. 4603-1*, May 1975

Electrical and Chemical Sensors for Biological Cell Research

D.J. Edell, V.M. McNeil, M.G. Curley, J.H. Wolfe *
Massachusetts Institute of Technology
Harvard-MIT Division of HST
Cambridge, Massachusetts 02139

Electrical and chemical micro-sensors for biological cell research allow for the continuous study of biological systems under "normal" physiological conditions. Two sensor technologies which take particular advantage of microfabrication technology will be discussed in this paper. One technology is being developed for monitoring the environment of cancer cells during radiotherapy, chemotherapy, and hyperthermia treatments. Of current interest is the measurement of temperature and interstitial free oxygen concentration distributions in cancer tissues prior to and during various treatments. The ability to fabricate small microstructures with well controlled geometries which allow repeatable, accurate measurements in a wide variety of tissues is being exploited in this research. The second technology to be discussed is being developed for monitoring the extracellular ionic currents from electrogenic cells in culture. The ability to build integrated circuits over large areas of a silicon wafer which can impedance transform the signals and multiplex a large array of contacts is being used in this research.

Many parameters can affect the response of cancer cells to radiotherapy, chemotherapy and hyperthermia treatments [1]. The dissolved oxygen concentration in tumor tissues is one important parameter which seems to be strongly related to the destruction of cancer cells during radiotherapy, and may also affect the response of cells to hyperthermia and chemotherapy. Oxygen concentration and temperature in normal tissue and cancer tumors varies widely over small distances. Accurate, multipoint measurements within the tumor of interest are essential for research and clinical therapies. Since the local environment of the sensor will be highly variable due to tissue property variations, a measurement technology which is independent of the environment is essential. Also, since the probes are to be inserted into living tissue, the size of the probe must be minimized.

The prototype probe being developed for cancer research is 1mm wide, 0.25mm thick, and 4 cm long. Oxygen sensors on the probe use the multicathode amperometric approach [2,3] implemented on a micron scale. The oxygen electrode design takes advantage of the hemispherical steady state oxygen diffusion field which forms about a very small, properly polarized hemispherical cathode on an insulating substrate. The diffusion field limits the transport of oxygen to the cathode surface and hence limits the current flow through the cathode. The steady state oxygen concentration about the cathode is given by:

$$C_x = C_o(1-r/x)$$

where:

C_x = oxygen concentration at x
 C_o = oxygen concentration at infinity
 r = cathode radius
 x = distance from cathode center

The steady state oxygen current about the hemispherical cathode is given by:

$$I = -8q DrC_o$$

where:

I = oxygen current
 C_o = oxygen concentration at infinity
 r = cathode radius
 D = oxygen diffusivity
 q = electron charge

By making the cathode radius very small, the oxygen concentration a small distance from the cathode is minimally disturbed which implies that the diffusion field surrounding the cathode is limited in extent. By coating the surface of the cathode with a layer of a material of known and stable characteristics, diffusion of oxygen to the cathode will be independent of the environment with the exception of variations in temperature. Temperature can be compensated for by incorporation of temperature sensors under the diffusion film on the substrate surface.

Since the magnitude of the oxygen current is proportional to the radius of the electrode, microcathodes which have very limited diffusion fields produce very low, difficult to resolve currents. Numerous microcathodes, operating in parallel and appropriately spaced to avoid significant interaction, will produce a steady state oxygen current of reasonable amplitude.

Detailed analysis of the diffusion fields of the multi-microcathode sensor is difficult and probably not necessary. However, considerable design insight can be derived from a simple, approximate model of the structure. The microcathodes actually fabricated lie at the base of a hole in the dielectric coating. Oxygen concentration gradients in these holes are assumed to be linear. At the surface of the dielectric, the oxygen concentration gradients are assumed to be hemispherical. Even though the microcathodes are spaced 20 radii apart, together they form a large area sink for oxygen current. Oxygen concentration gradients about the ensemble of microcathodes again are treated as hemispherical.

Results of the analysis show that a hemispherical microcathode would cause only a 5% depletion of the oxygen concentration 20 radii from the center of the microcathode in the absence of a well. The presence of a dielectric with a thickness equal to the diameter of the microcathode creates a microwell which reduces the oxygen depletion at 20 radii to about 1%. Approximate analysis of the ensemble of microcathodes was done assuming a 20 radii spacing of microcathode and a fixed area on which to place the microcathode. Shrinking the radius of each microcathode reduces the oxygen current per microcathode as r^{-1} , but at the same time, more microcathodes per unit area increases the oxygen current as r^2 . Thus, the optimal microcathode size is as small as possible until narrow channel transport effects dominate.

The performance of the oxygen sensors is in general agreement with the predictions. Results using uncoated sensors show typical polarographic responses and rapid electrical transient response times. Prototype sensors which have 506 two micron diameter micro-cathodes exhibit responses which are nearly flow independent which indicates a very limited diffusion field. Results of similar measurements using a single large cathode geometry on the same substrate shows a substantial flow dependence. Work on coating the sensors with thin films to stabilize the response to variations in local environment is under way.

Cell Culture Arrays

The study of the electrical activity of brain and heart cells can sometimes be simplified by culturing cells from these organs onto planar recording electrode arrays. This technique is ideally suited for studying the electrical interactions between neural [4] and cardiac [5] cells in a relatively controlled, two dimensional environment. The standard technique for producing arrays of electrodes for recording from cell culture preparations is to define the electrode and lead pattern on a glass substrate and use a polymer coating for a dielectric [6]. Typically ten to forty contacts are defined this way. Each contact must then be wired to the preamplifiers and data acquisition system. The most typical technique for accomplishing this is ultrasonic bonding of small gold wires.

Since electrode contact areas are typically small, the source impedance for the acquired signals is usually 0.1-10 megohms. While careful instrumentation design can minimize noise pickup in the high impedance leads, capacitive shunting of the signal and the number of electrode connections which have to be individually connected to external electronics limits the utility of the technology.

We are developing a monolithic array of independently addressable MOSFET sensors for use in monitoring the electrical activity of cells in culture. The gate of each MOSFET is connected to gold contacts on the surface of the silicon wafer for recording from nearby cells. Devices are selected by applying power to the drain bus of a particular row and recording from the appropriate source bus of a particular column. Electrical potentials created by ionic current flow in the vicinity of the gold electrode contacts create signals on the gates of the MOSFETs. The low impedance output of each device reduces signal attenuation due to shunt capacitances, and minimizes cross talk and noise pickup.

The cell culture recording matrix under development provides access to 256 recording sites and requires only 32 connections to the source and drain buses plus two connections for substrate bias and a solution reference. Using 16 channel parallel recording from the 16 source buses, it is possible to rapidly scan the array by stepping power through the 16 drain buses.

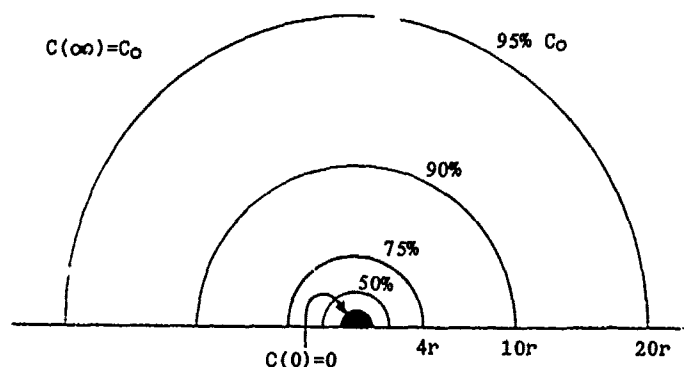
* Acknowledgements

This paper discusses results from two research efforts which each have a large number of participants. The hyperthermia project is sponsored by NIH-NCI Grant #CA37235, and involves H.F. Bowman, S.K. Burns, D.J. Edell, J.C. Weaver, M.G. Curley, L.M. Peznola, and J.H. Wolfe. The cell culture array is unsponsored research which at various times has involved D.J. Edell, R.G. Mark, M.S. Cafferty, L.D. Clark, D.A. Israel, V.M. McNeil, and P.M. Wheaton.

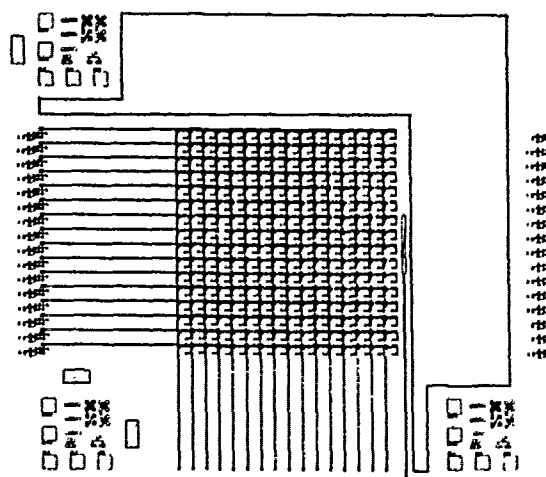
References

1. Oleson, J.R. and M.W. Dewhirst, Hyperthermia: An overview of current progress and problems. In: Hickey, R.C. (ed) Current Problems in Cancer, 8: 6, Chicago: Year Book Medical Publishers, 1983.
2. Fatt, I. and R. St. Helen, A multicathode polarographic oxygen sensor and its performance, J. Appl. Biol. 27, 435-437, 1969.
3. Siu, W., and R.S.C. Cobbold, Characteristics of a multicathode polarographic oxygen electrode, Med. Bio. Eng. 14, 109-120, 1976.

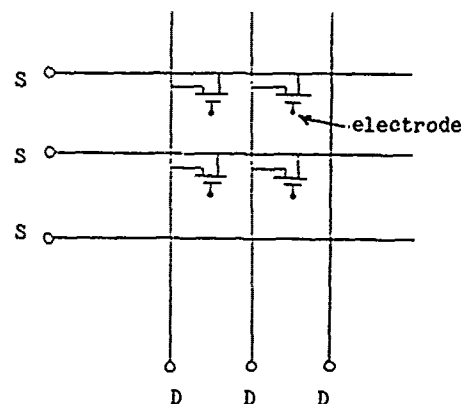
4. Thomas, CA, Springer, PA, Loeb, GE, Berwald-Netter, Y, Okun, LM. A miniature microelectrode array to monitor the bioelectric activity of cultured cells. Exptl. Cell. Res. Vol. 74: 61-66, 1972.
5. Shtark, MB, AS Ratushnyak, LV Voskresenskaya, and SN Olenov. A multi-electrode perfusion chamber for tissue culture research. Bull. Exp. Biol. Med. USSR 78: 1090-1092, 1974.
6. Gross, GW. Simultaneous single unit recording IN VITRO with a photoetched laser deinsulated gold multimicroelectrode surface. IEEE Trans. Biomed. Eng. BME-26: 273-279, 1979.



Oxygen Concentration Field for a Cathode of Radius r



Cardiac Cell Culture Array



Schematic Closeup of Cell Culture Array

CHARACTERIZATION OF PROTON CONDUCTING POLYMER BLENDS

by S. Petry-Weeks and A. J. Polak
Signal Research Center, Inc.
50 E. Algonquin Road, Box 5016
Des Plaines, IL 60017-5016

ABSTRACT

The proton conducting polymer blend of poly(vinyl alcohol) and phosphoric acid has been modeled using AC impedance techniques. Evidence indicates the presence of a separate phosphoric acid/water phase which is responsible for the proton conduction of the film. This is supported by differential scanning calorimetry, dielectric, and conductivity measurements. Conductivity versus temperature plots show Arrhenius-like behavior rather than the free volume type behavior associated with ion transport mechanisms dependent on polymer motion.

INTRODUCTION

"Fast-ion" conducting solid materials, which approach electrolyte solutions in conductivity, are an area of active research. These materials range from crystalline inorganic solids such as sodium beta alumina to ionic polymers such as poly(ethylene oxide) and poly(ethylene succinate) complexed with alkali metal salts. These polymeric complexes have ionic conductivities of 2×10^{-5} (ohm-cm) $^{-1}$ for PEO-LiSO₃CF₃ at 98°C [1] and 3×10^{-6} (ohm-cm) $^{-1}$ for PESC-LiBF₄ (3:1) at 65°C [2]. These high conductivities are only observed above the glass transition temperature of the polymer complex. Conduction is believed to occur primarily in the amorphous phase and is dependent on the local motion of the polymer. Thus, the ionic conductivity is adequately modeled by free volume theory and the Williams-Landel-Ferry (WLF) equation [3], which exhibits non-Arrhenius behavior.

The proton conducting polymer blends composed of poly(vinyl alcohol) (PVA) and phosphoric acid have conductivities from 10^{-5} to 10^{-8} (ohm-cm) $^{-1}$ at room temperature, depending on the acid content of the film. This system is unique in that it shows significant ionic conductivity below the glass transition temperature of the polymer; thus they are practical for sensor applications which operate at room temperature [4].

EXPERIMENTAL

Polymer Film Preparation:

Membranes were prepared from 100% hydrolyzed, Ave. MW = 86K to 133K, PVA dissolved in deionized water with the appropriate amount of 85% H₃PO₄. Composition ratios are in terms of moles polymer repeat unit to moles phosphoric acid. The solutions were poured into polycarbonate petri dishes and the water was allowed to evaporate under ambient conditions. Disks of the resulting films were cut out and platinum or gold electrodes sputter-deposited to ~500Å thickness.

Complex Impedance Measurements:

Complex impedance measurements were made using the GenRad Precision RLC Digibridge in an RC parallel circuit configuration over a frequency

range of 10 Hz to 100 kHz for a specified AC signal of fixed amplitude and frequency ω . The magnitude (denoted by boldface type) of the impedance can be calculated from:

$$Z = (R_p^2 / (1 + (\omega R_p C_p)^2))^{1/2} \quad \text{and}$$

$$\theta = -\tan^{-1} (\omega R_p C_p).$$

The real and imaginary parts of the admittance, which can be determined from the impedance, are given by:

$$G = \cos \theta / Z \quad \text{and} \quad B = -\sin \theta / Z, \quad (1)$$

respectively, which are then plotted in the complex admittance plane. These plots are then used to determine an equivalent circuit based on the physical and chemical nature of the system being modeled [5].

Since the impedance of the polymer films is highly dependent on their water content, the membranes were placed in a dry gas stream for approximately 24 hours before measurement. The films' physical and electronic properties stabilize at this point.

The samples were exposed to an atmosphere of 100% H₂ with an applied AC signal of 5 mV. Possible polarization effects were checked at 5 mV, 10 mV, and 1 V applied in 100% H₂ for a PVA/H₃PO₄ (3.8:1) film with blocking electrodes. No significant differences were noted.

Arrhenius Plots:

PVA/H₃PO₄ films were exposed to 0.1% H₂/99.9% He in a Mettler TMA 40 chamber for temperature control. Temperature programs were run in both directions with the same results. Impedance and phase angle readings were taken using a Hewlett Packard 4800A Vector Impedance Meter with analog output. The frequency was measured with an HP 5327B Timer Counter DVM. The complex admittance was determined from equation (1).

Dielectric Measurements:

All dielectric measurements were made using the Eumetric System II Microdielectrometer. High acid content measurements were made using the uncalibrated high conductivity sensors, which measure resistance only. Since these films are approximately the same thicknesses, relative resistances can be compared for trend analysis. Samples were prepared by dissolving 1 gram of polymer in 10-20 mL DI water, adding the appropriate amount of 85% phosphoric acid, and sonicating for 15 seconds to remove trapped air. Two to three drops of solution were placed on each sensor and the water allowed to evaporate at room temperature in dry nitrogen; the sensors were then stored in dry nitrogen until completion of the experiment. Measurements were made at 10 Hz.

A low acid film, 9.5 weight % acid on a water-free basis, was made on a calibrated low conductivity microdielectric sensor, which determines the real and imaginary components of the dielectric constant. The sample was prepared in the manner described above with diluted 85% phosphoric acid. The permittivity and dielectric loss were determined for the frequency range from 250 Hz, the lowest on-scale reading, to 10 kHz.

RESULTS AND DISCUSSION

The relative resistance of the polymer blend as a function of acid content was measured for a series of PVA/H₃PO₄ samples. The change in conductivity occurs in a discrete step, as opposed to a smooth change, from low to high acid compositions, suggesting a separate conducting phase. At low acid contents, the conducting phase would exist in small domains disconnected from each other. When a critical volume is reached, the separate domains are in close enough proximity to link up and form a continuous conducting phase. A similar scenario has been suggested for sodium ion conduction in Nafion soaked in salt solution [6].

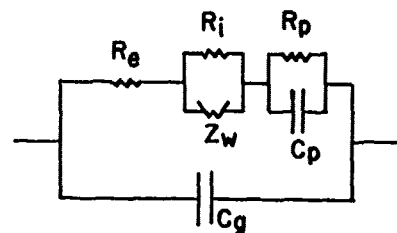
This is consistent with analysis by differential scanning calorimetry (DSC). In the proton conducting polymer blends studied, there is a second order transition due to phosphoric acid/water, distinct from the glass transition of the polymer. The temperature of this transition is a function of acid content, water content, and the polymer. The phosphoric acid/water plasticizes the polymer; however, the glass transition temperature of the polymer is well above room temperature.

A simple equivalent circuit composed of capacitors and resistors will produce complex admittance plots with one or more arcs centered on the real axis at the lower frequencies and a spur perpendicular to the real axis at higher frequencies. Each arc corresponds to a lumped RC combination. The spur is the result of the geometric capacitance, the capacitive coupling of the electrodes through a dielectric, i.e., the polymer electrolyte. In a diffusion controlled system, which is equivalent to a distributed RC network and termed the Warburg impedance (Z_w), the center of the arc is depressed below the real axis so that it forms a 45° angle with the origin and the spur forms a 45° angle to the real axis.

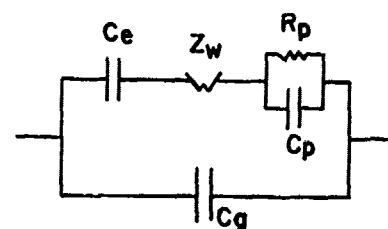
The basic physical model for the PVA/H₃PO₄ system can be broken up into a number of steps: contributions due to the electrodes, the electrode/electrolyte interface, and the polymer. By changing the experimental conditions, one can change the rate limiting (i.e., highest impedance) step for the total process and isolate, to some degree, the different processes for examination. The assumption made for these experiments is that processes involving the adsorption and dissociation of H₂ will occur so rapidly in a 100% hydrogen atmosphere that they will not affect the frequency response of the equivalent circuit over the frequency range studied.

Ohmic electrodes, in this case, platinum, are capable of injecting charge carriers (protons) into the electrolyte from an external source and are modeled by a resistor, R_e . Gold (blocking) electrodes are not and are modeled by a capacitor, C_e . Redox reactions occurring at the electrode/electrolyte interface should be discernible by complex admittance analysis and can be modeled by a resistor, R_i . The polymer can be

modeled as a resistor R_p and a capacitor C_p in parallel (or some unspecified impedance, Z_p), the magnitudes of which vary with the conductivity of the film. In low acid films, transport through the polymer becomes rate limiting and the impedance due to the polymer will predominate. For highly conductive polymers, this impedance will be very small and the impedance due to diffusion limitations after proton injection at the interface, Z_w , will predominate. Model equivalent circuits for both types of electrodes are shown in Figure 1.



Total ohmic electrode case



Blocking electrode case

Figure 1. Equivalent circuit models for complex impedance analysis.

Data presented in Figures 2 and 3 show the complex admittance as a function of polymer composition for the blocking and ohmic electrode cases. The compositions are chosen so that the films fall on each side of the step change in conductivity. These admittance plots are consistent with the equivalent circuit models developed in Figure 1. Values for the equivalent circuit components have not been calculated because of the variability in nominally identical films.

The data in the low acid plot, 3.8:0.25 mole ratio PVA/H₃PO₄ (Figure 2), approximates the "ideal" equivalent circuit. Both the bulk, R_p/C_p , and the redox reactions at the electrode/electrolyte interface, R_i , contribute to the response. Since the arc generated by the electrode/electrolyte interface is centered on the real axis, the resistor R_i is adequate in this case. The spurs due to the bulk electrolyte form an ~ 80° angle with the real axis. The high acid data, 3.8:1 mole ratio PVA/H₃PO₄ (Figure 3), approaches the distributed RC model for the diffusion limitation after proton injection into the polymer. The center of the arc forms an ~ 20° angle with the origin below the real axis and the spurs are at a 50-60° angle to the G axis.

Additional evidence that ionic conductivity (σ) in the bulk polymer predominates in the low acid sample is presented in Figure 4. The dielectric loss factor (ϵ'') is a function of the bulk ionic conductivity and the dipole motion in the sample, which yield a straight line and a parabola, respectively, as a function of frequency. In the

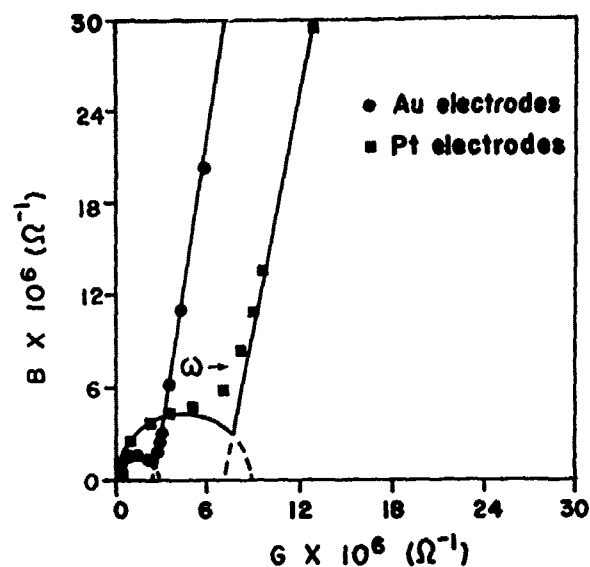


Figure 2. Complex admittance of PVA/H₃PO₄, 3.8:0.25 mole ratio.

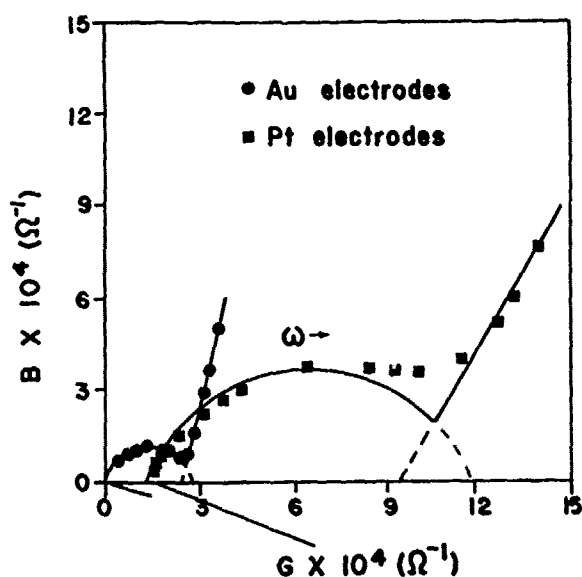


Figure 3. Complex admittance of PVA/H₃PO₄, 3.8:1 mole ratio.

region where $\epsilon'' \propto \sigma/\omega$, the slope for a $\log \epsilon''$ vs $\log \omega$ line due to ionic motion should be -1, as is the case.

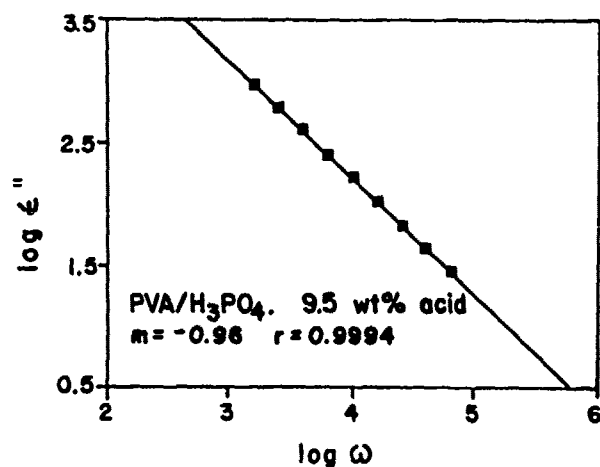


Figure 4. Ionic conductivity in a low acid PVA/H₃PO₄ film.

Processes occurring at the electrode/ electrolyte interface can be examined by plotting the impedance vs frequency^{-1/2} for the 3.8:1 film. Figure 5 is the same data used to generate the complex admittance plots in Figure 3. The data fall into the frequency dependent (Z_w) and frequency independent (R_i) regions discussed previously. As would be expected, the mass transfer limitations dominate the highly conductive PVA/H₃PO₄ polymer.

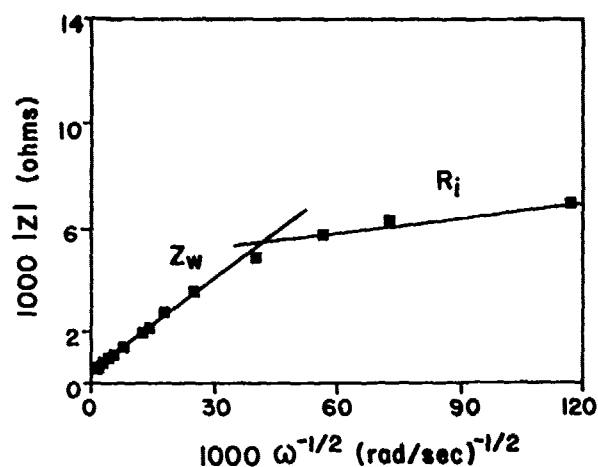


Figure 5. Impedance of a high acid PVA/H₃PO₄ film.

Plots of $\log \sigma T$ versus inverse temperature in the range of -40°C to 40°C show Arrhenius-type behavior (Figure 6), which is consistent with a separate electrolyte conducting phase, as opposed to the deviation characteristic of conduction due to free volume behavior. Conductivity is determined from the intercept of the spur with the real axis in the complex admittance plots and can be calculated by $\sigma = G/l/A$, where G is the value determined from the admittance plot, l is the film thickness, and A is the area of the electrode. The appropriateness of the G value was confirmed by comparing Arrhenius plots with both ohmic and blocking electrodes (run in 100% H₂).

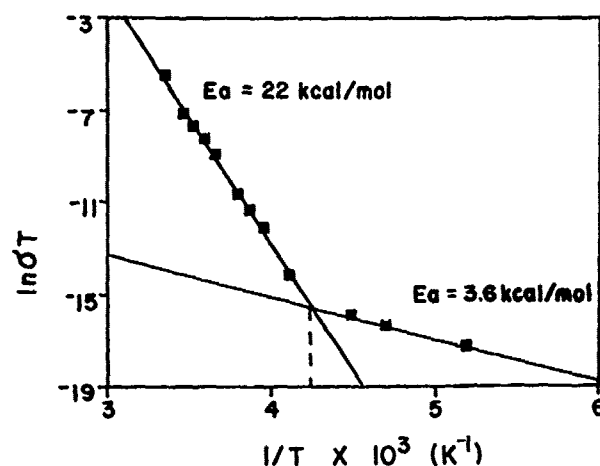


Figure 6. Arrhenius plot for PVA/H₃PO₄ proton conducting polymer blend.

The intersection of the two lines in Figure 6 denotes a change in transport mechanism and/or a change in the ionic transport number (the ratio of ionic conduction to total ionic and electronic conduction), assuming a Nernstian response. By measuring the EMF generated at a known hydrogen

concentration ratio, the ionic transport factor was calculated to be 1.0 (proton conduction only) from room temperature to -30°C . At -45°C , below the point where the two lines on the Arrhenius plot intersect, the ionic transport factor was calculated to be 0.5. The physical significance of the break at -40°C is not clear at this time. One possible interpretation is the freezing of the electrolyte solution conducting phase at this low temperature.

CONCLUSIONS

Diverse evidence points to a separate electrolyte conducting phase as the proton transport mechanism in the PVA/ H_3PO_4 proton conducting polymer blends. DSC analysis shows two second order transitions attributed to the polymer and electrolyte conducting phase. The temperature of the latter strongly depends on the acid and water contents of the films. A basic equivalent circuit model has been developed using AC impedance techniques and supported by additional dielectric and conductivity measurements. Arrhenius plots based on this model do not show free volume behavior expected from a transport mechanism closely linked to the movement of the polymer.

- [1] L. C. Hardy and D. F. Shriver, "Preparation and Electrical Response of Solid Polymer Electrolytes with Only One Mobile Species," J. Am. Chem. Soc., vol. 107, pp.3823-3828, June 1985.
- [2] R. Dupon et al, "Ion Transport in the Polymer Electrolytes Formed Between Poly(ethylene succinate) and Lithium Tetrafluoroborate," J. Electrochem. Soc., vol. 131, pp.586-589, June 1984.
- [3] M. L. Williams, R. F. Landel and J. D. Ferry, "The Temperature Dependence of Relaxation Mechanisms in Amorphous Polymers and Other Glass-forming Liquids," J. Am. Chem. Soc., vol. 77, pp.3701-3707, July 1955.
- [4] A. J. Polak, S. Petty-Weeks, and A. J. Beuhler, Sensors and Actuators, accepted for publication.
- [5] J. E. Bauerle, "Study of Solid Electrolyte Polarization by a Complex Admittance Method," J. Phys. Chem. Solids, vol. 30, pp.2657-2670, December 1969.
- [6] Wodzki et al, "Percolation Conductivity in Nafion Membranes," J. Appl. Polym. Sci., vol. 30, pp.769-780, February 1985.

PYROLYZED ORGANIC POLYMER NITROGEN DIOXIDE SENSOR

J.O. Colla

JOHNSON CONTROLS, INC.
507 E. Michigan Street
Milwaukee, Wisconsin 53201

ABSTRACT

The element described for sensing the presence of nitrogen dioxide in the environment consists of a pyrolyzed polyaromatic polymer film having semiconductive properties. Nitrogen dioxide effects a change in the electrical resistance of the pyrolyzed polymer. The presence of nitrogen dioxide causes the electrical resistance of the element to decrease, and the magnitude of resistance change is a function of nitrogen dioxide concentration. Concentrations as low as 1.3 ppm nitrogen dioxide can be readily and quickly sensed in an air environment.

INTRODUCTION

Some solid-state sensors, such as the Taguchi Gas Sensor, indicate the presence of oxidizable gases, such as hydrocarbons and carbon monoxide [1]. Another sensor, the Dolan Adsorptive Sensor, detects the presence of gases having a van der Waal's "a" constant above 6 [2]. While many of these gas sensors are capable of continuous and reversible detection, they are not specific to a particular gas. Considerable attention has been focused recently on the need for gas sensing devices that are highly selective for the detection of gaseous pollutants.

Efforts in our laboratory have focused on the development of solid-state gas detectors that respond reversibly to the presence of specific gases. The nitrogen dioxide sensor described in this paper is a product of this effort [3], [4].

The inherent tendency for many organic compounds to adsorb and/or absorb gases foretells their applicability for a gas sensing device. Vacuum pyrolysis of long chain polymers yields in some instances a semiconductive residue [5]. These two statements open the possibility of developing and using organic semiconductors as gas sensors and serve as the basis for the nitrogen dioxide sensor described in this paper.

SENSOR CONFIGURATION AND FABRICATION

The nitrogen dioxide gas sensor, which is shown in Fig. 1, consists of a pyrolyzed polymeric film that has a partially metallized surface, an alumina substrate for mounting the pyrolyzed film and contact tabs which provide a means to make electrical connections to the pyrolyzed film.

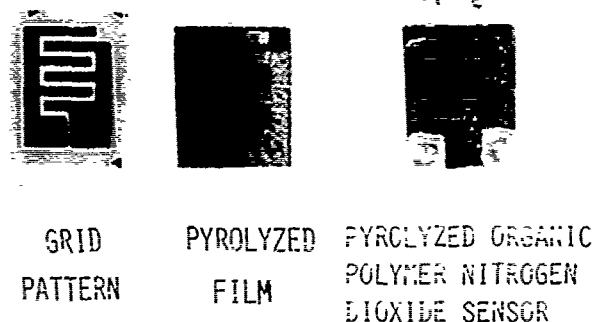


FIG. 1

The principal component of this sensor is a pyrolyzed polyimide film. Commercially available polyimide film (Kapton H) from E.I. DuPont de Nemours & Company, having a thickness of 0.001 inch, is metallized by electroless chemical methods. The metallization process involves the application of a thin nickel layer, and the subsequent application of a thin gold layer by means of electroless chemical techniques. Using a grid pattern negative and photofabrication methods, a selected portion of the metal layer in the form of a serpentine grid is removed from the surface of the polyimide film (see Fig. 1). In addition to outlining the active portion of the film, the gold layer provides noncorrosive electrical conductors and a means to make electrical connections.

The metallized polyimide is pyrolyzed by placing it between porous graphite plates (maintains a flat film) and heating in a vacuum furnace. A typical pyrolysis process is performed in a vacuum of 1×10^{-5} torr at a temperature of 610°C for 60 minutes. The pyrolysis process changes the electrical characteristics of the polyimide film from that of a dielectric to a semiconductor.

Pyrolysis is a complex chemical process dependent on temperature and time at temperature. It is believed that non-mobile unsaturated valence states exist in the semiconductive polyaromatic polymer after pyrolysis. As shown in Fig. 2, the structure retains its aromaticity, tending toward a condensation of the aromatic rings. The exact mechanism of the pyrolysis is not fully established, but the resulting semiconductivity and gas sensing properties of the pyrolyzed polyimide film are believed to be due to its molecular structure [6].

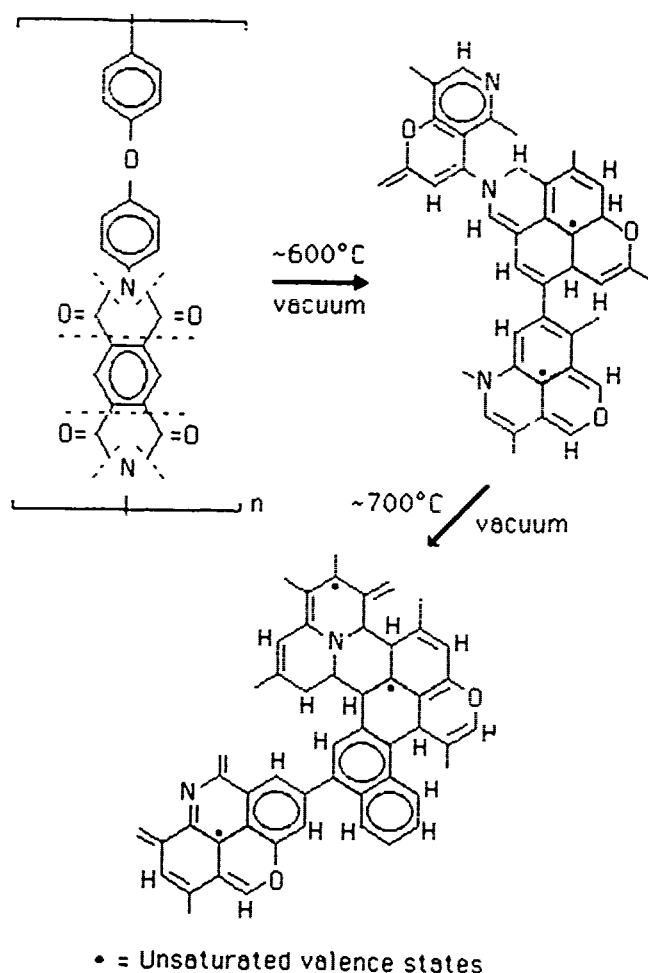


FIG. 2

The pyrolyzed film is mounted on an alumina substrate as shown in Fig. 1 and 3. The alumina substrate is not chemically reactive and is a good electrical insulator. It provides an ideal foundation for the fragile pyrolyzed polyimide film. The pyrolyzed film, having an approximate size of 1.27 cm by 1.016 cm is mounted on the alumina substrate with an epoxy resin.

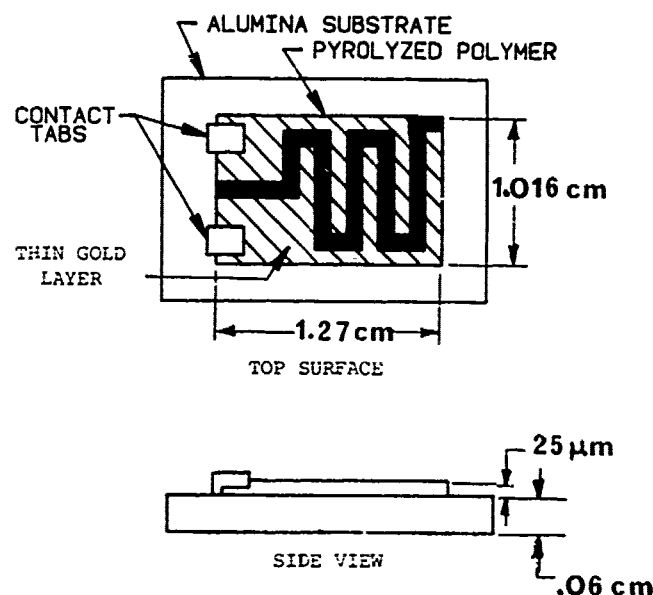


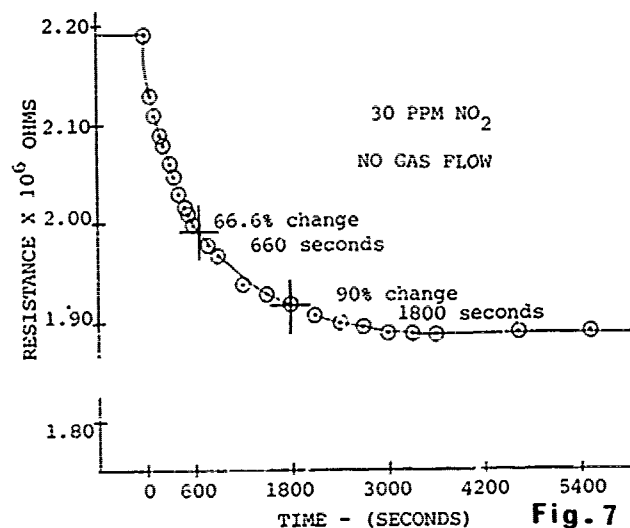
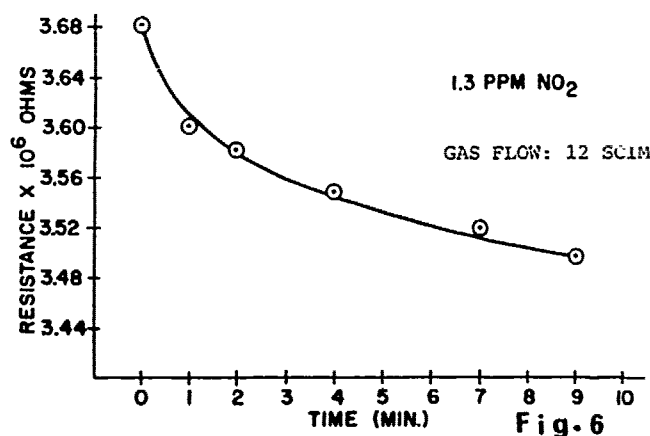
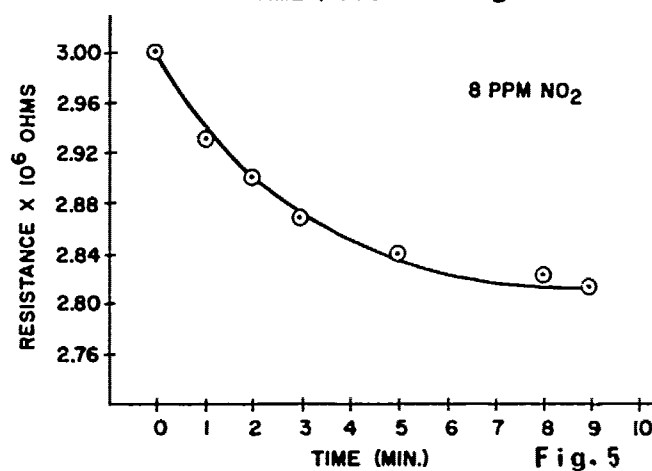
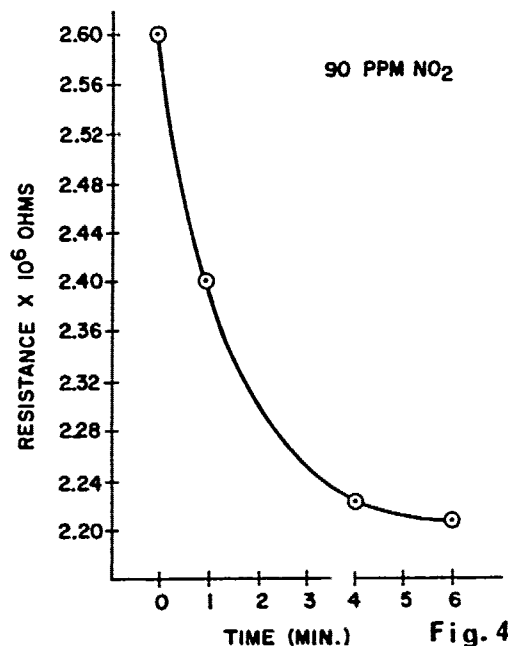
FIG. 3

Electrical wires cannot be soldered directly to the thin gold layer on the pyrolyzed film due to its fragile nature. A gold plated contact tab is bonded to each of the gold layer conductors on the polymer film using a gold filled epoxy resin. Lead wires are then soldered to the contact tabs (see Fig. 1).

SENSOR CHARACTERISTICS

The pyrolyzed polyimide sensor decreases in electrical resistance when exposed to nitrogen dioxide in an air environment (see Fig. 4 through 7). The short term response to various concentrations of nitrogen dioxide (from concentration certified gas cylinders), at an air flow rate of 12 SCIM is shown in Fig. 4 through 6. The electrical resistance of the sensor decreases when exposed to air containing nitrogen dioxide, and the magnitude of resistance change is dependent on the concentration of nitrogen dioxide in the air. For example, the percent decrease in resistance after 6 minutes exposure to nitrogen dioxide is 15.0%, 5.7%, and 4.3% respectively for nitrogen dioxide concentrations of 90 ppm, 8 ppm, and 1.3 ppm. When the sensor responds to a change in nitrogen dioxide concentration, time is required for the element to reach equilibrium with the new concentration of

nitrogen dioxide in air. In Fig. 7, the response characteristics are shown for a step change in nitrogen dioxide concentration from 0 ppm to 30 ppm nitrogen dioxide in air. These response data are for a pyrolyzed polyimide film in a closed vessel containing air in which an ampoule of nitrogen dioxide was ruptured. The time it takes the resistance of the sensor to change 66.6% and 90% is 660 seconds and 1800 seconds respectively at a zero flow rate.



The sensitivity of the pyrolyzed polyimide film to various other gases in air was also examined. The element was not sensitive to reducing gases such as carbon monoxide, methane, and butane, and the oxidizing gas sulfur dioxide.

The electrical resistance of the sensor was measured with a Keithley Electrometer-Model 610 C.

SUMMARY

The pyrolyzed polyaromatic polymer gas sensor described in this paper has a selective response to the presence of nitrogen dioxide in air. It has a design, construction and material composition that makes it unique and useful as a nitrogen dioxide gas sensor. The electrical resistance of the sensor decreases when exposed to nitrogen dioxide in air. This sensor is not sensitive to other gases in air such as carbon monoxide, methane, butane, and sulfur dioxide.

REFERENCES

- [1] R. Bukowski and R. Bright, Some Problems Noted in the use of Taguchi Semiconductor Gas Sensors as Residential Fire/Smoke Detectors, NBSIR 74-591. Washington: National Bureau of Standards Center for Fire Research, December 1974.
- [2] J.P. Dolan, "Detection Device," U.S. Patent 3,045,198: July 17, 1962.
- [3] J.O. Colla and P.E. Thoma, "Nitrogen Dioxide Sensing Element and Method of Sensing the Presence of Nitrogen Dioxide," U.S. Patent 4,142,400: March 6, 1979.
- [4] J.O. Colla and P.E. Thoma, "Method of Making a Nitrogen Dioxide Sensing Element," U.S. Patent 4,236,307: December 2, 1980.
- [5] F. Gulmann and L.E. Lyons, Organic Semiconductors. New York: John Wiley & Sons, Inc., 1967, Ch.8, pp.472-480.
- [6] H. Lee, D. Stoffey and K. Neville, New Linear Polymers. New York: McGraw-Hill, Inc., 1967, Ch.8, pp.230-251.

CHEMICAL MULTISENSORS WITH SELECTIVE ENCAPSULATION OF ION-SELECTIVE MEMBRANES

Felix J. Schwager*, Luc J. Bousse, Lyn Bowman, and J.D. Meindl
Stanford Electronic Laboratories, Stanford, CA 94305

* Present Address: Mettler Central Research, Greifensee, Switzerland.

Abstract

Chemical sensors fabricated with simultaneous wafer-scale encapsulation of ion-selective electrode membranes are described. The sensors are miniature ion-selective electrodes in chambers located on a silicon substrate. These chambers are made by anodically bonding to the silicon a #7740 pyrex glass wafer in which cavities have been drilled. Pores with dimensions selectable from 50 μm upwards are opened in the roofs of the chambers by drilling with a CO_2 laser. Each sensor die contains four cavities which are filled under reduced pressure with liquid membrane material which is subsequently polymerized. The transducers on the cavity floor are Ag/AgCl electrodes. Interconnects between the sensor chambers on each die and bonding pads are made in the silicon substrate.

Introduction

In the past decade, many researchers have attempted to fabricate chemical and biochemical sensors with silicon integrated circuit technology. The appeal of using electronic technology in this way is the prospect of reducing sensor size and increasing the number of sensor functions as was achieved with purely electronic IC's. The device which has received most attention is the ion-sensitive field-effect transistor (ISFET) which first combined chemical sensitivity and electronic functions in one device. ISFET sensitivity to many analytes has been achieved by manually coating the gate with an appropriate ion-selective membrane.

The hand application of membranes introduces several problems, however. First, the advantage of wafer-scale processing of sensors is lost. Second, the size of each sensor is constrained by the accuracy of this manual operation, rather than by the limits of photolithography. Third, since the membrane sits on top of the sensor, it is mechanically vulnerable and adhesion to the ISFET insulator degrades in a few days. Indeed, the absence of a satisfactory technique for membrane encapsulation obstructs the commercial development of chemical sensors on silicon.

Several attempts to improve membrane encapsulation methods have been reported. Blackburn and Janata [1] reported a suspended polyimide mesh over the gate area to anchor the membrane. Sibbald *et al.* [2], Brown *et al.* [3] and Kimura *et al.* [4] have all used photolithographically defined wells in a thick layer of photoresist to hold manually applied membranes. These methods have improved sensor lifetime from a few days to a few weeks and may have reduced the mechanical vulnerability of the resulting devices. Hand application of membranes, however, is incompatible with miniaturization and mass production.

In this paper we present a new method for membrane encapsulation which attempts to overcome these micropackaging problems. Membranes are entirely enclosed within chambers. Pores in the ceilings of the chambers provide contact to the environment, while electrochemical transducers are located on the floors of the chambers. Chambers are filled with liquid membrane material simultaneously at the wafer level. Our first implementation of this general idea is illustrated in Figure 1. The special case with which we demonstrated the general technique may be modified in several details to further improve manufacturability.

Silicon Wafer Processing

To demonstrate this technique, we used the silicon substrate for two purposes: as a level for interconnecting sensors inside chambers to bonding pads outside chambers, and as a substrate for anodic bonding. Our sensor die consisted of four chambers, each containing, for simplicity, a Ag/AgCl electrode, within chip dimensions of 10×7 mm. Silicon wafers (p-type, 11–20 $\Omega\text{-cm}$) were processed as follows:

1. Initial oxidation (4700 Angstroms);
2. Photolithographic patterning of the oxide;
3. Implantation of arsenic ($6 \times 10^{15} \text{ cm}^{-2}$);
4. Removal of all the initial oxide, followed by growth of a new 0.5 μm SiO_2 layer;
5. Deposition and doping of polysilicon (0.5 μm , 20 Ω/square);
6. Photolithographic patterning of the polysilicon bonding ring;
7. Photolithographic patterning of contact openings to interconnects;
8. Deposition and photolithographic patterning of silver electrodes;
9. Photolithography and chloridation of silver electrodes in ferric chloride solution.

Figure 2 shows a die before silver chloridation.

Chamber Fabrication and Filling

We fabricated chambers by mechanically drilling an array of cavities in pyrex glass wafers and anodically bonding the glass wafers to the silicon wafers. Fabrication proceeded as follows:

1. Mechanical drilling of cylindrical cavities in optically polished, 650 μm thick #7740 pyrex wafers. Either of two diameters (1.8 mm and 2.7 mm) of diamond drills were used to drill an array of cavities 400 μm deep. Depending on drill diameter, cavity volumes were 1 or 2.5 μl . Figure 2 is an SEM picture of the interior of a cavity produced by a coarse drill; smoother surfaces are produced with finer drills.
2. Anodic bonding (at 400°C, 800 V) of pyrex and silicon wafers with cavities aligned over the electrodes.
3. Laser drilling of pores through the ceilings of the chambers. A 20W CO_2 laser ($\lambda = 10.6 \mu\text{m}$) with a focused spot size of 50 μm and a stepper-motor controlled XY-table with 5 μm spatial resolution were controlled automatically by a microcomputer [5]. Each pore was made with a burst of 100 μs laser pulses. Arrays of pores of various diameters can be achieved; an array of five is visible in Figure 3. Each pore is funnel shaped, as shown in Figure 4.
4. Filling the chambers with liquid membrane material. Liquid membrane material (positive photoresist in this case) was roughly spread over pores on the top of the glass wafer. The bonded wafers were placed in a bell jar and the jar pumped down to ~600 torr gage pressure. After holding the bell jar at that pressure for 10 minutes, the jar was vented to atmosphere. Atmospheric pressure is sufficient to fill the depressurized chambers with aqueous or hydrophilic solutions.
5. Membrane polymerization.
6. Dicing and electrical bonding

Comments on the Technique

The principle of making ion-selective electrodes by covering Ag/AgCl electrodes with ion-selective membranes has recently been demonstrated by Rhodes [6]. The resulting structure is similar to a coated wire electrode. Our scheme allows the additional making amperometric measurements by means of a suitable metal electrode instead of the Ag/AgCl electrode.

Many variations on this general idea come quickly to mind. Clearly, either ISFETs or a variety of metal electrodes could be used as electrochemical transducers, and any aqueous or hydrophilic membrane material could be utilized. The technique is also compatible with on-chip signal processing circuitry. Sequential drilling of cavities in glass wafers followed by anodic bonding will probably prove to be less desirable than simultaneous anisotropic etching of cavities in silicon wafers followed by an alternative bonding technique. In that case, pores could be selectively drilled in silicon with a YAG laser. The impedances of individual electrodes may be trimmed during fabrication by varying the number of pores. Nothing about this technique restricts the number of chambers which may be accommodated in a given die. Furthermore, iteration of steps 3-5 of the chamber fabrication and filling procedure, with different chambers perforated in each iteration, permits several different selective membranes to be encapsulated on the same die.

More work is needed to explore the advantages, disadvantages, and optimal conditions for this approach to membrane encapsulation. For example, the best compromise between membrane enclosure for long lifetime and membrane exposure for low impedance remains to be determined. So, too, is the minimum practical chamber volume. Nor is the optimal drill coarseness for membrane adhesion known at present. The suggested variations on the chamber fabrication technique for improved manufacturability should also be tested. We are confident, however, that a variation of this general method will solve the micropackaging problems which have obstructed the practical implementation of integrated sensors utilizing chemically selective membranes.

References

- [1] G. Blackburn and J. Janata, *J. Electrochemical Soc.*, 129, 2580 (1982).
- [2] A. Sibbald, P.D. Whalley, and A.K. Covington, *Anal. Chim. Acta*, 159, 47 (1984).
- [3] R. Brown, R.J. Huber, D. Petelenz, and J. Janata, *Int. Conf. on Solid-State Sensors and Actuators*, Philadelphia 1985, p. 125.
- [4] J. Kimura, T. Kuriyama, and Y. Kawana, *Int. Conf. on Solid-State Sensors and Actuators*, Philadelphia 1985, p. 152.
- [5] L. Bowman, J.M. Schmitt, and J.D. Meindl, in: *Micromachining and Micropackaging of Transducers*, C.D. Fung et al. Editors, Amsterdam:Elsevier 1985, p. 79.
- [6] R.K. Rhodes, *IEEE Trans. Biomedical Eng.*, BME-33, 91 (1986).

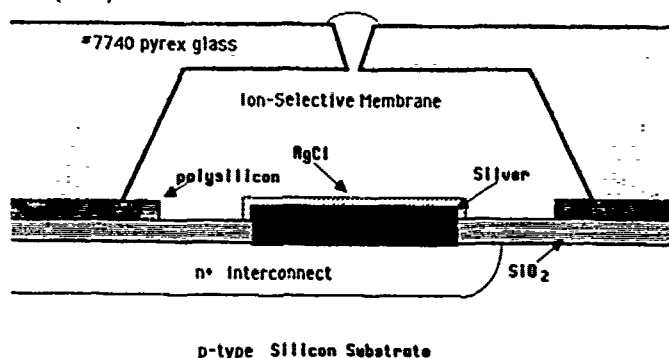


Figure 1. Diagram of the structure of the membrane chambers and the Ag/AgCl electrode.

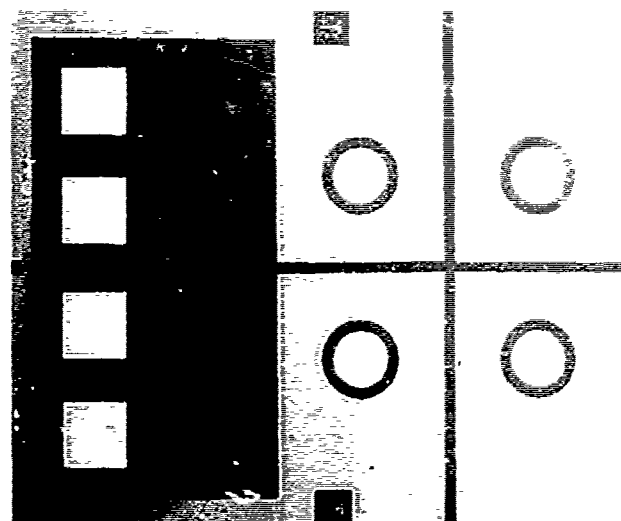


Figure 2. Silicon wafer with four electrodes and bonding pads before the glass wafer is bonded to it.

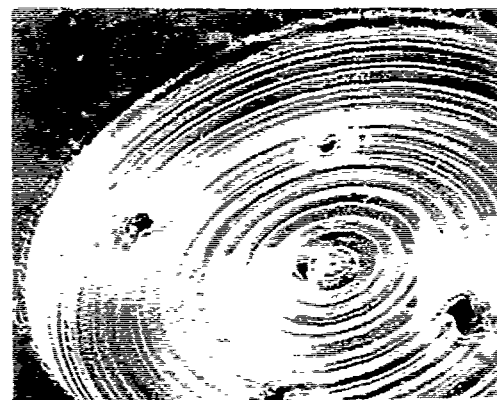


Figure 3. Interior view of a mechanically drilled, 2.7 mm diameter glass cavity with laser-drilled pores of different sizes in the upper surface.



Figure 4. Outside view of a pore drilled through the roof of a chamber.

FIBER OPTIC SENSORS

David A. Krohn, Ph.D.
EOTec Corporation
420 Frontage Road
West Haven, Connecticut 06516

Introduction

As industrial control requirements expand, more innovative sensors are urgently needed. In fact, there are presently several sensing requirements going unmet because adequate sensors are not available. Fiber optic sensors may go a long way toward meeting these needs due to their unique properties and distinct advantages. They are inert to hazardous or extreme environments and they have the potential to work over a wide temperature range. They are immune to radio frequency interference (RFI), electromagnetic interference (EMI) and toxic environments. They allow access into normally inaccessible areas. System flexibility is enhanced by remote sensing. Fiber optic sensors are in many instances passive and as a result, much more reliable than mechanical or electronic sensors. Systems can be designed with very high accuracies which can be easily interfaced with fiber optic data links back to control centers. Systems are now available to tie optical sensors into fiber optic data communication highways.

Most physical properties can be sensed fiber optically.¹ Light intensity, displacement (position), temperature, pressure, rotation, sound, strain, magnetic field, electrostatic field, radiation, flow, liquid level and vibration are just some of the phenomena that can be sensed.

Historically, most fiber optic sensor applications have been relatively simple absence or presence situations such as counting objects, tool break detection and rate counting. Technology has taken fiber optic sensors to the other extreme. Much research and development^{2,3,4} has been completed on ultra high accuracy military applications using interferometric techniques where accuracies of one thousandth of an angstrom have been achieved. Such high accuracies are required for gyroscope and hydrophone sensors.

A large number of both military and industrial applications will require analog physical property sensors more advanced than absence or presence sensors but considerably less complex than interferometers. It is important to note that the primary driving force for using fiber optics in these particular applications has been freedom from electrical noise.

Sensor Types

Intensity Modulated Sensors

Intensity modulated sensors^{5,6,7,8} are advanced versions of the simple absence or presence sensors. While counters and switches use the digital nature for an on/off pulse, transmissive and reflective fiber optic sensors are analog in nature. Such sensors modulate the intensity of the light output for measurement. Reflective sensors are the most widely used in this category.

Phase Modulated Sensors

Phase modulated sensors generally use interferometric techniques.⁹ Instead of using intensity, they measure a phase shift between two beams which causes an interference as a result of perturbations from the environment being sensed.

Due to their extreme sensitivity (5 orders of magnitude more sensitive than intensity modulated sensors) they have found potential use in hydrophone applications for the military. However, this sensor approach has been prohibitive from a cost standpoint for industrial use.

Applications

Digital Switches and Counters

Fayfield⁵ gave a review of switch/counter applications, such as broken thread detection, register mark detection and object detection in general. Transmissive and reflective sensors are primarily used. Figure 1 shows transmissive and reflective fiber optic sensors. In switch, counter applications, the lightpath is interrupted and the absence of signal is detected at the electro-optic interface. Fiber optic limit switches are especially attractive due to their non-contact nature which eliminates wear. As a general comment, fiber optic absence/presence sensors are more expensive than their photoelectric counterparts. The driving force for their use is almost always environmental difficulties. As the environmental problems become more severe, fiber optic sensors become more cost effective.

There is a large potential switch application in the machine tool area. Sensors can be used to gauge parts or determine if the cutting tool is present.

In almost all situations there is a high volume of liquid coolant flowing in the vicinity of the cutting tool. The coolant and the debris that it is carrying are fouling the optics by essentially blinding the optical probe.

There are commercial systems that have addressed this problem. The probes can be kept clean even in the presence of high volumes of coolant by using an air wipe concept. With a slight positive pressure over the end of the probe, coolant and debris are kept off the optical surface. The system is further enhanced if a spoiler is used in the air flow. The spoiler causes a turbulent swirling air flow which enhances the cleansing action. In normal field applications, most of the machinery that uses cutting tools has compressed air sources in close proximity so that installation is simple.

Target/background contrast is a major problem in reflective systems. Cutting tools and objects that are dirt or grease covered generally have poor reflectivity. With a reflective system, to detect such objects, the reflected light intensity must be maximized. There are basically two approaches. The first is to maximize the light output of the sensor. Almost all commercial units have a gain adjustment which should be set at the maximum value. It must be realized that commercial units from various manufacturers vary greatly with output differing by as much as 300%. Another approach is to place a highly reflective target, such as a retro-reflective material, on the object to be detected. There are situations in which reflectivity is too low for a reliable sensing function. In such cases, a transmissive system, which is independent of reflectivity is recommended.

Widespread use of digital fiber optic switches and counters has also been limited due to functionality. Most applications have been limited to absence/presence, since these are the simplest sensors to develop and use. Furthermore, they are essentially the only ones available. Digital sensing is now expanding to liquid level, temperature, and pressure.¹²

For the expanded digital sensor, the target provides the sensing function. If a target can be fabricated such that its position or state relative to the probe end is a function of some physical parameter to be sensed, then physical property sensors can be fabricated. Consider a reflective bimetal disc as one such target. As the surrounding area reaches its set point temperature, the disc defects. The distance between the probe and target changes correspondingly, affecting the amount of light reflected back to the probe which provides the basis for switching. Pressure sensing via fiber optics is provided by a method analogous to the bimetal temperature disc. A flexible pressure sensitive diaphragm with a reflective inner surface varies its distance from the fiber optic probe tip in

response to a pressure input. Using a snap diaphragm, a pressure set point is achieved.

Another technique for utilization of fiber optic probes involves the use of a prism tip for liquid level sensing.¹ Light traveling down one leg of the probe is totally internally reflected at the prism/air interface. Note that air (index of refraction=1) acts as a cladding material around the prism. As the prism contacts the surface of a liquid, light is stripped from the prism, resulting in a loss of energy at the detector. With the proper electronic circuitry, discrimination can be achieved between liquid types, such as gasoline and water, by the amount of light lost from the system, a function of the index of refraction of the liquid.

Displacement

Fiber optic reflective sensors are non-contact displacement sensors and, as such, have a broad application range. Much like inductive displacement proximity sensors, non-contact reflective fiber optic sensors provide excellent resolution and repeatability. Fiber optic sensors are not limited to metallic objects, but can be used with any material. Reflective fiber optic sensors have the potential of one microinch sensitivity. As the dynamic range of the sensor increases, however, the sensitivity decreases.

Used as a single point sensing system, they can be used for vibration monitoring, gauging parts, as well as measuring film thickness, shaft runout, eccentricity, axial motion and rotation. Fiber optic proximity sensors are affected by dirty environments which degrade the analog signal. This problem is minimized by working in the IR where light scattering is minimized; and by incorporating a positive air pressure at the probe tip as discussed earlier for digital applications.

The lightsource is typically an LED which varies in intensity by 1/2% per degree centigrade. To resolve this problem, a reference can be used which detects the intensity variations and corrects the LED output. The overall system effectiveness can often be enhanced by using a dual probe system with a common light source. The dual outputs can be divided to normalize light source variations as well as increase the output for a given movement, thereby increasing the accuracy. Dual probe sensors are positioned so that as the object comes closer to one probe, the output of that probe changes in a manner just inverse to that of the opposing probe. As the value of one goes down, the other goes up. The relationship holds true as long as both probes function either on the front slope or the back slope of the response curve (See Figure 1c). In addition to magnitude, such a configuration can provide directional information. Similar positioning effects can be achieved if one probe is working on the front slope while the other is working on the back slope. The

advantage is that the sensing probes can be placed on one side of the

object and no longer have to oppose one another. Dual probes are employed in applications such as measuring sheet thickness, concentricity, deviation or servo positioning, shaft diameter and alignment

Physical Properties

Temperature and pressure are two of the most important physical phenomena to be measured.¹² A bimetallic element attached to the end of reflective fiber optic probe provides the basis for an analog temperature sensor if the snap action is replaced with a smooth continuous movement. With this type of configuration, a linear temperature response can be obtained from 0 to 200°C with an accuracy of $\pm 1^\circ\text{C}$. Using a similar configuration, but replacing the temperature sensitive element with a diaphragm, produces a pressure sensor. Sensors with a dynamic range of 0 to 500 psi and accuracies better than 1% have been developed.

Other techniques for measuring temperature have been devised.^{14, 15} One approach uses a fiber optic probe on which the probe tip has a coating of rare earth phosphors. The phosphors emit fluorescent radiation when excited by UV light. The intensity of fluorescent radiation is a function temperature which can be detected fiber optically. This sensor approach has extreme accuracy approaching 0.1°C . The range is expanding. Initially temperatures could be measured up to about 200°C . Now temperature can be measured up to 1000°C using similar optical techniques. The major drawback to this approach is cost.

Analog fiber optic sensors are not in widespread use, but have been used in many trial industrial applications. Nearly all these sensors use intensity modulation. The major problems include: variations in lightsource intensity which directly effects the analog sensor output; microbending in the leads to and from the sensing region; and intensity variations associated with coupling and decoupling connectors.¹¹

Microbending losses in the fiber leads present a problem only if the leads move while the sensor is in operation. Large core plastic clad silica fibers (PCS) are the least sensitive to bending loss and the best suited for sensor leads. Furthermore, the sensitivity of the leads can be reduced if a protective cable construction surrounds the fiber to retard bending loss. Losses in the leads, if not properly controlled, can cause errors in excess of 5%. An interesting point is that as the lead length increases, the light level in the sensing systems decreases. Analog sensors function best when the leads are 100 meters or less. Digital sensors can work well to 1000 meters.

Connectorization also presents a problem in analog systems. Connectors vary slightly each time the connector is mated. Each connector, although precise, has some misalignment. The misalignment affects the light level in the system (fiber/fiber or fiber/device) and therefore, the sensor output. Typically, the reference fiber is not helpful here, since the reference leg and the sensor leg connectors each have their own characteristics upon mating. Once the system is assembled and calibrated, mating is not a problem if the connectors are not disconnected and reconnected. The problem is further minimized if high precision connectors are used.

Sensing/Communication System

As the requirements for factory and process automation increase, it will be necessary for several sensors to work together¹² and communicate over a common system. The sensors, both analog and digital, interface to a node which performs an electro-optic conversion and supplies digital sensing information which is multiplexed onto the fiber optic communications network. The information is then transmitted back to the host computer. The node is electrical and performs two conversions, opto-electrical for digital conversion and electro-optical for digital transmission. Electro-optic components to achieve the sensor/communication system integration are now commercially available.

SUMMARY

Fiber optic sensors are being widely used in digital applications for switches and counters. Applications are expanding to include temperature, pressure and liquid level switches. Analog fiber optic intensity modulated sensors are being used in a number of trial applications. Analog sensors still have a number of deficiencies including lightsource variations, microbending of optical leads and connector losses.

References

- [1] Krohn D.A., (1982), "Fiber Optic Sensors in Industrial Applications, An Overview", Proceedings of the ISA, Philadelphia, PA, Vol. 37, Part 3, p.p. 1673-84.
- [2] Spillman, W.B., Jr. and McMahon, D.H., (1980), "Frustrated Total Internal Reflection Multimode Fiber Optic Hydrophone", Applied Optics, Vol. 19, No. 1, p.p. 113-17. [3]
- [3] Bucaro, J.A. and Cole, J.H., (Oct. 1979), "Acousto-Optic Sensor Development", Conference Record, Electronics and Aerospace Systems Conference, Vol. 3, p.p. 572-80.
- [4] McMahon, D.H., Nelson, A.R. and Spillman, W.B., Jr., (Dec. 1981), "Fiber Optic Transducers", IEEE Spectrum, p.p. 24-29.

- [5] Fayfield, R.W., (Mar. 1982), "Fiber Optics and Photoelectric Sensing, A Good Combination", Instruments and Control Systems, p.p. 45-49.
- [6] AMP, (1982), "Fiber Optics Use Gains From Realistic Test Method", AMP Design Digest, Vol. 22, p.p. 6.
- [7] Kissinger, C.D. and Howland, B., (Feb. 24, 1976), "Fiber Optic Displacement Measuring Apparatus", U.S. Patent 3,940,608.
- [8] Bejczy, A.K. Primus, H.C. and Herman, W.A., (Mar. 1980), "Fiber Optic Proximity Sensor", NASA Tech. Brief, Vol. 4, No. 3, Item 63, JPL Report NP0-14653/30-42799.
- [9] Giallorenzi, T.G., et. al., (1982), "Optical Fiber Sensor Technology", IEEE J. Quantum Electronics, Vol. 18, No. 4, p.p. 626-64.
- [10] Krohn D.A., (1984), "Fiber Optic Displacement Sensors", Proceedings of the ISA, Houston, TX, Vol. 39, p.p. 331-340.
- [11] Krohn, D.A., (1985) "Field Experience with Fiber Optic Sensors," Proceedings of the ISA, Phil. PA. Vol. 40, p.p. 1051-61.
- [12] Krohn, D.A., (1983), "Fiber Optic Sensors in Industrial Applications, An Update", Proceedings of the ISA, Houston, TX, Vol. 38, Part 2, p.p. 877-90.
- [13] Coulombe, R.F., (Dec. 1984), "Fiber Optic Sensors-Catching up with the 1980's", Sensors, p.p. 5-8
- [14] Wickensheim, K.A., (Sept. 1981), "New Thermometry Technique Measures Component Temperature", Electronic Packaging and Production.
- [15] Gottlieb, M. and Brandt, G.B., (1979), "Measurement of Temperature with Optical Fibers Using Transmission Intensity Effects", Proceedings of the Electro-Optics Conference.

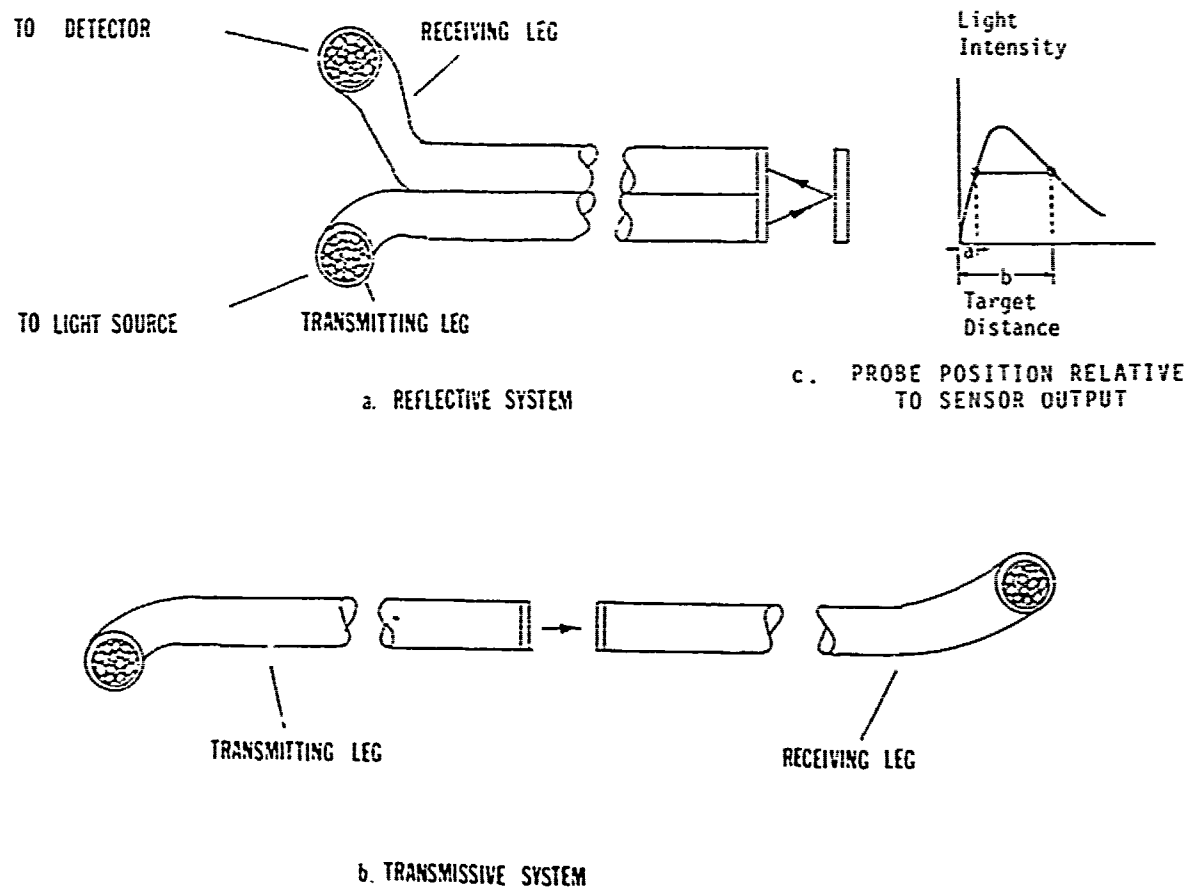


FIGURE 1 FIBER OPTIC SENSORS

OPTICAL SENSING OF MAGNETIC FIELDS

M. A. Butler and S. J. Martin
Microsensor Division 1142
Sandia National Laboratories
Albuquerque, New Mexico 87185

Introduction

The development of optical fiber technology has spurred the development of a wide range of optical sensors for many physical parameters.[1] Interferometric sensors where the fiber is coated with a magnetic material are now capable of sensitivities in the microgauss range [2] with potential for further improvement. These sensors, however, have bandwidths limited to the kilohertz range because of the nature of the magnetostrictive coating materials. The recent development of new magnetic semiconductors which show very large Faraday rotations make possible moderately sensitive devices (milligauss) with very large bandwidths (gigahertz).

In this talk, we would like to explore the limitations on optical sensing of magnetic fields using the Faraday effect imposed by the properties of the sensing material. Emphasis will be given to factors limiting the bandwidth of these devices.

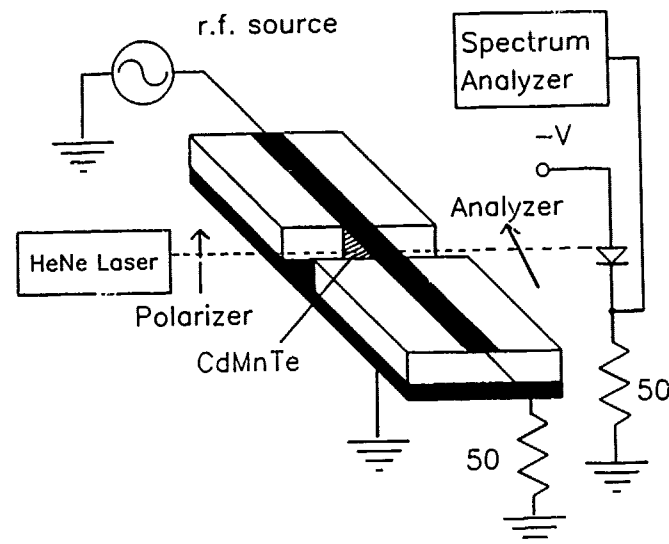
Faraday Effect

The Faraday effect involves modification of the dielectric response of a material by an applied magnetic field. This can come about through the modification of the electronic transition energies, the matrix elements and/or the populations of the spin split ground state. The first two factors normally lead to a "diamagnetic" or temperature independent Faraday effect and the last factor leads to a "paramagnetic" or temperature dependent Faraday effect. Simple models of these effects [3] show that the Faraday effect can be maximized by using light with a photon energy close to the electronic transition energy and by having a material with a strongly paramagnetic groundstate. This is the reason for the use of rare earth doped glasses.

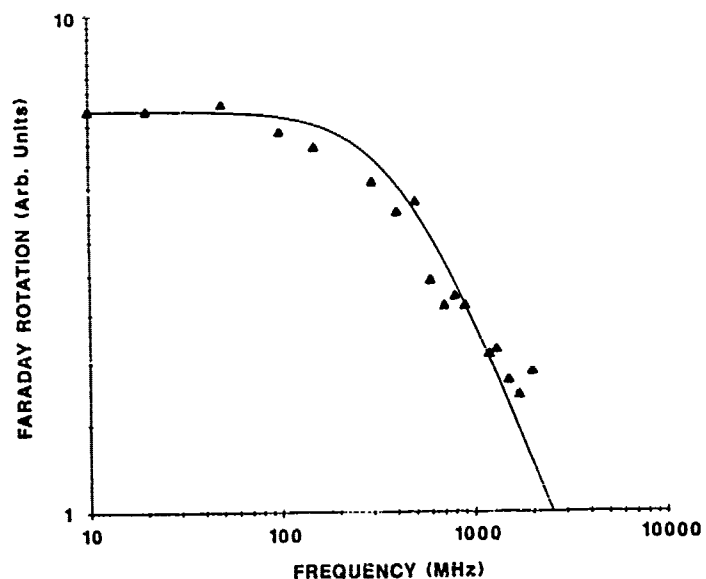
The dilute magnetic semiconductors are a relatively new class of materials which have been found to show very large Faraday effects.[4] These materials are exemplified by the $\text{Cd}(1-x)\text{Mn}(x)\text{Te}$ system which allows values of x up to 0.7 without a phase transition. In this material the bandgap of the semiconductor varies linearly with x allowing the tuning of the electronic transition energy to match the light source used. The Faraday effect is approximately proportional to the Mn concentration.

Experimental Results

Faraday rotation measurements have been made on several alloy compositions at a number of different wavelengths and at frequencies up to 10 gigahertz. These measurements were made by incorporating the sensing material into a microstripline as shown in Figure 1. R.F. power of



one watt passing along the microstrip produces an rms magnetic field in the sample of about 100 milligauss. By passing a linearly polarized light beam through the sample at right angles to the microstrip the polarization direction of the beam is modulated at the R.F. frequency. This modulation is detected by a polarizing analyzer, which converts the polarization modulation to amplitude modulation, and a fast photodiode. The frequency response of the $\text{Cd}(.9)\text{Mn}(.1)\text{Te}$ sample is shown in Figure 2. Other compositions show a



similar functional dependence to the frequency response with the rolloff frequency increasing with Mn concentration.

Spin Dynamics

The time (and thus the frequency) dependence of the Faraday effect can easily be shown to reflect the time dependence of the ground state magnetization. Thus, the frequency response of Faraday effect magnetic field sensors will be determined by the spin dynamics. It is well known [5] that for small applied fields the frequency response of a collection of spins is well described by the modified Bloch equations. The solution yields the functional form for the frequency response shown by the solid line in Figure 2.

$$M(\omega) = \frac{M_0}{\sqrt{1 + (\omega T)^2}}$$

The time constant T reflects the physical processes which allow the magnetization to respond to the applied magnetic field. In the magnetically dilute limit, the ground state magnetization can only grow by spin flips which require that energy be given up to the lattice. Thus the response is determined by "spin-lattice" relaxation processes. In the magnetically dense limit the magnetization is not a conserved quantity at low fields and the magnetization can be changed without transferring energy out of the spin system. In this case the response is determined by "spin-spin" relaxation processes. This is the appropriate description for the CdMnTe system concentrations considered.

Conclusions

The dilute magnetic semiconductors offer great possibilities as sensor materials for Faraday effect magnetic field sensors. The effect is very large and can be optimized for the light source to be used because of the tuneability of the bandgap. The frequency response is determined by the spin dynamics of the Mn spins and will allow bandwidths of several gigahertz.

References

1. T. G. Giallorenzi, J. A. Bucaro, A. Dandridge, G. H. Sigel, J. H. Cole, S. C. Rashleigh and R. Priest, "Optical Fiber Sensor Technology," J. Quantum Electronics, Vol. QE-18, 626, 1982.
2. C. J. Nielsen, "All Fiber Magnetometer with Magnetic Feedback Compensation," Proc. of SPIE, Vol. 566, 286, 1985.
3. C. J. Ballhausen, Introduction to Ligand Field Theory, New York: McGraw Hill, 1962, p. 211.
4. J. K. Furdyna, "Dilute Magnetic Semiconductors: An Interface of Semiconductor Physics and Magnetism," J. Appl. Phys., Vol. 53, 7637, 1982.
5. A. Abragam, The Principles of Nuclear Magnetism, London: Oxford University Press, 1961 p. 53.

ANOMALOUS EMISSIVITY FROM PERIODIC
MICRO-MACHINED SILICON SURFACES

Peter J. Hesketh

Benjamin Gebhart

Jay N. Zemel

Center for Sensor Technologies and Department of Electrical Engineering
Department of Mechanical Engineering and Applied Mechanics
University of Pennsylvania
Philadelphia, Pennsylvania 19104-6314

Thermal processes involving small micro-machined surface elements have begun to attract an increasing amount of attention. While much of the attention has been directed toward the cooling of integrated circuits, there remains a fundamental question about the nature of the interactions when the characteristic scale of the physical process becomes comparable to the dimensional scale of the local geometry. One of the simpler processes to investigate is the radiant heat transfer from a solid whose surface has been micromachined to form a regular periodic structure, e.g. a deep grating or a two dimensional array of pits or hillocks. Such surfaces will be referred to as micro-configured surfaces. Microconfigured surfaces have potential applications as adsorbers of gases, absorbers of radiation, and microheat exchangers. The results reported here are, to the best of our knowledge, not only the first experimental study of the thermal emissivity of deep gratings, but is also a subject for which essentially no direct theoretical study has been performed. A deep grating is defined as one where the ratio of the depth of the grating, h , to repeat distance or characteristic geometric scale, S , is equal to or greater than 0.5. The emissivity measurements were conducted in the range $0.14 \leq \lambda/S \leq 0.68$ where λ is the measured electromagnetic radiation wavelength. The resulting data demonstrated that surface geometry plays a highly significant role in the emissivity.

The experiments employed (110) oriented silicon wafers on which a $22\mu\text{m}$ "square wave" grating is etched to various depths using standard photolithography and a 40%wt. solution of KOH at 52°C . The width of the silicon ridge is $11\mu\text{m}$ as shown schematically in Figure 1a). A scanning electron micrograph of a $22\mu\text{m}$ deep grating is shown in Figure 1b). The peak amplitude to half width ratio, A , for this structure is $A=2$. Another grating with $A=4$ has also been investigated. After etching, the microconfigured wafers are then spin-coated with a phosphorus based dopant which is heated to 1250°C for 10 hours. The phosphorus surface concentration is in the $0.6\text{--}1.1 \times 10^{20}/\text{cm}^3$ regime which yields an effective skin depth for $\lambda > 5\mu\text{m}$ of $2\mu\text{m}$ or less. The back surface of the silicon wafer was also heavily doped to act as the heater element. A blackbody was constructed and its temperature was stable to better than $10\text{m}^\circ\text{C}$ during the course of the measurements. The temperature of the blackbody was used as a reference against which the temperature of the silicon sample was stabilized with a feedback control loop. Temperature fluctuations were typically less than 0.1°C during the course of measurement.

The initial studies were on silicon chips containing the microconfigured surface that had been sliced from the wafer. These chips were mounted in a specially designed low thermal loss holder. Calculators indicated that the thermal losses other than radiation are about 40% of the total energy input. In the temperatures range used, $300^\circ\text{C} < T < 400^\circ\text{C}$, significant difference in the energy input required to reach operating temperatures were observed for smooth and microconfigured surfaced samples. The emissivity measurement consisted of the black body source, the sample, a reflection system that permits viewing of the silicon surface, both smooth and microconfigured, down to azimuthal angles of 75° , as shown in Figure 2. The polar angle drive was controlled by a computer driven stepping motor thereby allowing the polar angle dependence of the emissivity to be measured with good precision. Measurements were carried out for azimuthal directions parallel ($\phi=0^\circ$) and perpendicular ($\phi=90^\circ$) to the grooves. The polarization measurements employed a Perkin-Elmer infrared polarizer at the slits of a Perkin-Elmer 112 NaCl prism spectrometer. A Judson HgCdTe infrared detector was used to measure the intensity of the radiation. The data was logged on a computer controlled system and that also controlled the stepping motor.

The basic measurements are shown in Figures 3 and 4. In Figure 3a), the wavelength dependence of the emissivity for both s and p polarization is shown for $\phi=0^\circ$ and $\theta=0^\circ$. Note the oscillatory and complementary character of the emissivity. A plot of the peak λ positions versus an integer yields a linear rather than a parabolic relation as seen in Figure 3b). The polar angular dependence of the emissivity is quite extraordinary. In Figures 4a) ($\phi=90^\circ$, a polarized radiation), 4b) ($\phi=0^\circ$, p polarized radiation), and 4c) ($\phi=0^\circ$, s polarized radiation), the polar angle position of the maxima in the emissivity decrease with increasing wavelength as shown in Figure 4e). However, in Figure 4d), ($\phi=90^\circ$, p polarized radiation) the emissivity does not show any pronounced peaks. Essentially the same behavior was observed on a sample with the same S value but $A=4$. The only plausible explanation available at present for both the mode and angular dependence of these measurements is that the grating couples a surface polarization to a radiative mode of the sample.

Two of the authors (P.H. and J.N.Z.) wish to acknowledge the partial support of the EEMS Program of NSF, D. Silversmith, Program Manager, under Grant ECS-84-12241. The authors wish to thank Professor H. Baltes for useful discussions and one of us (J.N.Z.) wishes to thank Professor A. Maradudin for a helpful conversation.

STRESS MODELING OF MICRODIAPHRAGM PRESSURE SENSORS
P. C. Tack*
Gould Measurement Systems Division, Oxnard, CA 93033
and H. H. Busta**
Gould Research Center, Rolling Meadows, IL 60008

Abstract

The finite element program analysis of Swanson Analysis System, Inc. was used to model the stress distribution of two monocrystalline silicon diaphragm pressure sensors. Configuration I consists of an anisotropically backside etched diaphragm into a 250 μ m thick, (100) oriented, silicon wafer. The diaphragm dimensions are $l=1000\mu$ m, $h=10\mu$ m, ($l/h=100$). The total chip dimension is 2500 μ m x 2500 μ m. The device is rigidly clamped on the back to a support substrate. Configuration II consists of a monocrystalline, (100), microdiaphragm which is formed on top of the wafer and whose area is reduced by a factor of 25 over Configuration I. The diaphragm dimensions are $l=200\mu$ m, $h=2\mu$ m, ($l/h=100$). The diaphragm is rigidly clamped to the silicon wafer. The stresses $\sigma_x(x,y)$ and $\sigma_y(x,y)$ were calculated at a gauge pressure of 300mm Hg and used to estimate the piezoresistive responses of resistor elements which were placed parallel and perpendicular near the diaphragm edges.

Introduction

Modeling of IC processing and device performance is becoming more and more popular as the complexity of processing increases and as device dimensions shrink into the near-micron and sub-micron regimes. This allows low cost evaluation of new processing and device ideas prior to mask design and commitment to wafer fabrication.

Some of the programs readily available are SUPREM (Stanford University) for process modeling, PISCES (Stanford University) and MINIMOS (Vienna University, Austria) for two dimensional devices modeling and SPICE (U.C. Berkeley) for circuit performance modeling.

As the complexity of sensor development increases and as the business impact of sensors and micromachined devices and systems continues to grow, it will become profitable to adopt some of the existing modeling tools and to develop new ones to help guide development effort.

In this paper, results of three-dimensional stress modeling of two silicon diaphragm sensor configurations will be presented. The results are then used to predict the piezoresistive response of given resistor configurations and comparisons with experimental results will be made.

Current affiliations

*Statham Division of Solatron Transducers,
2230 Statham Blvd, Oxnard, CA 93033

**Amoco Research Center, P.O. Box 400, Mail
Code F-4, Naperville, IL 60566

Stress Calculations

Configuration I

Configuration I is a silicon diaphragm sensor fabricated from (100), n-type silicon with a resistivity of 1.0 to 10.0 ohm-cm. The diaphragm dimensions are $l=1000\mu$ m, $h=10\mu$ m. The overall chip dimension is 2500 μ m. The wafer thickness is 250 μ m. Figure 1 shows the cross-section of this device. The stresses $\sigma_x(x,y)$ and $\sigma_y(x,y)$ of a quarter diaphragm were calculated using the finite element program of Swanson Analysis System, Inc., Version 4.2 [1]. The surface of the quarter diaphragm was divided into 12x12 divisions; the depth was divided into 4 elements. The values of the elastic constants E_x and E_y and of Poisson's ratio were taken from Ref. [2]. One of the edges of the diaphragm is aligned with the $\langle 110 \rangle$ direction.

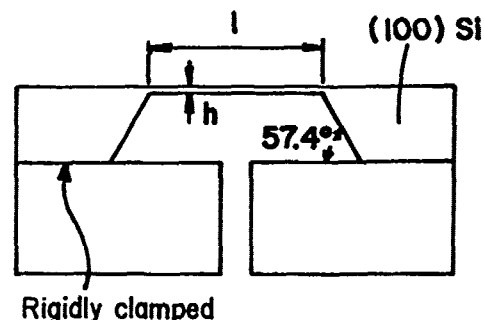


Figure 1 Cross-section of the silicon diaphragm sensor, Configuration I.

Figure 2 shows $\sigma_x(x,y)$ and $\sigma_y(x,y)$ for one quarter of the diaphragm at a gauge pressure of 300mm Hg. The coordinate system was chosen to be in the center of the diaphragm and x and y extend 500 μ m towards the edges. As can be seen, σ_x reaches a maximum in the center of the diaphragm near the edge ($x=500\mu$ m, $y=0$), goes through zero at $x=330\mu$ m and reaches a minimum at $x=0$, $y=0$. The profile of $\sigma_y(x,y)$ is identical to the one of $\sigma_x(x,y)$ except that it is mirror-imaged along the diagonal of the diaphragm.

Configuration II is a silicon sensor with the diaphragm fabricated on top of the wafer. It has the same l/h ratio of 100 as compared to Configuration I but its overall size is much smaller. Here $l=200\mu$ m and $h=2\mu$ m. The cross-section of the device is shown in Figure 3. Realization of such a diaphragm sensor in polycrystalline silicon is described in Ref. [3] and the attempt to form monocrystalline diaphragms by laser-recrystallization is described in Ref [4]. Advantages of this structure over Configuration I, in addition to the smaller size are: elimination of the hard-to-

control backside diaphragm etch process, elimination of the IR alignment step to align the resistor patterns in front of the wafer, provision of an overpressure stop and better control of the diaphragm thickness uniformity due to the LPCVD deposition process.

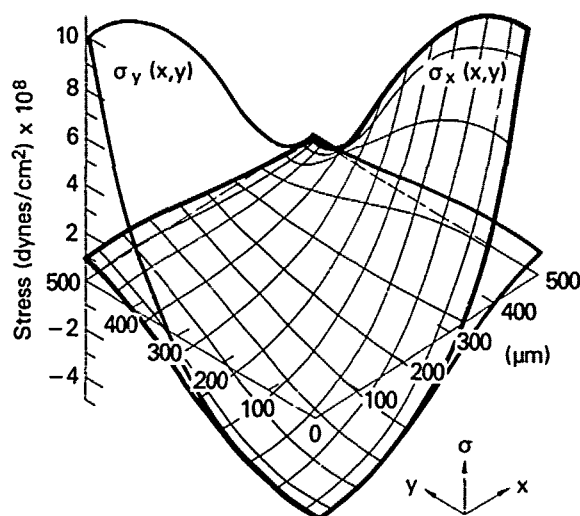


Figure 2 Stress distributions σ_x and σ_y for the sensor shown in Figure 1 at a gauge pressure of 300mm Hg.

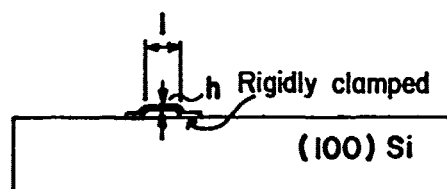


Figure 3 Cross-section of the silicon diaphragm sensor, Configuration II.

In this calculation it is assumed that the diaphragm is rigidly clamped to the silicon support wafer and that it is made of (100), monocrystalline silicon with one of its edges aligned with the $\langle 110 \rangle$ direction.

The results of the stress calculations at a gauge pressure of 300 mm Hg are shown in Figure 4 and are very similar in shape and magnitude to the results shown in Figure 2. Thus, in principle, by proper placement and geometry scaling of the resistor elements, Configuration II should yield the same sensitivity as Configuration I.

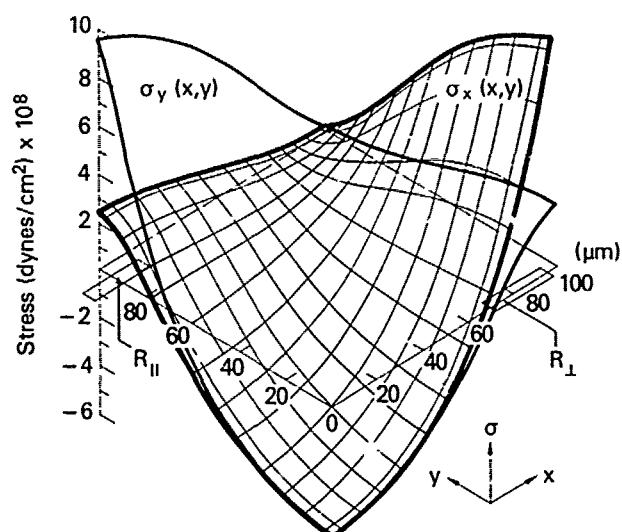


Figure 4 Stress distributions σ_x and σ_y for the sensor shown in Figure 3 at a gauge pressure of 300mm Hg.

Piezoresistance

The stress results shown in Figures 2 and 4 were used to estimate the piezoresistance of p+-diffused or ion implanted resistor elements into Configurations I and II. Figure 5 shows two resistor elements, one located parallel and one perpendicular to two edges of the diaphragm. Due to the magnitude of the stresses at these locations and the signs and magnitude of the piezoresistive coefficients of (100) p-type silicon, fully active bridge behavior can be obtained. This is the customary placement of the resistor elements for most of the sensors processed using Configuration I. The piezoresistive coefficients $\pi_{||}$ and π_{\perp} are defined in Ref. [2]. Here, " $||$ " means parallel to the current direction and " \perp " means perpendicular to the current direction, whereas in $\sigma_{||}$ and σ_{\perp} , the subscript " $||$ " means parallel to the edge of the diaphragm and " \perp " means perpendicular to it.

From Ref. [2] and Figure 5, the change in resistance parallel to the diaphragm edge due to the piezoresistive effect is given by

$$\left(\frac{\Delta R}{R}\right)_{||} = \pi_{||}\sigma_{||} + \pi_{\perp}\sigma_{\perp} = \pi_{||}\sigma_x(x=0,y) + \pi_{\perp}\sigma_y(x=0,y) \quad (1)$$

and correspondingly

$$\left(\frac{\Delta R}{R}\right)_{\perp} = \pi_{||}\sigma_{||} + \pi_{\perp}\sigma_{\perp} = \pi_{||}\sigma_x(x,y=0) + \pi_{\perp}\sigma_y(x,y=0) \quad (2)$$

This assumes that the length of the resistor elements is much smaller compared to the length of the diaphragm, i.e., stresses do not vary along the dimensions of the resistor.

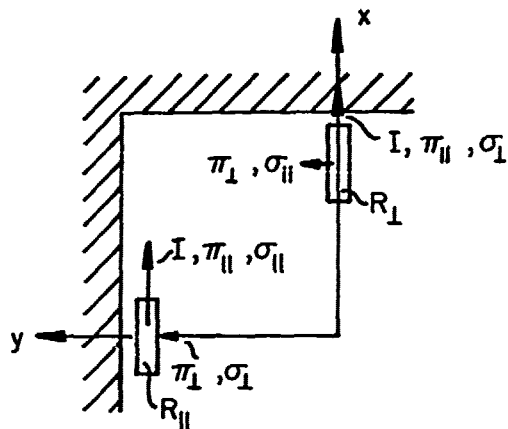


Figure 5 Location of R_1 and R_2 with respect to the diaphragm edges and the corresponding σ and π notations.

Figure 4 shows the outline of two resistor elements in Configuration II with dimensions of $5\mu\text{m} \times 25\mu\text{m}$. The elements are placed $5\mu\text{m}$ away from the edges.

By using equations (1) and (2), the resistance change of the parallel resistor is calculated to be $-2.27\%/300\text{ mm Hg}$ and that of the perpendicular resistor is $-1.32\%/300\text{ mm Hg}$. Here, the average stress values across the resistor dimensions were taken. The values of π_{\parallel} and π_{\perp} were taken from Ref. [2] and are $+40.5 \times 10^{-12}\text{ cm}^2/\text{dyne}$ and $-35.5 \times 10^{-12}\text{ cm}^2/\text{dyne}$, respectively.

By combining two parallel elements and two perpendicular ones into a Wheatstone bridge configuration, the output voltage is calculated as $V_o/V = 59.8\ \mu\text{V}/\text{V}/\text{mmHg}$.

A similar calculation was performed for Configuration I. Here the resistor element consists of two legs of $18\mu\text{m} \times 105\mu\text{m}$ which are parallel to each other, separated by $25\mu\text{m}$, and connected by a $50\mu\text{m} \times 61\mu\text{m}$ diffused region. Using the stress values from Figure 2, the expected piezoresistive changes are $-2.63\%/300\text{ mm Hg}$ for the parallel resistor and $+2.36\%/300\text{ mm Hg}$ for the perpendicular resistor. This corresponds to a pressure sensitivity of a Wheatstone bridge of $V_o/V = 83.2\ \mu\text{V}/\text{V}/\text{mm Hg}$.

Experimental Verification of Piezoresistance

A pressure sensor according to Configuration I was processed with $l=1000\mu\text{m}$ and $h=16\mu\text{m}$ and resistor elements as described above. Since sensitivity scales with $(l/h)^2$ [2], the expected sensitivity is reduced by a factor of $(10/16)^2$, the thickness ratio of the diaphragms. Thus, the expected sensitivity is $83.2 \times (10/16)^2 = 32.5\ \mu\text{V}/\text{V}/\text{mm Hg}$. Experimental results over a three inch wafer ranged from 25 to $30\ \mu\text{V}/\text{V}/\text{mm Hg}$ which is in good agreement with the calculation.

A pressure sensor according to Configuration II was processed with $l=200\mu\text{m}$ using polycrystalline silicon which was subsequently laser-recrystallized. The same resistor dimensions as in the calculation were used. The sensitivity was $10\ \mu\text{V}/\text{V}/\text{mm Hg}$ [4] which is by a factor of 6 lower than the theoretical result. Non-optimum crystallization to yield (100) silicon is the main cause for this discrepancy.

It has been shown that stress calculations of diverse silicon diaphragm pressure sensors can be used to obtain estimates of the expected piezoresistive response. The calculations can be used to help place resistor elements to obtain maximum or minimum piezo response and to help the sensor designer with the proper choice of resistor dimensions compatible with the required bridge resistance and acceptable power density.

Thanks go to R. Kreeger, Solatron transducers for his encouragement of this work and for providing the funds to perform the stress calculations.

References

- [1] Swanson Analysis System, Inc., P.O. Box 65, Houston, PA 15342.
- [2] S. K. Clark and K. D. Wise, "Pressure Sensitivity in Anisotropically Etched Thin Diaphragm Pressure Sensors," *IEEE Trans. on Electron Devices*, Vol. ED-26, pp. 1887-1896, December 1979.
- [3] H. Guckel and D. W. Burns, "Planar Processed Polysilicon Sealed Cavities for Pressure Transducer Arrays," in *Technical Digest of the IEEE IEDM*, 1984, p. 223.
- [4] H. Guckel, D. W. Burns, H. H. Busta and J. F. Detry, "Laser-Recrystallized Piezoresistive Micro-Diaphragm Sensor," in *Digest of Technical Papers of the International Conference on Solid-State Sensors and Actuators*, 1985, pp. 182-185.

Noise in Piezoresistive and Capacitive Sensors

Richard R. Spencer, Bruce M. Fleischer, Phillip W. Barth, and James B. Angell

Abstract

An analysis has been performed of the minimum resolvable input (*MRI*) for piezoresistive and capacitive pressure sensors as determined by fundamental noise mechanisms. Even though capacitive sensors have raw sensitivities that are an order of magnitude or more higher than those of piezoresistive sensors, the *MRI* of piezoresistive sensors (ignoring temperature coefficients and offsets) can be much lower than that of comparable capacitive sensors. Piezoresistive sensors may thus be more promising than capacitive sensors for applications requiring a large dynamic range (*DR*) and/or small *MRI*.

Glossary of Symbols

B_m	Measurement bandwidth (Hertz)
C_s	Capacitance of a capacitive pressure sensor (Farads)
d	Distance between plates of capacitor with $P = 0$ (μm)
<i>DR</i>	Dynamic range ($P_{\text{max}}/\text{MRI}$)
E	Young's modulus (mmHg)
h	Diaphragm thickness (μm)
k	Boltzmann's constant (Joules/K)
kT	Thermal energy of one electron (Joules)
L	Length of one side of a square diaphragm (μm)
<i>MRI</i>	Minimum Resolvable Input (mmHg)
P	Pressure on diaphragm (mmHg)
P_{max}	Maximum allowable input pressure (mmHg)
q	charge on an electron (Coulombs)
R	Resistance (Ω)
r	Radius of a circular diaphragm (μm)
S_{cap}	Capacitive sensitivity, defined as change in capacitance divided by reference-pressure capacitance (ppm/mmHg)
S_{piezo}	Piezoresistive sensitivity, defined as change in resistance divided by reference-pressure resistance (ppm/mmHg)
t	time
T	Absolute temperature (K)
V_b	Bias voltage applied to sensor (V)
ϵ	Permittivity of dielectric used for C_s and C_r ($\text{F}/\mu\text{m}$)
ν	Poisson's ratio
σ_{fract}	Fracture stress of silicon (mmHg)
σ_{max}	Maximum stress in diaphragm (mmHg)

This work was supported by Ford Corporation and the National Institutes of Health. Bruce Fleischer is supported by an AT&T Bell Laboratories PhD scholarship.

R. Spencer and B. Fleischer are graduate students at Stanford. Their mailing address is AEL 124, Stanford University, Stanford, CA 94305.

J. Angell is the Associate Chairman of the department of Electrical Engineering at Stanford. His mailing address is McCullough 162, Stanford University, Stanford, CA 94305.

P. Barth was with Stanford, he is now the Program Director, Special Sensor Development, at NovaSensor, 2975 Bowers Ave., Santa Clara, CA 95050.

Introduction

The purpose of this investigation is to determine the minimum detectable signal for a pressure sensor assuming that all systematic errors (*e.g.*, temperature coefficient and offset) have been eliminated. Capacitive and piezoresistive sensors are classified based on the method used to measure ΔC or ΔR . Noise in the detection and bias circuitry has been separated from noise in the sensor element proper where possible. In some configurations, however, circuit noise is an inherent part of the sensing method and so is included in the analysis.

Several comparisons of piezoresistive and capacitive sensors have been published (*e.g.*, [1,2,3]). Only the work by Chau and Wise [3] deals specifically with noise mechanisms, and that work did not consider the effects of different measurement techniques. Chau and Wise did show that Brownian noise is insignificant in all practical cases and it will not be considered here.

Capacitive Sensors

Chau and Wise imply that kT/C noise is dominant in all capacitive sensors. However, for many capacitive sensors kT/C noise is confined to a narrow bandwidth and does not affect the achievable resolution. Depending on the measurement technique used, the limit is determined by either shot noise integrated by the capacitor, kT/C noise, or noise in the switching operation (if a ratiometric scheme is used).

Detection circuitry for capacitive sensors often uses a current-controlled oscillator [4,1]. Since the currents used to ramp the oscillator must be switched, the dominant noise mechanism will be determined by the type of switches used. If the switches are MOS devices then the analysis is the same as for the RC oscillator circuit described below. If the switches are bipolar devices then their shot noise determines the fundamental limit to the performance.

With bipolar switches the only kT/C noise present is due to the resistance of the dielectric and has a bandwidth on the order of 10^{-3} Hz. The lower limit of the measurement bandwidth is much greater than the upper limit of the noise bandwidth and kT/C noise is not detectable. The minimum resolvable input for this shot noise limited case is

$$\text{MRI} = \frac{2}{S_{\text{cap}}} \sqrt{\frac{q}{C_s V_b}} \quad (1)$$

The plate-touching pressure is

$$P_{\text{max}} = \frac{5.33dEh^3}{r^4(1-\nu^2)} \quad (2)$$

and the dynamic range is

$$\text{DR} = 0.295r \sqrt{\frac{\epsilon V_b}{dq}} \quad (3)$$

Only two of these three quantities are independent (the dynamic range is defined as the maximum input pressure divided by the *MRI*). P_{max} is derived from the circular-diaphragm sensitivity equation in [3] and the equation for the deflection at the center of the diaphragm in [5].

Equations have also been derived for capacitive sensors where kT/C noise is the dominant mechanism (e.g., RC relaxation oscillators). The maximum input pressure is the same as above and the other equations are

$$MRI = \frac{5.44}{S_{cap} V_b} \sqrt{\frac{kT}{C_s}} \quad (4)$$

and

$$DR = .167 V_b \sqrt{\frac{C_s}{kT}} \quad (5)$$

These equations were derived by assuming that $t = RC_s$ is the parameter measured. The jitter in t was found using a method similar to Abidi's [6].

If a ratiometric measurement scheme is used then the MRI is determined by the circuit implementation. In a simple MOS-switch charge-sharing approach the kT/C noise resulting from the switch resistance is dominant. If more complicated switched capacitor schemes are used then the MRI is determined by op-amp noise, random errors in charge cancellation, and other sources determined by the particular design. Although promising, this technique is more complicated than the others discussed and no sensors using it have been described in the literature.

Piezoresistive Sensors

For piezoresistive sensors two general measurement techniques are possible: a ratiometric scheme (including the classic bridge configuration), or an RC oscillator. In both cases the dominant noise mechanism is thermal noise in the piezoresistor. P_{max} , defined to be the rupture pressure, is found using equations for S_{piezo} , σ_{peak} , and σ_{fract} [1].

$$P_{max} \approx 8.96 \times 10^6 \left(\frac{h}{L} \right)^2 \quad (6)$$

For piezoresistive RC sensors the MRI is the same as noted above for capacitive RC sensors except that the appropriate sensitivity must be used:

$$MRI = \frac{5.44}{S_{piezo} V_b} \sqrt{\frac{kT}{C}} \quad (7)$$

and

$$DR \approx .03 V_b \sqrt{\frac{C}{kT}} \quad (8)$$

For the ratiometric piezoresistive sensor (assuming a standard bridge configuration)

$$MRI = \frac{2\sqrt{4kTRB_m}}{S_{piezo} V_b} \quad (9)$$

and

$$DR \approx \frac{.022 V_b}{\sqrt{4kTRB_m}} \quad (10)$$

Summary

Using these equations it is possible to compare the performance limits of capacitive and piezoresistive sensors. These equations also show how the MRI , DR , and P_{max} scale as long as the assumptions used in deriving them remain valid. The table below compares the calculated MRI for four representative sensors (adapted from [3]).

Minimum Resolvable Input ¹ (mmHg)				
Sensing Method	Ultraminiature		Ultrasensitive	
	Piezo (C1)	Cap (A1)	Piezo (D1)	Cap (B1)
Ratiometric	1.6×10^{-4}	see note 2	7.1×10^{-5}	see note 2
RC Oscillator	5.9×10^{-4}	1.7×10^{-2}	2.8×10^{-4}	1.0×10^{-2}
Current Controlled Oscillator ³	N/A	6.7×10^{-2}	N/A	4.1×10^{-2}

Notes:

1. Unless stated otherwise, a 3 V supply and a 100 Hz B_m have been used.
2. Depends on exact circuit configuration, see text.
3. These numbers do not use a 100 Hz B_m and can be improved slightly. How much improvement is possible depends entirely on circuit design and device performance, but the MRI will always be larger than for the piezoresistive case.

Acknowledgements

We thank Lyn Bowman for his participation in the early discussions of this work.

References

- [1] Craig S. Sander. *A Bipolar-Compatible Monolithic Capacitive Pressure Sensor*. PhD thesis, Stanford University, December 1980.
- [2] Y. S. Lee. *A Silicon Capacitive Pressure Transducer: Performance Characteristics and Limitations*. PhD thesis, University of Michigan, December 1981.
- [3] H. L. Chau and K. D. Wise. Scaling limits in batch-fabricated silicon pressure sensors. In *Transducers'85*, pages 174-177, IEEE, 1985.
- [4] Michael John Sebastian Smith. *An Integrated Circuit for a Biomedical Capacitive Pressure Transducer*. PhD thesis, Stanford University, June 1985.
- [5] Wen H. Ko and Min-Hang Bao, and Yeun-Ding Hong. A high-sensitivity integrated-circuit capacitive pressure transducer. *IEEE Trans. on Electron Devices*, ED-29(1):48-56, Jan 1982.
- [6] Asad A. Abidi and Robert G. Meyer. Noise in relaxation oscillators. *IEEE Journal of Solid State Circuits*, SC-18(6): 794-802, December 1983.

Selden B. Crary

Electronics Department
General Motors Research Laboratories
Warren, Michigan 48090

ABSTRACT

Thermal modeling techniques are demonstrated as they apply to a generic integrated microsensor with a heat source located on an anisotropically etched silicon diaphragm. One- and two-dimensional conduction formulas, boundary layer convective heat transfer, a method of images approach for chip-level conduction, and the finite-element method are discussed, with examples, as they apply to the generic microsensor.

I. INTRODUCTION

Thermal management of digital and analog integrated circuits has received considerable attention [1-4]. The additional thermal management challenge presented by integrated microsensors has received considerably less attention [5]. This paper demonstrates the development of a thermal model for a heated chemically sensitive microsensor and addresses issues relevant to microsensor integration. The geometry of the generic heated microsensor treated here is given in Sec. II. Simple conduction and convection models are presented in Secs. III and IV. A chip-level model of thermal conduction which leads to an important conclusion about integrability is introduced in Sec. V, and the resulting lumped electric-circuit analogue is discussed in Sec. VI. Section VII demonstrates the use of the finite-element method as a means of achieving increased accuracy in calculations of conduction heat flow.

II. GEOMETRY OF A GENERIC HEATED MICROSENSOR

The generic microsensor considered here is shown in Fig. 1. It consists of an $80\text{ }\mu\text{m} \times 120\text{ }\mu\text{m}$ poly-Si heater located in a buried layer on a $250\text{ }\mu\text{m}$ square Si membrane. The heater is connected by two $1\text{ }\mu\text{m}$ -thick Al leads and is used to heat a thin, chemically sensitive element, which also has two leads. The membrane is taken as a $2\text{ }\mu\text{m}$ -thick B^+ -implanted Si diaphragm fabricated on a $300\text{ }\mu\text{m}$ thick $\times 3\text{ mm}$ square $\langle 100 \rangle$ -Si chip. Two $1\text{ }\mu\text{m}$ -thick layers of silicon dioxide are used as dielectric insulators. Typical values for the temperature-dependent thermal conductivities of the various materials are taken from the literature [6,7].

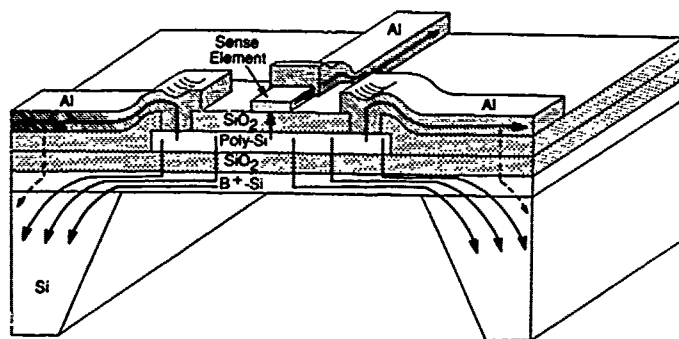


Fig. 1 Schematic representation of heat flow paths away from the heater.

III. SIMPLE CONDUCTION MODELS

Because of the planar character of many device geometries, simple one- and two-dimensional heat conduction formulas are often appropriate. This is especially true if the thermal conductivities of adjacent materials are significantly different, as in the case of boron-doped Si and SiO_2 , where the ratio of conductivities can be 50:1. For example, in Fig. 1 the downward-flowing heat currents from the poly-Si heater will flow through the SiO_2 with little lateral deviation. The thermal resistance of this region can then be modeled adequately as the resistance of a rectangular parallelepiped. Similarly, the heat currents through the silicon membrane are essentially lateral and simple formulas for the thermal resistance of rectangular annuli can be applied to obtain an estimate for this region. The more complex regions can be treated with the lumped-element approach by partitioning the structure in some more or less reasonable way, often using average, or equivalent, lengths and areas. This is commonly done [7], although caution must be exercised and accuracy cannot be expected.

IV. CONVECTION

For IC's, convection is generally not an important issue at the chip level, but must be considered in selecting an appropriate package [8]. For the sensing element under consideration here, however, we allow that convection could be important. The Rayleigh number must exceed a geometry-dependent critical value for natural convection to occur. If our microsensor is mounted in a typical TO-style can (with holes for gas flow), then the Rayleigh number turns out to be approximately 6000, well above the usual range of critical values, 1100-1700 [9]. Thus, natural convection is likely. The thermal resistance, $R = \Delta T/Q$, of the natural convection path is given by $L/(A \cdot \text{Nu} \cdot \kappa)$ [10], where L is the length of the side and A is the area of the square membrane region, Nu is the Nusselt number for the geometry, κ is the thermal conductivity of air, ΔT is the difference in temperature between the heated region and the can, and Q is the total heat flux due to natural convection. Using $L = 250\text{ }\mu\text{m}$, $A = 6.25 \times 10^4\text{ }(\mu\text{m})^2$, $\Delta T = 400^\circ\text{C}$, the value of κ at 200°C , and the range 5 to 8 of average values for the Nusselt number [11], R is estimated to be in the range 13 000 to 21 000 K/W. This range of thermal resistances is large compared to other thermal paths for this sensor. In addition, natural convection is unlikely underneath the diaphragm region because the Rayleigh number there is well below 1000. Thus, natural convection is not an important thermal conduction mechanism for this microsensor.

Forced convection, however, may also be present, especially if the sensor is not protected from flows being directed across the heated sensing element. A complete analysis of the heat transport under forced flow conditions is complex. An estimate can be obtained for specific cases, however, and this is done here assuming a flow speed of 100 mm/s over the chip.

Following the standard integral method used in boundary layer theory [12], the heat flux per unit area from an infinitely long heated strip of arbitrary, continuous wall temperature in the presence of a steady parallel flow of gas (see Fig. 2) is given by

$$q_w(x) = 0.323 \kappa \left(\frac{U_0}{\eta} \right)^{1/2} \text{Pr}^{1/3} \int_{x^*=x_0}^x \frac{(dT_w(x^*)/dx^*) dx^*}{x^{1/2} [1 - (x_0/x)^{3/4}]^{1/3}}$$

where $T_w(x^*)$ is the wall temperature a distance x^* downstream from the leading edge of the chip; x_0 is the unheated length of the chip upstream from the heated strip; ρ and η are the density and dynamic viscosity, respectively; U is the free-stream flow speed of the gas; $\text{Pr} = \eta C_p / \kappa$ is the Prandtl number for the system, which includes the specific heat of the flowing gas; and it is assumed that the temperature of the leading edge of the chip is at the ambient temperature. For the case at hand $\text{Pr} = 0.73$. Applying this formulation to a diaphragm assumed to be at 400°C , except at its leading and trailing edges, where surface temperature gradients of $\pm 20^\circ\text{C}/\mu\text{m}$ are assumed to connect the membrane to the rest of the chip at 0°C , gives

$$q_w(x) = 0.323 \kappa \left(\frac{U_0}{\eta} \right)^{1/2} \left(\frac{4}{3} \text{Pr} \right)^{1/3} (20 \text{ K}/\mu\text{m}) r_w(x)$$

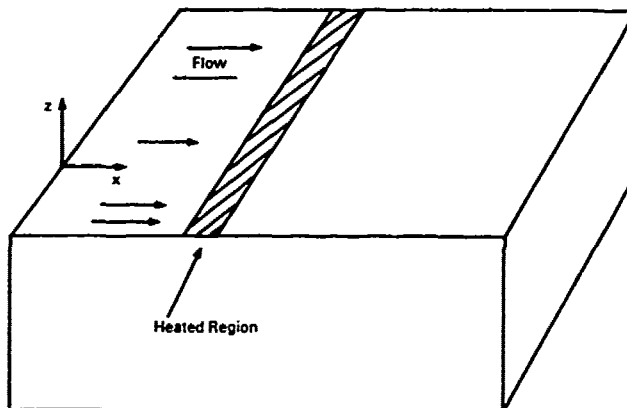


Fig. 2 Geometry considered in the estimate of heat lost to forced convection. The origin of the coordinate system is at the leading edge of the chip, as shown.

The function $r_w(x)$ is shown plotted in Fig. 3 and demonstrates the relative rates of surface heat flux from the membrane as a function of downwind position. The negative values of $r_w(x)$ on the extreme downwind side indicate a net influx of heat in that region of the diaphragm. This procedure gives an estimate of the upper bound on the forced-convection heat flux likely for this heated membrane region, 1.1 mW. This is a minor heat loss path for this sensor. Extension of this procedure to the entire chip surface, assumed for the purposes of the estimate to be at 100°C and cooled by a flow at 0°C , gives 22 mW, which is significant. Turbulent convection, if present, would be expected to increase the heat flux appreciably.

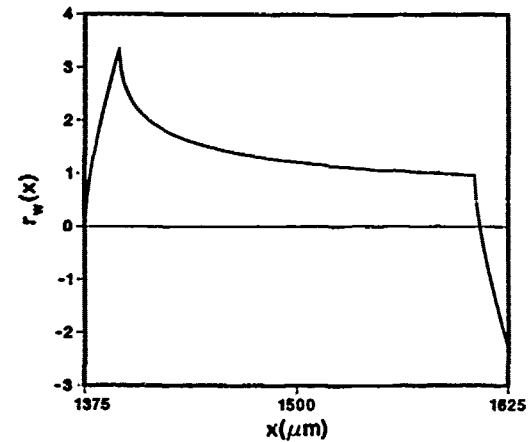


Fig. 3 The convection integral $r_w(x)$ plotted versus position along the $250 \mu\text{m}$ long membrane region, which is centered on the 3 mm square chip. The integral has units $(\mu\text{m})^{1/2}$.

V. CHIP-LEVEL CONDUCTION

The surface temperature field of a chip is of importance for integration of a microsensor with circuitry. Bilotti's work discusses some of the physical concepts of importance [13], and a number of other authors have made analyses [14]. A simple physical picture that has proven useful conceptually and computationally is presented. Essentially, an alternating series of image sources, Fig. 4, leads to the Green's function for surface heat sources in an infinite slab model with an isothermal lower surface [15]. The temperature anywhere in the slab is found by summing up the contributions from the source and image sources.

$$T = T_0 + \sum_i \frac{2Q_i}{\kappa R_i}$$

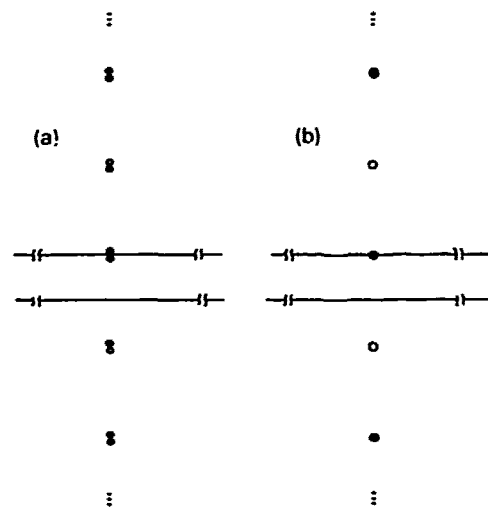


Fig. 4 Placement of real and image sources in the method of images approach. In (a) the filled circles represent the real source and image sources with the same sign and magnitude as the real source, and unfilled circles represent image sources with the opposite sign. In (b) all the sources have magnitude twice that of the real source.

The sum is over the infinite string of charges, R_i is the distance from charge i to the field point in the chip, and T_0 is the temperature of the lower surface. The resulting top-surface temperature is shown in Fig. 5 which demonstrates the exponential falloff in surface temperature [13] and the near-field dependence, which is R^{-1} for $R < t$, where t is the thickness of the chip. Vertical temperature profiles are given in Fig. 6.

There is only one length scale in the steady-state problem, t , and therefore finite-chip size effects are only of importance within about one thickness unit of the chip edge. Thus, Figs. 5 and 6 give an accurate picture of the temperature everywhere of interest. Extended sources of arbitrary shape can be treated by superposition. Sources not on the surface can be treated in a similar fashion. The essential point is that there is a fast, 13.6 dB/thickness unit, falloff of temperature in the far field, and that any desired surface temperature ($T > T_{\text{header}}$) can be obtained by moving away from sources in steps of size t . Also, because of the single-length-scale character of the problem, defects in the isothermal boundary assumption will be annealed out in a distance $\sim t$ away from the defect, and the essential result is unchanged in the presence of bonding defects that cover a small fraction of the area of the lower surface [16].

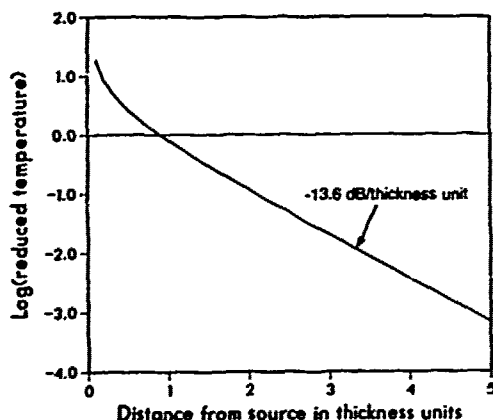


Fig. 5 Surface chip temperature as a function of distance from a point source of surface heat flux. The exponential falloff of 13.6 dB per thickness unit is evident for distances greater than one thickness unit.

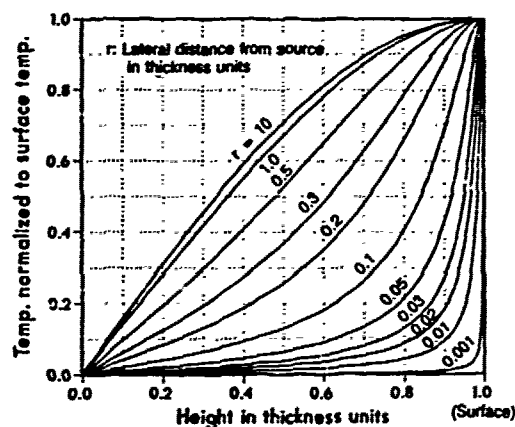


Fig. 6 Temperature profiles, from thermally anchored heat sink to chip surface, parameterized by the lateral distance from a point source of surface heat flux. Taken together, Figs. 5 and 6 give the temperature everywhere in a semi-infinite chip model.

The sensor being considered contains a membrane region which can be considered as a heat source connected by a small area A to a chip with a hole in it, as in Fig. 7a. For $A \ll 2\pi t^2$ the heat flow is in the $T-R^{-1}$ regime. What matters, then, is the surface area through which the heat in the membrane pours out into the chip proper. The picture in Fig. 7a can thus be replaced by the one in Fig. 7b, for which the thermal resistance is simply $R = (2\pi k r)^{-1}$. For the generic microsensor, this gives $R_{\text{chip}} \sim 60 \text{ K/W}$.

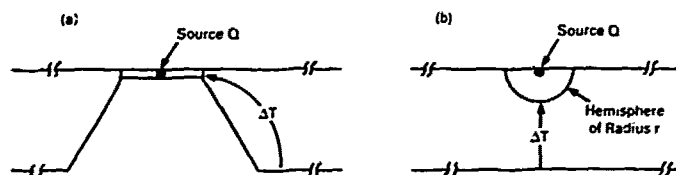


Fig. 7 The thermal resistance of the chip is defined as $\Delta T/Q$, where ΔT is the temperature difference between the isothermal lower boundary and the edge of the diaphragm region, as shown schematically in (a). To estimate the thermal resistance a hemisphere of radius r is introduced that has the same contact area between source region and chip region.

VI. LUMPED MODEL

The above calculations can be used to construct a lumped model, as in Fig. 8. For this sensor, the thermal resistance of greatest importance in reducing power consumption is that of the membrane, and the thermal resistance of the package is of greatest importance to keeping the chip circuitry near ambient temperature. Use of such lumped-element models is common, but cannot be expected to give accurate results, due to obvious limitations.

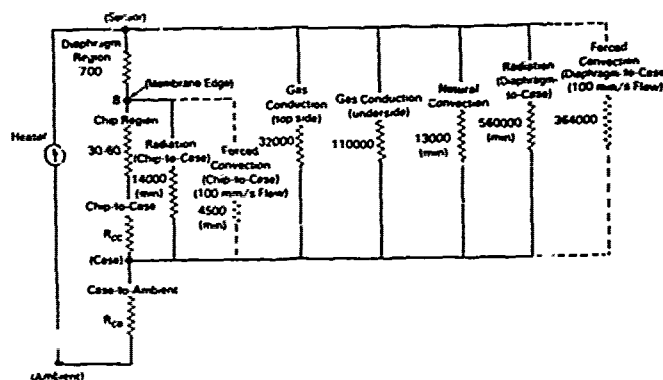


Fig. 8 Lumped thermal model of the generic microsensor. Approximate thermal resistances of heat flow paths are given in kelvins per watt. The most important resistances are those in the left-most resistance channel. Forced convection can be important when flow is present.

VI. FINITE-ELEMENT METHOD

Off-the-shelf finite-element codes are capable of readily providing $<5\%$ error in a solution of the heat conduction equation with complex boundary and forcing conditions, even with temperature-dependent thermal conductivity. We have demonstrated this with MSC-NASTRAN [17] as the code using simple right parallelepipeds to model the relatively complex membrane region. The pre- and post-processing software is available that can reduce the model building and analysis time considerably. An example of the output is shown in the left-hand side of Fig. 9, which shows isothermal lines on the chip surface for one quadrant

of our model. Design changes can be tested quickly. For example, the effect of introducing a micromachined hole in order to increase the thermal isolation of the sensing element can be explored by simply removing appropriate elements and rerunning the code. The right-hand side of Fig. 9 shows isothermal lines for a quadrant of the membrane with such a hole, and the effect of the hole is apparent. Other design changes, or changes in assumptions about boundary conditions, forcing functions, or material properties (including temperature-dependence) can be explored in a similar manner. Also, transient analysis is available in some codes, as are boundary conditions that take into account convective and radiative heat flow.

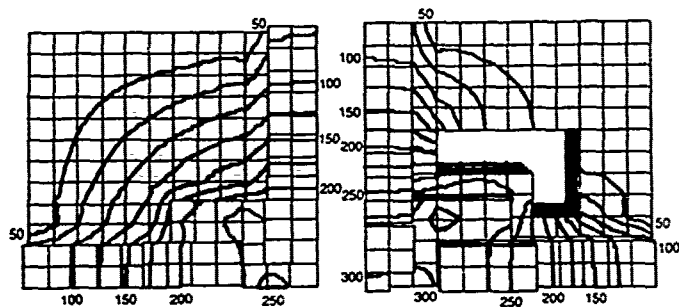


Fig. 9 Finite-element-method generated isotherms for a three-dimensional model of a generic micro-sensor fabricated on a micromachined silicon membrane. In the left figure is shown one quarter of the model, which includes a buried heater located in the lower right-hand corner. In the figure on the right are plotted isotherms for a mirror image of the model after a micromachined hole has been introduced. The finite-element method allows for efficient investigation of sensor design modification.

In the membrane model without the hole the thermal resistance is 1020 K/W ($\pm 5\%$) which is $\sim 30\%$ higher than the value obtained from the lumped model of Sec. VI. About one-half of this difference is due to explicit inclusion of temperature-dependent material properties in the finite-element calculation. The other half is due to the ability of the finite-element method to deal with thermal conduction in a quasi-continuous, as opposed to lumped-element, manner. Continued improvement in pre- and post-processing capabilities will allow increased accessibility to the finite-element method to sensor designers and modelers, and increased computational speed and storage capabilities will allow increased accuracy of computations.

VIII. SUMMARY

The heat currents in a generic heated microsensor have been analyzed using one-dimensional conduction models, an integral technique for forced convective heat transport, a method-of-images approach for determining the temperature field of a chip, and the finite-element method for increased accuracy of conduction calculations. It is expected that the finite-element method will be used increasingly in the areas of micro-sensor design and modeling.

IX. REFERENCES

1. M. Mahalingham, "Thermal Management in Semiconductor Device Packaging," *Proc. IEEE* **73**, 1396 (1985).
2. A. D. Kraus and A. Bar-Cohen, *Thermal Analysis and Control of Electronic Equipment* (Hemisphere; Washington, D.C.; 1983).

3. E. A. Herr, A. Poe, and A. Fox, "Reliability Evaluation and Prediction for Discrete Semiconductors," *IEEE Trans. Reliab.* **R-29**, 208 (1980).
4. R. W. Keyes, "A Figure of Merit for IC Packaging," *IEEE J. of Solid-State Circuits*, **SC-13**, 265 (1978).
5. U. Steger and H. Reichl, "Thermal Simulation of Integrated Digital Transducers," *Sensors and Actuators* **4**, 621 (1983); R. B. Luning and L. A. Gaudreau, "Computer-Aided Infrared Sensor Thermal Design," *Proc. SPIE Int. Soc. Opt. Eng.*, **327**, 105 (1982).
6. F. P. Incropera and D. P. DeWitt, *Fundamentals of Heat Transfer* (Wiley, New York, 1981), pp. 763-768; C. Y. Ho, R. W. Powell, and P. E. Liley, "Thermal Conductivity of the Elements: A Comprehensive Review," *J. Phys. Chem. Ref. Data*, **3**, Suppl. 1 (1974), pp. 587-590; and W. R. Runyan, *Silicon Semiconductor Technology* (McGraw-Hill, New York, 1965), Chapters 6 and 10.
7. G. R. Lahiji and K. D. Wise, "A Batch Fabricated Si Thermopile Infrared Detector," *IEEE Trans. Electron Devices*, **ED-29**, 14-22, 1982.
8. Reference 2, Chapt. 23.
9. L. D. Landau and E. M. Lifshitz, *Fluid Mechanics* (Addison-Wesley, Reading, 1968), p. 214.
10. L. C. Burmeister, *Convective Heat Transfer* (Wiley, New York, 1983).
11. W. J. King, *Mech. Eng.* **54**, 347, (1932), and Ref. 10, pp. 552-3.
12. A. Bejan, *Convection Heat Transfer* (Wiley, New York, 1984), pp. 52-57.
13. A. A. Bilotti, "Static Temperature in IC Chips with Isothermal Heat Sources," *IEEE Trans. Electron Devices* **ED-21**, 217 (1974).
14. W. T. Matzen, R. A. Meadows, J. D. Merryman, S. D. Emmons, "Thermal Techniques as Applied to Functional Electronics Blocks," *Proc. IEEE* **52**, 1496 (1964); V. L. Hein, "Convection and Conduction Cooling of Substrates Containing Multiple Heat Sources," *Bell Syst. Tech. J.*, **46**, 1659 (1967); P. R. Gray and D. J. Hamilton, "Analysis of Electrothermal Integrated Circuits," *IEEE J. of Solid-State Circuits*, **SC-6**, 8 (1971); J. Ebrahimi, "Analysis of Thermal Impedance for Conventional and Beam Lead IC Chips," *IEEE Trans. on Electron Devices*, **ED-18**, 1139 (1971); R. D. Lindsted and R. J. Surty, "Steady-State Junction Temperatures of Semiconductor Chips," *IEEE Trans. on Electron Devices*, **ED-19**, 41 (1972); A. G. Kokkas, "Thermal Analysis of Multiple-Layer Structures," *IEEE Trans. on Electron Devices*, **ED-21**, 671 (1974); R. Castello and P. Antognetti, "Integrated-Circuit Thermal Modeling," *IEEE J. of Solid-State Circuits*, **SC-13**, 363 (1978).
15. P. M. Morse and H. Feshbach, *Methods of Theoretical Physics* (McGraw-Hill, New York, 1953).
16. M. Mahalingham, M. Nagarkar, L. Lofgran, J. Andrews, D. R. Olsen, H. M. Berg, "Thermal Effects of Die Bond Voids in Metal, Ceramic, and Plastic Packages," *Proc. 34th Electronic Components Conf.*, May 1984, pp. 469-477.
17. MSC-NASTRAN is a tradename of the McNeal-Schwendler Corporation, Los Angeles, CA 90041.

Comparison of Five Readout Techniques for an Integrated Magnetometer

James Lenz, Ken Kawai, Richard Fryer, and Lee Strandjord

Honeywell Systems and Research Center
P.O. Box 312
Minneapolis, MN 55440

Abstract

Five readout techniques for an integrated permalloy magnetic sensor are investigated. Measurements of scale factor, minimum detectable signal, and long term stability are compared. Significant improvements using more complex modulation techniques are not readily attained over the commonly used DC readout method.

Introduction

Integrated sensor technology offers the capability to include several electronic functions directly with the transducer. Functions such as temperature compensation, self-checking, self-calibration, auto-ranging, and I/O adaptability are examples of electronic circuits which could be part of a "smart sensor". The design of these functions is highly dependent on the knowledge of the transducer's response and the readout method for generating the transducer's electrical signal. This paper deals with a comparison of several readout techniques for an integrated magnetic transducer.

Magnetic Transducer Characterization

The integrated magnetometer involves sputter-depositing four resistors composed of a magneto-resistive material onto a Si substrate. Permalloy is used as the magneto-resistive material because of its relatively high magneto-resistive coefficient, its low magnetostriction coefficient, and its compatibility with IC fabrication processes. The four permalloy resistors form a bridge and are designed so that the unbalanced voltage is a function of the external magnetic field.

Resistor Design

The thickness of the permalloy layer is 300 angstroms and the sheet resistance is $10 \Omega/\square$. Each resistor in the bridge is approximately $100K \Omega$. The permalloy resistors have a relatively large, but well matched temperature coefficient of $2400 \text{ PPM}/^\circ\text{C}$ ($@25^\circ\text{C}$) $\pm 30 \text{ PPM}/^\circ\text{C}$. Figure 1 shows the TCR linearity is within $\pm 1\%$ from -40°C to 100°C for seven transducer chips.

Two designs of permalloy sensor chips were evaluated. The difference between the two is that one includes a cobalt thin film overcoat providing a permanent magnetic bias to the permalloy resistors and the other chip design is without the cobalt magnet.

Figure 2 shows a typical magneto-resistance curve for our permalloy resistors. The purpose of the cobalt magnet layer is to shift the operating point of the transducer

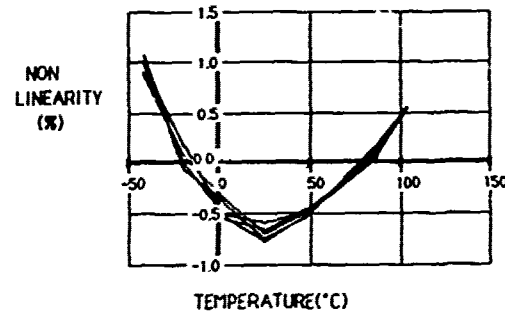


FIGURE 1, Nonlinearity of temperature coefficient for Permalloy resistors

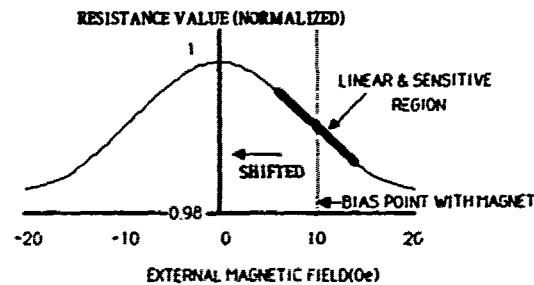


FIGURE 2, Magneto-resistance curve for Permalloy. The dash line represent the bias point due to the Co magnet.

to the most sensitive and linear position for DC external field measurements. The sensor chips have dimensions of 100×200 mils and are mounted in a special package having no magnetic material.

Angular Response

The response of the sensor as a function of angle is shown in Figure 3. The zero angle position was chosen as being along the resistor length. The maximum sensitivity occurs at 90° and 270° for both the chips with and without cobalt magnets. This result concurs with that expected for the transducer's permalloy bridge layout.

Noise

The noise in the bridge was measured using batteries and an ultra-low noise circuit to record the bridge output. This data, plotted in Figure 4, shows $1/f$ noise dominates to 100 Hz and a white noise of 10 $\text{nV}/\sqrt{\text{Hz}}$ dominates above 100 Hz.

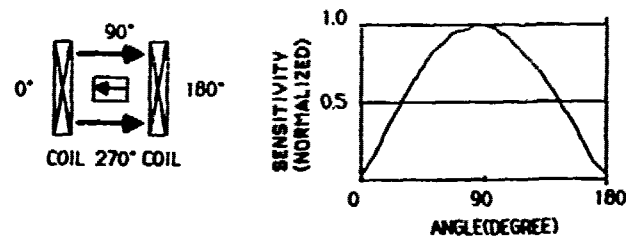


FIGURE 3, Angular response of Permalloy magnetic sensor

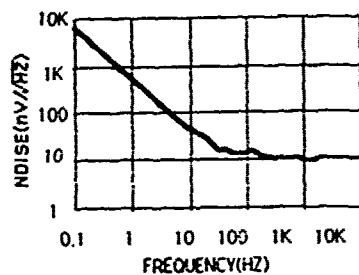


FIGURE 4. Noise spectrum for resistor bridge of magnetic sensor

Readout Techniques

Five readout techniques were studied for the two sensor chip designs. Each method is described below and labeled by two parameters - the bridge voltage and magnetic biasing waveforms.

1. DC-DC: This method shown in Figure 5, is a completely DC readout of the sensor and is the technique most often used for many integrated sensors. A 12.8V battery is used to bias the bridge and an ultra-low-noise op amp (CP-37) is used as a pre-amp. A second order low pass filter is used on the output.

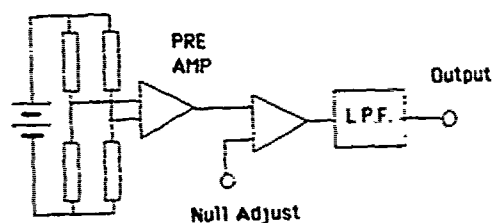


FIGURE 5. DC-DC read out technique
DC bridge bias and DC magnetic bias, open loop

2. AC-DC: Figure 6 shows this method's block diagram where an AC voltage is used to bias the resistor bridge. This allows one to use a phase sensitive detection scheme (i.e. a lock-in amplifier). The minimum detectable signal is enhanced because through the AC carrier the $1/f$ noise inherent in the bridge can be side stepped. However, the stability of the phase shifter is critical to this method's accuracy and drift.
3. DC-AC: In this method, shown in Figure 7, an AC magnetic signal is applied to the chip through an external electro-magnetic coil. The external field then affects the magnitude, phase, and frequency (due to harmonic generation) of the sensors response as illustrated in Figure 8.
4. AC-AC: This method (Figure 9) is similar to an AM radio signal. Two modulations are applied to the sensor at different frequencies. A major concern for this method is the separation of the modulation frequencies and the bandwidth of the transducer to accommodate both modulations.

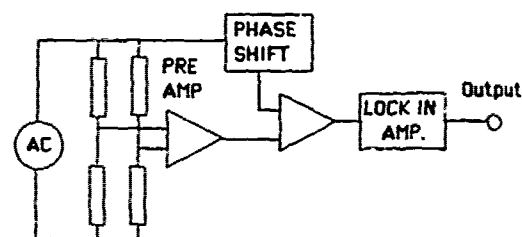


FIGURE 6. AC-DC read out technique
AC bridge bias and DC magnetic bias, open loop

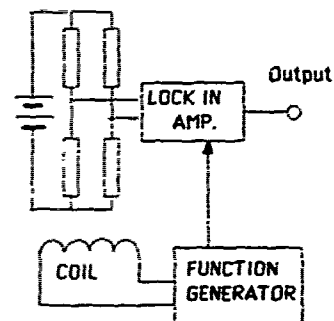


FIGURE 7. DC-AC read out technique
DC bridge bias and AC magnetic bias, open loop

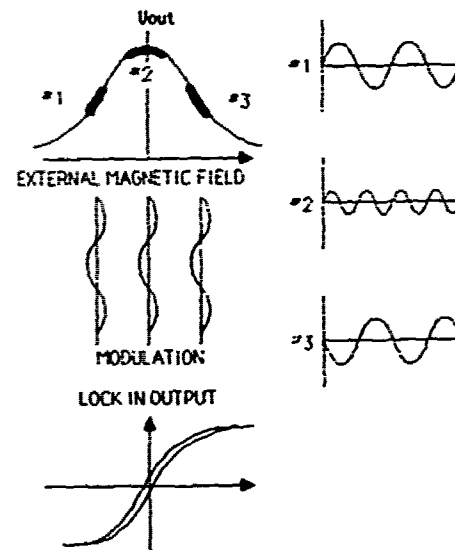


FIGURE 8. Waveform due to magnetic modulation about three point on the magneto-resistance curve

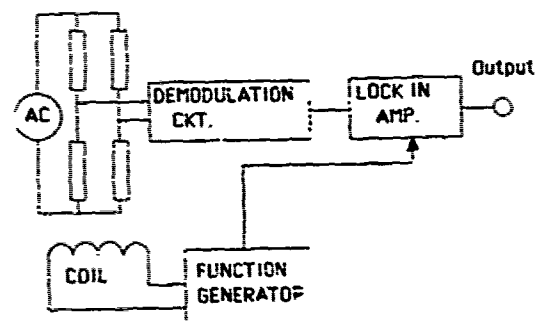


FIGURE 9. AC-AC read out technique
AC bridge bias and AC magnetic bias, open loop

5. DC-AC, closed loop: The previous four methods have shown open loop sensor readout schemes. This method, illustrated in Figure 10, modifies the DC-AC method for a closed loop operation. The peak of the magnetic response curve (Figure 8) was selected as the closed loop operating point. This peak is a unique point in the sensor's response where only harmonics of the modulation field are evident and the fundamental is suppressed. A DC bias is added to the modulation coil to offset the external field and this voltage is used as the sensor readout.

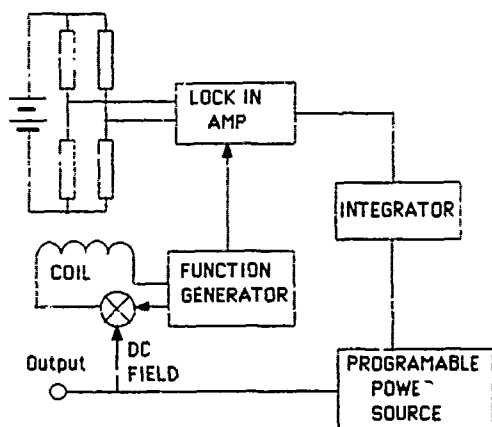


FIGURE 10, DC-AC closed loop read out technique
DC bridge bias and AC magnetic bias, closed loop

Measurement Results

The above methods were compared for scale factor, minimum detectable signal, and long term stability. In each method the bandwidth of the readout was adjusted for a DC to 10 Hz response to external magnetic fields. During the testing the chips were mounted inside a zero gauss chamber which included a coil for applying uniform magnetic fields to the sensor.

Sensor chips incorporating cobalt magnets were primarily used for methods 1 and 2 and transducers without the cobalt were primarily used for methods 3, 4, and 5.

Scale Factor

The scale factors measured for the open loop methods are listed in Table 1. Also listed are the modulation conditions for the measurement. The scale factor sensitivity is expressed as the voltage output per Gauss of externally applied magnetic field (DC to 10 Hz). The sensitivity of the AC methods depends on the modulation frequency and amplitude. Figure 11 plots the scale factor for the AC-DC method as a function of the modulation frequency.

This roll-off in frequency response shown in Figure 11 results from a relatively large capacitance along and between each resistor in the bridge. This limitation in frequency response then made it impossible to operate the AC-AC readout technique with any reasonable sensitivity. In order to operate

SENSING METHOD	SENSITIVITY	BRIDGE VOLTAGE	MAGNETIC MODULATION
DC-DC	58mV/G	12.8V DC	
AC-DC	43mV/G	12Vp-p 1KHZ	
DC-AC	10.6mV/G	12.8V DC	5 Gp-p 1KHZ
AC-AC		12Vp-p 10KHZ	1 Gp-p 1KHZ

TABLE 1, Summary of scale factor for sensitivity measurement

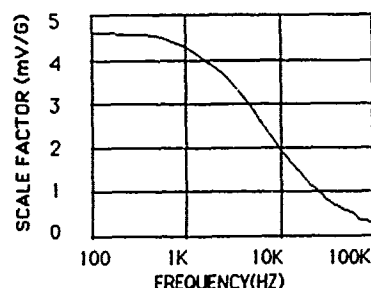


FIGURE 11, Scale factor as a function of frequency for AC-DC read out technique

the AC-AC method the two modulation frequencies must be separated so that each can be demodulated without distorting the other modulation. Table 1 lists the extremes for the two modulations which still resulted in poor performance.

The modulation magnitude also affects the scale factor. Amplitude changes in the bias voltage modulation have a linear relationship with the scale factor. However it was discovered that amplitude changes in the magnetic modulation had a non-linear effect. Figure 12 shows the scale factor as a function of magnetic modulation amplitude for the DC-AC readout technique. Below 2Gpp and above 5Gpp unresolved non-linear phenomena are occurring.

Minimum Detectable Signal

The minimum detectable signal (M.D.S.) was measured by first optimizing the technique's signal to noise ratio (SNR) by amplifying

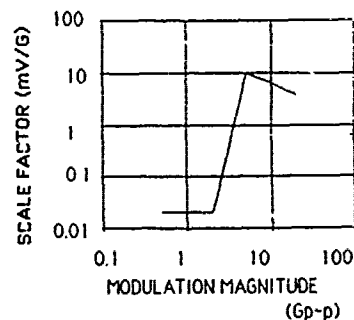


FIGURE 12, Scale factor as a function of magnetic modulation amplitude for DC-AC readout technique

the output. Then the smallest applied magnetic field that produced a SNR slightly greater than 1 was recorded. This data for the M.D.S. is listed in Table 2. For the reasons above the AC-AC method was not used. The best result was for the DC-DC method with an amplifier gain of 80 dB.

The hysteresis in the M.D.S. between the DC-DC and DC-AC, closed loop methods for large changes in the external field (± 3.4 G) the DC-DC M.D.S. had 200 mG hysteresis and the DC-AC, closed loop had 70 mG. For small field changes (± 0.1 G) the hysteresis was 10 mG and 2 mG respectively.

SENSING METHOD	M.D.S.	BRIDGE VOLTAGE	MAGNETIC MODULATION
DC-DC	0.5mG	12.8V DC	
AC-DC	1.2mG	12Vp-p 1KHZ	
DC-AC	60mG	12.8V DC	5 Gp-p 1KHZ
DC-AC (CLOSED LOOP)	30mG	12.8V DC	5 Gp-p 1KHZ

TABLE 2, Summary of minimum detectable signal measurement

Long Term Stability

Twelve hour stability runs for the DC-DC and DC-AC, closed loop techniques are shown in Figure 13. Shown in these plots are the

sensor output for a constant external field and room temperature as a function of time. These runs were made during the night to reduce the effects from environment noise (i.e. people and building). Table 3 summarizes this data.

SENSING METHOD	DRIFT(12h)	BRIDGE VOLTAGE	MAGNETIC MODULATION	TEMP.
DC-DC	12~20mG	12.8V DC		1.5°C CHANGE
DC-AC (CLOSED LOOP)	4~8mG	12.8V DC	5 Gp-p 1KHZ	1°C CHANGE

TABLE 3, Summary of long term stability measurement

Summary

Five readout techniques for an integrated magnetic sensor have been investigated. The DC-DC and DC-AC, closed loop methods produced the best results. The DC-DC case had the best minimum detectable signal and the closed loop method greatly improved the sensor's long term stability. It is hoped this characterization will lead to methods for self-checking and improved calibration for these magnetic sensors. An important point to also note from this data is that more complicated electronic readout schemes, such as the modulation techniques, do not guarantee orders of magnitude improvement in performance over a carefully designed DC readout method.

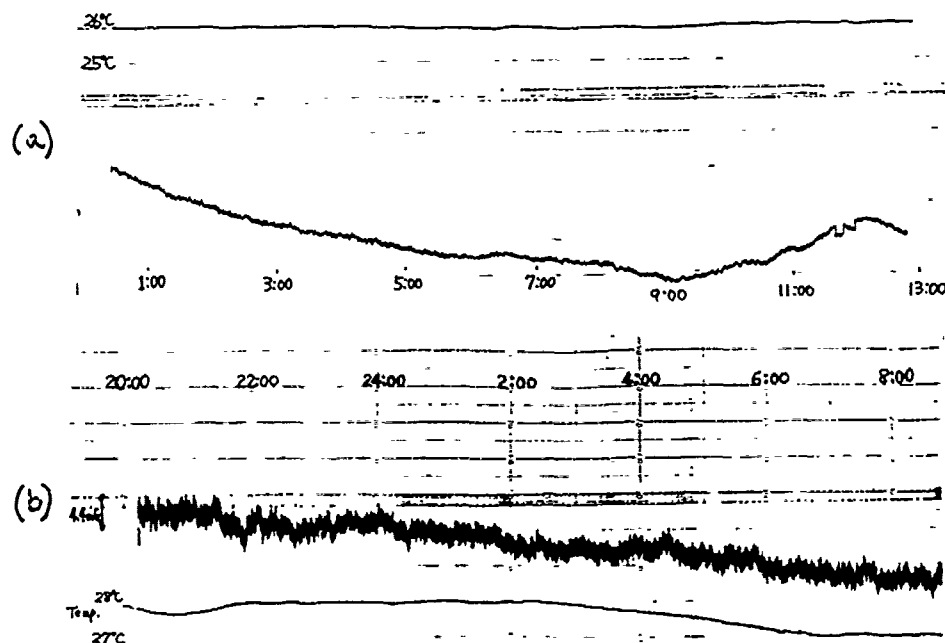


FIGURE 13, Stability runs showing sensor output and room temperature for magnetic sensor
(a) DC-DC for transducer with Co magnet
(b) DC-AC, closed loop for transducer without Co magnet

SENSORS FOR PROCESS CONTROL REQUIREMENTS FOR DESIGN AND TEST

William L. Thompson
Bailey Controls Company
29801 Euclid Avenue
Wickliffe, Ohio 44092

Abstract

Sensors for industrial process control have to meet many and varied requirements. The eventual specific applications may even be unknown to the designer and manufacturer as some industries are very close on details of their proprietary processes. Sensor research provides a new technique for quantifying a physical parameter. The task is then to identify it with a need in the marketplace and match the sensor with the requirements of that application. A process control sensor is rarely targeted for a single application. An awareness of the details of and breadth of requirements may assist in the development process of a sensor that has eventual application in the process control marketplace.

Markets

Industrial process markets include:

- Chemicals
- Petroleum
- Pulp and paper
- Foods
- Electric utilities
- Steam and heating
- Maritime
- Waste water treatment
- Ceramics
- Metals refining and processing
- Cement

Each market may have specific requirements and environments for the measuring equipment it uses to extract the process variable information it needs for use in its control systems.

Requirements and Specifications

Economic considerations are very important. The required measuring function is important but cost may appear more important when trying to sell the device to a customer.

Those involved in selling sensors (included in transmitters) have (or should have) an understanding or feel for the needs and requirements for the market they serve. Market research reports from consultants, etc., are available or can be generated identify requirements. More important they can predict if there is a market, and if so how many, to whom, and for how much? This is needed to get funding to continue development.

Similar devices already on the market can be used to develop target specifications. Some "market surveys" consist of tabulating competitors specifications and saying "do slightly better at less cost".

There is usually a disparity between an adequate sensor and ideal sensor (the golden one). An excellent device doesn't always sell. Sometimes a dependable, adequate one sells over the "better" one. The trick is to know when you have an adequate one that will sell.

Can the sensor fill a niche or is it targeted as a universal design? Process control sensors typically attempt to fit a wide range of applications. If it fills a niche, try to find additional applications. Also the niche market should be related to the company's mainstream control system business.

Design Considerations

The sensors must be connected to a control system. A sensor generates a signal, usually electrical, proportional to the process variable being measured. This signal must then be amplified (conditioned) and transmitted to a control system. Often a signal must be transmitted up to 500 feet or more. The sensor signal is typically amplified and converted to a 4-20 mA format or in the near future, a digital format before transmission. A 4-20 mA two-wire loop places restrictions on the processing that can be done at the sensor but is especially important in retrofit applications. Also there is much inertia in changing formats of measurement systems.

Input-output isolation is often necessary in transmitters. Many sensors make electrical contact to the process system being monitored. The control system typically has many sensors and also has a ground point different from any of the several sensors. Thus for noise and safety considerations, any sensor not isolated electrically from the process installation being measured should have electrical isolation from the control system's input.

The transmitter, including the sensor, must be able to function in the environment where the process variable is being sensed. Some of the environments are quite hostile.

Sensors must be designed for long life and ease of replacement. Spare parts considerations are very important. In an installation with perhaps 200 of a given sensor, covering many different measurement ranges, the user doesn't want to stock more than one spare or type of spare if at all possible, or at least minimize the number of spares that must be stocked. This brings up considerations such as rangeability, turndown, elevation, and suppression. A particular sensor-transmitter may be adjusted significantly away from optimal performance to minimize the number of ranges that have to be handled. The associated circuitry must be capable of accommodating these adjustments at the stated accuracies.

Consider the measurement of excess oxygen or combustibles in the exit gases of a lime kiln. If your automotive sensor suddenly began experiencing a heavy dose of lime dust the sensor would be the least of your worries. However this measurement must contend with the abrasive lime dust all the time since measurements taken after the precipitators introduce errors due to stream dilution prior to the measurement point.

Flue gas measurements for oxygen, combustibles, etc. are hampered by the presence of abrasive particles, sulfur dioxide, etc. Poisoning elements often are present in the process fluid being measured. Catalytic sensors are easily poisoned by the presence

of the wrong materials--lead for example. Sulfur dioxide causes a degradation; however, this can often be reversed.

Materials compatibility is also important. The fluids in contact with your sensor and its housing must not attack and degrade or destroy the sensor system. Would you like to have acid rain in your sensor? Many applications involve acid fumes or hot gases that generate acids when combined with water. These do not cause problems unless the temperature drops below the dew point. When this happens a coating of acid forms on the materials in the area. This in conjunction with dissimilar metals gives an electrolytic cell. It also leads to corrosion. This can occur in the measurement fluid or in the general ambient of the measuring equipment. Also oxygen service for a transmitter with silicone oil fill fluid is a problem since silicone oil is flammable in the presence of high concentrations of oxygen.

Many of the markets have potentially flammable atmospheres at their measuring locations. An example is that of coal slurry preparation, which has free hydrogen present. The sensor, its associated circuitry and connecting wires must not be able to cause an explosion or fire.

Smart Electronics

Microprocessors are being used in the electronics packages for sensors. This permits error correction to be incorporated in the transmitter packages even while using a 4-20 ma current loop format. Remote gain changes, zeroing, etc. is possible. Analog or digital communications is possible. Digital communications is possible both directions. Investigations are underway regarding local area networks of sensors.

Testing

Engineering testing and separate Qualification testing is performed on sensor based products. Testing is done to cover the possible applications and to give independent review of the several specs. Testing is also done for information only on others, for example operating outside of the specified ranges.

An analytical determination is made when possible determine what the test results should be and identify when some new or outside factors have entered the picture.

Test procedures and equipment accuracies must be well documented in order to be sure of the test results.

Tests

Elevation and suppression
Turndown
Output loading
Ambient temperature range
Process fluid temperature range
Pressure range

Flow conditions
Radiation
Shock
Vibration
Position sensitivity
Response time
RFI
EMI
Dielectric withstand voltage
Reproducibility
Power supply effect
Relative humidity effect
Input-output isolation
Linearity
Hysteresis
Repeatability
Dead band
Accuracy
Long term drift
Lightning suppression
IEEE Surge Withstand
Overrange influence

Other Considerations

Certification -- OSHA requires third party review for any equipment operating in hazardous (flammable or explosive) locations. Almost all Canadian process control equipment sales require certification by CSA (Canadian Standards Association). Also in the event of Product Litigation it is helpful to be able to show that the product was reviewed by a third party to demonstrate that it was designed with proper care.

Flow effect -- Non-intrusive sensors are preferred. If not then specify the pressure drop in process fluid flow.

Maintenance -- What will it cost to service? What is the replacement parts policy (maybe the life of the installation is for 40 years)? Can it be calibrated online or must it be returned to the Calibration Lab or Instrument Shop for calibration and ranging?

Reliability -- What MTBF, MTTR or Availability numbers will the customer use in his system reliability calculations and predictions?

Adjustments -- Design for no adjustments or make the adjustments external so that they can be made without taking the cover off.

Specifications -- Are your specifications Typical, Worst Case or Statistical?

Installation -- Your little gem will likely be installed with a wrench and large screwdriver (and hammer?)

Housing -- Is the housing suitable for corrosive environments? Will it withstand (meet the piping codes for) the operating pressure and for containing an explosion. Will it keep out any adverse ambient (survive cleansing with a fire hose, etc.)?

Flexible Tactile Sensing Arrays for Robotics: Architectural Robustness and Yield Considerations

Phillip W. Barth*, Mark J. Zdeblick, Zenon Kuc, and Patricia A. Beck
Center for Integrated Systems
Stanford University
Stanford, California 94305

*Present address:
NovaSensor
2975 Bowers Avenue
Santa Clara, CA 95050

The Robot Skin project at Stanford is an attempt to create new tactile sensing technology for general-purpose robot manipulators. Such manipulators, designed to be functionally equivalent (at least) to the human hand, will require sensor arrays that fulfill several requirements: (1) many sensor elements (on the order of 64-256) to minimize tactile imaging time, (2) close spacing of small sensing elements for fine spatial discrimination, (3) ability to be molded to a convex fingertip surface for taction on concave surfaces, (4) ability to sense both force and temperature in order to fully mimic biological touch, (5) tolerance to over-scale forces without damage, and (6) "graceful" failure in use, i.e., functional survival of most of the array when part of it is damaged. In addition to the above, which are considered requirements, several other characteristics are desirable. Foremost is the ability to sense shear forces, which provide information on actual or incipient slip of a grasped object. It also appears desirable for tactile sensor arrays to possess some local pattern-processing capability which can lower the transmission bandwidth required to the robot's central information processor. In order for such sensor arrays to be useful in practical systems, cost constraints must also be considered; such constraints argue for automated and/or batch fabrication of the arrays. Finally, given the differences between biology and various non-biological technologies, it may be possible to achieve functionality not available to biological touch, e.g., by including capacitive proximity sensing capability in such arrays.

No tactile sensor array developed to date fills all, nor even most, of these requirements and desires well. Several investigators have recently developed tactile sensing arrays suitable for imaging shapes on hard, flat surfaces (e.g., [1-3]), but not well suited for taction on curved surfaces. Others have developed single tactile sensors suitable for incorporation into arrays (e.g., [4]), which will probably prove uneconomical when large numbers of sensors are needed. Still others have developed flexible capacitive arrays [5-6] suitable for use on curved surfaces but incapable of obtaining temperature or proximity data. The purpose of the present effort is to develop a technology base suitable to the achievement of all of the above goals, and to incrementally demonstrate useful steps toward those goals.

The proposed physical structure of such arrays, based on previously developed technology for linear thermometer arrays [7], places silicon islands in a flexible polyimide substrate (Figure 1). The islands are interconnected by leads embedded in the substrate; each island will contain one or more force sensors, and may also contain temperature and proximity sensors. To date the island shapes have been successfully fabricated in polyimide substrates for one-sensor islands (suitable for normal force sensing) and for four-sensor islands (suitable for sensing both shear and normal forces), both of these in 5x5 arrays. Complete process integration in a purely passive force sensor array is under way for these designs. Eventually 16x16 arrays with active signal processing are contemplated.

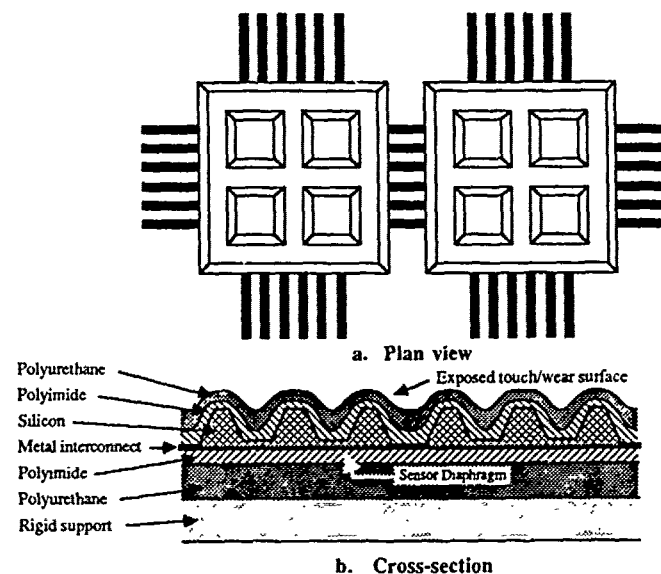


Figure 1. Adjacent sensor islands with interconnections

In service these arrays will be subject to wear and tear in the same way that biological skin is, but without the self-repair capability of living tissue. Leads will break between islands, islands will be crushed and broken, and eventually the array must be replaced. To delay replacement as long as possible, robust physical and electronic architectures are needed.

Sensor placement on each island can be either near the perimeter of the island or internal to the island, and has a strong effect on physical robustness. Initial designs placed sensors on flaps near the island edges. This arrangement leads to high sensitivity because loading forces are largest at island edges. However, computer modeling predicts a non-linear voltage-versus-force response because of compression effects in the underlying support layer, making it difficult to detect normal and shear forces separately. In addition, the flap arrangement is expected to result in fragility because wires embedded in the polyimide will have little strain relief at the island edges, and because the flaps will be subject to the maximum stress occurring anywhere on the island. Internal placement of the sensors results in a linear response, maximum polyimide thickness at island edges for good strain relief of the leads, and uniform loading over most of the island.

Electronic robustness is ensured by choosing the most fault-tolerant addressing scheme consistent with addressing time and silicon area availability. Possible addressing schemes including the following: one hard-wire connection to each sensor, one wire to all sensors with sequential or serial-address readout, row-column addressing with and without redundant wires, parallel-to-serial shift register readout, and a "global bus" mesh with serial or parallel addressing.

The most promising architectures appear to be row-column address schemes with redundancy; such schemes provide near-optimum robustness with minimal circuit area and fast address times. A computer simulation of wear, in the form of random cuts occurring over time in the interconnections, has been developed and applied to row-column address schemes of several types, and shows that closely-spaced redundant wires aid in achieving robustness (Figure 2).

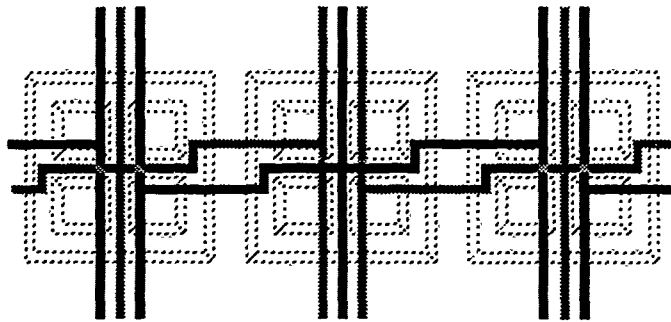


Figure 2. Triply-redundant column addressing with single-pixel separation of redundant lines

The designs presently being constructed use conventional diaphragm fabrication by etching from the wafer backside. The yield-reducing problems with this type of technology are well known. In addition, for the present application where each island is effectively a force

sensor rather than a pressure sensor, the diaphragms fabricated by backside etching may be subject to damage from pointed objects. Purely front-sided sensor fabrication, like that advocated by Guckel (e.g., [8]), offers the possibility of higher yield and greater robustness. We are pursuing a modification of previous techniques for fabricating sensor diaphragms out of polycrystalline silicon, with the goal of creating capacitive force sensors (Figure 3) for the next generation of tactile sensing arrays. The modified fabrication techniques allow etching of a sacrificial spacer layer beneath the diaphragm through an array of holes which covers the entire diaphragm area, as opposed to etching from only the edges of the diaphragm. The technique should greatly shorten the etch times required, and so permit insulating standoffs necessary for the capacitor structure to remain in place.

Any flexible array containing closely-spaced rigid islands in a rectilinear arrangement is flexible only along the rows and columns between islands. When such arrays are placed on robot fingertips this limits the fingertip shapes to variations on the theme shown in Figure 4, where coverage of most of the fingertip is achieved by bending the array along two axes. This arrangement leaves a "blind spot" which will probably be acceptable in most applications. The blind spot can be eliminated by extra care in layout of the array and shaping of the fingertip, but such steps will add extra cost and will probably not be justified in most cases.

Acknowledgement

This work has been sponsored by the NASA Ames Research Center and by the NASA-funded Center for Aeronautics and Space Information Sciences at Stanford.

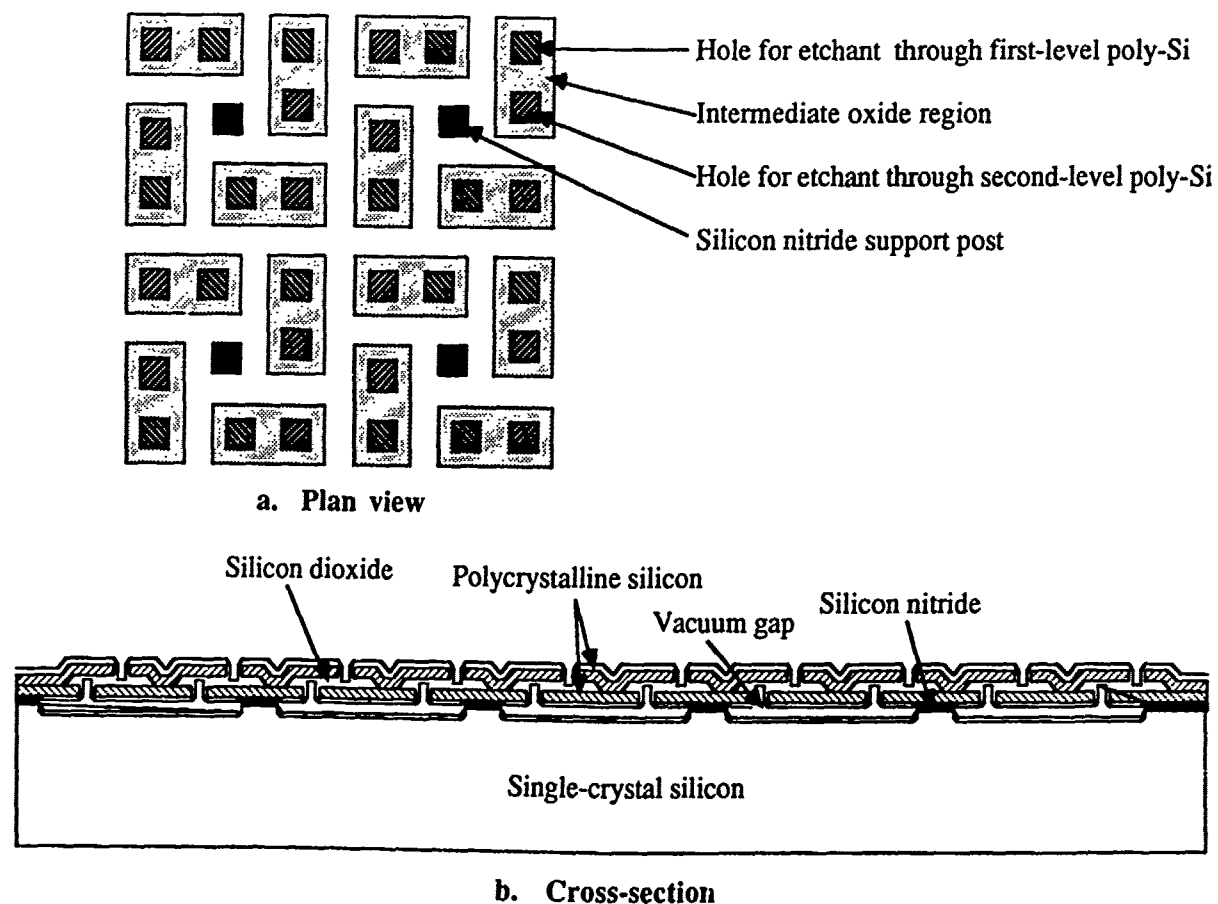


Figure 3. Two-level Polysilicon Diaphragm Structure

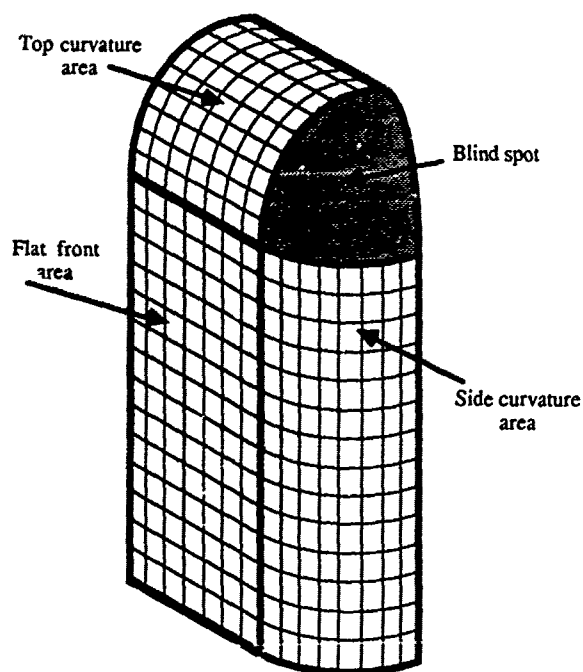


Figure 4. Tactile array attachment to a fingertip (two axes of bend available)

References

- [1] R.M. White and A. King, "Tactile Array for Robotics Employing a Rubbery Skin and a Solid-State Optical Sensor," paper 2.1, Transducers '85, Digest of Technical Papers, IEEE Catalog No. 85CH2127-9, pp 18-21, June 1985.
- [2] K.J. Chun and K.D. Wise, "A Capacitive Silicon Tactile Imaging Array," paper 2.2, Transducers '85, Digest of Technical Papers, IEEE Catalog No. 85CH2127-9, pp 22-25, June 1985.
- [3] K. Wong and J. Van der Spiegel, "A Shielded Piezoresistive Tactile Sensor Array," paper 2.3, Transducers '85, Digest of Technical Papers, IEEE Catalog No. 85CH2127-9, pp 26-28, June 1985.
- [4] K. Petersen, C. Kowalski, J. Brown, H. Allen, and J. Knutti, "A Force-Sensing Chip Designed for Robotic and Manufacturing Automation Applications," paper 2.4, Transducers '85, Digest of Technical Papers, IEEE Catalog No. 85CH2127-9, pp 30-32, June 1985.
- [5] Ron Fearing, Artificial Intelligence Laboratory, Stanford University Computer Science Department. (Unpublished)
- [6] Michael R. Neuman and Chung-Chiun Liu, "Fabrication of Biomedical Sensors Using Thin and Thick Film Microelectronic Technology." Micromachining and Micropackaging of Transducers, Clifford Fung, *et al*, editors, Elsevier Science Publishing Co. Inc., New York, 1985. ISBN 0-444-42560-8. pp 225-238.
- [7] Phillip W. Barth, Sharon L. Bernard, and James B. Angell "Flexible Circuit and Sensor Arrays Fabricated by Monolithic Silicon Technology," IEEE Transactions on Electron Devices, Vol. Ed-32, No. 7, pp 1202-1205, July 1985.
- [8] H. Guckel, D.W. Burns, H.H. Busta, and J.F. Detry, "Laser-Recrystallized Piezoresistive Micro-Diaphragm Sensors," 1985 Conference on Solid-State Sensors and Actuators, Digest of Technical Papers, IEEE Catalog No. 84-62799, pp 182-185.

APPLICATION-SPECIFIC PACKAGING FOR CUSTOM MICROMECHANICAL STRUCTURES

S.C. Terry, J.H. Jerman,
J.W. Knutti and H.V. Allen

Transensory Devices, Inc.
44060 Old Warm Springs Blvd.
Fremont, CA 94538

Introduction

The majority of the pioneering work in the development of silicon sensors and microstructures has taken place in universities and research laboratories, where device response is of prime importance. With the growth of the sensor field, more attention has been paid to packaging considerations because of the realization that the package is a key part of the interface between the sensor and the world. Although micromechanical elements share common fabrication technologies with integrated circuit devices, commercial sensors can rarely be housed in standard IC packages.

Most commercial devices developed to date have begun with the design of the sensor or transducer chip itself, and a package for the chip was then selected to accommodate the broadest range of applications. Users of sensors in these "generic" packages could easily and reliably design them into specific products and systems.

As the diversity of micromechanical structures has increased, the emergence of a systems approach to sensor and instrument design has fostered more interest in application-specific devices. In addition, the limitations of generic packages are providing the impetus towards the simultaneous design of the micromechanical device and the system in which it is to be used. The design of the chip is beginning to be tailored to its package and to its intended application. In such cases, the boundaries between the device, its package, and the system become less clear.

Generic vs. Application-Specific Design

The design of both a silicon microstructure and its package has widely different sets of performance, use, and cost objectives depending on whether the device is intended for generic use in a wide variety of markets or it is intended for a specific application. In the generic case, the package is designed for multiple uses and is planned to appeal to the widest possible market.

The generic device must typically have a package with a form factor that is compatible with standard fittings used in the instrumentation and machine manufacturing industries. It has to be convenient to handle and easy for the customer to design into a system. The cost typically has to be kept low in order to make the use of the device attractive in many markets and applications. Considerable economy is achieved if the same micromechanical chip can be incorporated in many different packages. The specification of the device and package is often a compromise between the performance needs of many markets.

Much of the advantage in using silicon micromachining techniques is lost due to packaging that does not fully exploit the increased performance and decreased cost and size of the silicon devices. Only by addressing the packaging issues as a part of system design can the optimum performance be obtained.

With an application-specific device, the cost-performance tradeoffs can be evaluated with the exact knowledge of their impact on the use of the device and on the system in which it is incorporated. When the system and component package are designed together, the interface between them can be optimized for performance, convenience, reliability, and cost.

When designing from the systems point of view, the incorporation of a silicon sensor or micromechanical structure can follow one of three paths:

- 1) The device can be incorporated in a generic package with a standard interface,
- 2) A custom package can be designed for a standard or a custom chip or,
- 3) The packaging issues can be incorporated into the design of the device itself.

It is the third approach which takes full advantage of the mechanical and electrical properties of silicon and can lead to the complete elimination of the package.

The Device as its own Package

The trend in high performance sensor systems is to address packaging issues and sensor design simultaneously, and, in many cases, to incorporate aspects of packaging in the sensor structure itself. The incorporation of packaging features into sensor design is driven by four major factors.

- 1) Individual sensor performance can be improved when limitations caused by conventional packaging, such as size, internal volume, thermal mass, or inertia, are removed.
- 2) The requirements of a planned system force unique approaches to sensor design and packaging, as is the case in indwelling medical systems.
- 3) Wafer level packaging reduces piecewise assembly and test time, thus reducing costs.
- 4) The desire to integrate sensors with electronics or other mechanical components requires the use of an application specific package, as in chemfets, capacitive accelerometers, or multiplexed tactile elements.

In some instances, improved sensor action or coupling to the environment can be achieved when the device is unencumbered by a package. A classic example of this is a strain gauge that was developed at Stanford University in the 1970's [1]. The device, as sketched in Fig. 1, was designed for a biomedical application in which the minute contractions of a rabbit's oviduct were to be monitored. The 1-mm diameter of the oviduct and the minuscule forces involved prohibited the use of a conventional package and standard silicon strain gauge. The silicon device was designed to include etched silicon suture loops with which the surgeon could attach the device to the oviduct, and a thin beam with a diffused piezoresistor to measure bending. With thin platinum wires attached to the gold bonding pads, the complete unit was covered with a 1-micron thick layer of Parylene for electrical insulation and biocompatibility. The mechanical, electrical, and chemical issues involved in the design of the sensor and the package were considered simultaneously, insuring adequate performance for the specific application.

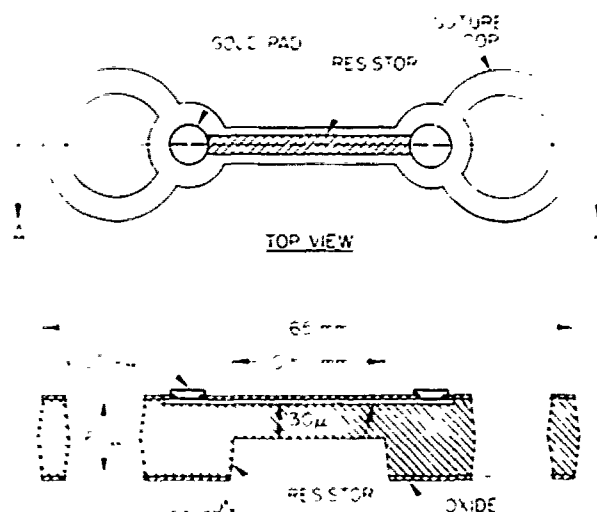


Fig. 1 - Etched Silicon Force Transducer

A more recent example of such a self-packaged device is the multielectrode micro-probe for biopotential recording, developed by a group under Ken Wise at the University of Michigan [2]. This device consists of a narrow probe shank with twelve electrodes and a larger silicon area with multiplexing and buffering circuitry. Again, the interference of external packaging cannot be tolerated, and the self-packaged device adequately addresses the multitude of packaging requirements.

In systems where several of the micromachined components are used together, the cost of piecewise assembly and testing can be reduced by integrating the sensors together. This approach is exemplified by a mass flow sensor designed and fabricated by Transensory Devices for Innovus Corporation. For redundancy, this silicon device contains four flow channels, each with flow sensors. The sensors are tested together and mounted as a unit into the final system, a mass flow controller. The silicon device, shown schematically in Fig. 2, consists of two micromachined pieces of silicon bonded together to form the gas flow channels. The mating groove in the cap provides controlled, symmetrical flow past the sensor bridge, and the cap seal provides isolation between the redundant flow channels. The device is its own

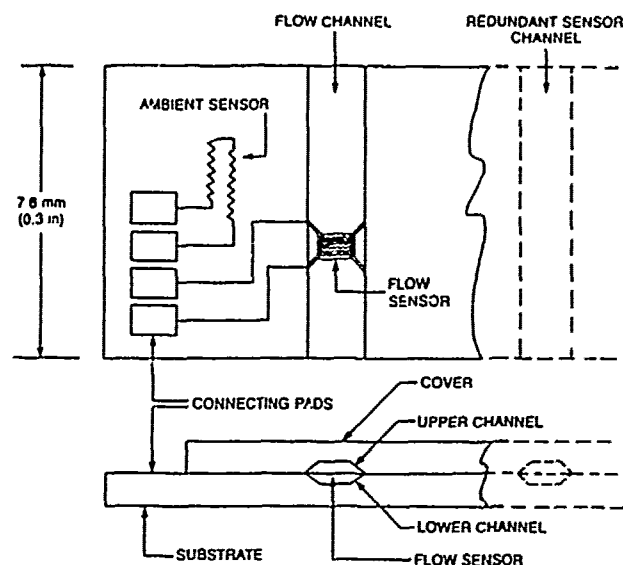


Fig. 2 - Schematic Layout of Innovus Mass Flow Sensor

package. The sensing elements are fabricated on one of the wafers and are, in a sense, packaged by the silicon cap. The completed device can be routinely handled with little or no concern for damaging the delicate sensor elements.

The increased performance of this sensor is due to the combination of efficient thermal design, tight processing control, and advanced packaging techniques. By virtue of this increased performance, a more advanced mass flow controller can be realized.

Elimination of the separate package for a device can also be forced by unique requirements posed by system integration. As separate components are integrated together on a single silicon structure, their individual packaging and interface requirements have to be jointly satisfied. The "external" part of the system may dictate more of the device design than the miniaturized, micromachined silicon structures. As the size of the device is increased, the need for a package for the silicon device also decreases.

An example of a highly integrated mechanical system is the miniature gas chromatograph which was commercialized by Microsensor Technology [3]. This device incorporates a gas chromatography system comprised of miniature valves, a thermal conductivity detector, flow restrictors, and interconnecting gas channels on a three-inch diameter silicon wafer, as shown in Fig. 3. The motivation behind integrating the system lay in both the more efficient chromatography which could be achieved with closely-coupled, low-volume components and the small size of the resulting system. The overall size of the device was not dictated by the silicon structures but was determined by the external components such as solenoids, gas connections, and pressure sensors. These components are bolted to the glass and silicon device. As is evident in the photograph of the device in Fig. 4, the bolt holes themselves take up a significant amount of the available silicon area. The system was optimized with the components literally built around the silicon device. No package was necessary or desirable.

Although the instrument itself is a chemical sensor, the major packaging considerations are mechanical, in insuring that gas paths are leak-free and dead

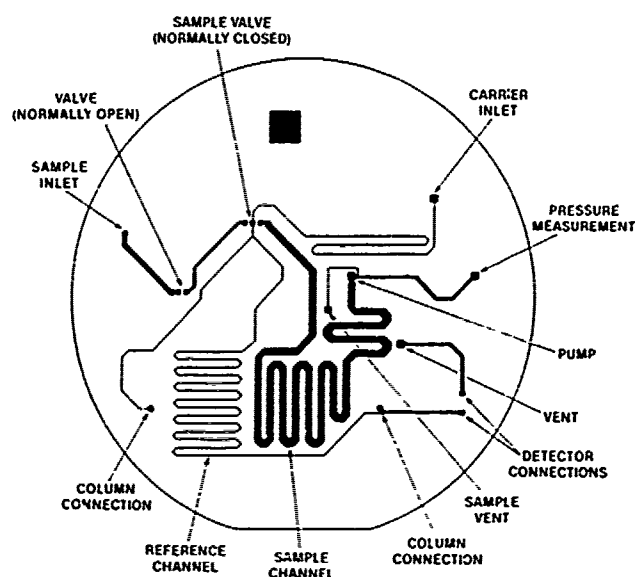


Fig. 3 - Layout of Miniature Gas Chromatograph on a 3-inch Diameter Silicon Wafer

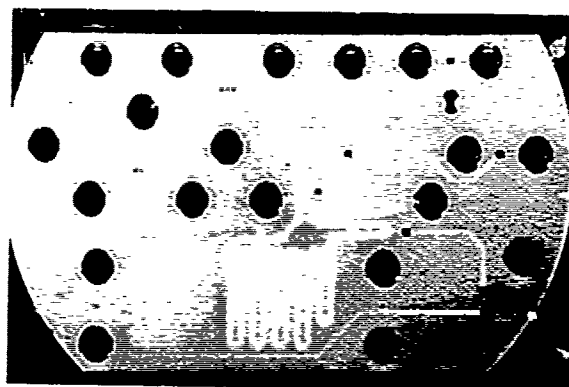


Fig. 4 - Photograph of Completed Silicon/Glass Gas Chromatograph

volumes are minimized. The packaging is truly application specific, in the sense that the GC wafer cannot be used in anything other than its intended application. In addition, the system design is tightly coupled to the sensor design, so that any changes in one typically require changes in the other. This tight coupling allows the maximum performance to be achieved from the sensor and from the system.

Consequences of Application Specific Packaging

Although the use of these advanced packaging techniques results in increased system performance, more care must be taken during the system design phase. Typically the device itself is called upon to provide more environmental protection than in a traditional packaging approach. The combination of deposited passivation layers, glass-to-silicon bonding, and silicon-to-silicon sealing offers a variety of ways to address these protection issues. These additional sealing steps, along with providing appropriate interfaces to the physical and electrical worlds, typically increase process complexity over a generic packaging design. Because these additional process

steps are performed at the wafer level, however, the added cost per chip/system can usually be less than that of the more complicated individual packaging at final assembly. In some cases, this also means that an application-specific silicon device increases in size over a generic counterpart, due to the silicon area dedicated to packaging. This possible area loss influences die cost, and this tradeoff must be addressed during system design to achieve the lowest total-system-cost-to-performance ratio.

Conclusion

Modern design practices support the method of top-down system design. If a system includes a sensor element, the performance and cost targets for the sensor must be set during system design. When these targets preclude the use of a generic device, then an application specific device and package become necessary. The sensor design can then be studied and the degree of application-specific packaging can be varied to best satisfy the system specifications. Recent examples show that inclusion of packaging aspects into the sensor itself result in higher performance systems than would be possible using generic packages. In the extreme case, the sensor becomes its own package. In all cases, the evaluation of the system cost/performance tradeoffs must include the total cost of the integrated packaging versus the discrete package.

References

- [1] T.A. Nunn, J.B. Angell, T.S. Nelsen, "Force Transducer for Oviduct Instrumentation," Proc. Biomedical Engineering Society, pp. 29-30, Jan. 1973.
- [2] K.D. Wise, K. Najafi, "A Micromachined Integrated Sensor with On-chip Self-test Capability," Technical Digest of IEEE Solid-State Sensor Conferences, pp. 12-16, June 1984.
- [3] S. Saadat, S.C. Terry, "A High-Speed Chromatographic Gas Analyzer," American Laboratory May 1984.

CONSIDERATIONS IN THE HIGH-VOLUME PRODUCTION
OF HYBRID PRESSURE SENSOR MODULES
FOR AUTOMOTIVE APPLICATIONS

R. Brown, K. Catron, W. Wright
Delco Electronics Corporation
Kokomo, Indiana 46902

I. INTRODUCTION

This paper will present some of the methods and requirements for taking a pressure sensor module from the laboratory to a point where it is a commercially practical product using existing technology. The specific market addressed is the automotive market in which volumes of 6 to 8 million units per year are common.

II. TECHNOLOGY DESCRIPTION

The technology used at Delco Electronics Corporation to build the module consists of a piezo-resistive pressure sensing cell with resistors in a bridge configuration. The cell is formed by using an anisotropic etch resulting in a diaphragm 1 mil thick (Fig. 1). The temperature correction thermistors for the cell and the functional adjust resistors are printed on an alumina substrate. Also on the substrate are two EMC (electromagnetic compatibility) capacitors and an integrated circuit operational amplifier which is attached to the substrate by automated pattern recognition integrated circuit flip chip mounting equipment. Welded wires are used to connect the cell housing to the substrate and to connect the substrate to the package which contains the electrical connector (Fig. 2). The functional adjust and temperature compensation are accomplished by computer-controlled laser abrade of the printed resistors (Fig. 3). The module is then passivated, covered, and tested. Both differential and absolute units are available (Fig. 4).

III. REQUIREMENTS

The module must operate in the harsh underhood environment. Temperature extremes of -40° to $+125^{\circ}\text{C}$ are encountered along with many different fluids and vapors including intake manifold gases. This harsh environment requires stringent product assurance tests before even low-volume production can be considered. Some examples of environmental conditions and product assurance tests required, and some general requirements are (Fig. 5):

1. Analog output voltage proportional to pressure over a 90 kPa range.
2. Operate from $5.1\text{ V} \pm .36\text{ V}$ dc supply.
3. Output voltage ratiometric to supply voltage.
4. Accuracy = 1.5% of full scale pressure.
5. Sensor output must stabilize in less than 12 milliseconds in response to pressure change with output noise level less than 10 millivolts.
6. The design must meet all requirements over a temperature range of 0 to $+125^{\circ}\text{C}$, relative humidity of 0 to 100%, and over all the electrical and environmental conditions encountered over the complete pressure range.

7. The module must be unaffected by automotive vapors at temperatures of 150°C , shall not leak or expose any electrical connection to manifold gases for an operable life of 6 years or 120,000 miles.

8. The design shall meet the following tests with no degradation allowed in the electrical or mechanical specification:

- * 1,000 cycles of -40° to $+125^{\circ}\text{C}$.
- * 2,000,000 cycles of 15 kPa to atmosphere.
- * 1,000 combined cycles of above temperature and pressure.
- * 500 hours each of biased and unbiased 85°C and 85% relative humidity.
- * 3 mechanical shocks of 50 G for 11 ms in 3 axes.
- * Low- and high-frequency vibration in 3 axes.
- * Automotive fluid compatibility for 30 min. at 100°C (dip test).
- * Extended exposure to NOx and humidity combination.
- * Drop test of one meter.
- * Unbiased 5% salt fog for 48 hours with contacts and port sealed.
- * Autoclave at 121°C and 15 psig for 96 hours.
- * 100,000 cycles of 2 times operating pressure.
- * EMI exposure of 100 V/m in automobile.
- * 5 hours exposure to "Arizona dust" (with agitation).

The above requirements must be met while also meeting demands for ever-tightening specifications covering such items as: wider temperature ranges, tighter transfer function error bands, and higher level EMI protection.

IV. TIMING

The traditional approach to new product development and production was to do the development work without involving manufacturing engineering till late in the design stage. This serial approach to designing and producing a product did not work well and cannot be used today for several reasons.

The first reason that serial design-production engineering cannot be used today is the need of manufacturing engineering to know if new technologies will be required to produce a product. New processes may need to be developed along with the product development.

The second reason that a serial design-production engineering approach will not work today is the time required to obtain equipment for manufacturing the new product. Because a majority of the equipment required will be custom designed and built, it is not uncommon to have delivery times approach, and sometimes exceed, a full year (Figs. 6, 7, 8). Manufacturability must be considered before committing the design to paper. Therefore, the above design audit tests should be satisfied before equipment can be committed. An example of timing required for a 1989 MY program follows (Fig. 9):

Working Backwards to Arrive at a Start Date

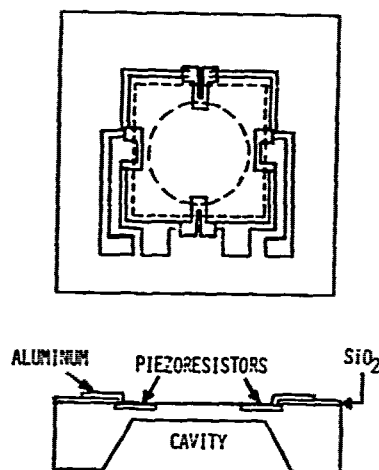
Start of production	1989 MY
Equipment in place and running	March 1988
Equipment ordered (1 yr. lead time)	March 1987
Equipment spec., quotes, and vendor selection	Oct. 1986
Engineering qualification complete (Engineering and proto samples designed, built, and passed all Product Assurance tests)	Aug. 1986

In an effort to eliminate time from program schedules, design engineering and production engineering must work on the programs in a cooperative design approach from the initial product concepting stages.

A third reason that a parallel engineering approach must be used is to meet Total Quality System requirements, a small part of which is shown in Fig. 10. An assessment of the criteria leading to a quality product must be made in the design phase. By recognizing areas where quality may be sacrificed, all options to eliminate the quality problem can be evaluated early in the design and the best solution used.

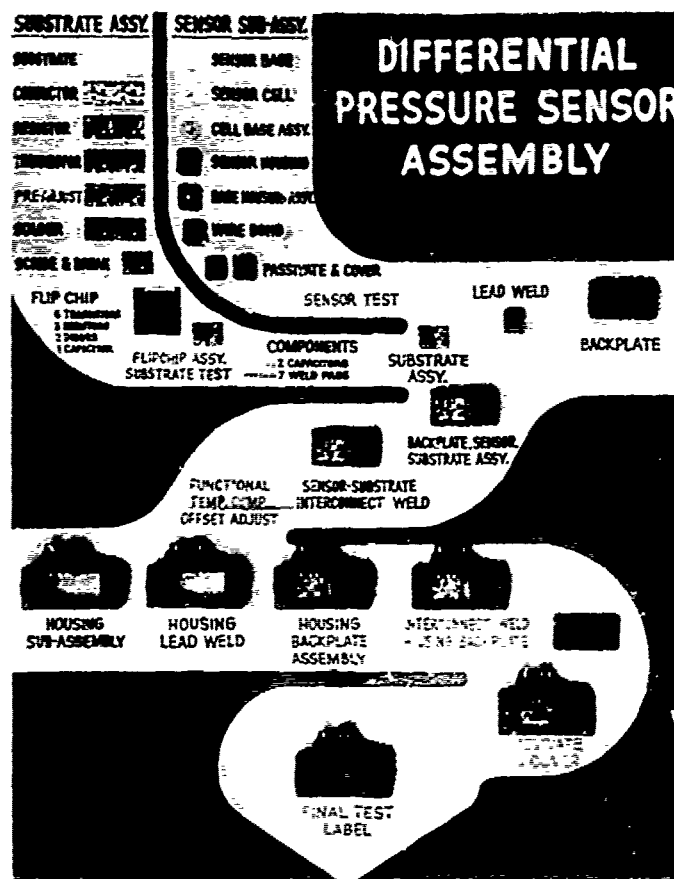
V. CONCLUSIONS

The final pressure sensor module which evolves, must not only be producible in high volume, meet the specification, pass product assurance testing, meet continuing quality requirements, work in the application, and be very reliable, but must also be in a price range that is attractive compared to competitive products. This can only be achieved by involving the necessary disciplines in the design effort, establishing rigid accelerated product assurance tests which correlate to the real world, using statistical process control "in house" and at the vendor level, anticipating potential problems when introducing changes in design and solving the potential problems before they become crises by establishing effective product engineering support groups.



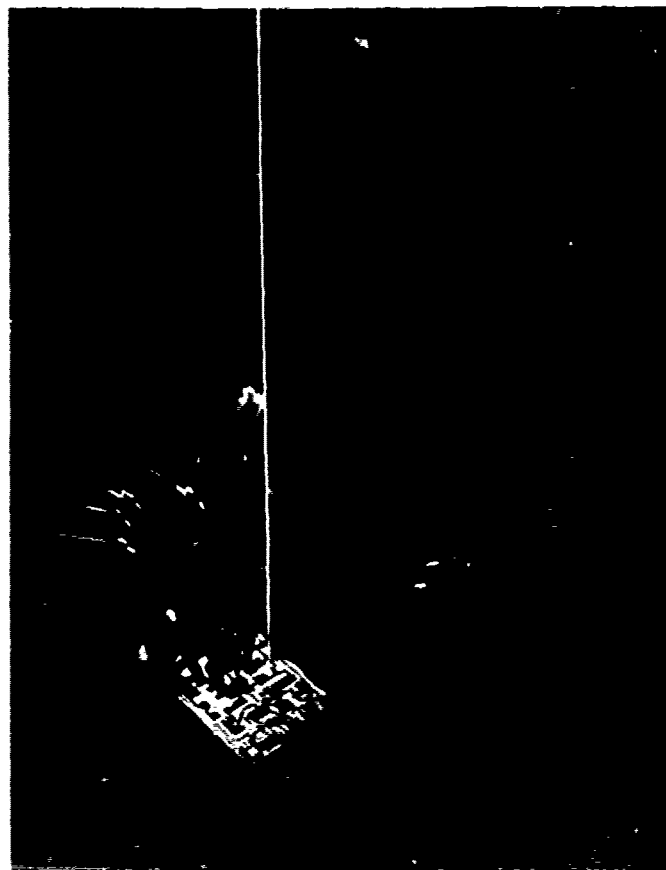
PRESSURE SENSOR CHIP

Figure 1



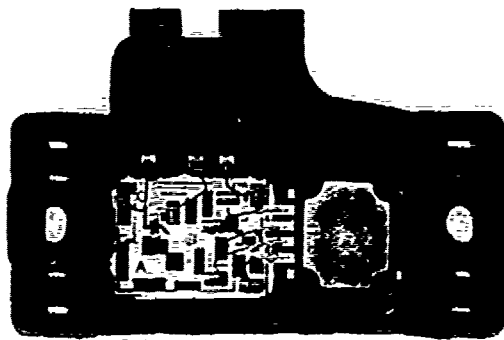
ASSEMBLY

Figure 2



LASER TRIM

Figure 3



ABSOLUTE MODULE

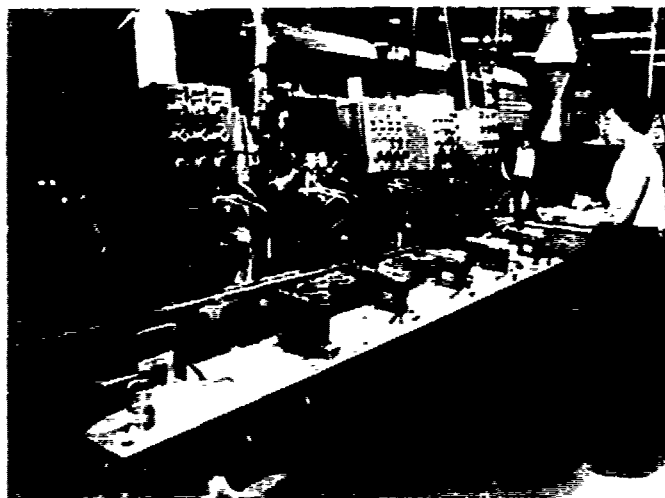
Figure 4

REQUIREMENTS

1. Analog output voltage proportional to pressure over a 90 Kpa range.
2. Operate from 5.1v +/- .25v D.C. supply.
3. Output voltage ratioetric to supply voltage.
4. Accuracy = 1.5% of full scale pressure.
5. Sensor output must stabilize in less than 12 milliseconds in response to pressure change with output noise level less than 10 millivolts.
6. The design must meet all requirements over a temperature range of 0 to +125 degrees centigrade, relative humidity of 0 to 100%, and over all the electrical and environmental conditions encountered over the complete pressure range.
7. The module must be unaffected by automotive vapors at temperatures of 150 degrees centigrade, shall not leak or expose any electrical connection to manifold gases for an operable life of 6 years or 120,000 miles.
8. The design shall meet the following tests with no degradation allowed in the electrical or mechanical specifications:
 - 1. 1,000 cycles of -40 to +125 degrees centigrade
 - 2. 2,000,000 cycles of 15Kpa to atmosphere
 - 3. 1,000 combined cycles of above temp. and press.
 - 4. 500 hr., each of biased and unbiased 95 degrees centigrade and 95% relative humidity
 - 5. 7 mechanical shocks of 50 G for 11 ms in 3 axes
 - 6. Low and high frequency vibration in 3 axes
 - 7. Automotive fluid compatibility for 30 min. at 100 degrees centigrade (dip test)
 - 8. Extended exposure to MDX and humidity combination
 - 9. Drop test of one meter
 - 10. Unbiased 5% salt fog for 48 hours with contacts and port open
 - 11. Biased 5% salt fog for 500 hours with contacts and port sealed
 - 12. Autoclave at 121 degrees centigrade and 15 psig for 96 hr.
 - 13. 100,000 cycles of 2 times operating pressure
 - 14. EMI exposure of 100 v/a in automobile
 - 15. 5 hr. exposure to "Arizona dust" (with agitation)

GENERAL REQUIREMENTS

Figure 5



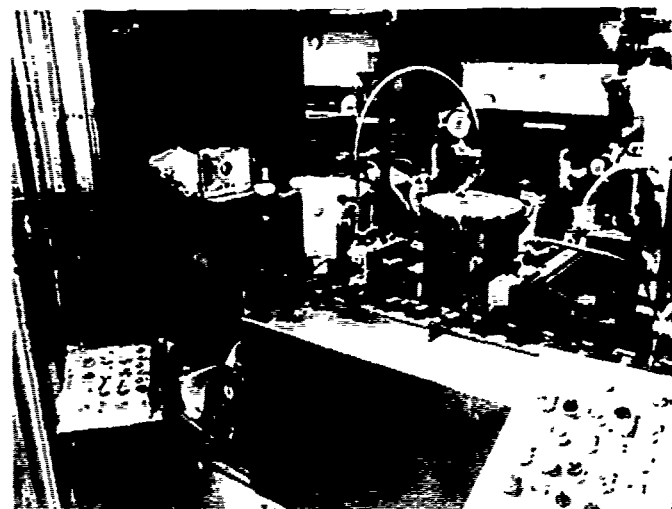
SUBSTRATE ASSEMBLY

Figure 6



HOUSING BACKPLATE ASSEMBLY

Figure 7



FILL AND COVER

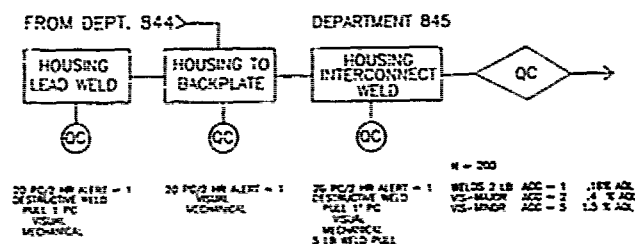
Figure 8

SCHEDULE

Start of production	1989 MY
Equipment in place and running	March 1988
Equipment ordered (1 yr lead time)	March 1987
Equipment spec., quotes, & vendor selection	Oct. 1986
Engineering Qualification complete (Eng., and Proto samples designed, built, and passed all Product Assurance tests)	Aug. 1986

TIMING FOR '89 MY PROGRAM

Figure 9



QC EXAMPLE

Figure 10

AN INTEGRATED ON-CHIP PRESSURE SENSOR
FOR ACCURATE CONTROL APPLICATIONS

by Joseph M. Staller & William S. Cumberledge

Abstract

Recent developments in microprocessor technology have opened up entire new vistas for control and monitoring applications that had previously been either too costly or impractical from an engineering standpoint. The result has been an overall increase in both reliability and accuracy of the control function, accompanied by a dramatic decrease in cost. The co-requirement for these improvements, a low-cost pressure sensor element capable of communicating directly with the MPU, is now available to further push the state of the art: the Motorola MPX3000.

In the past, pressure sensing has been largely accomplished using mechanical techniques of questionable reliability and often requiring complex, expensive electronic interface circuitry if a control function was to be included as part of the measurement. The introduction of semiconductor pressure a few years ago increased reliability and reduced the cost, but these early units still had the need for off-chip temperature compensation and calibration, and the output, in millivolts, required additional signal conditioning before it could interface with the controlling microprocessor. The idea of a low-cost sensor with all of these functions built into a single chip has been talked about for some time, but until now, the technology melding had not been sufficiently accomplished to offer a commercially available product.

The transition from basic sensing element to integrated sensor has involved the blending of sophisticated micro-machining techniques, thin-film resistor technology and bipolar wafer processing, each with its own particular processing problems.

The problems, and attendant solutions, that will be addressed in detail in the paper are:

1. Sensor technology - past and present
2. Cavity etch - present approach, alternates, etch stop
3. Thin-film resistor technology
4. Laser trimming techniques
5. Amplifiers - modifications to fit sensor processing, basic requirements for this application, alternate types

Future plans for new sensor devices will also be discussed.

S. J. Martin, A. J. Ricco, and T. E. Zipperian
Sandia National Laboratories, Albuquerque, New Mexico

A number of gas and vapor sensors have been constructed using surface acoustic waves (SAW) to detect the presence of adsorbed molecules [1-4]. Since the acoustic energy of the SAW is confined to the near-surface region of the substrate, the propagation characteristics are extremely sensitive to surface perturbations. Several mechanisms have been identified whereby adsorbed species may perturb the SAW propagation characteristics. Changes in surface conductivity [5], stiffness [6], electric constant, or mass density [6], alter the SAW velocity and/or attenuation and may contribute to a SAW sensor response. The surface wave propagation path is typically covered with a coating which selectively sorbs the species to be sensed. By judicious choice of coatings, selective sensors may be constructed.

We depart from the conventional implementation of SAW devices as gas sensors to describe how they may be used to measure adsorption isotherms and to perform thermal desorption spectroscopy. Adsorption isotherms are measurements, made at constant temperature, of surface coverage as a function of gas or vapor partial pressure for the species of interest. In thermal desorption spectroscopy (TDS) a measurement is made (at constant pressure) of surface coverage while ramping the surface temperature. TDS measurements are typically performed with single crystals under ultra-high vacuum conditions to study fundamental aspects of adsorption. By using the SAW device to measure surface coverage, isothermal measurement and thermal desorption spectroscopy may be performed with a single solid state device rather than the conventional mass spectrometer, albeit without the mass specificity offered by such an instrument. The device may thus be used in atmospheric sensor applications as well as in UHV studies.

The surface acoustic wave thermal desorption sensor utilizes a piezoelectric single crystalline ST-quartz substrate with input and output interdigital transducers positioned on either side of a meander-line heater, Fig. 1. The 20 finger-pair transducers have a periodicity of 32 μm , giving rise to a center frequency of 97 MHz. The acoustic beamwidth of the device is approximately 3 mm. The meander-line heater has a conductor width equal to 4 acoustic wavelengths; since this width is a multiple of half the acoustic wavelength, wave reflections by the heater are minimized.

In order to gain maximum sensitivity in measuring surface coverage, the device is used as the feedback element of an oscillator circuit. Adsorbed molecules perturb the SAW propagation velocity, hence the oscillator frequency, due to mass loading of the wave. The SAW device functions as an extremely sensitive microbalance, capable of measuring submonolayer coverage of the quartz surface. Short term changes in surface mass density on the order of 10^{-10} g/cm² are readily measurable.

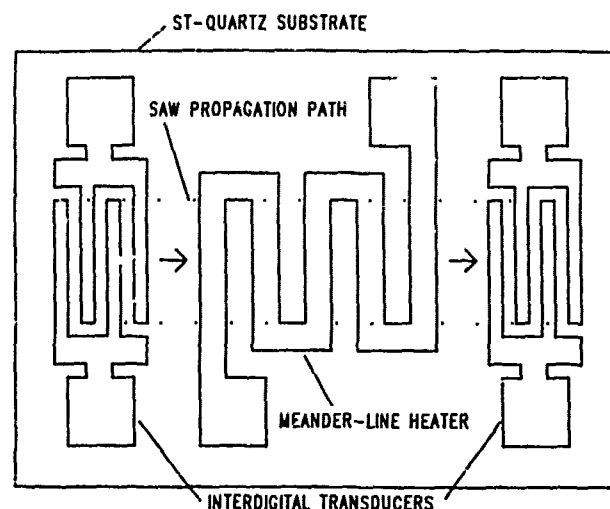


Figure 1 Surface acoustic wave device configuration used for measuring adsorption isotherms and thermal desorption spectra of organic vapors.

Adsorption Isotherms

In order to examine the coverage dependence upon vapor pressure, or adsorption isotherm, the SAW sensor was used to measure coverage while continuously varying ambient vapor concentration. A vapor/N₂ mixture was introduced into the sealed device chamber, continuously varying the vapor pressure from 3% to 97% of the saturation vapor pressure (p_s) at 20 C.

As seen in the adsorption isotherm of Fig. 2, the frequency shift occurring during methylene chloride (CH₂Cl₂) exposure indicates a general increase in coverage with increased vapor fraction p/p_s . The solid line in Fig. 2 shows the variation in vapor coverage with increasing p/p_s , while the dashed line is for decreasing p/p_s . Considering that monolayer coverage corresponds to a surface density of roughly 10^{15} cm⁻², full monolayer coverage by methylene chloride should result in a frequency shift of 21 ppm [7]. The horizontal line shows the frequency shift calculated for full monolayer coverage. The entire adsorption/desorption cycle was performed over a two hour period. The device shows little hysteresis and it is apparent that surface coverage goes to zero when the organic vapor is eliminated from the chamber. Coverage increases nearly monotonically with vapor pressure, reaching a full monolayer for p/p_s near .85. For greater values of p/p_s , a rapid increase in coverage is observed, probably due to multilayer formation (condensation) [7].

Thermal Desorption Spectra

Thermal desorption measurements can be made with the device shown in Fig. 1 by ramping the surface temperature while simultaneously monitoring the oscillation frequency. The SAW device functions as an indicator of surface coverage, substituting for a mass spectrometer in conventional thermal desorption spectroscopy. In order to demonstrate the measurement of thermal desorption using a SAW device, the vapor mixture was maintained at 10 C while the substrate surface temperature was ramped from 10 to 50 C. A static vapor/N₂ mixture was maintained in the device chamber stabilizing at $p/p_s = 0.8$, resulting in an initial coverage of slightly less than a monolayer.

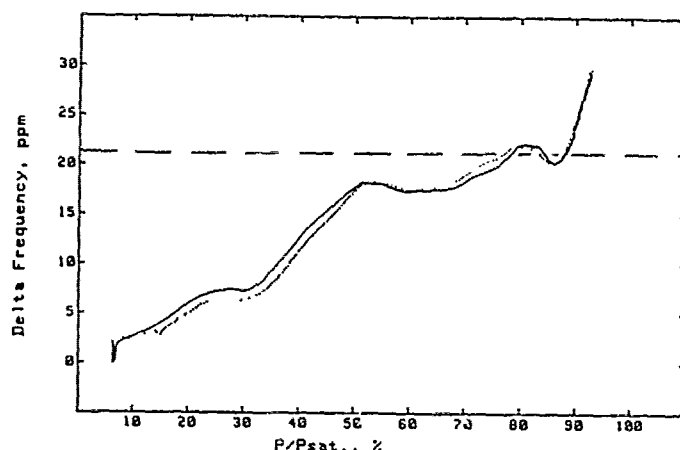


Figure 2 Adsorption isotherm revealing surface coverage for various partial pressures of methylene chloride. The horizontal line indicates monolayer coverage.

To increase the surface temperature monotonically, the current through the meander-line heater was ramped from 0 to 75 mA over a period of 375 seconds. During the ramp cycle, the resistance of the meander-line heater was monitored, as well as the SAW oscillator frequency. Resistance of the Cr/Au heater serves as an excellent measure of the surface temperature of the device. (To accurately obtain the surface coverage as a function of surface temperature, it is necessary to subtract the oscillation frequency measured in vapor from that obtained in nitrogen only.)

The TDS curve of Fig. 3 shows that surface coverage decreases dramatically as the surface temperature is increased. In the TDS of methylene chloride, the overall frequency shift is 19 ppm, agreeing closely with the expected shift of 21 ppm for removal of a full monolayer. The features appearing in the adsorption isotherm (Fig. 2) are duplicated in the TDS of Fig. 3, with the interchange of temperature and pressure as the coverage determining variable.

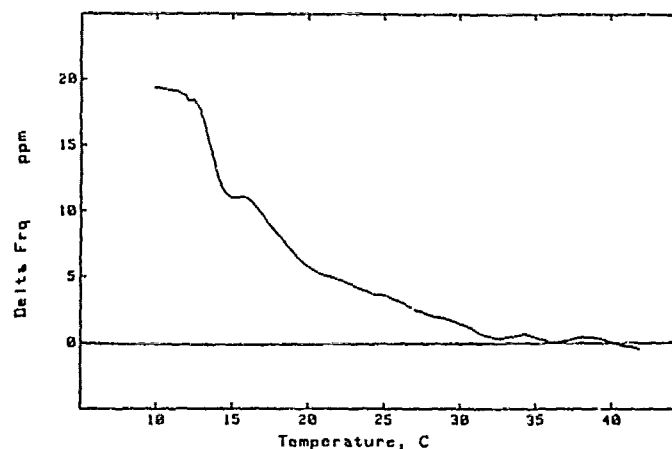


Figure 3 SAW thermal desorption spectrum obtained in a methylene chloride ambient with $p/p_s = 0.8$ at 10 C.

It has been shown that by incorporating a heater as an integral part of a SAW device, a sensor can be constructed which is capable of measuring thermal desorption spectra. A greater spread in the temperatures at which molecules are desorbed, and thus greater discrimination between species, could be obtained by using coatings which form stronger chemical bonds rather than relying on physisorption.

The authors would like to thank K. S. Schweizer, M. A. Butler, R. C. Hughes, and T. L. Aselage of SNL for helpful technical discussions, as well as J. M. Clifton for fabricating the devices. This work was performed at Sandia National Laboratories and supported by the U. S. Department of Energy under contract number DE-AC0476DP00789.

References

1. H. Wohltjen and R. Dessy, *Anal. Chem.*, 51, 1458, 1979.
2. A. Bryant, D. L. Lee, and J. F. Vetelino, 1981 *Ultrasonics Symposium Proceedings*, IEEE: New York, p. 171, 1981.
3. A. W. Barendsz, J. C. Vis, M. S. Nieuwenhuizen, E. Nieuwkoop, M. J. Vellekoop, W. J. Ghijsen, and A. Venema, 1985 *Ultrasonics Symposium Proceedings*, IEEE: New York, 1985.
4. A. D'Amico, A. Palma, and E. Verona, 1982 *Ultrasonics Symposium Proceedings*, IEEE: New York, p. 308, 1982.
5. A. J. Ricco, S. J. Martin, and T. E. Zipperian, "Surface Acoustic Wave Gas Sensor Based on Film Conductivity Changes", *Sensors and Actuators*, in press.
6. H. Wohltjen, *Sensors and Actuators*, 5, 307 1984.
7. S. J. Martin, A. J. Ricco, D. S. Ginley, and T. E. Zipperian, "Isothermal Measurement and Thermal Desorption Using SAW Devices", submitted to IEEE Transactions on UFFC, special issue on acoustic sensors, 1986.

THERMODYNAMIC STUDY OF HYGROSCOPIC POLYMERS USING SURFACE ACOUSTIC WAVES

John G. Brace and Thomas S. Sanfelippo
Johnson Controls, Incorporated, G-3
5757 North Green Bay Avenue
Milwaukee, Wisconsin 53201

Shrinivas G. Joshi
Department of Electrical Engineering and Computer Science
Marquette University
1515 West Wisconsin Avenue
Milwaukee, Wisconsin 53233

Abstract

In the course of developing a sensor for simultaneous humidity and temperature sensing, we have investigated surface-acoustic-wave (SAW) transducers for use as tools in characterizing materials of interest in sensing applications. In this paper we report a computer-controlled test system for characterizing oscillator-based sensors and demonstrate the utility of SAW oscillator measurements for gaining insight into sorption processes in glassy polymers.

Introduction

Surface-acoustic-wave (SAW) devices are now being used extensively in the storage and processing of analog and digital signals. Their applications range from sophisticated radar, sonar and communications systems to mass-produced components for radio and television receivers. Since surface wave propagation is very sensitive to external variables, low-temperature-coefficient cuts and design are employed, and protective packaging - typically hermetically sealed - is used for signal processing applications requiring immunity from environmental effects.

From the viewpoint of the sensor technologist, in contrast, strong sensitivity to a particular environmental effect is at the heart of development of a useful sensor for that effect. Thus, in recent years, considerable interest has been evinced in developing physical and chemical sensors based on SAW technology. A preliminary report of a pressure sensor appeared in 1975 [1]. The first chemical sensor based on SAW technology was a vapor sensor reported in 1979 [2], and since then numerous SAW sensors of chemical and biological interest have been discussed [3-8].

We are particularly interested in the development of vapor sensors for water vapor, and have demonstrated simultaneous humidity and temperature sensing with a dual-delay-line SAW device [9,10]. When used in a dual-oscillator configuration [10], this sensor produces direct frequency outputs that are easily measured with a digital frequency counter. One frequency is linearly related to temperature, while the other is a function of relative humidity.

Historically, a variety of techniques has been brought to bear on the complex problem of water vapor interaction with solids [11]. Water-polymer interactions have been extensively studied with a wide range of physical, analytical and spectroscopic techniques [12]. Gravitric measurements have been used in the study of both energetics and kinetics of sorption [13]. Most recently, Huang [14] attempted to apply thermodynamic analysis to electrical data from polymeric humidity sensors, in an effort to gain an understanding of the energetics of sorption from direct sensor measurements at several temperatures. Since propagation of surface acoustic waves is highly sensitive to changes in mass and mechanical properties of overlayers deposited in the propagation region of SAW devices [7], it should be possible to use the device as a transducer to aid in characterizing materials of interest in sensing applications as they interact with vapors. This paper de-

monstrates the use of SAW sensors for studying the water-vapor sorption energetics and kinetics in hygroscopic polymers.

Experimental

SAW device fabrication:

The experimental device used 15-finger-pair interdigital transducers (IDT's) of Al having a periodicity of 52.5 μm , center-to-center spacing between transducers of 5 mm and an aperture of 3.5 mm. Conventional photolithography was used to define the pattern. Multiple delay lines were fabricated on a 0.5 mm thick, 128°-rotated Y-cut, X-propagating LiNbO_3 substrate. The uncoated delay line had a center frequency of 74.3 MHz, time delay of 1.3 μsec , and a 6-dB bandwidth of approximately 4.8 MHz. The untuned, unmatched insertion loss in a 50-ohm system was 10 dB.

Polymer materials and coating:

Hygroscopic polymers were deposited by spin-coating from solution onto the delay lines, followed by thermal treatment. All were in the glassy state at temperatures used for this investigation. Polyimide (PI) films of 2-4 μm thickness were deposited by using PI2545 solution (DuPont) and baking for one hour at 130°C in air. The film was then patterned using conventional photolithography. In this state the film is partially imidized and contains some residual hygroscopic solvent. Fully imidized, solvent-free and high density polyimide was prepared on some sensors by baking for two hours at 350°C in N_2 . Both partially and fully imidized films were tested. Cellulose acetate butyrate (CAB) films of 1-5 μm thickness were deposited from diacetone alcohol solution. Polymers of 17, 39 and 51 wt.% butyrate, respectively, (Eastman Chemicals Co.) were used. These films were baked for one hour at 130°C under vacuum. Cross-linked CAB films of 1-5 μm thickness were also prepared by similar means, using a proprietary solution composition.

Sensor configuration:

For most experiments the SAW delay line was connected in the oscillator configuration [10]. The amplifier was a model HP8447A broad-band amplifier (Hewlett-Packard), driving a 50-ohm variable attenuator (HP335C), with the delay line in the feedback path of the amplifier to produce a delay-line-stabilized oscillator. The oscillation frequency was measured with a digital frequency counter (HP5385A) for display and transfer via GPIB. Since multiple delay lines were fabricated on a single substrate, some sensors were configured as dual oscillators by connecting adjacent delay lines to form separate oscillator loops.

Test cell:

The SAW sensor was mounted inside an air-tight stainless steel cell provided with gas inlet and outlet, rigid insulated signal feedthroughs and a thermocouple. For most experiments the thermocouple was attached to the LiNbO_3 crystal.

Test system configuration:

The test cell was inserted into a computer-controlled sensor test system capable of controlling cell temperature and pressure, test-gas dew point, and flow rate. For this investigation, cell temperature and gas dew point were controlled in order to produce a well-defined relative humidity (RH) inside the test cell. Humidity could be varied from near 0% RH to 100% RH by controlling the mixing ratio of dry and wet nitrogen gas within a moisture calibrator (Ondyne Model 10). Cell temperature could be varied between -40° and $+100^{\circ}\text{C}$ by controlling a programming potentiometer remote to an oven (Delta MK2300). Step functions of relative humidity within the test cell were generated by controlling two solenoid valves to isolate the cell from the gas stream.

All test system measurement and control functions were implemented with a general-purpose interface (Elexor Associates PL-100) under the control of a Tandy/Radio Shack Model 100 computer. Frequency measurements from the SAW oscillators were ported to the computer from the digital counter via an IEEE488 \leftrightarrow RS-232C protocol converter (Network Supply GPNET Model 10). Custom software written for the system was used to generate humidity and temperature parameters within the test cell, and collect isotherms, isobars and transient-response data. All system parameters and sensor test data were stored temporarily in the computer, then transferred as necessary via modem to a mainframe (VAX 11/785).

Results

Dual-delay-line sensor:

A sensor having two identical SAW delay lines was patterned with PI2545 such that one delay line was coated with partially imidized polyimide, while the other was uncoated. As expected, frequency of the 'coated' oscillator decreases with increasing relative humidity, at constant temperature. This is shown in Fig. 1.

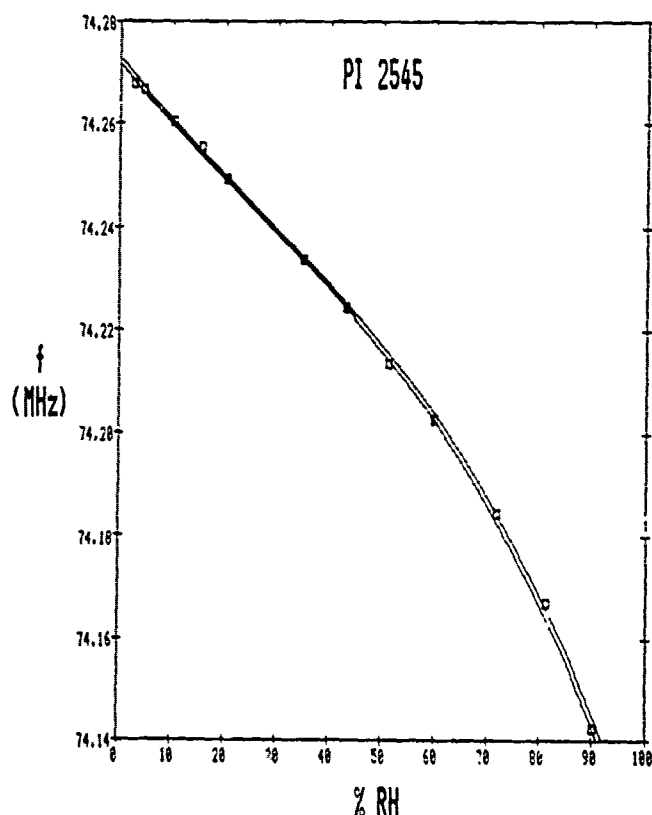


Fig. 1. Variation of SAW oscillator frequency with relative humidity for a polyimide-coated delay line at 23.5°C .

Between 5% and 60% RH, the frequency varies almost linearly with humidity, with a slope of $-1.1\text{ KHz per } 1\%$ change in RH. It is also apparent that the 'coated' oscillator operates satisfactorily for relative humidity values approaching 100%.

Fig. 2 presents the combined effects of humidity and temperature on the two oscillators. Both were connected in the oscillator configuration and oscillator frequencies were recorded from both as a function of humidity, at a series of temperatures between 10° and 40°C .

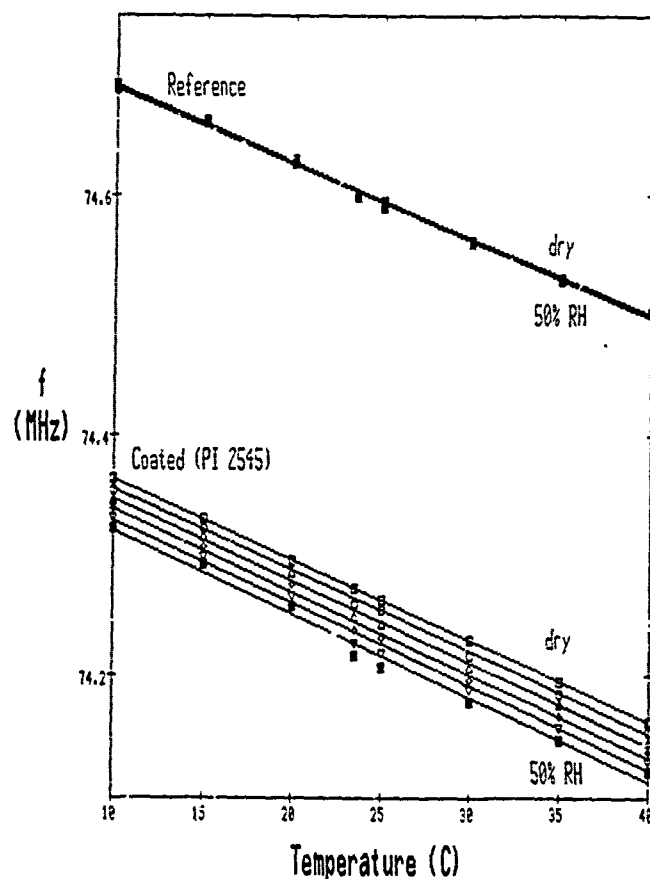


Fig. 2. Variation of oscillator frequency with temperature and humidity for uncoated and polyimide-coated delay lines.

Frequencies at equally spaced RH increments (dry gas, 10%, 20%, 30%, 40%, 50% RH) are plotted at each temperature for each oscillator. The lines drawn through the data points in Fig. 2 are least-squares fits. Both oscillators show similar, but not identical, temperature effects. The TCF of the polymer-coated delay line is slightly larger in magnitude than that of the reference. In addition, the reference oscillator is only weakly perturbed by humidity variations until relatively high humidities ($\text{RH} > 75\%$) are reached, whereas the coated oscillator is strongly sensitized to humidity within the temperature range studied.

Differential thermodynamic functions:

The differential enthalpy, entropy, and free energy of sorption of water in each polymer were calculated from the temperature variation of frequency in the sorption isotherms, using the conceptual approach of Huang [14]. A linear background correction for the TCF of the polymer-coated sensor in dry gas was made. The experimental thermodynamic functions for water in the cellulose derivative CAB 381 are presented in Fig. 3, calculated from adsorption isotherms at 10.1 , 19.8 , 29.9 , 40.0 and 49.9°C .

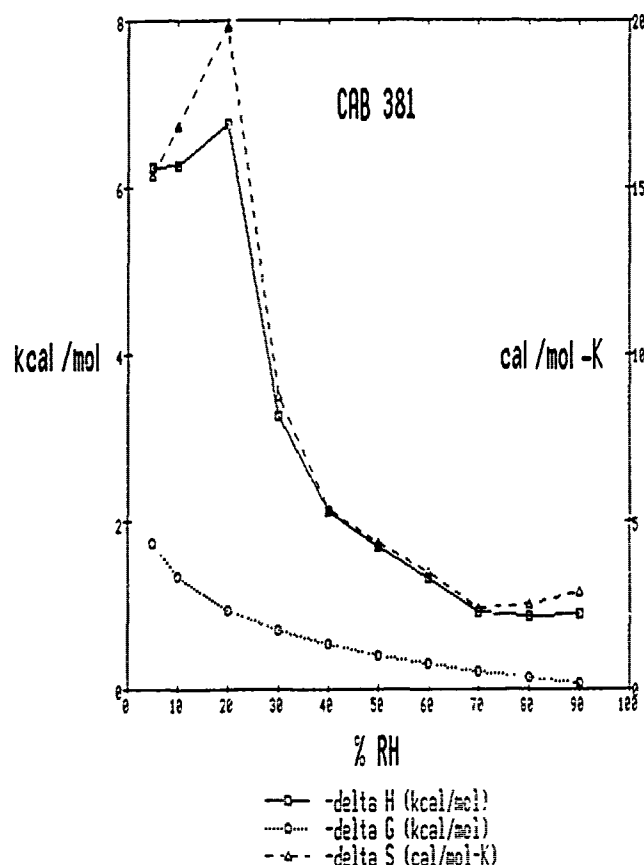


Fig. 3. Differential thermodynamic quantities for water in CAB 381 polymer as a function of relative humidity. Left ordinate: $-\Delta H$, $-\Delta G$. Right ordinate: $-\Delta S$.

A physical adsorption of the water vapor is indicated by the range of differential enthalpies observed. The large negative and relatively constant ΔH at low relative humidities suggests strong bonding with the polymer, possibly involving two hydrogen bonds per water molecule. The increasingly negative ΔS found at low humidities also suggests a decrease in randomness of the adsorbed water molecules. Taken together, the approximately constant ΔH and increasingly negative ΔS suggest Langmuir-type adsorption behavior within the first monolayer [15], i.e., up to about 20% RH in Fig. 3.

Following completion of the monolayer, the rapid decline in magnitude of the differential enthalpy with increasing humidity suggests that multilayer adsorption is occurring, wherein cohesive interactions between molecules of the outer layer(s) are much more important (i.e., contribute to the thermodynamic equilibrium) than are interactions of the first layer [16]. The similarity in shape of the enthalpy and entropy functions (in this regime of relative humidity) suggests that the sorbed water which does contribute to thermodynamic equilibrium is approaching the liquid state [17].

Sorption Kinetics:

The transient response of SAW oscillator sensors to step changes in humidity was studied by monitoring the frequency at constant temperature. Very rapid response was generally observed from the CAB-coated sensors. The time constant, τ , for both adsorption and desorption was 5 ± 1 s at room temperature, in agreement with the amplitude and phase time dependence [10]. Much slower response was observed from partially and fully imidized PI coatings, with a time dependence that varied with step direction and humidity at initiation of

the step. A typical transient-response result from a fully imidized PI coating (two sequential steps in humidity) is shown in Fig. 4.

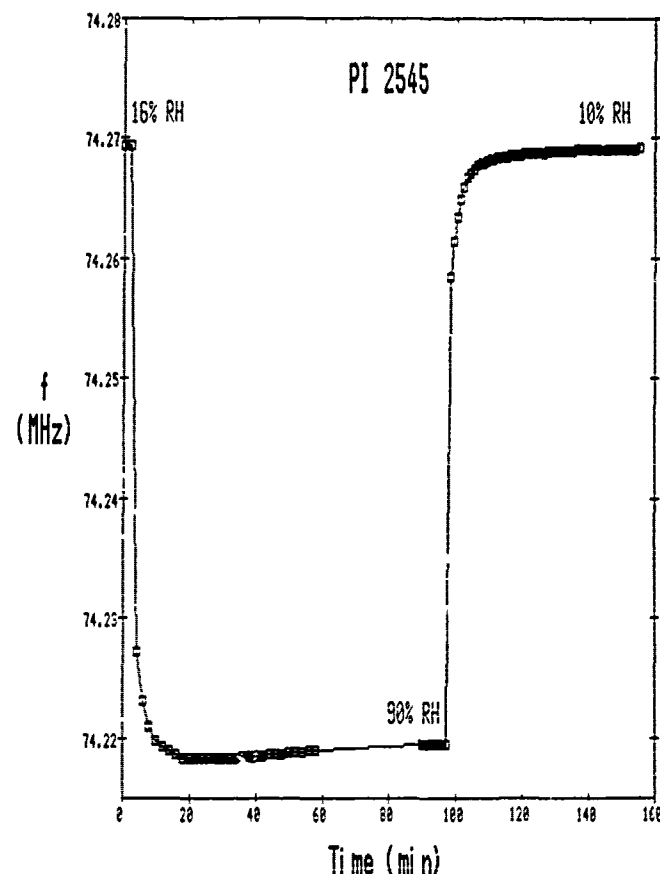


Fig. 4. Transient response of polyimide-coated SAW delay line at 23.5°C.

Analysis shows that the evolution of frequency with time in Fig. 4 does not follow a single exponential, although diagnostic plots (log frequency vs. log time) [18] of the adsorption and desorption data do reveal regions of characteristic slope. Three regimes or stages in the kinetics may usually be discerned in each step: an initial, rapid stage is followed by a slower intermediate stage, followed by a slow transition to thermostatic equilibrium. We propose that the regimes correspond to 1) rapid adsorption/desorption at surface sites; 2) diffusion of water in the polymer; and 3) relaxation of the plasticized polymer, respectively. There is, of course, overlap in the kinetics so that rapid site adsorption/desorption is envisaged as being concurrent with the other, slower, processes.

The 'undershoot' evident in the frequency during the adsorption step of Fig. 4 is frequently, but not always, observed, and only in the adsorption process. Analogous transients have been noted by others [5] during the adsorption of hydrogen on Pt. A possible explanation is found in the perturbation result of Wohltjen (eqn. 1 of ref. 7), in which the predicted frequency shift due to the presence of an overlayer in the SAW propagation region contains a term dependent on the overlayer mass per unit area and a term of opposite sign containing overlayer modulus. During adsorption of water, it is logical that modulus changes near the crystal/polymer interface should occur subsequent to mass changes in the polymer film. The effect of mass increase should be reflected almost instantaneously as a decrease in frequency, whereas any decrease in polymer modulus should lag somewhat and result in a small increase in frequency, as is seen in the adsorption step in Fig. 4.

In the case of several of the polymers studied, the desorption kinetics are found to differ from adsorption kinetics by having a higher initial rate and a more extended diffusion-controlled regime. The higher initial rate probably reflects a slightly lower energy barrier for desorption of surface water. The more lengthy diffusion-control regime in desorption is likely due to the necessity for all water to diffuse out of the bulk of the polymer before it can be released at the surface.

Conclusions

Measurements of SAW sensor frequencies in an automated test system have been used in a study of the thermodynamics and kinetics of water-vapor sorption in some hygroscopic polymers. The thermodynamic results indicate physical adsorption, point to a Langmuir-type behavior in the monolayer and suggest that a liquid-like multilayer description is appropriate at higher humidities. The kinetic results are consistent with a multistage sorption process that is expected for glassy polymers. We believe that these results demonstrate the usefulness of the SAW transducer as a new tool for materials research. It is possible to utilize its high surface sensitivity as a complement to traditional thermal and gravimetric methods.

References

- [1] T. M. Reeder and A. J. Demaria, U. S. Patent 3,978,731, Sept. 1976.
- [2] H. Wohltjen and R. E. Dessy, "Surface acoustic wave probe for chemical analysis," Anal. Chem., vol. 51, pp. 1458-1475, 1979.
- [3] A. Bryant, D. L. Lee and J. F. Vetelino, "A surface acoustic wave gas detector," Proceedings IEEE 1981 Ultrasonics Symp., pp. 159-162.
- [4] C. T. Chuang, R. M. White and J. J. Bernstein, "A thin-membrane surface-acoustic-wave vapor-sensing device," IEEE Electron Device Lett., vol. EDL-3, No. 6, pp. 145-148, 1982.
- [5] A. D'Amico, A. Palma and E. Verona, "Surface acoustic wave hydrogen sensor," Sensors and Actuators, vol. 3, pp. 31-39, 1983.
- [6] J. E. Roederer and G. J. Bastiaans, "Microgravimetric immunoassay with piezoelectric crystals," Anal. Chem., vol. 55, pp. 2333-2336, 1983.
- [7] A. Snow and H. Wohltjen, "Poly(ethylene malate)-cyclopentadiene: A model reactive polymer-vapor system for evaluation of a SAW microsensor," Anal. Chem., vol. 56, pp. 1411-1416, 1984.
- [8] H. Wohltjen, A. Snow and D. Ballantine, "The selective detection of vapors using surface acoustic wave devices," Proceedings 1985 Int. Symp. on Solid-State Sensors and Actuators, pp. 66-70.
- [9] J. G. Brace and S. G. Joshi, "Investigation of a surface-acoustic-wave sensor for simultaneous detection of relative humidity and temperature," Proceedings 1985 Int. Symp. on Moisture and Humidity, pp. 225-227.
- [10] S. G. Joshi and J. G. Brace, "Measurement of humidity using surface acoustic waves," paper no. PB-10 presented at the IEEE 1985 Ultrasonics Symp., San Francisco, CA., Oct. 16-18, 1985.
- [11] J. Texter, K. Klier and A. C. Zettlemoyer, "Water at surfaces," in Prog. Surf. and Membrane Sci., vol. 12. New York: Academic Press, 1978, pp. 327-403.
- [12] Ibid., pp. 330-331.
- [13] J. A. Rupley, P.-H. Yang and G. Tollin, "Thermodynamic and related studies of water interacting with proteins," in Water in Polymers, ACS Symp. Ser.; 127. Washington: American Chemical Society, 1980, pp. 111-132.
- [14] P. H. Huang, "Electrical and thermodynamic characterization of water vapour/polymeric film system for humidity sensing," Sensors and Actuators, vol. 8, pp. 23-28, 1985.
- [15] A. W. Adamson, Physical Chemistry of Surfaces, third ed. New York: Wiley, 1976, pp. 548-634.
- [16] H.-G. Burghoff and W. Pusch, "A model of physical adsorption of gases," J. Appl. Polymer Sci., vol. 24, pp. 1479-1495, 1979.
- [17] Adamson, p. 602.
- [18] C. H. M. Jacques, H. B. Hopfenberg and V. Stannett, Polym. Sci. & Tech., vol. 6, p. 73, 1974.

SILVER MULTI-LAYERS FOR PLANAR Ag/AgCl REFERENCE ELECTRODES

M. Lambrechts, J. Suls, W. Sansen
Katholieke Universiteit Leuven
Departement Electrotechniek, ESAT
Kardinaal Mercierlaan 94
B-3030 Heverlee, Belgium

ABSTRACT

The behaviour of different multi-layers for silver micro-electrodes is reported. Adhesion, lifetime and the use as a silver/silverchloride reference electrode for biomedical applications has been investigated. The electrodes are incorporated in a planar CMOS-process with a special lift-off technique. The electrodes are used in the development of implantable glucose and oxygen sensors and ion-selective electrodes.

INTRODUCTION

During the last years the research on planar chemical sensors has increased enormously. Since all chemical sensors need a reference electrode, stability and lifetime of this electrode determines the usefulness of the sensor.

For biomedical applications such as dissolved oxygen (Clark-cell) or glucose sensors, usually a Ag/AgCl reference electrode without reference electrolyte is employed. Blood plays in those cases the role of electrolyte.

The potential E at the Ag/AgCl electrode is determined by following equation known as the Nernst equation :

$$E = E^{\circ} - \frac{RT}{nF} \ln [Cl^{-}]$$

where

E° = the standard electrode potential

R = the gas constant

T = the absolute temperature

n = number of electrons participating in the reaction

F = the faraday

$[Cl^{-}]$ = the Cl^{-} -concentration

As in human blood the variations of the Cl^{-} -concentration are very small, the potential at a Ag/AgCl electrode in blood is practically constant. So, in most cases, no internal reference electrolyte is necessary. However, due to the relative high Cl^{-} -concentration, blood is very corrosive. Therefore the corrosion resistance of planar electrodes is of primordial importance.

PROCESSING

A sensor process (ref.1) compatible with a standard 3 μ CMOS process has been developed (fig. 1). The sensor materials are applied after the complete CMOS process. This excludes processing temperatures above 450°C. The process is based on highly doped polycrystalline silicon as interconnection layer between the electrochemical electrodes and the bonding pads. The electrodes are embedded in a silicon dioxide layer, the intermediary oxide between polysilicon and aluminium. This is achieved with a special lift-off technique (ref.2). Lift-off has the inherent advantage that the process is identical for all metals that can be evaporated or sputtered. Patterning of "difficult" metals like Pt, Au or multi-layers is selfevident.

An ideal lift-off profile with overhang is obtained during the wet etching of the silicon dioxide layer (fig. 2). So, etching of contact holes and patterning

of the lift-off mask is done in one step. Each electrode material only needs one extra mask. Adhesion of the electrodes is also improved due to the polysilicon under it. Noble metals like Pt and Au adhere well to polysilicon but do not adhere to silicon dioxide. This has been verified with the Scotch-tape test.

Adhesion of silver to silicon, polysilicon and silicon dioxide however is very poor. Therefore an intermediate film layer as Ti or Cr is used to promote adhesion. These metals corrode easily; mechanical and electrical contact is then lost. So, for Ag/AgCl reference electrodes loss of adhesion is one of the main failure mechanisms. Four different metallisation methods have been investigated : Ag, Cr/Ag, Ti/Ag and Ti/Pd/Ag.

Small electrodes (1.6 mm x 1.1 mm) have been manufactured with the same process as described. All layers are deposited successively with an electron gun evaporation system, (see Table 1). Evaporation is done immediately after the SiO_2 etching. Chemical chloridation of the electrodes is carried out on wafer or on the packaged chip in a $FeCl_3$ (1 %) solution. After encapsulation of the bonding region with a commercial epoxy the response to a varying Cl^{-} -concentration is measured. Lifetime tests have been carried out on the four different metallisation methods.

MEASUREMENTS

The potential at the different Ag/AgCl electrodes has been measured against a conventional Ingold Ag/AgCl reference electrode with an internal reference electrolyte. The Cl^{-} -concentration in the solution was varied between 10^{-4} M and 1 M. Initially the behaviour is nearly Nernstian for all metallisation methods. A typical response is shown in fig. 3. However some electrodes started drifting after a few hours; this was related to loss of adhesion of the metal layer. To examine this phenomenon an accelerated lifetime test has been set up.

A significant number of electrodes (24 per metallisation) were immersed in physiological solution at room temperature. Physiological solution simulates blood in its Cl^{-} -concentration and pH (7.4). Every hour the solution was agitated in an ultrasonic way to remove the corroded parts of the metallisation.

With the pure silver electrodes adhesion was lost immediately (fig. 4a). Loss of adhesion of the Ti/Ag was observed after a few hours (fig. 4b). The average lifetime is 2.75 hours. For both metallisation methods the complete electrode lost adhesion. Corrosion of the Cr/Ag electrodes in contrast, started with the formation of blisters and holes. The average time before blister or hole formation is 46 hours (fig. 4c).

The Ti/Pd/Ag electrodes however withstood this lifetime test without any problem. After three months no corrosion or loss of adhesion was observed. On chloridated samples the average lifetime was halved. No damage was found on the chloridated Ti/Pd/Ag electrodes after 3 months. This proves that Ti/Pd/Ag electrodes are far superior to all the other metallisation methods.

An other research group obtained similar results for solar cell metallisations (ref. 3). They related the excellent corrosion resistance to a modification of the anodic potential of the active metal by introduction of palladium, so that a passive oxide is formed when the film is exposed to an electrolyte. Palladium also serves as diffusion barrier for oxygen and moisture. It inhibits the corrosion of the Ti layer and so preserves adhesion of the Ag film.

APPLICATIONS

The Ti/Pd/Ag metallisation has been used with success for different applications. The process described above is now used in the development of implantable glucose and oxygen sensors. For these applications stability and reproducibility of the electrode potential is not critical because the current measurement is carried out at a plateau in the current-potential curve. No problems were encountered with Ti/Pd/Ag/AgCl reference electrodes.

The electrodes were tested as a Clark-cell with Ag cathode and anode (ref.4). The results were positive. Ti/Pd/Ag/AgCl electrodes were deposited on a complete CMOS circuit described in ref.5. For this application, ion-selective sensors, stability and reproducibility is more critical.

CONCLUSION

Planar Ag/AgCl electrodes are incorporated in a standard CMOS process. The corrosion resistance of different multilayers has been investigated. By introduction of palladium as an intermediate layer between titanium and silver, the corrosion resistance increases tremendously without affecting the Nernstian behaviour of the electrode. Immersed in physiological solution, a lifetime of more than three months was observed. The Ti/Pd/Ag/AgCl metallisation has been used with success for different applications.

ACKNOWLEDGMENTS

M. Lambrechts acknowledges support of the IWONL and J. Suls of IMEC, Belgium. We wish to thank J. Vandeput and V. Muls for processing the devices.

REFERENCES

- (1) W. Sansen, M. Lambrechts, J. Suls, "Fabrication of voltammetric sensors with planar techniques", in *Proc. of Transducers '85*, 1985, pp 344-347.
- (2) J.M. Frary, P. Seese, "Lift-off techniques for fine line metal patterning", *Semiconductor International*, pp. 72-88, December 1981.
- (3) D.J. Sharp, "Corrosion inhibition in sputter-deposited thin-film systems using an intermediary layer of palladium", *J. Vac. Sci. Technol.*, Vol. 16, pp. 204-207, Mar./Apr. 1979.
- (4) M. Koudelka, A. Grisel, "Miniaturized Clark-type oxygen sensor", in *Proc. of Transducers '85*, 1985, pp. 418-422.
- (5) I. Lauks, J. Van der Spiegel, W. Sansen, M. Steyaert, "Multispecies integrated electrochemical sensor with on-chip CMOS circuitry", in *Proc. of Transducers '85*, 1985, pp. 122-124.

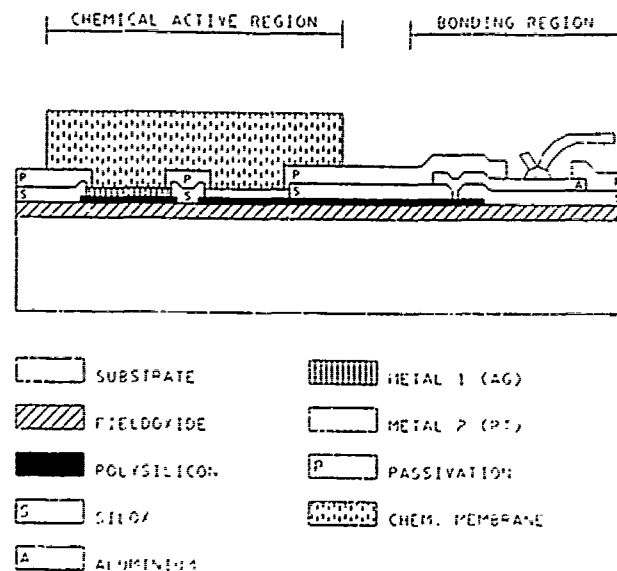


Fig. 1 Cross-section of a CMOS compatible chemical sensor

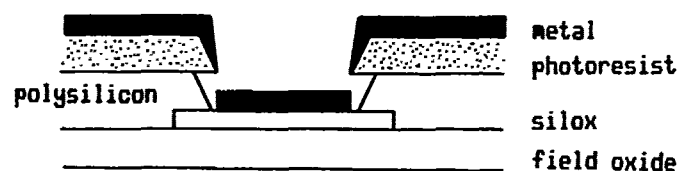


Fig. 2 Lift-off profile with overhang

Metal	Thickness [nm]	Evaporation rate [nm/s]
Ti	50	2.5
Cr	50	2.0
Pd	50	1.5
Ag	900	10.0

Table 1

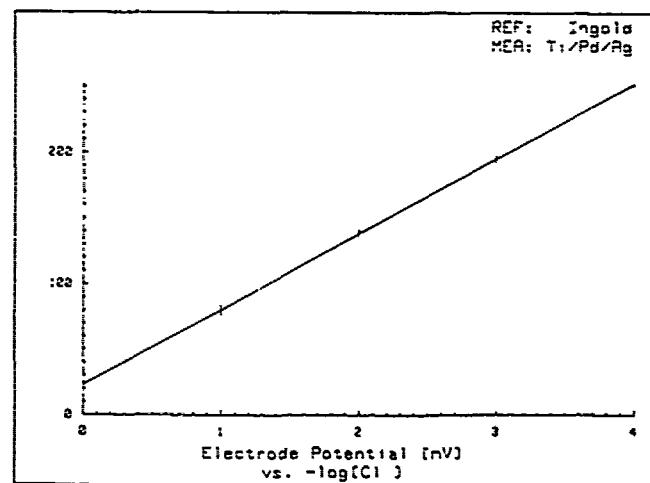


Fig. 3 Cl^- response of a planar Ag/AgCl electrode (Slope = 57 mV/decade)

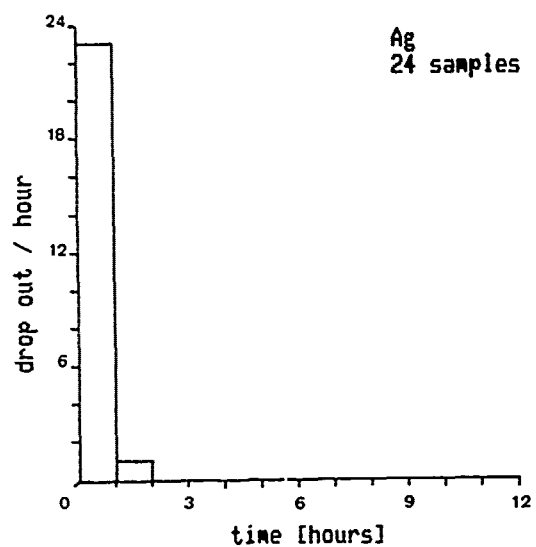


Fig. 4.a. Lifetime profile of a Ag layer
(not chloridated)

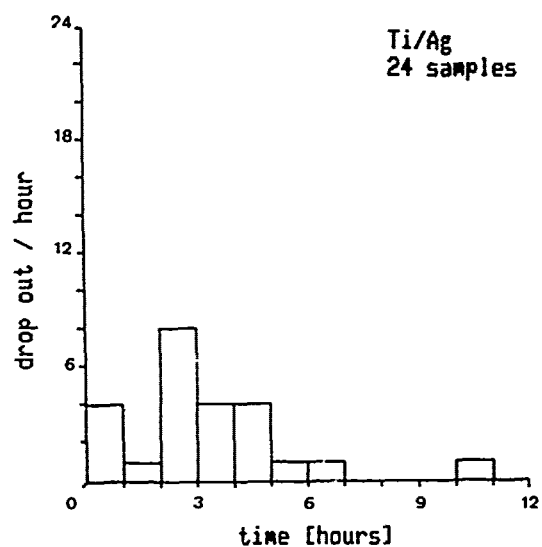


Fig. 4.b. Lifetime profile of a Ti/Ag layer
(not chloridated)

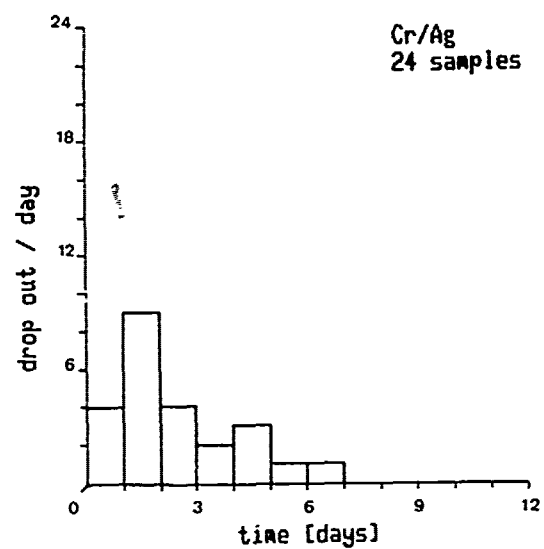


Fig. 4.c. Lifetime profile of Cr/Ag layer
(not chloridated)

THE STRUCTURE AND PROPERTIES OF RF REACTIVE SPUTTERED IrO_2 FILMS

Kenneth G. Kreider
National Bureau of Standards
Bldg. 221, Rm. B-312
Gaithersburg, MD 20899

Abstract

Iridium oxide films were reactively sputtered on alumina substrates at temperatures ranging from 300-600°K in order to relate the structure of the film to its electrical properties. X-ray diffraction of the films indicated a transition from an amorphous to crystalline structure with increasing temperature which was accompanied by a increasing electrical conductivity. Details on sputtering conditions, film adhesion, and structural characteristics of the films are also presented.

Introduction

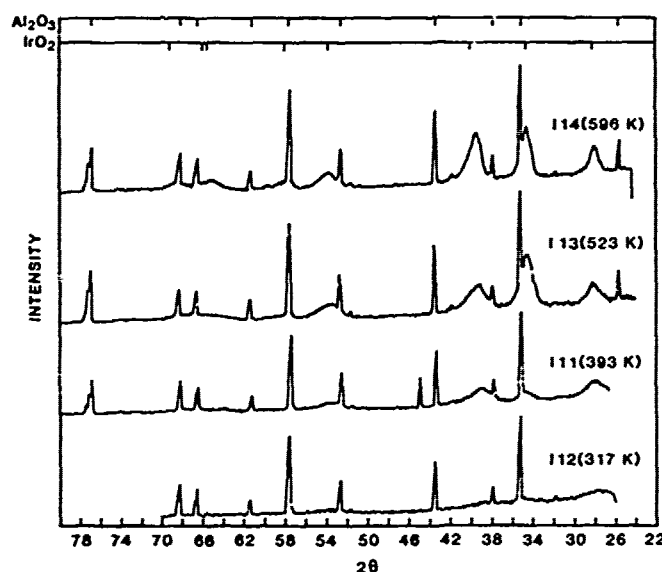
The electrochemical properties of iridium oxide have stimulated investigations related to its use as an electrochromic film [1] and as a pH sensor [2]. In considering iridium oxide as an electrochromic sensor, Hackwood et al. [3] noted the contrasting behavior of the amorphous and crystalline phases. They found the sputtered amorphous films to be much more stable than the anodically grown crystalline films and studied the amorphous to crystalline transition in the sputtered films. A similar contrast between anodically prepared films and sputtered films [2] was found when the iridium oxide is used as a pH sensor. Studies of the structure of iridium oxide have led to an evolving understanding of the electronic state of the iridium and its oxidation and hydration in aqueous environments. The electrochemical reactions are also structure sensitive and therefore are affected by the crystallinity of the anhydrous bulk material as well as the hydration of the surface. Since the corrosion resistance, solution response to concentrated ions, redox potential, and overall pH measurement performance appear to be sensitive to the fabrication parameters and structure of iridium oxide, this study was conducted to relate sputtering conditions to the electrical, physical, and chemical properties of the films.

Experimental

Iridium was sputtered from a pure (99.99%) iridium 5 cm diameter target with a 13.5 MHz RF planar magnetron source using approximately 0.15 Pa total pressure and a 20 cm target to substrate distance. Argon (99.999%) and oxygen (99.99%) were mixed and monitored using a side tap, separately pumped mass spectrometer. The pressure values reported below were within $\pm 10\%$ of the mass spectrometer argon-to-oxygen ratios measured except for the two lowest oxygen mixtures. Thickness was monitored using a quartz oscillator and was measured using weight gain on a typically 4x8 cm area of the alumina substrates. These measurements were confirmed using thallium interferometry. Heating was accomplished using an aluminum block heater. X-ray diffraction spectra of all coatings were made with $\text{Cu K}\alpha$ radiation and calibrated with the alumina substrates. Electrical resistivity measurements were made with a four point probe test and adhesion tests were made with a commercial epoxy bonded tab tensile tester.

Results

In order to determine the sputtering conditions for obtaining iridium oxide from the pure iridium target, both the sputtering atmosphere argon-oxygen ratio and the power level on the target which controls the rate were varied. X-ray diffraction data indicated that high power levels (200 watts or 15 watts/cm²) and partial pressures of 0.026 Pa of oxygen lead to metallic iridium deposits. Low power levels (50-100 watts or 2.5-5 watts/cm²) and oxygen partial pressures of greater than 0.13 Pa lead to films of iridium oxide in which no iridium X-ray lines were observed. With the low oxygen pressures and low power levels, films included both Ir and iridium oxide. The substrate temperatures used during deposition ranged from 310°K to 596°K. The X-ray patterns for the deposits made at the lowest temperatures indicated either amorphous or very fine grained iridium oxide since only the [110] peak at $d = 0.3178 \text{ nm}$ was discernible for the rutile structure but this could represent an amorphous pattern. A Scherrer calculation of the grain size for crystalline rutile [110] peak would indicate a size of 2-3 nm (Fig. 1). The rutile pattern was clearly evident for deposits made at 393°K including the [110], [101], [200], and [211] peaks. At higher temperatures, 523K and 596K, the [220], [310], [112], and [301] peaks were also developed and the grain size calculation indicated an 8 nm diameter for 596K.



Figur. X-Ray Diffraction Intensity for IrO_2 Films Produced at 317-596°K.

The higher deposition temperature also had a direct effect on the electrical resistivity as measured with a four point probe. A nearly linear relationship was observed for films made at 50 watt and 0.16 Pa oxygen between the substrate temperature and resistivity. This value was $1.7 \times 10^{-4} \text{ ohm cm}$ at 596K and $8.5 \times 10^{-4} \text{ ohm cm}$ at 310K (Fig. 2). The lower resistivity for films made at higher temperatures is

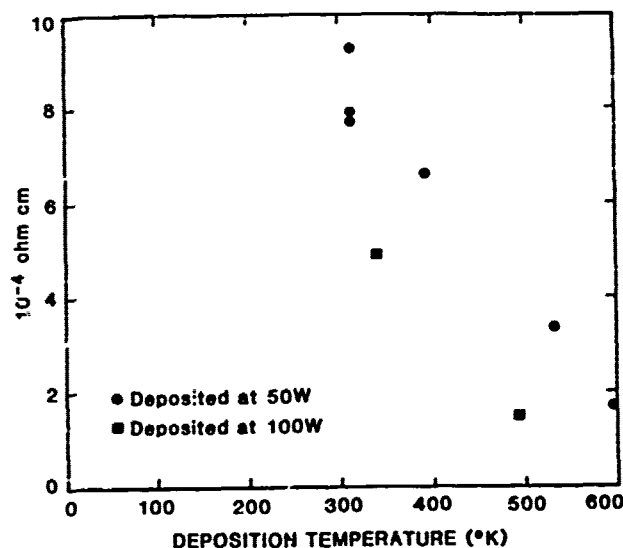


Figure 2. Effect of Deposition Temperature on IrO₂ Film Resistance.

comparable to Hackwood's results indicating a decrease in resistivity of films made at room temperature upon annealing. The films made with low oxygen partial pressure and consisting primarily of iridium had lower resistivities (0.5×10^{-4} ohm cm) even though they were produced at the lower temperatures. Also, films produced at 100 watts power level and therefore at a faster rate tended toward lower resistivities indicating the possibility of high iridium-to-oxygen ratios (oxygen deficiencies) even though no evidence of iridium metal as a phase was present in the X-rays.

The details of the relationships between deposition rate, sputtering atmosphere, substrate temperature and the structure and properties of the film will be presented as well as the results of the adhesion tests of the films.

Conclusions

The substrate temperature during reacting sputtering of iridium oxide from iridium has a direct effect on the grain size and crystallinity of the film changing from amorphous or extremely fine grained deposits at 310K to crystalline deposits at 596K. The high temperature deposits have much lower resistivity. The change from high resistivity, nearly amorphous to low resistivity and crystalline appears to be a gradual one as the temperature of deposition is increased.

References

- [1] L.M. Schiavone, W.C. Dautremont Smith, G. Beni and J.L. Shay, "Improved Electrochromic Behavior of Reactively Sputtered Iridium Oxide Films," *Appl. Phys. Lett.*, **35**, 10 (1979), 823.
- [2] M.F. Yuen, I. Lauks and W.C. Dautremont Smith, "pH Dependent Voltammetry of Iridium Oxide Films," *Solid State Ionics*, **11** (1983), 19.
- [3] J. Hackwood, A.H. Dayem and G. Beni, "Amorphous-Normetal-to-Crystalline Transition in Electrochromic Iridium Oxide Films," *Phys. Rev. B*, **26**, 2 (1982), 471.

THE RESPONSE OF ULTRATHIN PALLADIUM GATE SENSORS TO HYDROGEN AND CARBON MONOXIDE

G. Jordan MacLay and Kevin W. Jelley

Microelectronics Laboratory
Department of Electrical Engineering and Computer Science
University of Illinois at Chicago
P.O. Box 4348, Chicago, IL 60680

Abstract: MOS sensors were made using gates of Pd 25 and 40 Å thick. The resistance across the gate, as well as the gate to substrate capacitance showed sensitivity in air to CO at 180°C and to H₂ at room or elevated temperatures.

I- Introduction

In recent years, MOS devices have been fabricated with a variety of transition elements for the gate electrodes (1,2). Devices with palladium gates have shown sensitivity to hydrogen (10ppm to 1%). These devices typically have gates which are 500-1000 Å thick, on thermal oxides 500-1000 Å thick, and are operated at 150°C to enhance the response and eliminate adsorbed water. The gate acts as a catalyst in the dissociative chemisorption of the hydrogen. The hydrogen atoms diffuse thru the gate to the oxide interface where they produce a dipole layer. The voltage drop over the layer appears as a shift in the capacitance-voltage curve. Palladium gate MOS devices have also shown sensitivity to carbon monoxide. Carbon monoxide is adsorbed on the surface but is unable to diffuse through the palladium layer. The response to carbon monoxide has been obtained by using a modified palladium gate which is porous or in which holes 1.5 to 3.0 micrometers in diameter have been patterned to permit the carbon monoxide to reach the oxide interface (3,4).

Our goal is to employ an ultra-thin film of palladium or palladium in combination with other metals in order to obtain a MOS device sensitive to CO and hydrogen, and that would allow us to differentiate between the two gases. A MOS hydrogen sensor with a Pd gate 30 Å thick and a 350 Å permeable gold overlayer, on 100 Å of SiO₂ has been shown to be sensitive to hydrogen at room temperature with response and recovery times significantly less than those of thick Pd gate sensors operated at elevated temperatures (5). It is necessary to determine if the thick gold overlayer, which prevents the sensor from responding to CO, is necessary to obtain a sufficiently conductive gate electrode.

Many evaporated metal films a few tens of Å thick or less are porous and tend to consist of an array of islands separated by approximately 5 to 100 Å. The morphology of the island structure depends on the metal, the film thickness, the substrate, the temperature, and the rate of deposition (6). As the film thickness increases, a critical thickness is reached at which the islands begin to merge, and form larger, irregular shaped islands. A gate film which is slightly beyond the critical thickness may be suf-

ficiently conductive to act as a gate electrode and sufficiently porous to allow penetration of CO to the Pd/SiO₂ interface. The adsorbed CO is expected to alter the conductivity of the gate by changing the potential seen by the electrons tunnelling between the islands.

II - Experimental

We have fabricated MOS gas sensors with ultra-thin films of Pd 25 and 40 Å thick. The sensors were fabricated on p-Si, 7 (ohm-cm)⁻¹, with a thermal oxide 100 Å thick, grown in dry oxygen at 900°C. Circular electrodes 2.25 mm in diameter were deposited thru an evaporation mask using an e-beam system in a oil free vacuum chamber with a base pressure of 10⁻⁸ torr. Two electrical contacts were made to each gate using gold wire and a high temperature conductive polyimide adhesive cured at 150°C. The bottom contact was obtained by evaporating aluminum on the heavily doped surface and annealing at 350°C in N₂ for 30 minutes. Packaged devices were mounted in TO-5 headers using polyimide. Testing was done in a aluminum test fixture with high temperature capability (\pm 0.5°C) and a very small purge volume.

Measurements were made of the capacitance (C) as a function of bias or time for concentrations of CO from 100 ppm to 10,000 ppm CO in air, and concentrations of H₂ from 10 ppm to 800 ppm in air. Measurements were also made of the impedance (Z_g) between the two electrodes on the gate in the different ambients.

III - Results

At room temperature both the 25 Å and the 40 Å devices showed sensitivity to H₂ but not CO. At 180°C both the 40 Å and the 25 Å devices showed sensitivity to CO and H₂. For the 25 Å device the change of the threshold voltage ΔV_t as measured by the shift of the C-V curve, varied from 40 mV as the concentration of hydrogen was increased from 10 ppm to 800 ppm (Fig 1). At 10 ppm, the sensitivity to H₂ is about 4.5 mV/ppm H₂ in air; above 200 ppm H₂, the sensitivity is constant at 0.2 mV/ppm H₂ in air, up to the maximum concentration tested of 800 ppm. No evidence of saturation was seen. This curve for H₂ is similar in shape to that obtained for CO at 180°C. For CO at

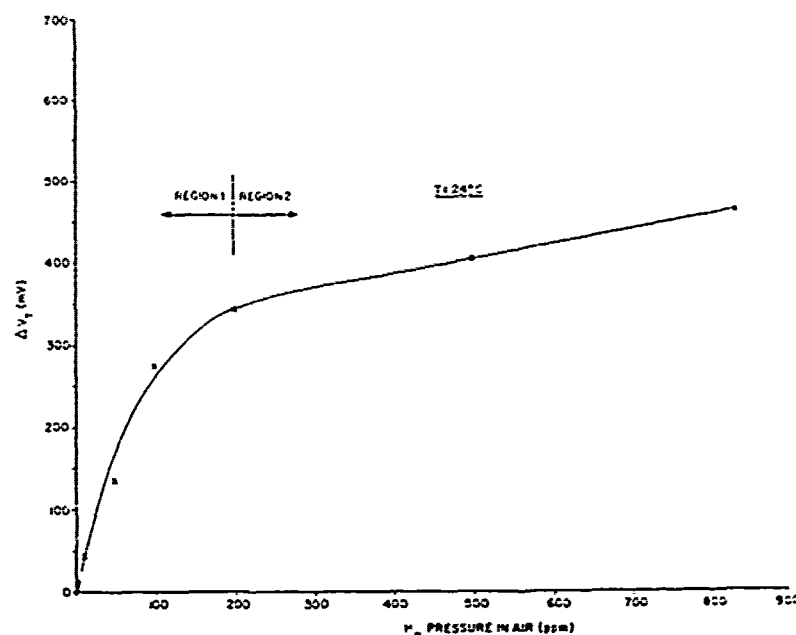


Fig. 1. Shift in threshold voltage ΔV_T versus concentration of H_2 in air for a 25 Å Pd gate sensor. $T = 24^\circ C$.

180°C, the sensitivity at low pressures is approximately 0.14 mV/ppm CO/air. Above 1000 ppm the sensitivity is constant at 0.03 mV/ppm CO/air. The response does not appear saturated at 10,000 ppm.

The change in the impedance across the gate Z_g is plotted as a function of the concentration of H_2 in air in Fig. 2. The sensitivities for H_2 is 0.25 ohms/ppm H_2 in air at 10 ppm, and a constant value of 0.02 ohms/ppm H_2 in air for concentrations above 200 ppm. For CO in air the sensitivity at low pressure is 0.07 ohm/ppm CO/air; above 1000 ppm the sensitivity is constant at 0.004 ohms/ppm CO/air for the range measured.

A plot of C and Z_g as a function of time for exposure to 800 ppm H_2 /air with recovery in pure O_2 is shown in Fig. 3. No drift is seen in the capacitance or impedance for room temperature operation. When operated at high temperature the capacitance and impedance show some long term drift. The capacitance and impedance have very similar time responses.

IV - Discussion

The long term drift in the CO response observed is similar to that seen in Pd gate hydrogen sensors operated at elevated temperatures. The hydrogen induced drift is thought to be due to hydrogen atoms entering the oxide since it can be eliminated by the use of a nonpermeable layer such as Al_2O_3 or silicon nitride under the gate metallization (2). If the drift in the response to CO is due to diffusion of the CO into the oxide, it is unclear why the gate impedance Z_g should drift also. No drift is seen for oper-

ation at room temperature for H_2 sensing. During response or recovery the time dependence of the change in C and Z_g are very similar, indicating that both may depend on the same limiting physical process.

The change in the impedance across the gate in the presence of H_2 or CO is probably due to adsorbed dipoles changing the potential between islands forming the gate. This change will affect the tunnelling current and therefore the resistance.

In certain cases the accumulation capacitance is observed to increase on exposure to CO or H_2 , corresponding to the increase in the gate conductivity, and therefore the effective gate area. At low frequencies the gate impedance is purely resistive and the films are ohmic over the voltages tested; as the frequency is increased the impedance becomes more capacitive. We may interpret this as due to the shunting effects of the capacitance of the metal islands with the substrate. The island structure may be viewed as as a distributed RC network. Consistent with this interpretation, we observe that as the test frequency is increased, the effective area of the gate decreases, and the accumulation capacitance decreases.

References

- [1] I. Lundstrom, D. Soderberg, *Sensors and Actuators*, 4, 593 (1984).
- [2] I. Lundstrom and C. Svenson in "Solid State Chemical Sensors," ed. by J. Janata, R. Huber, Academic Press, New York (1985).
- [3] D. Krey, K. Dobos, and G. Zimmer, *Sensors and Actuators*, 3, 169 (1983).

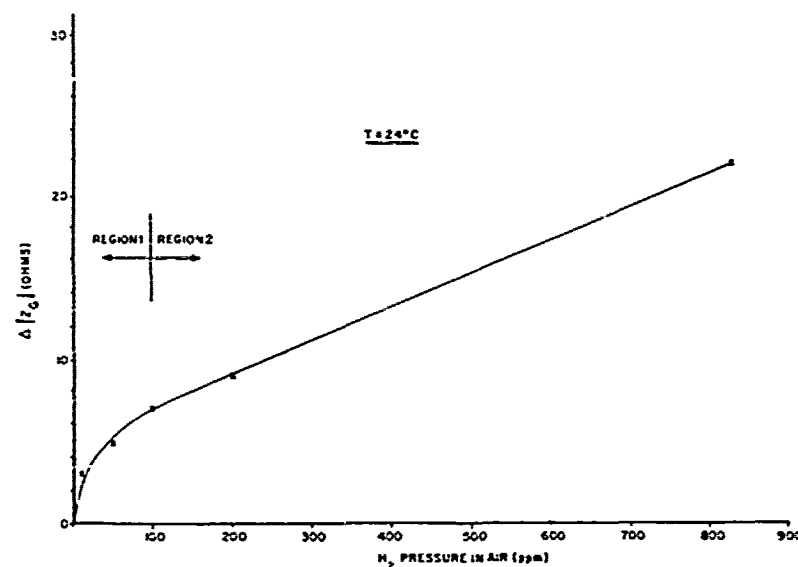


Fig. 2. Change in the impedance ΔZ_g across the gate versus concentration of H_2 in air for a 25 Å Pd gate sensor. $T = 24^\circ C$

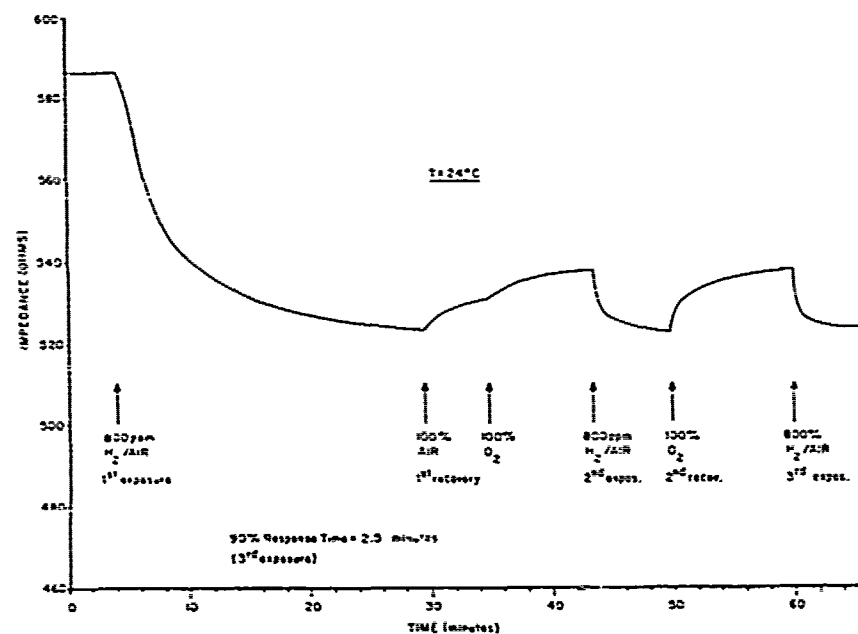


Fig. 3. Impedance Z_g (across the gate) versus time in 800 ppm H_2 in air for a 25 Å Pd gate sensor. $T = 24^\circ C$.

- [4] K. Dobos and K. Zimmer, IEEE Trans. Elec. Dev., ED-32, no. 7, (1985).
- [5] J. Maclay, IEEE Trans. on Elect. Dev., ED-32, no. 7, (1985).
- [6] K.L. Chopra, "Thin Film Phenomena", McGraw-Hill (1969).

Scot P. McArthur and James W. Holm-Kennedy
Physical Electronics Laboratory
Department of Electrical Engineering
University of Hawaii at Manoa
Honolulu, HI 96822

Abstract

A capacitively coupled silicon accelerometer with the proof mass supported by a thin silicon membrane is described. The device offers convenient A/D conversion via conversion of acceleration to an oscillator frequency change. Air mass loading is shown to decrease the device sensitivity. The reduced sensitivity is attributed to the effect of air compressibility on the apparent membrane stiffness and air damping.

The prototype accelerometer described here is a variable capacitor silicon device (Fig. 1).¹ The primary transducer consists of a thin silicon membrane supporting a central silicon proof mass element placed over an Al electrode plane recessed into a glass substrate to create an air dielectric capacitor. The silicon membrane functions as a support spring which is displaced by acceleration.² The displaced proof mass modulates the capacitance between the proof mass lower (conducting) surface and the Al plate. Acceleration is first transformed into a proof mass displacement, which in turn is transformed into a capacitance change. The capacitance is converted to a frequency using an RC oscillator circuit. In this manner the analog capacitance is easily converted to a digital signal if a frequency counter is employed. The shift from the frequency oscillator's center frequency is proportional to the acceleration. For the present system, the frequency shift was converted to an output voltage proportional to the frequency shift in order to exploit the various functions and signal processing

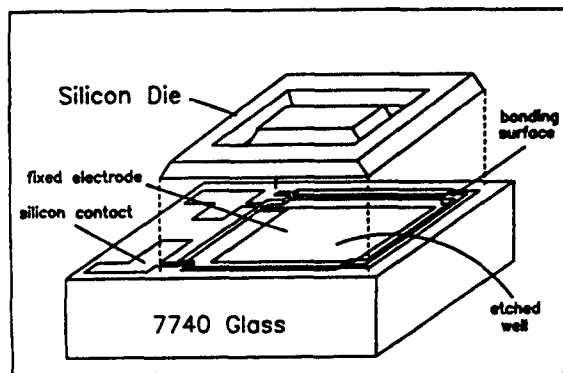


Fig. 1 Exploded View of Inertial Gauge

¹A more extensive treatment will be submitted for publication. Also see Scot McArthur, M.S. Thesis, "Silicon Diaphragm Accelerometers," University of Hawaii, 1984.

²Capacitively coupled membrane pressure sensors have been described by others and are commercially available. Likewise, a variety of different silicon micromechanical accelerometers have been reported in the literature: see, for example, Peterson, et al. [1], Chen and Muller, et al. [2], Rudolf [3] and Raylance and Angell [4].

capability of an HP spectrum analyzer. The sensor circuitry output voltage $v_0(t)$ was also proportional to the acceleration.

By testing the device at different pressures and acceleration frequencies, it was found that the air loading can dramatically affect (reduce) device sensitivity. Air compressibility effectively increases the proof mass' spring constant thereby decreasing the displacement amplitude and related device sensitivity. The device resonant frequency is also shifted to higher frequencies. Air damping also affected device response.

Experimental test results and their analysis, including the effects of air loading are presented below.

The Low Frequency Primary Transfer Function

The mass loaded silicon diaphragm (Fig. 1) was modeled as a mechanical oscillator. The low frequency ($f \ll f_0$, $f_0 \equiv$ resonant frequency) primary transfer function $T_{YA}(f)$ is the measure of the proof mass displacement Y_A per unit of acceleration A , and at low frequencies can be expressed as

$$T_{YA}(f) \Big|_{f \ll f_0} = M/K_T \quad (1)$$

Here M is the proof mass and K_T is the spring constant (stiffness) arising from the supporting silicon membrane bending and stretching stiffness.

To compute $T_{YA}(f) \Big|_{f \ll f_0}$. The proof mass was separated from the membrane, weighed, and found to be

$$M = 5.4 \times 10^{-6} \text{ kg} \pm 0.18 \times 10^{-6} \text{ kg} \quad (2)$$

A theoretical calculation of the plate stiffness yield

$$K_T \Big|_{TH} = 510 \text{ Nt/M} \quad (3)$$

and a theoretical primary transfer function of

$$T_{YA} \Big|_{f \ll f_0} \approx 1.06 \times 10^{-8} \text{ M/M/sec}^2 \quad (4)$$

$$\approx 106. \text{ }^\circ \text{ A/M/sec}^2$$

The related resonant frequency (without air loading) was calculated to be

$$f_0 \Big|_{NL} \approx 1550 \text{ Hz} \quad (5)$$

where "NL" stands for "no airloading".

The Secondary Transfer Function

The secondary transducer is comprised of two parts: the variable capacitor oscillator which converts acceleration into a change in oscillator frequency, and a demodulator circuit which converts the frequency shift to a proportional voltage v_0 . The

acceleration thus results in a voltage output directly proportional to the magnitude of the acceleration A_N normal to the proof mass. The magnitude of the secondary transfer function is dependent upon the device geometry and the sensing circuitry used.

The total capacitance C_T determining the oscillator frequency is comprised of parasitic capacitance C_p , an acceleration dependent capacitance C_M arising from the membrane, and the capacitance between the conductive lower portion of the proof mass and the recessed Al plate, C_A , which is the principal acceleration dependent capacitance. It is easily shown for small proof mass displacements that the full acceleration capacitance C_T can be written in terms of the proof mass displacement Y_A

$$C_T(Y_A) = C_0 \left[1 - \frac{C_1}{C_0} (Y_A/d) \right] \quad (6)$$

where C_0 is the total capacitance under conditions of zero acceleration. The effects of parasitic capacitance are included in Eq. (5) and act to diminish the device sensitivity, i.e., to reduce C_1/C_0 , and the device sensitivity. For the prototype device under discussion here

$$\begin{aligned} C_0 &\approx 32.6 \text{ pf} \\ \text{and} \\ C_1 &\approx 13.3 \text{ pf} \end{aligned} \quad (7)$$

resulting in an acceleration dependent capacitance of

$$C_T = 32.6 [1 - 5.48 \times 10^{-6} Y_A] \text{ pf} \quad (8)$$

(The acceleration induced proof mass displacement Y_A is in Angstroms.)

The specific transfer function of interest depends on the electrical output parameter of interest, whether it be capacitance, frequency or voltage. For output voltage $V_0(t)$, voltage is of interest, then

$$T_{VA}(f) = T_{vf}(C_T) T_{fc}(Y) \times T_{CY}(Y) \times T_{YA}(A_N) \quad (9)$$

where A_N is the normal component of acceleration, T_{vf} represents the conversion of frequency to voltage, T_{fc} represents conversion of capacitance to shift to frequency shift, T_{CY} represents conversion of proof mass displacement to capacitance and T_{YA} represents conversion of acceleration to proof mass displacement. These transfer functions in general are frequency dependent. For the present prototype device operating at low frequencies (well below resonance), and for the sensing electronics used, the transfer function from acceleration to voltage T_{VA} was

$$T_{VA} = 2.07 \times 10^{-2} \text{ volts/M/sec}^2 \quad (10)$$

If frequency is the electrical output parameters of interest, the frequency transfer function for the present prototype device and electronics was

$$T_{AF} = 12.38 \text{ Hz/M/sec}^2 \quad (11)$$

High Frequency Behavior and the Effects of Air Loading

To gauge the effects of air loading on device's frequency dependence, a series of tests using oscillating and transient accelerations over a wide range of frequencies were performed at pressures ranging from $1.01 \times 10^5 \text{ Nt/M}$ (1 atm pressure) down to

$2 \times 10^3 \text{ Nt/M}^2$ (about 0.02 atm pressure). The AC accelerometer tests as a function of air loading were performed using a shaker table, a reference piezoelectric accelerometer, a pressure controlled chamber, a spectrum analyzer and various oscillator and pulsed driving sources. Oscillatory accelerations up to 3 G's were used. Pulsed acceleration has frequency components of magnitudes up to approximately 0.1 G.

AC device performance was evaluated using three different types of measurements: static acceleration (gravity); AC acceleration and transient acceleration. These measurements were used to experimentally evaluate the mechanical model constants K_T and R_m (R_m models air loading losses and will be reported elsewhere) of the primary transducer. Air loading was investigated by measuring the accelerator transfer functions as a function of ambient air pressure from 0.02 atm to 1.0 atm.

Using the results of static measurements, the proof mass displacement at 1 G was determined to be

$$Y_g = 229 \text{ \AA} \pm 18 \text{ \AA} \quad (12)$$

which yields an experimental value for the stiffness constant

$$K_T = 2310 \text{ N/M} \quad (13)$$

This is approximately a factor of five greater than calculated from theory. The discrepancy is attributed to the stiffening effects of Boron doping of the support membrane.

The second class of experiments measured the oscillator transfer function $T_{YA}(f)$ over a 10 KHz frequency range. These experiments were run at pressures ranging from one atmosphere ($101 \times 10^3 \text{ N/M}^2$) down to 0.02 atmospheres ($2 \times 10^3 \text{ Nt/M}^2$). $T_{vf}(f)$ was used to calculate silicon accelerometer's primary transfer function $T_{YA}(f)$ and the mechanical constants of the mass loaded spring with air loading. Air loading on the device was characterized in terms of the effect on the stiffness K_T and the mechanical resistance R_m .

The results of the extensive wave form and static analysis yielded

$$T_{YA} = (2.33 \pm 0.18) \times 10^{-9} \text{ M/M/sec}^2 \quad (14)$$

A separate value of K_T without air loading was inferred from the low frequency AC experiments to be

$$K_T = 2318 \pm 180 \text{ Nt/M} \quad (15)$$

which is in good agreement with Eq. (13). The related low frequency transfer function (without air loading) is

$$\begin{aligned} T_{TA}(f_L) \Big|_{NL} &\approx 2.3 \times 10^{-9} \text{ M/M/sec}^2 \\ &\approx 23 \text{ \AA/M/sec}^2 \end{aligned} \quad (16)$$

In the presence of air at 0.02 atm, we found the air loaded transfer function to be

$$T_{YA}(f_L) \approx 12 \text{ \AA/M/sec}^2 \quad (17)$$

and at 1 atm,

$$T_{YA}(f_L) \approx 0.62 \text{ \AA/M/sec}^2 \quad (18)$$

(Here f_L indicate low frequencies, i.e., frequencies well below resonance). Clearly air loading seriously affects device sensitivity.

The secondary transfer function was found to be

$$T_{yy}(f_L) \approx 0.2 \text{ mV/A} \quad (19)$$

The transfer functions for converting acceleration to voltage was

$$T_{VA}(f_L) \Big|_{NL} \approx 4.6 \text{ mV/M/sec}^2, \quad (20)$$

$$T_{VA}(f_L) \Big|_{0.02 \text{ atm}} \approx 2.4 \text{ mV/M/sec}^2. \quad (21)$$

and

$$T_{VA}(f_L) \Big|_{1 \text{ atm}} \approx 0.1 \text{ mV/M/sec}^2. \quad (22)$$

The silicon accelerometer's undamped resonant frequency is also strongly dependent upon air loading due to the effects of air compressibility. The dependence of the stiffness K_T on air pressure P_0 (Nt/M²) was established to be

$$K_T = 2310 + 2.11 P_0 \quad \text{Nt/M} \quad (23)$$

resulting in mechanical resonant frequencies of

$$f_0 \Big|_{NL} = 3.29 \text{ KHz} \quad (24)$$

and

$$f_0 \Big|_{1 \text{ atm}} \approx 31.8 \text{ KHz} \quad (25)$$

Figure 2 illustrates the effects of air loading on device sensitivity up to about 0.3 atm. Above 0.3 atm, the spectrum analyzer signal was too weak to yield reliable data due to suppressed device sensitivity. It should be noted that this study in no way attempted to maximize the device sensitivity, i.e., to maximize the values of transfer functions, but instead concerned itself in characterizing the frequency

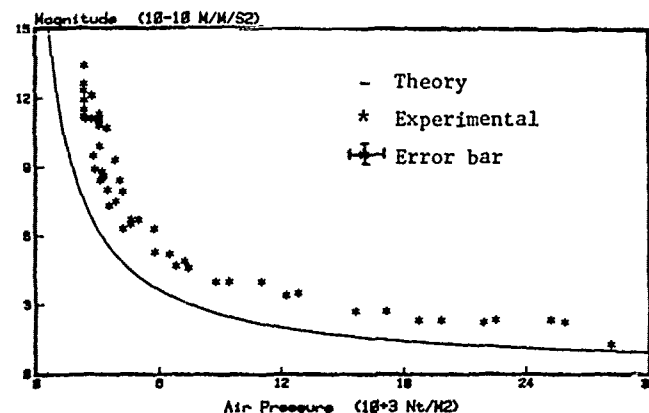


Fig. 2 Theoretical Transfer Function and Measured Primary Transfer Function

dependence of device performance as affected by air loading. Performance sensitivity could easily increase by four orders of magnitude or more by appropriate design of oscillator and voltage converter, and by modifying the well depth and device area which was 7.5 μM in the present case.

Acknowledgment

The authors wish to acknowledge the assistance of Hawaii Institute of Geophysics personnel.

References

- [1] K.E. Peterson, et al., ED 29, 23 (1982).
- [2] P.L. Chen, R.S. Muller, et al., ED 29, 27 (1982).
- [3] F. Rudolf, Sensors and Actuators 4, 191 (1983).
- [4] L.M. Raylance and J.B. Angell, ED 2, 1911 (1979).

SIMULATION OF DIAPHRAGM-TYPE IC PRESSURE SENSORS

H. REIMANN and Y. FATHI

SENSYM INCORPORATED, 1255 REAMWOOD AVENUE,
SUNNYVALE, CA 94089

ABSTRACT

THIS PAPER REPORTS ON SENSITIVITY CALCULATIONS OF MONOLITHIC, PIEZORESISTIVE PRESSURE SENSOR CHIPS. THE STRESS ANALYSIS IS BASED ON A SERIES EXPANSION FOR THE DEFLECTION OF A CLAMPED THIN PLATE. WE HAVE DETERMINED THESE COEFFICIENTS WITH A LEAST-SQUARE FIT TO THE RESULTS OF A FINITE ELEMENT ANALYSIS. BOTH SQUARE AND RECTANGULAR DIAPHRAGMS ARE MODELED FOR MATERIALS WITH ANISOTROPIC ELASTIC AND PIEZORESISTIVE PROPERTIES. AVERAGING IS PERFORMED OVER THE AREA OF EXTENDED PIEZORESISTORS. EXPERIMENTAL RESULTS ARE PRESENTED FOR BRIDGE- AND SHEAR- ELEMENTS. THE AGREEMENT BETWEEN MEASUREMENT AND SIMULATION IS EXCELLENT.

INTRODUCTION

MONOLITHIC SILICON PRESSURE SENSOR CHIPS WITH PIEZORESISTIVE SENSING ELEMENTS ON A MICROMACHINED DIAPHRAGM ARE COMMERCIALY AVAILABLE FROM MANY MANUFACTURERS. NEW DEVELOPMENTS ARE IN PROGRESS TO MEET THE REQUIREMENTS OF SMALL SIZE (CATHETER TIP), HIGH SENSITIVITY (0.1 PSI PRESSURE RANGE), OR THE INTEGRATION OF COMPENSATION CIRCUITRY.

COMPUTER AIDED DESIGN IS REPLACING THE TIME CONSUMING EVALUATION OF NEW CHIPS THROUGH THE PROCESSING OF PROTOTYPES. SENSOR SIMULATION ALLOWS THE DESIGNER TO CONSIDER DIFFERENT LAYOUTS, USE THE RESULTS IN AN INTERACTIVE WAY TO OPTIMIZE THE DESIGN AND TO TEST THE STABILITY OF THE DESIGN WITH REGARD TO FABRICATION TOLERANCES.

THE CALCULATION OF THE SENSITIVITY OF A PIEZORESISTIVE PRESSURE SENSOR IS PERFORMED IN THREE STEPS:

1. STRESS CALCULATION. GIVEN THE GEOMETRY OF THE STRUCTURE, THE ELASTIC PROPERTIES OF THE MATERIAL AND THE APPLIED PRESSURE DIFFERENCE, THE STRESS DISTRIBUTION IN THE DIAPHRAGM IS CALCULATED.
2. PIEZORESISTIVE TRANSDUCTION MECHANISM. THE RESISTIVITY OF THE MATERIAL CHANGES AS A FUNCTION OF THE STRESS COMPONENTS.
3. SENSOR RESPONSE: THE RESISTIVITY CHANGES ARE TRANSLATED INTO THE OUTPUT VOLTAGE OF THE SENSING ELEMENT.

IN THIS PAPER, PRESSURE SENSORS MANUFACTURED BY ANISOTROPIC ETCHING OF (100)-SILICON ARE CONSIDERED. THE ETCHSTOP ON (111)-PLANES LEADS TO RECTANGULAR DIAPHRAGMS CONSTRAINED BY A RIGID FRAME. FIGURE 1 SHOWS THE GEOMETRY AND INTRODUCES THE COORDINATE SYSTEM. THE BASIC ASSUMPTIONS OF THE MODEL ARE:

1. DIAPHRAGM: THIN PLATE OF DIMENSIONS $L \times W \times H$, EDGES IDEALLY CLAMPED, BOUNDARY NONLINEARITIES NEGLECTED.

2. SMALL DISPLACEMENTS: ONLY LATERAL FORCES CONSIDERED, GEOMETRIC NONLINEARITIES NEGLECTED.
3. ANISOTROPIC MATERIAL CONSTANTS OF SILICON.
4. ETCHSTOP ON (111)-PLANES: FOR A WAFER THICKNESS T , MASK LENGTH M , AND DIAPHRAGM THICKNESS H , THE LENGTH OF THE DIAPHRAGM IS

$$L = M - \sqrt{2} (T - H) \quad (1)$$

GIVEN THE DEFLECTION OF THE DIAPHRAGM, KINEMATICS DETERMINES STRAIN AND STRESS COMPONENTS. UNFORTUNATELY, AN ANALYTICAL SOLUTION EXISTS FOR CIRCULAR PLATES ONLY. FOR RECTANGULAR PLATES VARIATIONAL METHODS USING A SERIES EXPANSION FOR THE DEFLECTION [1], OR NUMERICAL INTEGRATION USING FINITE DIFFERENCES MUST BE USED [5].

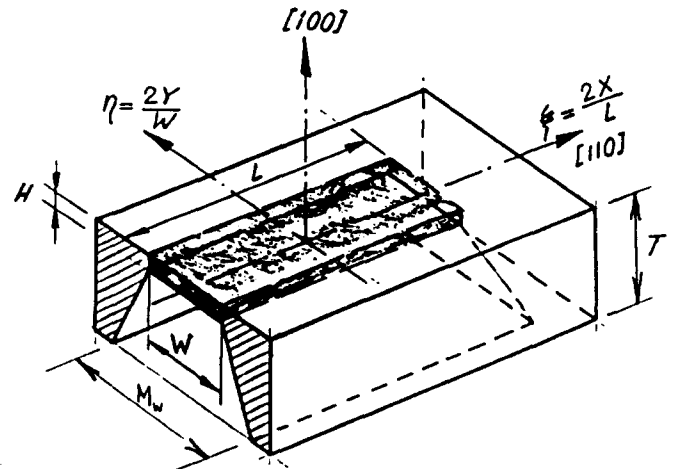


FIG. 1: PRESSURE SENSOR CHIP MICROMACHINED IN (100)-SILICON.

STRESS ANALYSIS

STARTING POINT FOR THE ANALYSIS IS AN EXPRESSION FOR THE DEFLECTION $w(\xi, \eta)$ OF THE DIAPHRAGM. THIS FUNCTION IS WRITTEN AS A SUPERPOSITION OF BASE FUNCTIONS ϕ WHICH HAVE PROPER SYMMETRY AND BOUNDARY CONDITIONS. THE COEFFICIENTS OF THE SERIES EXPANSION ARE DETERMINED BY THE MINIMUM OF THE POTENTIAL ENERGY (RITZ-GALERKIN METHOD). TIMOSHENKO [1] HAS WORKED OUT THE PROBLEM WITH 4 BASE FUNCTIONS,

$$\phi_1 = (1 - \eta^2) \cos^2 \xi, \quad \phi_2 = \eta^2 \cos^2 \xi, \quad \phi_3 = \xi^2 \cos^2 \eta, \quad \phi_4 = \xi^2 \eta^2 \cos^2 \xi \quad (2)$$

AND HAS PRESENTED THE SOLUTION FOR THE SQUARE PLATE WITH ISOTROPIC ELASTIC CONSTANTS.

IN THIS WORK, THE SAME SERIES EXPANSION IS USED FOR THE RECTANGULAR PLATE. THE EXPRESSION FOR THE DEFLECTION IS

$$w(\xi, \eta) = w(0, 0) * F(\xi, \eta) \quad (3)$$

$$F(\xi, \eta) = (\eta^2 - 1) \cos^2 \xi \left[1 + c_1 \eta^2 + c_2 \xi^2 + c_3 \eta^2 \xi^2 \right]$$

WHERE $W(0,0) = C_0 W^4 P/D$ IS THE DEFLECTION AT THE CENTER OF THE PLATE, F IS A NORMALIZED FUNCTION FOR THE DEFLECTION, P IS THE PRESSURE DIFFERENCE ACROSS THE PLATE, AND $D = E' h^3 / (12(1-\nu'^2))$ IS THE FLEXURAL RIGIDITY. THE GEOMETRY IS DEFINED IN FIGURE 1. THE 4 COEFFICIENTS $C_0 \dots C_3$ ARE DETERMINED BY A LEAST-SQUARE FIT TO THE RESULTS OF AN INDEPENDENT FINITE ELEMENT ANALYSIS (FEA).

'ABAQUS' [2] WAS USED AS THE FINITE ELEMENT CODE. ONE-FORTH OF THE PLATE WAS MODELED WITH A MESH OF 4×4 AND 10×10 SECOND ORDER SHELL ELEMENTS. THIS ANALYSIS WAS PERFORMED FOR A SERIES OF PLATES WITH ASPECT RATIOS BETWEEN 1 AND 4. FOR EACH ASPECT RATIO THE DEFLECTION WAS FITTED WITH EQUATION (3), AND THE RESULTING DEFLECTION COEFFICIENTS WERE AGAIN FITTED WITH CUBIC SPLINES TO DETERMINE THE GENERAL DEPENDENCE ON THE ASPECT RATIO. FIGURE 2 SHOWS THE RESULTS, AND THE FOLLOWING TABLE GIVES SELECTED VALUES FOR THE SQUARE AND ONE RECTANGULAR PLATE.

	L/W	C_0	C_1	C_2	C_3
TIMOSHENKO	1	$1.264E-3$	0.2645	0.2645	0.309
FEA (S_1)	1	$1.38E-3$	0.219	0.219	0.320
FEA (S_1)	2	$2.64E-3$	1.444	0.0223	0.338

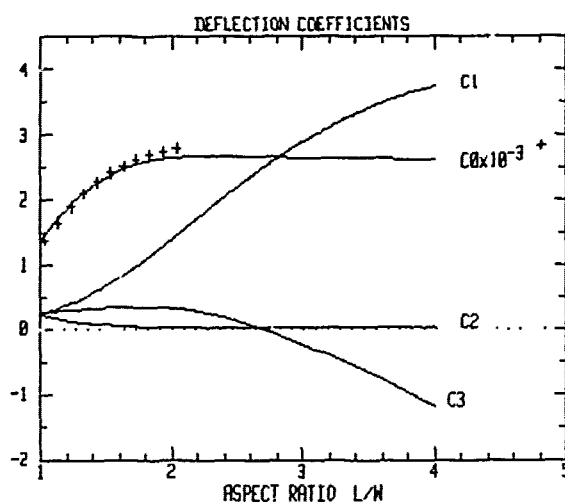


FIG 2. DEFLECTION COEFFICIENTS FOR A RECTANGULAR PLATE. DATA POINTS ARE TAKEN FROM TABLE 35 OF REFERENCE [1].

KINEMATICS DETERMINES THE STRAIN COMPONENTS ϵ_x AS SECOND DERIVATIVES OF THE DEFLECTION AND THE STRESS COMPONENTS σ_x AS LINEAR COMBINATIONS OF THE STRAIN COMPONENTS.

THE EFFECTIVE ELASTIC MODULI FOR THE COORDINATE SYSTEM OF FIGURE 1 ARE $E_{xx}' = 1.70$, $E_{xy}' = 0.107$, YOUNG'S MODULUS $E' = 1.67$ (ALL IN UNITS OF 10^{12} DYN/CM²), AND POISSON RATIO $\nu' = 0.063$ [4].

THE RESULTS ARE WRITTEN AS THE PRODUCT OF AN AMPLITUDE FACTOR AND TWO NORMALIZED FUNCTIONS F_{xx} AND F_{yy} DESCRIBING THE STRAIN DISTRIBUTION ACROSS THE PLATE.

$$\begin{aligned} \epsilon_x(\xi, \eta) &= A * (F_{xx} + \nu' * F_{yy}) \\ \epsilon_y(\xi, \eta) &= A * (\nu' * F_{xx} + F_{yy}) \end{aligned} \quad (4)$$

WITH $A = 48 * C_0 * f(z') * P * (W/H)^2$,

$$\begin{aligned} F_{xx}(\xi, \eta) &= \alpha^2 (\eta^2 - 1)^2 \{ [C_2 - 2] + \eta^2 [C_3 - 2C_1] + \\ &\quad + 6\xi^2 [(1 - 2C_1) + \eta^2 (C_1 - 2C_3)] + 15\xi^4 [C_2 + \eta^2 - C_3] \} \\ F_{yy}(\xi, \eta) &= (\xi^2 - 1)^2 \{ [C_1 - 2] + \xi^2 [C_3 - 2C_2] + \\ &\quad + 6\eta^2 [(1 - 2C_2) + \xi^2 (C_2 - 2C_3)] + 15\eta^4 [C_1 + \xi^2 - C_3] \} \end{aligned} \quad (5)$$

$f(z') = 1 - (2 * z' / H)$ DESCRIBES THE LINEAR DECREASE FROM THE SURFACE ($z' = 0$) TO THE NEUTRAL PLANE, AND $a = L/W$ IS THE ASPECT RATIO OF THE PLATE.

THE SHEAR STRESS IS NEEDED FOR THE COORDINATE SYSTEM WITH (100)-AXES. THIS INVOLVES A ROTATION OF 45 DEGREES AND LEADS TO THE RESULT. $\sigma_s = (\sigma_x - \sigma_y) / 2$.

FIGURES 3 AND 4 ILLUSTRATE THE NORMALIZED STRESS DISTRIBUTIONS FOR A SQUARE AND A RECTANGULAR PLATE WITH ASPECT RATIO 2.

PIEZORESISTANCE AND SENSOR RESPONSE

THE PIEZORESISTIVE TENSOR (Π) RELATES THE STRESS COMPONENTS TO ANISOTROPIC CHANGES OF THE RESISTIVITY. FOR THE PLANAR PROBLEM OF THE THIN DIAPHRAGM, THERE ARE THREE LATERAL STRESS COMPONENTS AND THREE BASIC 'SHEET RESISTORS'. R_x , A 2-POINT RESISTOR WITH CURRENT IN THE X-DIRECTION; R_y , A 2-POINT RESISTOR ALIGNED TO THE Y-DIRECTION; AND R_{xy} , A 4-POINT RESISTOR WITH CURRENT IN THE X-DIRECTION AND AN ELECTRICAL FIELD RESPONSE IN THE Y-DIRECTION. r IS USED FOR THE STRESS INDUCED RELATIVE CHANGE OF RESISTANCE.

FOR THE ORIENTATIONS OF PRACTICAL IMPORTANCE, THE PIEZORESISTIVE TENSOR HAS THE FORM.

$$\begin{pmatrix} \Pi_{xx} & \Pi_{xy} & 0 \\ \Pi_{xy} & \Pi_{yy} & 0 \\ 0 & 0 & \Pi_{zz} \end{pmatrix}$$

THIS DETERMINES THE TWO PIEZORESISTORS IMPLEMENTED IN THE SIMULATION PROGRAM

1. THE 2-POINT RESISTOR ALIGNED PARALLEL TO ONE OF THE EDGES OF THE DIAPHRAGM.

$$\begin{aligned} R_x &= \Pi_{xx} \sigma_x + \Pi_{xy} \sigma_y & R_y &= \Pi_{yy} \sigma_y + \Pi_{xy} \sigma_x \\ \Pi_{xx} &= \frac{1}{2} (\Pi_{11} + \Pi_{22}) & \Pi_{yy} &= \frac{1}{2} (\Pi_{11} - \Pi_{22}) \end{aligned} \quad (6)$$

2. THE 4-POINT RESISTOR [7] ALIGNED AT AN ANGLE OF 45 DEGREES TOWARDS THE EDGE OF THE DIAPHRAGM.

$$\begin{aligned} R_{xy} &= \Pi_{12} \sigma_s \\ \Pi_{12} &= \Pi_{xy} & \sigma_s &= \frac{1}{2} (\sigma_x - \sigma_y) \end{aligned} \quad (7)$$

THE 'VALUES OF THE PIEZORESISTIVE COEFFICIENTS DEPEND ON THE PEAK CONCENTRATION OF THE RESISTOR DOPING PROFILE. THE FOLLOWING VALUES ARE CONSISTENT WITH PUBLISHED DATA [3] FOR P-TYPE SILICON (UNITS 10^{-12} CM²/DYN)

$$\begin{aligned} \Pi_{11} &= 96.5 (1 - 0.202 \log(N/1E18)) \\ \Pi_{12} &= 2.46 (1 - 0.226 \log(N/1E18)) \\ \Pi_{22} &= -0.46 (1 - 0.268 \log(N/1E18)) \end{aligned}$$

IN THE SIMULATION PROGRAM, MEANDER-LIKE RESISTORS CAN BE LAYED OUT ON THE DIAPHRAGM THE GEOMETRY IS BROKEN DOWN INTO SQUARES (IF

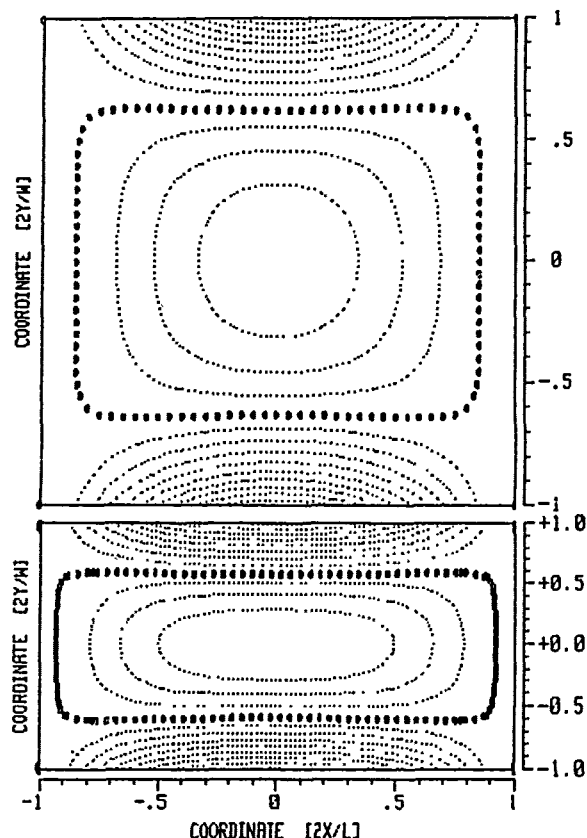


FIG. 3. CONTOUR PLOT FOR THE STRESS COMPONENT G_x FOR A SQUARE AND A RECTANGULAR PLATE WITH ASPECT RATIO 2. STEP INCREMENT=0.5.

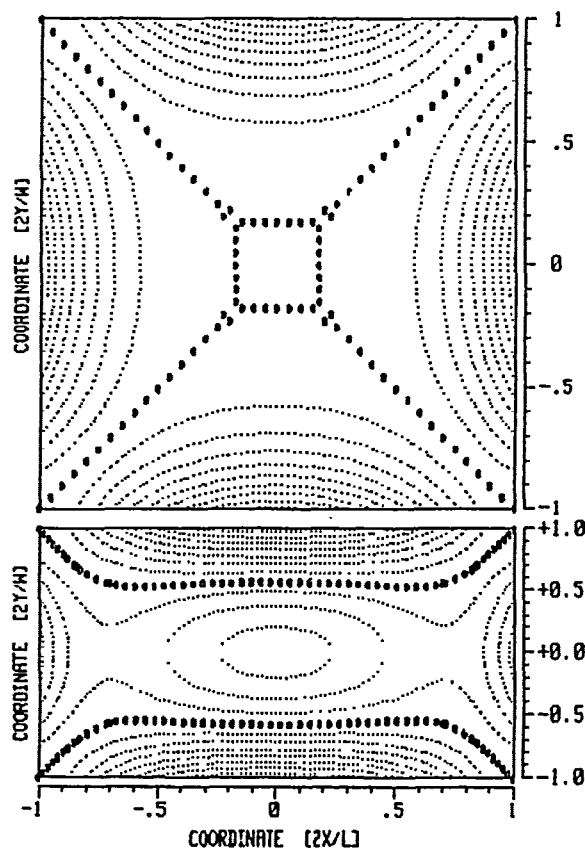


FIG. 4. CONTOUR PLOT FOR THE SHEAR STRESS G_s ([100]-AXES) FOR A SQUARE AND A RECTANGULAR PLATE. STEP INCREMENT=0.25.

THE LINEWIDTH, AND THE STRESS COMPONENTS ARE AVERAGED OVER THE NUMBER OF THE SQUARES.

AS THE LAST STEP, INDIVIDUAL RESISTORS ARE COMBINED TO A SENSING ELEMENT, AND THE OUTPUT VOLTAGE IS CALCULATED. TWO STRUCTURES OFFER A DIFFERENTIAL OUTPUT VOLTAGE V_{OUT} , RATIO-METRIC TO THE SUPPLY VOLTAGE V_{IN} .

1. WHEATSTONE BRIDGE OF FOUR 2-POINT RESISTORS:

$$V_{OUT}/V_{IN} \approx (r_1 - r_2 + r_3 - r_4) / 4 \quad (7)$$

2. SHEAR ELEMENT = 4-POINT RESISTOR.

$$V_{OUT}/V_{IN} = K_0 * r_{xz} \quad (8)$$

THE CONSTANT K_0 DEPENDS ON THE GEOMETRY OF THE ELEMENT. FOR A RECTANGULAR ELEMENT WITH DIMENSIONS $L \times W$ AND A HOMOGENEOUS CURRENT DISTRIBUTION: $K_0 = W/L$.

THE TRANSFER FUNCTION $V_{OUT}/V_{IN} = S * P$ DEFINES THE SENSITIVITY S OF THE DEVICE.

RESULTS

FOR A GIVEN RESISTOR LAYOUT, WAFER THICKNESS AND CAVITY MASK, THE CONTROL OF THE DIAPHRAGM THICKNESS LEADS TO A SERIES OF CHIPS WITH DIFFERENT PRESSURE RANGES. THE FINAL RESULT OF THE SENSOR SIMULATION IS A CALCULATED CURVE FOR THE SENSITIVITY AS A FUNCTION OF THE DIAPHRAGM THICKNESS. THIS CALCULATION TAKES THE GEOMETRY OF THE MICROMACHINED STRUCTURE, LOOKS UP THE DEFLECTION COEFFICIENTS FOR THE GIVEN ASPECT RATIO, CALCULATES THE STRESS DISTRIBUTION, AVERAGES OVER THE RESISTOR LAYOUT, LOOKS UP THE PIEZORESISTIVE COEFFICIENTS AND CALCULATES THE SENSITIVITY. AT THIS POINT, THE RESPONSE CAN BE FITTED TO MEASURED DATA POINTS BY ADJUSTING A SCALE FACTOR. NOTICE, THAT THERE ARE NO OTHER ADJUSTABLE PARAMETERS IN THE MODEL.

FIGURE 5 SHOWS A COMPARISON OF CALCULATED AND MEASURED DATA. THE DATA POINTS ARE AVERAGES OF A SERIES OF 10 DEVICES, POSITIONED AT THE SPECIFIED DIAPHRAGM THICKNESS. THE EXAMPLE IS FOR A WHEATSTONE BRIDGE ON A SQUARE DIAPHRAGM. THE INSERT SHOWS THE RESISTOR LAYOUT. THE SAME KIND OF COMPARISON WAS PERFORMED FOR A SHEAR ELEMENT ON A SQUARE DIAPHRAGM AND A WHEATSTONE BRIDGE ON A RECTANGULAR DIAPHRAGM. IN EACH CASE, SIMULATION AND MEASUREMENT AGREE WITHIN 10 % (SCALE FACTORS BETWEEN 0.9 AND 1.1).

DISCUSSION

THE 'TIMOSHENKO-FORMULA' HAS BEEN USED BY MANY GROUPS FOR STRESS CALCULATIONS OF THE SQUARE DIAPHRAGM. ITS PSEUDO-ANALYTICAL APPROACH OFFERS A FAST AND CONVENIENT SOLUTION FOR A DESKTOP COMPUTER. COMBINING IT WITH THE FINITE ELEMENT METHOD, MAKES THE APPROACH ACCESSIBLE TO ANISOTROPIC MATERIALS, RECTANGULAR DIAPHRAGMS, AND WITH PROPER MODIFICATIONS, TO NONLINEAR CORRECTIONS DUE TO LARGE DEFLECTIONS AND BOUNDARY CONDITIONS.

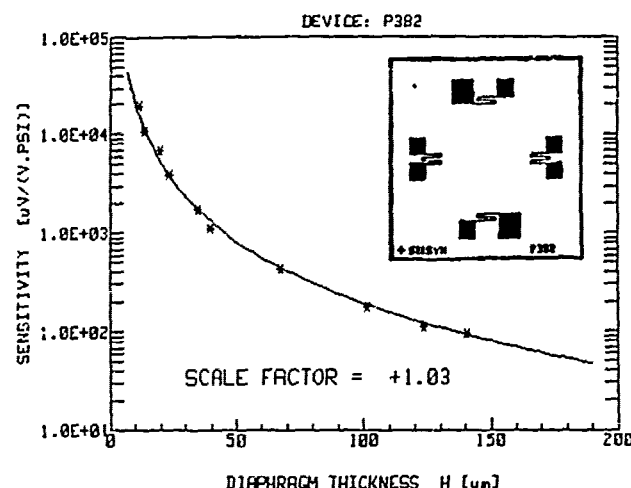


FIG. 5. COMPARISON OF MEASUREMENT AND SIMULATION FOR A SERIES OF PRESSURE SENSOR CHIPS

TYPICAL AGREEMENT BETWEEN THE ORIGINAL FINITE ELEMENT ANALYSIS AND THE VALUES CALCULATED WITH THE FITTED SERIES EXPANSION IS WITHIN 1% FOR THE STRESS ALONG THE Y-AXIS, BUT REACHES 10% FOR VALUES ALONG THE LENGTH OF THE RECTANGULAR DIAPHRAGM. MINOR STRAIN COMPONENTS CAN BE OFF BY A FACTOR OF 2. GOING FROM 4x4 TO 10x10 ELEMENTS IN THE FEA CHANGES THE COEFFICIENTS BY A FEW PERCENT. THE AGREEMENT BETWEEN MEASURED AND CALCULATED SENSITIVITIES IS TYPICALLY WITHIN 10 PERCENT. THE MAJOR UNCERTAINTY IS THE EXACT THICKNESS OF THE DIAPHRAGM.

THE INHERENT STRENGTH OF A SIMULATION PROGRAM IS ITS INTERACTIVE USE IN THE DESIGN AND DATA ANALYSIS PROCESS. ONLY A FEW EXAMPLES CAN BE PRESENTED HERE.

(A) FIGURE 6 SHOWS THE TRANSITION FROM A SQUARE TO A RECTANGULAR DIAPHRAGM FOR A GIVEN RESISTOR LAYOUT (SEE INSERT) AND CONSTANT DIAPHRAGM WIDTH. THE SENSITIVITY INCREASES DUE TO THE CONTRIBUTION OF THE CENTER RESISTORS; IT LEVELS OFF WHEN THE STRESS DISTRIBUTION APPROACHES THAT OF A BRIDGE-LIKE STRUCTURE ACROSS THE WIDTH OF THE DIAPHRAGM.

(B) MANUFACTURING VARIATIONS DUE TO CHANGES IN WAFER THICKNESS, FINITE ETCH RATE IN THE [111]-DIRECTION, MASK REGISTRATION, ETC. CAN BE SIMULATED. A POINT-LIKE SHEAR ELEMENT NEAR THE EDGE OF THE DIAPHRAGM IS MOST SENSITIVE, WHILE A DESIGN LIKE THE ONE IN FIGURE 6 REJECTS MANY OF THESE VARIATIONS.

(C) THE NONLINEARITY IN THE PRESSURE RESPONSE HAS ITS CAUSE IN 3 CONTRIBUTIONS: SECOND ORDER PIEZORESISTIVE COEFFICIENTS [8], MEMBRANE STRESS (LARGE DEFLECTIONS) [8], AND NONLINEAR BOUNDARY CONDITIONS REFLECTING THE ASYMMETRY OF THE MICROMACHINED STRUCTURE. THE DEVICE IN FIGURE 5 HAS A MEASURED PRESSURE NONLINEARITY OF LESS THAN 0.1 PERCENT (GAGE AND BACKGAGE) FOR ANY DIAPHRAGM THICKNESS BETWEEN 35 AND 150 MICRON AND A DESIGN RULE OF 20 mV/V FULL SCALE OUTPUT. AT 35 MICRON THE DEFLECTION AMOUNTS TO 8.5% OF THE DIAPHRAGM THICKNESS, AND THE MAXIMUM STRAIN IS 40 PPM. AT 15 MICRON AND A REDUCED OUTPUT OF 10 mV/V, THE DEFLECTION IS 6.4 MICRON, THE STRAIN IS 210 PPM, AND THE MEASURED PRESSURE NONLINEARITY IS 0.2% IN THE GAGE CONFIGURATION, BUT ABOUT 2% IN THE BACKGAGE CONFIGURATION.

QUADRATIC PIEZORESISTIVE COEFFICIENTS HAVE BEEN IMPLEMENTED IN THIS SIMULATION PROGRAM. THE ABOVE EXAMPLE DEMONSTRATES THE NEED TO DEAL WITH THE ASYMMETRY OF THE MICROMACHINED STRUCTURE. THE SERIES EXPANSION FITTED TO THE RESULTS OF A FINITE ELEMENT ANALYSIS HAS THE FLEXIBILITY TO IMPLEMENT THESE CORRECTIONS [6].

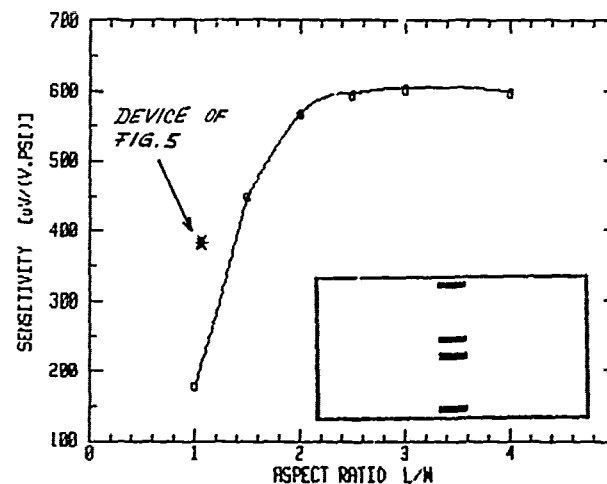


FIG. 6: SENSITIVITY vs. ASPECT RATIO FOR A GIVEN RESISTOR LAYOUT AND CONSTANT DIAPHRAGM WIDTH.

TO SUMMARIZE, THE PRESENTED METHOD ALLOWS THE TRANSFER OF RESULTS FROM THE MAINFRAME TO A SIMULATION PROGRAM IMPLEMENTED ON A PERSONAL COMPUTER. WE HAVE SIMULATED A WIDE VARIETY OF DIFFERENT CHIP DESIGNS AND FOUND EXCELLENT AGREEMENT WITH MEASURED SENSITIVITIES.

REFERENCES

- [1] S. TIMOSHENKO and S. WOINOWSKY-KRIEGER, THEORY OF PLATES AND SHELLS, NEW YORK, MCGRAW-HILL 1959, ch. 81, pp. 347-48
- [2] HIBBITT, KARLSSON and SORENSEN, INC., PROVIDENCE RI. 'ABAQUS', A FINITE ELEMENT CODE FOR STRUCTURAL ANALYSIS.
- [3] RESEARCH TRIANGLE INSTITUTE, TECHNICAL DOCUMENTARY REPORT No. ASD-TDR-63-316, Vol. 5, JULY 1964.
- [4] J.J. WORTMAN and R.A. EVANS, "YOUNG'S MODULUS, SHEAR MODULUS, AND POISSON RATIO IN SILICON AND GERMANIUM", J. APPL. PHYS. VOL. 36, pp. 153-156, JANUARY 1965.
- [5] K.W. LEE and K.D. WISE, "SENSIM: A SIMULATION PROGRAM FOR SOLID-STATE PRESSURE SENSORS", IEEE TRANSACTIONS ON ELECTRON DEVICES, Vol. ED-29, pp. 34-41, JAN. 1982.
- [6] S. SUZUKI and Y. YAGI, "OPTIMUM DESIGN OF SILICON PRESSURE SENSOR BY NONLINEAR FINITE ELEMENT METHOD", PROC. 2nd SENSOR SYMPOSIUM (JAPAN), 1982, pp. 163-165.
- [7] Y. KANDA, "OPTIMUM DESIGN CONSIDERATIONS FOR SILICON PRESSURE SENSORS USING A FOUR-TERMINAL GAUGE", SENSORS AND ACTUATORS, Vol. 4, pp. 199-206, OCTOBER 1983.
- [8] K. SUZUKI, T. ISHIHARA, M. HIRATA and H. TANIGAWA, "NONLINEAR ANALYSES ON CMOS INTEGRATED SILICON PRESSURE SENSOR", PROC. IEDM 1985, PAPER 5.8.

H. P. Baltes¹, W. Allegretto², A. Nathan¹, and Y. Sugiyama³

¹Department of Electrical Engineering / ²Department of Mathematics
The University of Alberta
Edmonton, Alberta, Canada T6G 2G7

³Electrotechnical Laboratory
1-1-4, Umezono, Sakura-Mura
Niihari, Ibaraki, Japan

Abstract: We present two-dimensional numerical solutions of carrier transport (comprising the electrostatic potential and current density) in semiconductor magnetic sensors in the presence of nonuniform, locally inverted induction $B_z(x, y)$. The variations in B and device geometries considered restrict the application of previous analytical methods. We illustrate our results by considering a split-drain device structure and studying its response for various induction configurations.

Introduction

A magnetic field sensor (MFS) is an input transducer that converts the magnetic field \vec{H} into a useful electronic signal. Semiconductor MFS exploit the galvanomagnetic effects (such as Hall voltage, carrier deflection, magnetoresistance, and magnetoconcentration), which arise from the action of the Lorentz force $\vec{F} = q(\vec{v} \times \vec{B})$ on moving charge carriers (electrons and holes). Here q denotes the elementary charge, \vec{v} the velocity of charge carrier and $\vec{B} = \mu_0 \vec{H}$ is the magnetic induction. The magnetic permeability μ_0 for semiconductors (Si, GaAs, InSb) is approximately 1. The magnitude of the sensor response is controlled by the product of the carrier Hall mobility and the magnetic induction B . Hence, high carrier mobility is crucial for achieving high sensitivity [1].

MFS detecting uniform fields are used in a variety of applications [1]. In the presence of nonuniform, locally inverted magnetic induction $B_z(x, y)$, an extended range of applications is also possible. Such nonuniform magnetic field configurations are crucial if semiconductor MFS are to be used for the detection of submicron displacements, vibrations, bubble domain velocities, magnetic ink patterns in banknotes and credit cards [2]. The variations in the device structures and $B_z(x, y)$ imply that standard analytical or related modeling methods are no longer applicable except in the limiting cases (see [2] and references therein).

In this paper, we present two-dimensional numerical solutions of the carrier transport (comprising the electrostatic potential and current density distributions) in semiconductor MFS, in the presence of nonuniform, locally inverted magnetic fields. This enables us to deal with general device geometries and induction configurations, not subject to the restrictions found in earlier work.

Model Equations

The action of the Lorentz force manifests itself in the carrier transport equations. We consider N-type Hall devices (bulk or linear MOSFET's) with the magnetic field $\vec{B} = (0, 0, B_z)$ perpendicular to the direction of current density and $B_z = B_z(x, y)$.

We assume that diffusion currents and temperature gradients are negligible. For not too large magnetic induction \vec{B} , the two-dimensional electron current density obeys the equation

$$\vec{j}_n(x, y) = -q n \vec{\nabla} \psi(x, y) + \mu_n^* [\vec{B} \times \vec{j}_n(x, y)] \quad (1)$$

where μ_n^* and μ_n denote the Hall and drift mobility of electrons, respectively, n the carrier concentration and $\psi(x, y)$ the two-dimensional electrostatic potential. Equation (1) comprises the *isothermal* galvanomagnetic effects for electrons, accounting for the direct effects of temperature on carrier concentration and mobility. But it does not include thermomagnetic or thermoelectric effects [1]. Equation (1) corresponds to the leading terms of a weak-field expansion and involves relative errors of $(\mu_n^* B)^2$ [3]. They provide a good approximation ($\mu_n^* B \leq 0.3$) for N-type bulk material; hence it can be used for $|\vec{B}| \leq 2T$ for Si, $|\vec{B}| \leq 600$ mT for GaAs and $|\vec{B}| \leq 40$ mT for InSb [1].

Assuming uniform mobilities, μ_n^* and μ_n and zero net recombination, the divergence of $\vec{j}_n(x, y)$ in (1) yields

$$\frac{\partial}{\partial x} [(1 + \tilde{s}^2)^{-1} (\frac{\partial \psi}{\partial x} + \tilde{s} \frac{\partial \psi}{\partial y})] + \frac{\partial}{\partial y} [(1 + \tilde{s}^2)^{-1} (-\tilde{s} \frac{\partial \psi}{\partial x} + \frac{\partial \psi}{\partial y})] = 0 \quad (2)$$

where $\tilde{s} = \mu_n^* B_z$. Note that \tilde{s} is x, y dependent because $B_z = B_z(x, y)$. The boundary conditions for ψ in (2) consist of a Dirichlet condition prescribed by the applied voltage, V_a at the electrodes (see Fig. 1). Everywhere else the standard condition, $\vec{j}_n \cdot \vec{n} = 0$ is adopted, where \vec{n} is the outward normal vector. Subject to the above conditions, equation (2) is then discretized on a triangularized domain (see Fig. 1) using a Galerkin finite element approximation, and the resulting matrix is solved by an adaptive Successive Over Relaxation (SOR) procedure [4].

Results and Discussion

Our results are illustrated by considering three material types of bulk Hall devices: Si, GaAs and InSb with their mobilities assumed to be 0.08 m²/Vs, 0.5 m²/Vs, and 7.1 m²/Vs respectively. We have also assumed that the free carriers are electrons with a concentration of 10¹⁷ cm⁻³. Split-drain device structures, $W = L = 100$ μ m, $d = 20$ μ m, are considered (see Fig. 1) with a locally inverted magnetic induction perpendicular to the device plane. As opposed to the conventional Hall plate structure illustrated in [4] where the Hall voltage is the computed signal, the

the split-drain device is biased with constant voltage sources and the relative current imbalance, $\delta = (I_1 - I_2) / (I_1 + I_2)$ is computed.

Equipotential and current lines are shown in Figs. 2 to 4 for different orientations of induction "inversion". For the device with a longitudinal strip domain (Fig. 2), we see that Hall effect prevails (current flow is parallel to the "inversion" boundaries and potential lines are skewed). In the case of the transverse strip domain (Fig. 3), the potential lines are parallel to the inversion boundaries and carrier deflection prevails (current lines are skewed by the local Hall angle). In the general case of the bubble domain (Fig. 4), the operating mechanisms of the device can be visualized neither in terms of Hall effect nor carrier deflection; these mechanisms are involved in a complex way on both sides of the inversion boundary. Similar to the results discussed in [4], at regions far away from the electrodes and inversion boundaries (e.g., in the device centre), equation (2) reduces to Laplace's equation and smooth divergence free electric fields are observed as predicted by analytical models [2]. The behavior of the fields become complicated at the vicinity of the electrodes and at the inversion boundaries.

Figure 5 shows the relative current imbalance as the bubble domain moves along the x-direction at two different positions in the device; $y = 75 \mu\text{m}$ (curve A) and $y = 50 \mu\text{m}$ (curve B). The values on the abscissa denote the distance between the centre of the domain and the centre of the device. The relative current imbalance behaves more or less linearly between $+10 \mu\text{m}$ and $+50 \mu\text{m}$ (Fig. 5). We note that for bubble positions remote from the drain vicinity, there is a reduction in δ as well as its gradient. With respect to spatial resolution, the optimum bubble position is at the vicinity of the drains. Previous theoretical calculations of the Hall output were performed only for the bubble located at the device centre. These calculations were based on an *ad hoc* weighted combination of the Hall outputs for the longitudinal and transverse cases [2].

Conclusion

In this paper, we have reported the two-dimensional numerical solutions of carrier transport in semiconductor magnetic field sensors under nonuniform, locally inverted magnetic fields. The effects of the device boundaries and "inversion" boundaries, on the electric field and current density, restricts simpler models solely based on Hall effect or carrier deflection, to very specific cases of device geometry and magnetic field.

References

- [1] H. P. Baltes and R. S. Popović, "Integrated semiconductor magnetic field sensors," *Proc. IEEE*, in press.
- [2] Y. Sugiyama, "Fundamental research on Hall effects in inhomogeneous magnetic fields," *Researches of the Electrotechnical Laboratory*, No. 838, Tokyo: Electrotechnical Laboratory, 1983.
- [3] O. Madelung, *Introduction to Solid-State Theory*, Berlin: Springer, 1978,
- [4] A. Nathan, W. Allegretto, H. P. Baltes, and Y. Sugiyama, "Modeling of Hall devices under locally inverted magnetic field," *IEEE Electron*

Device Lett., submitted.

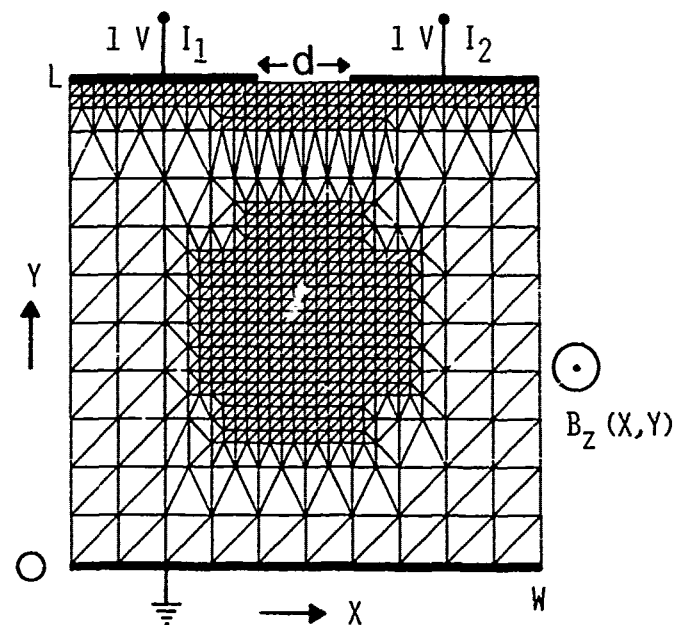


Fig. 1. Two-dimensional geometry of split-drain device with an adaptively generated finite element grid of 621 nodes and 1168 elements. This grid was employed in the simulation of device with bubble domain of radius $20 \mu\text{m}$, located in the centre of the device. The device is biased with voltage sources, $V_a = 1.0 \text{ V}$.

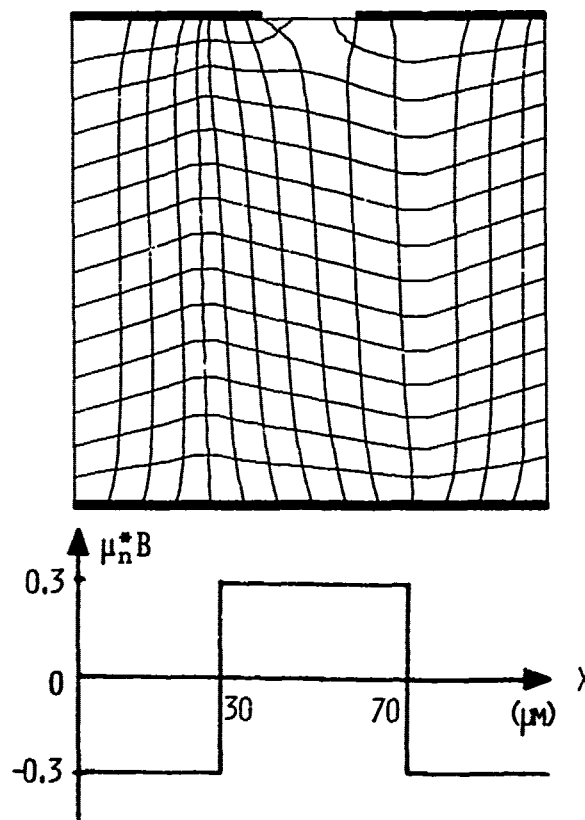


Fig. 2. Equipotential and current lines for device with longitudinal strip domain; $(\delta/B)_{\text{Si}} = -2.2\%/T$, $(\delta/B)_{\text{GaAs}} = -13.9\%/T$, $(\delta/B)_{\text{InSb}} = 0.20\%/mT$.

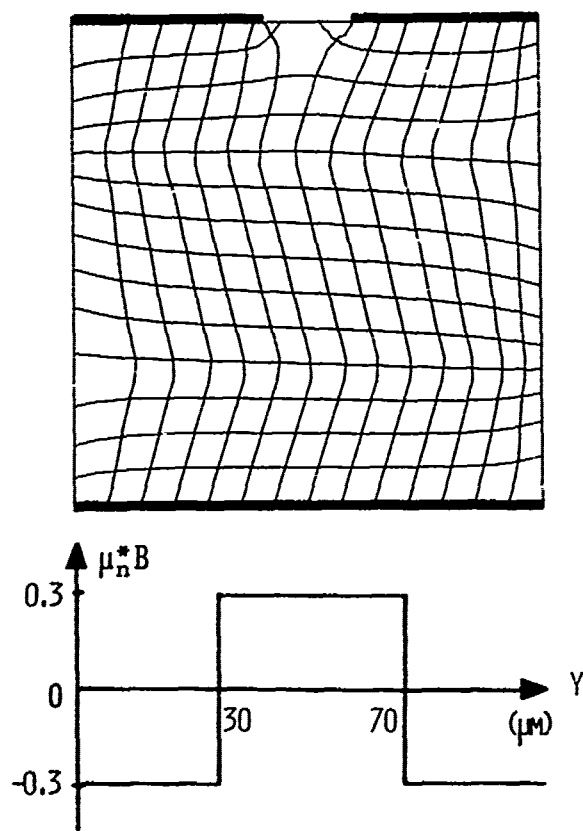


Fig. 3. Equipotential and current lines for device with transverse strip domain; $(\delta/B)_{Si} = -0.88\%/T$, $(\delta/B)_{GaAs} = -5.5\%/T$, $(\delta/B)_{InSb} = -0.08\%/T$.

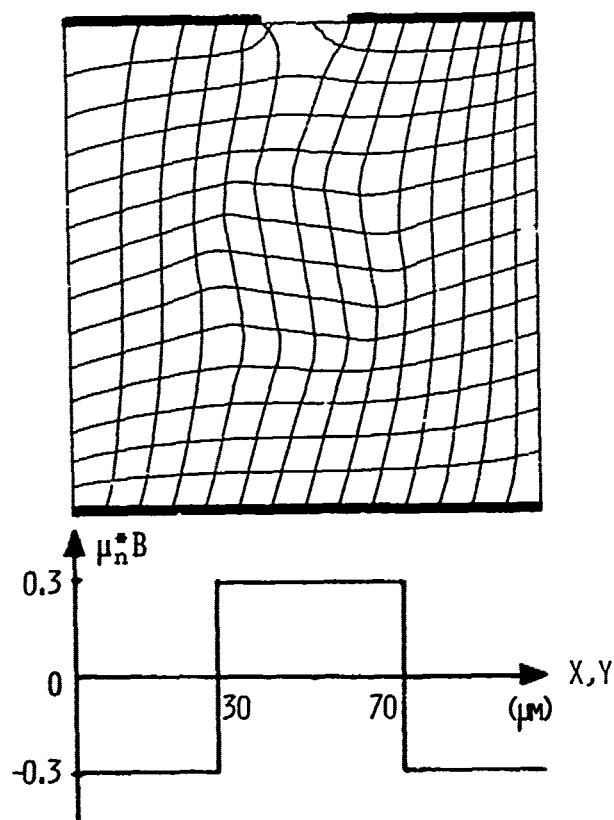


Fig. 4. Equipotential and current lines for device with bubble domain (Fig. 1); $(\delta/B)_{Si} = -3.0\%/T$, $(\delta/B)_{GaAs} = -18.9\%/T$, $(\delta/B)_{InSb} = -0.27\%/T$.

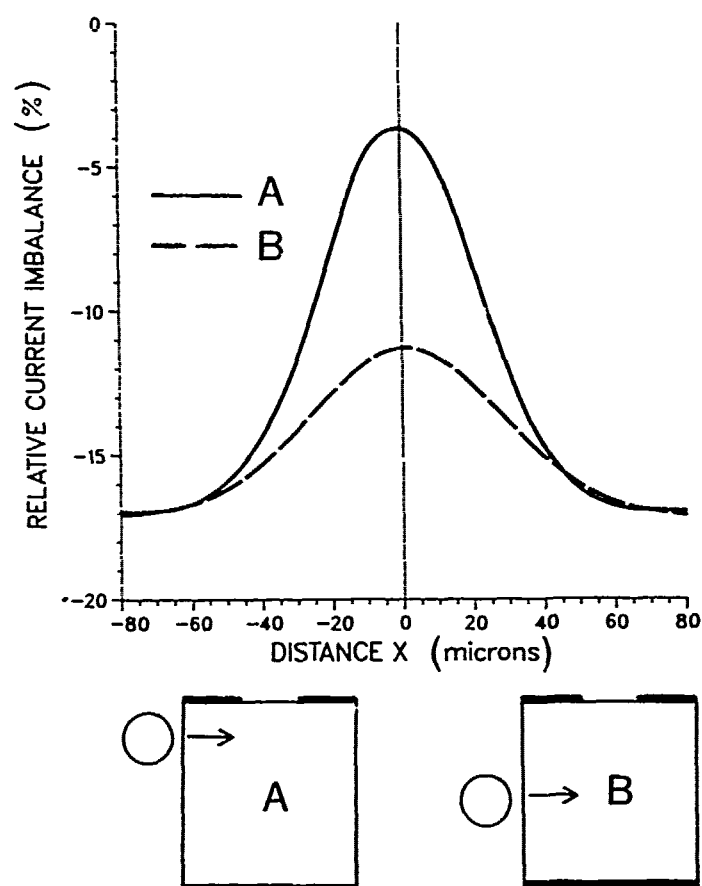


Fig. 5. The relative current imbalance, δ as a function of bubble domain location in device for; A: bubble centred at $Y = 75 \mu m$. B: bubble centred at $Y = 50 \mu m$.

MINIATURE RADIATION DOSIMETER FOR IN VIVO RADIATION MEASUREMENT

R. C. Hughes, D. Huffman, J. V. Snelling,
T. E. Ziporian, and A. J. Ricco

Sandia National Laboratories
P. O. Box 5800
Albuquerque, NM 87185

C. A. Kelsey
University of New Mexico
Cancer Research Center
Albuquerque, NM 87131

The use of ionizing radiation from various sources for the treatment of tumors is widespread. Some 250,000 individuals will start radiation treatments each year. At present, it is not common practice to instrument the patient with dosimeters, although there are passive dosimeters like thermal luminescent dosimeters (TLDs) which are available. There are no commercial devices for in vivo, real time, dosimetry of patients. The dose to be given the patient is determined from computer modelling and the calibration of the radiation sources.

We will describe a miniature dosimeter which has been mounted in a 1 mm catheter. The active device is a radiation sensing field effect transistor (hereafter called a RADFET) which can be used in either an active or passive mode.^{1, 2} The RADFET in a catheter is designed to be used during implant radiation therapy of the breast, prostate, cervix, among other modalities.

The RADFET operates in a fashion similar to the chemically sensitive field effect transistor (CHEMFET). Ionizing radiation produces electron-hole pairs in the gate dielectric (SiO_2) of the MOSFET. In the specially prepared SiO_2 of the RADFET, there is a great excess of hole traps over electron traps. The applied gate voltage sweeps the electrons out leaving a net positive charge of trapped holes. The net charge is proportional to the total dose received by the RADFET. The charge is measured by the threshold voltage shift of the RADFET. A new circuit, with some similarities to circuits used for CHEMFETs, will be described for making differential measurements of the threshold shift as a function of radiation dose. The threshold shift of a RADFET as a function of radiation dose is given in the Figure. The sensitivity of the RADFET is defined as the slope of the response in the Figure, and it is seen to decrease at the higher dose levels. The decrease in sensitivity is caused by the internal space charge build-up inside the gate oxide which increases electron-trapped hole recombination and inhibits electron diffusion to the contacts. The dashed line in the Figure is a fit to the data by the formula:

$$\Delta V_{th} = A \cdot (1 - \exp(-B \cdot \text{dose})), \text{ where for these devices}$$

$$A = 4.05 \text{ volts and } B = 3.39 \times 10^{-5} \text{ rad}^{-1}$$

This formula can be used to convert the RADFET readings into dose in rads. The sensitivity of the RADFET in a catheter is found to be unaffected by the temperature over a wide range in temperature (experimentally, -180C to 100C), and when it is operated with the proper drain to source current, the threshold voltage does not change with temperature.

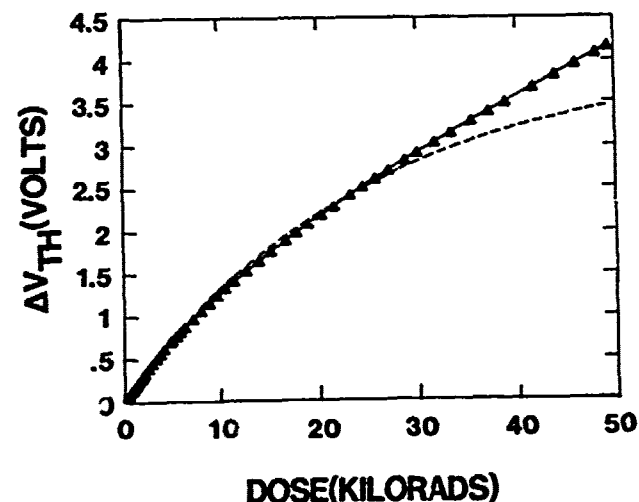


Figure Caption: The change in threshold voltage of a RADFET as a function of the dose in rads. The solid line through the data points is a guide to the eye and the dashed line is from a formula given in the text.

The RADFET has several advantages over the commonly used TLDs. The RADFET can be monitored continuously using very low power and voltage and thus can give the dose rate as well as the total dose. The TLD needs to be inserted in a special reader after exposure and the information is erased during read-out; the threshold shift of the RADFET is relatively permanent within a few percent over many months. The RADFET is much smaller for the same sensitivity than the TLD chip. The silicon chip is extremely rugged, comparable to the TLD chip, but the wires and wire bonds are more vulnerable to mechanical effects. The RADFET can also be operated with no voltage bias during exposure, although the sensitivity is a little smaller than with a bias.

Because of the economics of microelectronic fabrication, RADFETs can be produced for a very low cost; single MOSFETs of the required sophistication are a dollar or less at retail. There does need to be development work on processing to obtain repeatable hole and electron trap concentrations in the oxide. For a range of sensitivities, RADFETs with different thicknesses of the gate dielectric need to be fabricated. The threshold voltage is a DC property of the device and care during fabrication is needed to prevent drift of the threshold voltage with time due to phenomena like ion contamination of the oxide. Because of the inherent advantages of RADFETs over other forms of radiation dosimetry, we expect to see increasing use of RADFETs in the future.

References:

1. R. C. Hughes, "Theory of Response of Radiation Sensing Field Effect Transistors," J. App. Phys., 58, 1375, 1985.
2. A. G. Holmes-Seidle, "The Space-Charge Dosimeter; General Principles of a New Method of Radiation Detection," Nuc. Inst. and Methods, 121,169, 1974.

Steady State and Transient Behavior of the
Pd-SnO_x MIS Oxygen Sensors

J.F. Xu*, W.P. Kang and B. Lalevic

Department of Electrical Engineering, Rutgers University,

P.O. Box 909, Piscataway, N.J. 08854

T. Poteat

AT&T Bell Laboratories, Murray Hill, N.J. 07978

ABSTRACT

Results on the device characteristics of the O₂ gaseous sensors are presented. These sensors are fabricated in the MIS configuration Pd-SnO_x-Si₃N₄-SiO₂-Si-Al with highly resistive SnO_x as oxygen adsorptive element. Partial pressures of O₂ below 0.1 torr can be detected at room temperature by these devices. Steady state and transient behavior are described as a function of O₂ partial pressure and temperature. Adsorption and desorption rates and time constants are determined. Activation energy for O₂ adsorption in SnO_x is found to be 1.6 k cal/mol.

INTRODUCTION

Since the first observation [1,2] on the conductivity change in metal-oxide resistor on gaseous adsorption, various types of gaseous sensors using semiconductors have been developed. Two principal types of gaseous sensors have emerged: a) Sensors based on the conductivity changes upon gaseous adsorption and b) MOS, MOSFET and Schottky diode sensors where the changes in metal work function upon gaseous adsorption are reflected in the I-V characteristics, change in the threshold voltage or a shift in flat band voltage [3,4,5].

Oxygen sensors based on resistivity change on oxygen adsorption have been fabricated with sintered blocks or sputtered, evaporated or oxidized thin films of TiO₂, ZrO₂, SnO_x, Nb₂O₅ and others [6,7]. Another group of oxygen sensors is made of the electrochemical ZrO₂ cell, with the EMF output related to the oxygen pressure [8]. Oxygen detection with the above devices, requires however higher operating temperatures (>250°C).

We report here on a new type of O₂ sensors based on different detection mechanism related to the changes in ionic charge of the adsorptive metal oxide in the MIS capacitor. The device is fabricated in the following MIS configuration: Pd-SnO_x-Si₃N₄-SiO₂-Si-Al with highly resistive SnO_x as oxygen adsorptive element. The increase in ionic charges in SnO_x upon O₂ adsorption is reflected in the depletion region of Si and thus produces a shift in the flat band voltage of the MIS capacitor. This effect is essentially the same as that of impurity ions in SiO₂ on MOS device characteristics. Since these new devices are based on the ionic charges in isolating layer of MIS capacitor where more than 10⁸ ions/cm³ can produce a shift in flat band voltage, they are much more sensitive than the devices based on resistance changes. This was confirmed by our experiments, which have shown device detection capability of <0.1 torr O₂ partial pressure at 300°K.

We report on compositional, structural and electronic properties of SnO_x films and on the following parameters characterizing the device: 1) pressure detection range as a function of temperature, 2) shift in the flat band voltage ΔV_{FB} as a function of pressure at a given temperature; 3) ΔV_{FB} as a function of temperature at various partial pressures of oxygen; 4) Adsorption and desorption rates and time constants as a function of pressure and temperature.

Further experiments were carried on the electroadsorption process, detection mechanism and determination of ionic concentration in SnO_x upon oxygen adsorption.

Experimental Methods

Pd-SnO_x-Si₃N₄-SiO₂-Si-Al MIS capacitors were fabricated on <100> p-type Si, 5-10 Ω resistivity using standard procedures. A 50Å layer of SiO₂ is deposited first on Si wafer, followed by a deposition of 600Å thick Si₃N₄ layer. SnO_x adsorptive oxide layer 400-800Å thick was subsequently grown by deposition of Sn film and its thermal oxidation at $\approx 400^\circ\text{C}$. A thin $\approx 5\text{\AA}$ catalytic Pd layer was deposited over SnO_x and an Au film 1000Å thick but of much smaller circular area than Pd layer was finally deposited.

SnO_x composition depends on the oxidation temperature and time. Auger Electron Spectroscopy was used to determine SnO_x composition which shall give optimal device characteristics. So far the most promising composition seems to be SnO_{1.27}. Resistivity of SnO_{1.27} is about $4 \times 10^7 \Omega\text{-cm}$ and relative dielectric constant is 4.9. SEM has shown a continuous SnO_{1.27} film with the grain size less than 1000Å.

The device under testing was placed inside a vacuum chamber, provided with heating stage. Oxygen alone or in a gaseous mixture was introduced into the chamber through a leak-rate valve. Subsequent shift, ΔV_{FB} , was measured at 1MHz from the C-V plot or by a constant capacitance voltage tracking circuit previously described. [4]

Results

As stated previously, oxygen adsorption or desorption by the device results in a shift in flat band voltage ΔV_{FB} which is determined from the C-V curves. Combined results of the observed ΔV_{FB} upon oxygen adsorption at a given temperature for various values of the O₂ partial pressure, and at a given pressure for different temperatures are given in Table 1. It is seen in Table 1

*Visiting Scientist, East China Normal University, Shanghai, PRC.

Table I
 ΔV_{FB} Shift with O_2 pressure
 at Several Ambient Temperatures

TABLE I

$T(^{\circ}C)$ \ $P(\text{mm})$	100	200	500	1000
26 $^{\circ}C$	5	20	32	40
75 $^{\circ}C$	20	30	59	79
100 $^{\circ}C$	39	52	72	81

that ΔV_{FB} increases with increasing temperature or pressure. At pressures below 1 torr, ΔV_{FB} increase linearly with increasing pressure. However in the measured pressure range from 1 to 60 torr, the linear relationship is replaced by a saturation trend where $\Delta V_{FB} \propto P^n$, with $n = 0.2$ for lower temperatures (20-35 $^{\circ}C$) and $n=0.12$ for higher temperatures (35-90 $^{\circ}C$).

Transient behavior of a device during O_2 adsorption process was studied in terms of the adsorption time rates and adsorption time constants. Adsorption rates are determined from the time rate of ΔV_{FB} i.e. $\frac{d\Delta V_{FB}}{dt}$ and adsorption time constant τ is

defined as the time necessary to achieve 90% of the total device response at a given O_2 pressure. These two parameters are investigated as a function of pressure and temperature. The experimental values for $\frac{d\Delta V_{FB}}{dt}$ and τ for two ambient temperatures as a function of O_2 partial pressure are given in Table II, while the dependence of $\frac{d\Delta V_{FB}}{dt}$ and τ on temperature at a given pressure is presented in Table III.

Table II

Rate of change of ΔV_{FB} and time constant τ as a function of pressure of 50 $^{\circ}C$ and 80 $^{\circ}C$.

TABLE II

$T(^{\circ}C)$ \ $P(\text{torr})$	50 $^{\circ}C$		80 $^{\circ}C$	
	$\frac{d\Delta V_{FB}}{dt} (\frac{mV}{min})$	$\tau(\text{min})$	$\frac{d\Delta V_{FB}}{dt} (\frac{mV}{min})$	$\tau(\text{min})$
0.1	1.5	8.5	3.1	8.5
0.4	6	5.5	13	5.5
1	12	3	25.5	3.2
4	15	2.8	36.5	2.2
10	25	2	47.5	1.6
60	25	2	64.1	1.6

Table III
 Time rate of ΔV_{FB} and adsorption time constant τ at different temperature for the O_2 pressure of 400 μm .

T	$\frac{dV_{FB}}{dt} (\frac{mV}{min})$	$\tau(\text{min})$
30 $^{\circ}C$	-1.2	6.5
45 $^{\circ}C$	-2.48	4.4
62 $^{\circ}C$	-4.45	4.7
77 $^{\circ}C$	-6.52	4.2
92 $^{\circ}C$	-9.80	4.6
106 $^{\circ}C$	-17.0	4.4

As seen in Table II, $d\Delta V_{FB}/dt$ increases initially with increasing pressure and levels off at higher pressures. The adsorption time constant decreases with increasing pressure and at higher remains at a steady value. Table I.I shows a sharp increase in $d\Delta V_{FB}/dt$ with increasing temperature at constant pressure, while τ remains essentially independent of temperature.

The value for the O_2 adsorption activation energy E_a in SnO_2 can be obtained from the above measurements. The initial rate of the adsorption process is related to the oxygen pressure by:

$$\left. \frac{d\Delta V_{FB}}{dt} \right|_{\text{init}} = \frac{1}{\Delta V_{FB\text{max}}} \left. \frac{d\Delta V_{FB}}{dt} \right|_{\text{init}} = K_1 P_{O_2}$$

when K_1 is given by

$$K_1 = A e^{-E_a/RT}$$

Therefore, the slope of the plot of $\ln \left[\frac{1}{\Delta V_{FB\text{max}}} \right]$

$\left. \frac{d\Delta V_{FB}}{dt} \right|$ vs $\frac{1}{T}$ is proportional to E_a . This plot is shown in Fig. 1 for two different samples and the estimated value for E_a is about 1.6 $\frac{\text{kcal}}{\text{mol}}$.

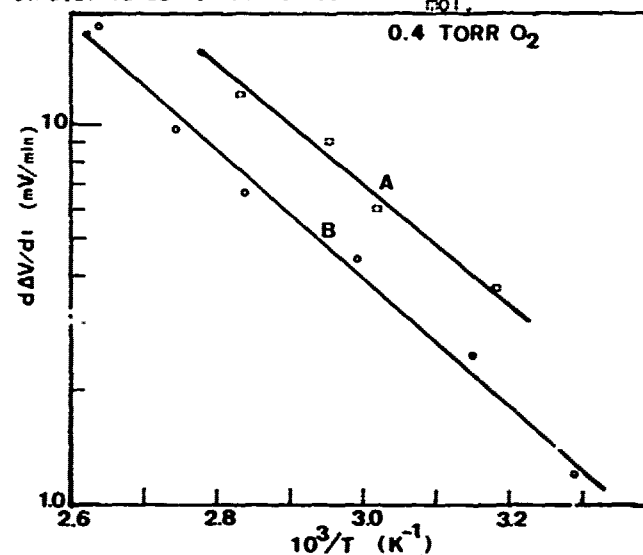


Fig.1 plot of $\frac{d\Delta V_{FB}}{dt}$ vs $10^3/T$ (K^{-1})

Device transient behavior during oxygen desorption process was investigated as a function of O_2 partial pressure and temperature. The rates of desorption process $d\Delta V_{FB}/dt$ as a function of temperature for the O_2 adsorption partial pressure of 0.4 torr are given in Table IVa, while the data for $d\Delta V_{FB}/dt$ at 80°C for different adsorption pressures are given in Table IVb.

Table IV

Desorption rate of change $d\Delta V_{FB}/dt$ at a) a constant O_2 adsorption pressure of 0.4 torr and b) at 80°C for different adsorption pressures.

a) $T=80^\circ\text{C}$

$P(\text{torr})$	$\frac{d\Delta V_{FB}}{dt} / \text{init.} \left(\frac{\text{mV}}{\text{min}} \right)$
0.1	1.3
0.4	3.28
1.0	4.1
4.0	4.3
10.0	4.6

b) $P_{O_2} = 0.4 \text{ torr}$

$T(^{\circ}\text{C})$	$\frac{d\Delta V_{FB}}{dt} / \text{init.} \left(\frac{\text{mV}}{\text{min.}} \right)$
51	1.4
80	3.28
100	3.76
122	4.7

The plot of $\frac{d\Delta V_{FB}}{dt}$ vs. P_{O_2} (torr) at 80° is given in Fig. 2. At lower pressure $\frac{d\Delta V_{FB}}{dt} / \text{init.}$ is directly proportional to pressure, while at higher pressure $\frac{d\Delta V_{FB}}{dt} \propto P_{O_2}^{0.17}$. As seen in Fig. 2 $\frac{d\Delta V_{FB}}{dt}$ levels at $\sim \frac{5 \text{ mV}}{\text{min}}$ for the adsorption pressure > 10 torr. The desorption rates increase almost linearly with temperature, at a given pressure, as shown in Table IVb.

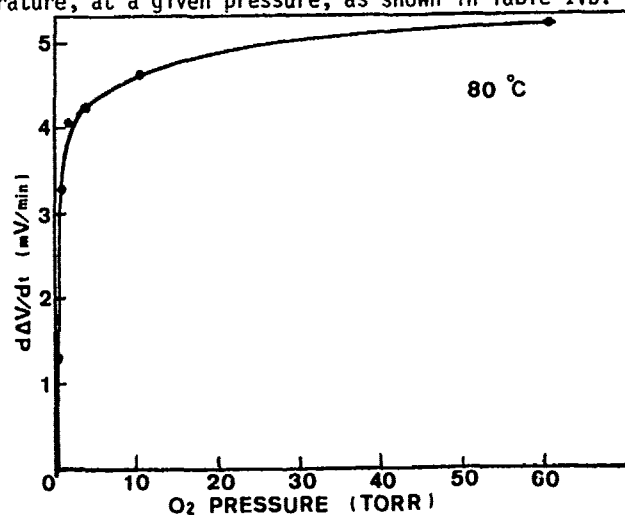


Fig. 2 Plot of $d\Delta V_{FB}/dt$ vs P_{O_2} at 80°C

Conclusions

It has been demonstrated that Pd-SnO_x-MIS gaseous sensors can be effectively used for detection of oxygen at 300°K at the operating pressure of O_2 below 0.1 torr. The characteristic device parameters and its steady state and transient response have been described as function of O_2 partial pressure and temperature in the region of interest.

Further experiments have been performed to clarify the detection mechanism, and they will be presented elsewhere. These experiments have confirmed the device operation is based on O_2 adsorption in SnO_x and subsequent effect at the ionic excess in SnO_x on the depletion region of the MOS capacitor. The number of the adsorbed ions at a given pressure and temperature has been determined by the triangular voltage sweep (TVS) measurements and found to be in agreement with theoretical calculation of ΔV_{FB} shift.

References

1. T. Seiyama, A. Kato, K. Fujiishi and M. Nojotami, Anal. Chem. 34, p. 1502, 1962.
2. G. Heiland, Z. Phys. 138, p. 459, 1954.
3. I. Lundstrom, "Hydrogen Sensitive MOS-Structures," Sensors and Actuators, 1 pp. 400-426, 1981.
4. T. Poteat and B. Lalevic, "Transition Metal Gate MOS Gaseous Detectors, IEEE Trans. Electron Devices vol. ED-29, pp. 123-126, 1982.
5. P. Ruths, S. Ashor, S. Fonash and J. Ruths, "A Study of Pd-MIS Schottky Barrier Diode Detector," IEEE Transaction Electron Devices ED-28 pp. 1003-1003, 1981.
6. H. Windischman and P. Mark, "A Model for the Operation of a Thin Film SnO_x Conductance Modulation Carbon Monoxide Sensors," J. of Electrochem. Soc. 129, pp. 627-633, 1979.
7. E.M. Logothetis, "ZrO₂ Oxygen Sensors in Automotive Applications," Adv. Ceramics 3, pp. 388-405, 1981.
8. W.J. Fleming, "Engine Sensors: State of the Art," SAE paper 820904, 1982.

JOINT ANGLE SENSORS FOR CLOSED-LOOP CONTROL

Wen H. Ko and Chih-Lei Miao

Electronics Design Center, Case Western Reserve University
Cleveland, Ohio 44106

ABSTRACT

In order to substitute braces that have built-in goniometers and to provide feedback signals for closed-loop control of lower-extremity Functional Neuromuscular System in paraplegics, a stretchable capacitive sensor has been developed to accurately detect angular movement in joints. Promising clinical evaluations on the knee joints of a paraplegic and a volunteer have been done. The evaluations show great promise for the possibility of implantation applications.

INTRODUCTION

Research in Functional Electrical Stimulation is being undertaken utilizing a closed-loop computer controlled 32 electrode stimulating system to enable paraplegics to walk normally as well as safely. Essential elements of this control system include sensors which measure the parameters to control and analyze movement of a walking subject. The sensor outputs and analyzed results will be used to activate the control function semiautomatically without the conscious aid of a human operator. One of the sensors needed in this system is a sensor to measure the joint angle. The present way to achieve this purpose is by using a mechanical brace with a built-in goniometer on each joint. The size, weight, accuracy and reliability of existing goniometers are not satisfactory. Problems include sliding of the device with movement, short lifetime, noise and poor cosmetic appearance. In addition, a goniometer can only operate with a bulky brace, requiring patients to wear the brace at all times. Therefore, it is desirable to develop an improved sensor for joint angle measurement, either for a surface mount or an implant inside the body. Human joints are complex structures and the pivot point of the angular motion shifts during a loop of the movement cycle. This makes conventional angular encoders unable to be used. After trying several designs the following approach has been adopted.

DESIGN

Figure 1a and 1b illustrate the conceptual design and the operating principle of the sensor. The design is based on the fact that the change in capacitance is proportional to the angular displacement of the joint. The

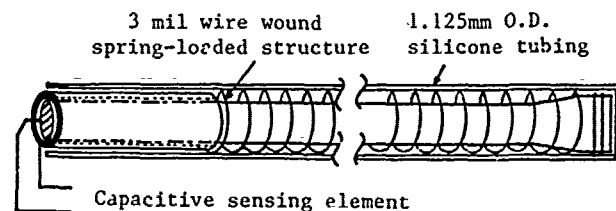


Figure 1a The Conceptual Design of the Joint Angle Sensor.

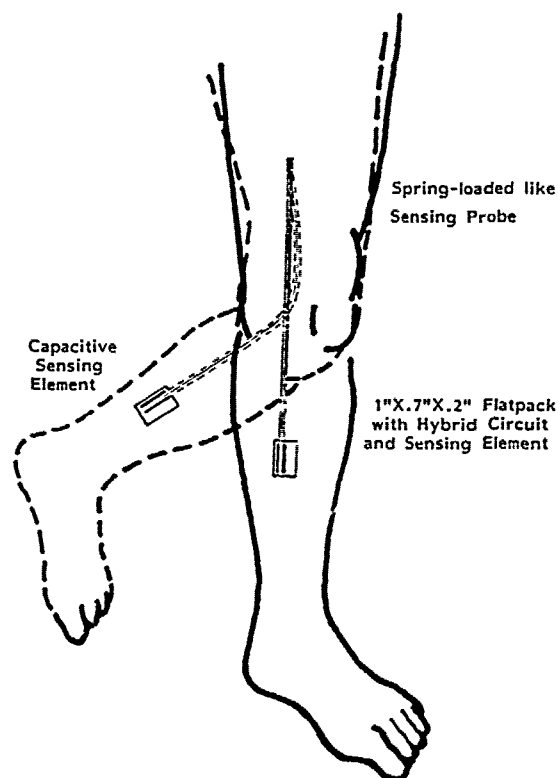


Figure 1b The Operation Principle of the Joint Angle Sensor.

sensing element is encapsulated in medical grade silicone rubber tubing with an outer diameter of 1.125 mm. The signal processing circuit incorporates CMOS hybrid circuitry packaged in a 1" x 0.7" x 0.2" metal flatback. [1] This circuit converts the capacitance changes of the sensing element into a DC output voltage. The circuit draws less than 1 mA using an 8 - 9 volt battery. A photograph of the prototype device is shown in Figure 2.

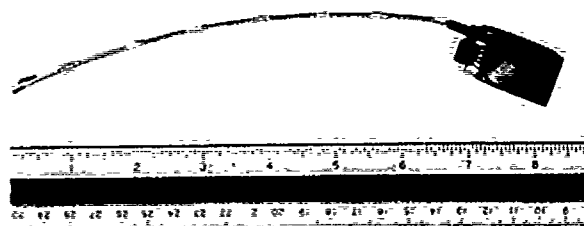


Figure 2 A Photograph of the Prototype Joint Angle Sensor.

EXPERIMENTAL RESULTS

The measured static characteristics of the sensor are listed in Table 1. The sensitivity of the sensor is 0.95 mV/pf; the stability, over 72 hours, is 10 mV drift at a 5 volt full output swing. Its temperature coefficient is -30 mV/°C. It has been tested throughout a temperature range of 4.5 °C to 48.9 °C (40 °F to 120 °F). Dynamic testing was performed by comparing this sensor, mounted near the knee, to a goniometer built in brace worn by the same person. The frequency response from 0 Hz up to more than 10 Hz is flat within 0.7 dB. Comparison of the goniometer to the joint angle sensor and the frequency response data are illustrated in Figure 3a and 3b.

Table 1 Specifications of the Joint Angle Sensor

PERFORMANCE	
Total Range	-0 to +180 degrees
Linear Range	+0 to +160 degrees
Accuracy	+ 22 mV/degree
Threshold and Resolution	±0.5 degree
Linearity	±1 percent angle
Repeatability	±0.5 degree
ELECTRICAL	
Voltage Supply	3 volts
Voltage Supply Range	6 to 15 volts
Current Draw	<1 mA
Voltage Output	0.95 V/pf
Output Impedance	100 Kohm

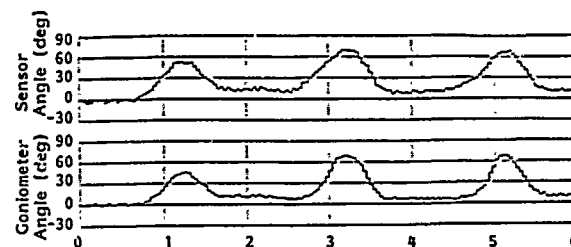


Figure 3a Comparison of the output of the Sensor to the Output of the Goniometer. (25 Hz Sampling rate)

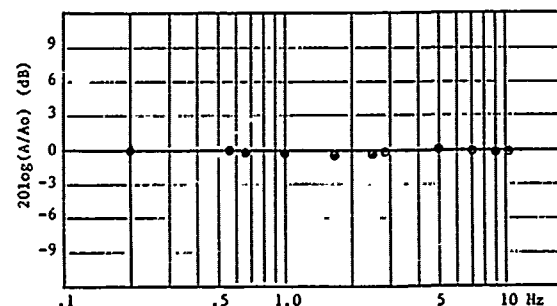


Figure 3b Frequency Response of the Joint Angle Sensor.

ENVIRONMENT

Temperature Range	+40 °F to +120 °F
Temperature Shift	+1.4 degree/°C

RESULTS

If desired, the small temperature shift of the sensor can be compensated by electronic circuitry. The sensor appears to have good performance characteristics for both surface mounting and implant applications. Nevertheless, for widespread application, the capacitance measurement circuit will need to be integrated into a chip. Further studies are needed to eliminate calibration and mounting errors, as well as to design a biocompatible implant packages and procedures.

REFERENCE

1. G.J. Yeh, I. Dendo and W.H. Ko. "Switched Capacitor Interface Circuit for Capacitive Transducers", in Transducer '85, International Conference on Solid-State Sensors and Actuators, June, 1985, pp. 60 - 63.

EFFECT OF PROCESS CONDITIONS ON ALUMINUM OXIDE THIN FILM USED IN pH ISFET

Anthony S. Wong, Ph.D. and Peter W. Cheung, Ph.D.
Electronics Design Center
Case Western Reserve University
Cleveland, Ohio
and
Microsensor Research Laboratory
University of Washington
Seattle, Washington

Abstract

Inorganic oxide material, such as aluminum oxide, may not give linear and stable pH response as predicted from the site binding model. Investigation of the relationship between process conditions and overall film properties is described. Pyrohydrolytic aluminum oxide exhibits very distinct microscopic structures under different process conditions. The TEM results show good correlation with the leakage current and the maximum dielectric breakdown strength. These findings are useful in augmenting pH ISFET sensor design.

Introduction

With the increasing demand of miniaturized sensor for process control and monitoring in various medical and industrial applications, solid state physical and chemical sensors have gained importance from the advancement of solid state technology and physics. One type of chemical sensor is the solid state ion-sensitive field-effect transistor (ISFET) [1]. This paper focuses on the physical and electrical characterization of the chemical vapor deposited (CVD) aluminum oxide as a pH sensitive dielectric towards the development of the pH ISFET.

Various theories on the sensing mechanism of the bare gate ion-sensitive field-effect transistor (ISFET) have been developed in the past decade; such as diffusion, gel layer, ion exchange, surface state modulation, polarized interface, mobile polarizable interface and electrochemical cell. The more recent development of the site binding model such as Schenck [2], Siu [3], and Fung [4] has shed light in the modelling of electrolyte-oxide-semiconductor (EOS) and electrolyte-insulator-semiconductor field-effect transistor (EISFET) systems. Most of the theories, however, have not accounted for the relationship between the microscopic structure of the bare gate dielectric layer with its chemical response.

Based on the existing theories, the major criterion for acceptable pH sensitive gate dielectric material is that it offers a small difference between the amphoteric dissociation and association constants of the hydrolyzed surface sites. The dielectric should also have low solubility. Equally important is that the fabrication method of the pH dielectric material should be compatible with solid state technology, controllable and reproducible.

Metal oxide of the same material, such as aluminum oxide, has been reported behave differently in electrolyte environment. Abe [5] has reported that CVD aluminum oxide displayed linear pH response. Wong [6] has found diverse pH response of aluminum oxide. The diversity in the point of zero charge (PZC) of aluminum oxide in the literature is another indication that the same oxide compound may exhibits wide range of surface properties. These evidences indeed point to the importance in understanding the oxide processing conditions in order to adapt the site binding surface parameters for better interpretation

of the sensing theory of the oxide bare gate pH ISFET. These findings prompted the investigation of the relationship between process conditions and overall film properties.

This paper presents an important aspect of the oxide bare gate pH ISFET's sensing mechanism by considering the microscopic structure of the pH sensitive inorganic oxide layer with respect to its electrical and physical characteristics. The hypothesis is that these thin films, even though they are the same inorganic oxide compound, differ in microscopic structures which in turn alter the surface properties. Experimental studies presented in this paper focus on the post-annealing effect of the pH sensitive aluminum oxide layer using ellipsometry, current-to-voltage measurement technique and transmission electron microscopy.

Aluminum Oxide Deposition Procedure

Substrate Material

Silicon, moderately doped with resistivity of 5 ohm-cm, is selected as the substrate material. Two types of samples are prepared: single dielectric layer of aluminum oxide on silicon (AS) and double dielectric layers aluminum oxide-silicon dioxide on silicon (AOS). To form AOS structure, n-type (100) silicon wafers are oxidized in oxygen environment at 1050°C to form silicon dioxide layer with thicknesses between 600 to 1000 Angstroms.

Experimental Set-up

A vertical cold wall chemical vapor deposition system (Applied Materials model AMV 800) has been modified for the preparation of CVD aluminum oxide. The rotating susceptor can hold seven pieces of two inch diameter wafers in the slightly recessed areas. Susceptor temperature is monitored by a optical pyrometer above the bell jar aligned with the center of the recessed area.

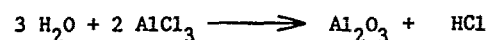
Aluminum chloride, a white powder at room temperature, is sublimed above 100°C to give sufficient vapor for the CVD reaction. Its vapor pressure is approximately linear with temperature between 105°C to 125°C. The sublimator temperature is set at 115°C during CVD deposition. All gas lines are wrapped with silicon rubber heating tapes to maintain temperature higher than 130°C to minimize aluminum chloride vapor condensation [Figure 1]. Since aluminum chloride is extremely exothermic when contacts with water, small amount of moisture in the gas lines will cause the aluminum chloride to react and form undesirable aluminum oxide particulates. Precautions have been taken to minimize moisture in the gas lines.

Pyrohydrolysis of Aluminum Oxide

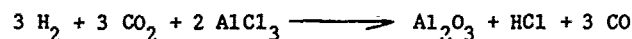
After thermal-grown silicon dioxide step, the wafers are immediately loaded into the CVD reaction

chamber. The wafers are then heated up slowly to avoid thermal shock. At the deposition temperature, a hydrogen annealing step is performed prior to the CVD deposition. A sufficiently high gas flow rate is needed to remove excess water vapor and by-products generated during the reaction.

Pyrohydrolysis of aluminum chloride in a hydrogen and carbon dioxide atmosphere can be written as two reactions. Firstly, hydrogen reacts with carbon dioxide to form gaseous water and carbon monoxide as by-product. Secondly, reaction of gaseous water with aluminum chloride vapor forms aluminum oxide with HCl gas as by-product. These two reactions are listed below,



and the net reaction is,



At 850°C deposition temperature, the deposition rate is approximately 160 Angstroms/min..

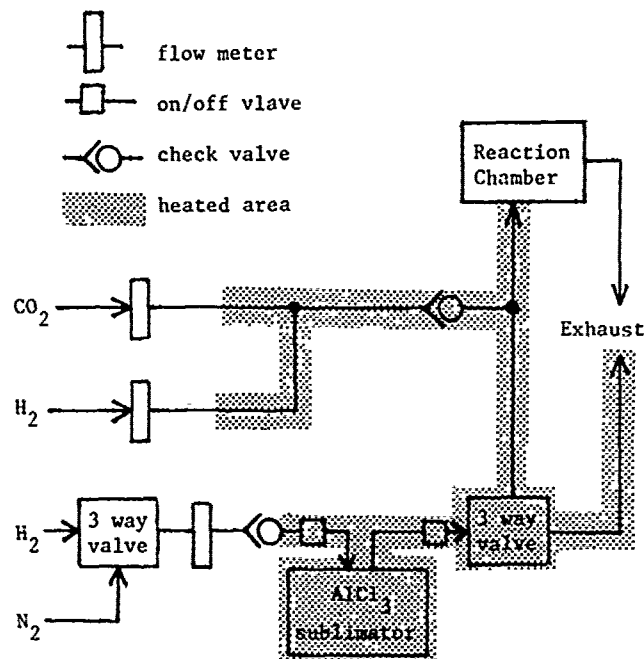


Figure 1. Experimental Set-up for Chemical Vapor Deposited Aluminum Oxide.

Methods of Approach

Aluminum oxide, 1000 to 2000 Angstroms thickness, was deposited onto the wafers both with and without thermally grown silicon dioxide. The samples, further annealed in different temperatures, were divided into three groups. Group one (AS) wafers, with annealing temperature equal or below 850°C, were measured with ellipsometry. Then the wafers were subjected to inert atmospheric annealing at 1000°C for less than thirty minutes and measured again with ellipsometer. The same procedure was repeated after 1175°C annealing.

Group two (AOS) wafers were metallized with aluminum dots (40 mils diameter) on top of the CVD aluminum oxide and metallization on the back of the wafer. These samples were investigated using current-to-voltage technique which was an indirect indication of the aluminum oxide film's electrical integrity in relation to processing conditions. Leakage current density and maximum dielectric breakdown strength were the measured parameters.

To correlate the microscopic structure of aluminum oxide thin films to their processing conditions, transmission electron microscopy technique was used to study grain size, film uniformity and phase. Group three (AS) wafers were cut into 3 x 3 mm² square pieces and the silicon substrates were thinned down by silicon etch. A thin aluminum oxide section was left at the center of the square piece for TEM studies.

Experimental Results and Discussions

Ellipsometer Results

Initially, aluminum oxide thickness and refractive index were measured at six different locations on wafers numbered one to six [Figure 2]. Ellipsometer results of the aluminum oxide with thickness of 1000 to 1700 Angstroms showed 1.73 refractive index. Then the wafers were subjected to annealing at 1000°C for half an hour and ellipsometry results were obtained. The wafers were further annealed at 1175°C for thirty minutes and ellipsometry results were again taken. There were no drastic change in ellipsometry results for samples annealed below 1000°C. After post annealing at 1175°C, however, the CVD aluminum oxide thickness decreased approximately 25% which indicated possible increase of film density

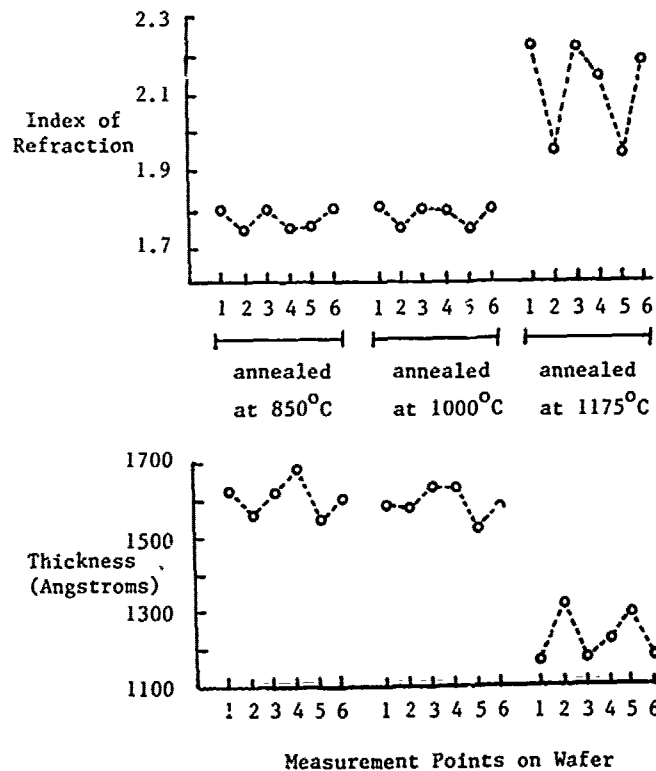


Figure 2. Results of Film Thickness and Refractive Index for CVD Aluminum Oxide Annealed at 850°C, 1000°C and 1175°C.

and refractive index. The variations in thickness and refractive index of such samples indicated a nonuniform shrinkage of the CVD aluminum oxide.

Electrical Characterization

Leakage current results [Figure 3], for different annealed samples, were an indication of aluminum oxide thin film's electrical integrity relating to the process conditions. Maximum dielectric strength of the CVD aluminum oxide could be an indication of the tolerance of maximum electrical field imposed on the sensor. Aluminum oxide thicknesses were measured by an ellipsometer and the results were used to calculate the applied electrical field strength across the samples. The samples, post-annealed at 850°C, 1000°C and 1175°C, under an applied voltage of 1×10^6 volt/cm indicated an increase in leakage current two order of magnitude from 5.8×10^{-9} Amp/cm² to 1.3×10^{-7} Amp/cm². At high annealing temperature, there was good correlation between the current-to-voltage results with ellipsometry results. The dielectric strength also decreased as the post-annealing time or temperature increased. Samples with a short annealing time or no post annealing showed the highest dielectric strength in the order of 4.0×10^6 V/cm. As the post-annealing time or temperature increased, the dielectric strength was decreased to 1.4×10^6 V/cm.

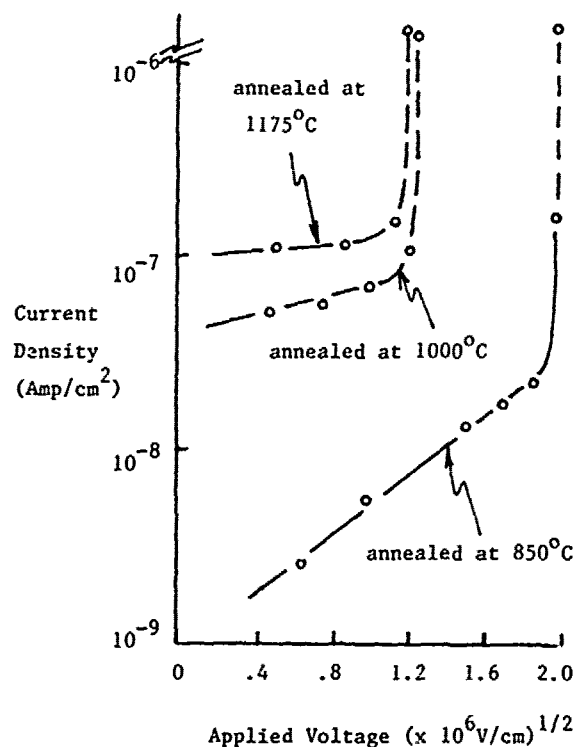


Figure 3. Current Density of Post-annealed MAOS Structure as a Function of Applied Voltage.

Transmission Electron Microscopy Results

In order to further correlate the CVD aluminum oxide thin film to processing conditions, a Philips model EM 400 transmission electron microscopy was used because of its superior resolution and phase study capability compared to SEM or AUGER analytical techniques. Considered in the TEM analysis were the grain size, film uniformity, phase of the CVD film, polycrystalline or crystalline structure. At the depositing and annealing temperature of 850°C, the film appeared to be polycrystalline gamma phase with fine grain structure [Figure 4]. Diffraction pattern of the CVD aluminum oxide, deflected as a broad ring, was an indication that the sample was an amorphous solid with a small amount of polycrystalline structures.

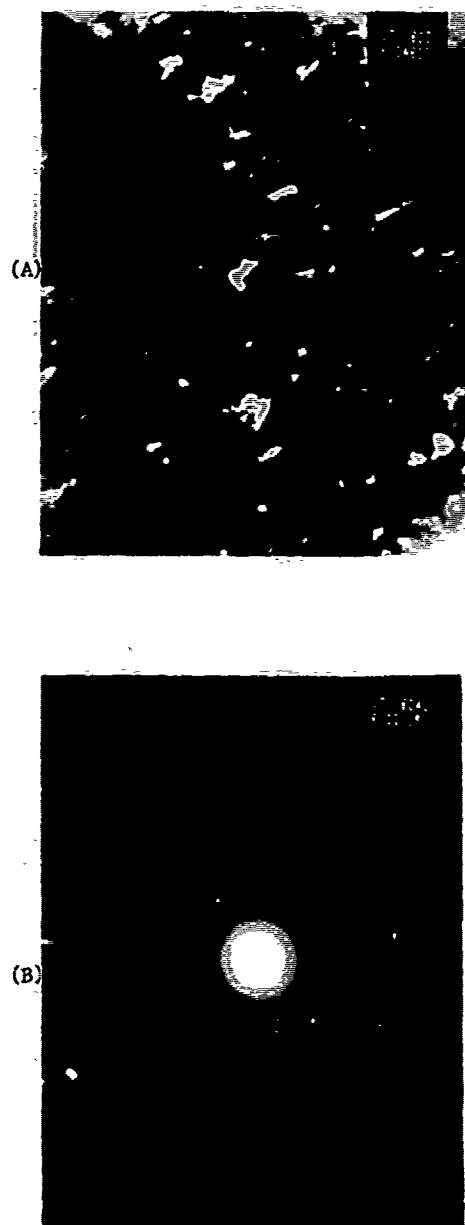


Figure 4. TEM Results of CVD Aluminum Oxide Annealed at 850°C. (A) Grain Structure (46000x), (B) Diffraction Pattern.

The sample under annealing temperature of 1000°C had a diffraction pattern vastly different from the previous patterns. It had definite diffraction spots with a very faint ring pattern superimposed on it. The coherent scattering indicated that the structure had more of a crystalline form. In addition, from the d spacing, the phase structure of this sample was composed of gamma phase and alpha phase indicating transition from the gamma phase to the alpha phase.

For the sample annealed at 1175°C, two phases were detected, a gamma and an alpha phase. The alpha phase showed very distinct spot pattern which indicated crystalline structure [Figure 5]. At 1175°C, there was a much wider range of grain size between 0.13 to 0.54 micron. The larger grains appeared in a rectangular form with a definite grain boundary. There was a good correlation with the previous ellipsometry results; increased in film density and index of refraction with increased in temperature.



Figure 5. TEM Results of CVD Aluminum Oxide Annealed at 1175°C, (A) Grain Structure (46000x), (B) Diffraction Pattern.

Conclusion

Based on the previously suggested site binding model, pyrohydrolytic aluminum oxide has been selected as a pH sensitive dielectric with the possible improvement of the pH response over the silicon dioxide. Studies of aluminum oxide thin films, with specific annealing conditions, by ellipsometry, current-to-voltage technique and transmission electron microscopy confirm the importance of process conditions which definitely affect the relationship between the microscopic structure and the electrical properties of the oxide material. Properties of the CVD aluminum oxide, refractive index, leakage current density, electrical breakdown field strength, phase and grain size have been determined experimentally. When the CVD aluminum oxide is processed at approximately 850°C with minimal or no post annealing, the film is gamma phase with polycrystalline structure. Thus, metal oxide thin film processed differently will have diverse electrical and physical properties. It is concluded that an accurate prediction of its pH response based on the oxide surface parameters given in the literature is not possible because the processing conditions changes surface properties. These findings are useful to augment the sensor design. Furthermore, the difference on pH sensitivity and stability of aluminum oxide as a pH sensitive layer under different process conditions may be partially explained by this study.

References

- [1] A.A. Saaman and P. Bergveld "A Classification of Chemically Sensitive Semiconductor Devices", Sensors and Actuators, 7:75, 1985.
- [2] Schenck, J. F. "A Transistor Method for Measuring Changes in Double Layer Potentials", Journal of Colloid and Interface Science, 61(3):569, 1977.
- [3] Siu, W.M. and Cobbold, R.S.C. "Basic Properties of the Electrolyte-SiO₂-Si System: Physical and Theoretical Aspects", IEEE Transactions on Electron Devices, ED-26:1805, 1979.
- [4] Fung, C.D., Cheung, P.W. and Ko, W.H. "A Generalized theory of an Electrolyte-Insulator-Semiconductor Field Effect Transistor", IEEE Transactions on Electron Devices, ED-33(1):8, 1986.
- [5] Abe, H., Esashi, M. and Matsuo, T. "ISFET's using Inorganic Gate Thin Films", IEEE Transactions on Electron Devices, ED-26(12):1939 (1979).
- [6] Wong, A.S. "Theoretical and Experimental Studies of CVD Aluminum Oxide as a pH Sensitive Dielectric for the Back-contacts ISFET Sensor", Ph.D. dissertation, Case Western Reserve University, May 1985.

Acknowledgement - This research is supported in part by Semiconductor Chemical Transducer Resource, Biotechnology Resource Grant, Division of Research Resources, National Institute of Health, NIH grant #RR-02024.

RESONANT STRUCTURES FOR INTEGRATED SENSORS

Martin A. Schmidt and Roger T. Howe

Microsystems Technology Laboratories
Department of Electrical Engineering and Computer Science
Massachusetts Institute of Technology
Cambridge, Massachusetts 02139

I. Abstract

This paper reviews mechanically resonant microsensors and the design issues for this class of sensors. We apply Rayleigh's Method to determine the resonant frequencies of common microstructures, and show that it provides insight into perturbing the resonance in sensing applications. Resonant microsensors that measure mass loading and force or pressure are studied. We conclude with a discussion of some of the important issues in resonant microsensor design.

II. Introduction

Mechanically resonant structures are attractive as transducing elements in microsensors. Resonant frequencies are made sensitive to chemical or physical signals by coating the structure with sensitive films or by coupling mechanical loads to the structure[1,2]. Since the sensor output is a shift in resonant frequency, it can be measured precisely and converted to digital form by simple counting, in contrast to voltage or current outputs, which require conventional analog-to-digital conversion. Furthermore, spurious drifts in the resonant frequency can be canceled by taking the difference in resonant frequencies between matched structures as the output.

Over the past two decades, these advantages have motivated work on quartz mechanical resonators[15-18], quartz bulk wave resonators and surface-acoustic-wave (SAW) oscillators using piezoelectric substrates or thin films[8-13,19-24], and micromachined mechanical resonators[7,14,25-29]. Resonant microsensors have been demonstrated that measure pressure, acceleration, applied force, temperature, deposited film thickness, and gas or vapor concentration.

We begin this review with a discussion of Rayleigh's Method for calculating the resonant frequencies of

mechanical structures[3-6], and its extension to acoustic systems. This energy method provides insight into the design of resonant microstructures and is used to compare the sensitivities of microbridge and SAW vapor sensors. Resonant microsensors for force and pressure are also examined. In conclusion, we discuss some of the important design considerations for the development of useful resonant microsensors.

III. Mechanical Resonance

A. Rayleigh's Method

Rayleigh's Method is a vibration analysis technique in which the maximum potential energy of vibration is equated to the maximum kinetic energy to solve for the resonant frequency[5]. An example of this method is the calculation of the first resonant frequency ω_r of a stretched string, shown in Figure 1. The maximum potential energy of stretching occurs at the maximum deflection, whereas the kinetic energy maximum occurs as the string moves through the center line. We equate these energy terms, for an assumed mode shape $Y(x)$, to find ω_r . The exact first mode shape of a vibrating string is $Y(x) = \sin(\pi x/L)$; substitution into the equation in Figure 1 yields the exact resonant frequency:

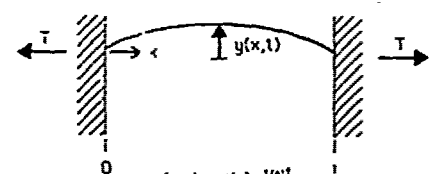
$$\omega_r = \pi \sqrt{\frac{T}{\rho A}} \frac{1}{L}$$

The power of Rayleigh's method is that any reasonable mode shape which satisfies the boundary conditions yields a good estimate of the resonant frequency. It can be shown that any estimate of the first resonant frequency by this method is greater than or equal to the true resonant frequency[3]. Thus, Ritz's iterative method of minimizing ω_r by varying $Y(x)$ can be used to improve the estimate.

B. Beams, Bridges, and Plates

Table 1 summarizes the resonant frequency calculations for three typical micromechanical structures: cantilever beams, bridges, and plates. The potential energy contains contributions due to bending for all three structures, represented as the second derivative of the mode shape. The bridge and plate may also contain potential energy terms due to axial forces, shown for the bridge only. This term is identical to the vibrating string potential energy and may be present due to applied loads or built-in stresses in the structure. Rotational inertia and shear energy can be added for any of these structures, although in most cases these are negligible[17]. A variety of boundary conditions are possible, but most micromechanical structures are best modelled with built-in (clamped) ends.


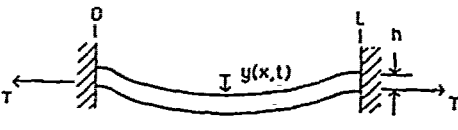
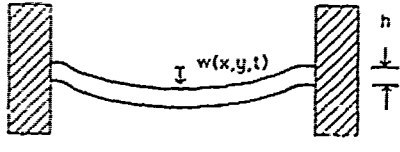
All of these results neglect the effect of the fixed ends on resonant frequency, based on the assumption that the deflections at the center of the structure are small compared to the thickness. When these deflections become significant, axial tension develops and introduces another energy term[4]. This energy is a non-linear function of both the amplitude of vibration as well as any static deflection due to applied loads.



$$KE_{MAX} = \omega^2 \frac{\rho A}{2} \int_0^L v^2(x) dx \quad PE_{MAX} = \frac{T}{2} \int_0^L \left(\frac{dY(x)}{dx} \right)^2 dx$$

$$\omega^2 = \frac{\frac{T}{2} \int_0^L \left(\frac{dY(x)}{dx} \right)^2 dx}{\frac{\rho A}{2} \int_0^L v^2(x) dx}$$

Figure 1. Rayleigh's Method calculation of resonant frequency. ρA = mass / length of string.

<p style="text-align: center;">BEAM</p>  <p style="text-align: center;">$y(x,t) = Y(x)e^{j\omega t}$</p>	$\omega^2 = \frac{\frac{EI}{2} \int_0^L \left[\frac{d^2 Y(x)}{dx^2} \right]^2 dx}{\frac{\rho A}{2} \int_0^L Y^2(x) dx}$
<p style="text-align: center;">BRIDGE</p>  <p style="text-align: center;">$y(x,t) = Y(x)e^{j\omega t}$</p>	$\omega^2 = \frac{\frac{EI}{2} \int_0^L \left[\frac{d^2 Y(x)}{dx^2} \right]^2 dx + \frac{T}{2} \int_0^L \left[\frac{dY(x)}{dx} \right]^2 dx}{\frac{\rho A}{2} \int_0^L Y^2(x) dx}$
<p style="text-align: center;">PLATE</p>  <p style="text-align: center;">$w(x,y,t) = W(x,y)e^{j\omega t}$</p>	$\omega^2 = \frac{\frac{D}{2} \iint \left[\left(\frac{d^2 W}{dx^2} + \frac{d^2 W}{dy^2} \right)^2 - 2(1-\mu) \left[\frac{d^2 W}{dx^2} \frac{d^2 W}{dy^2} - \left(\frac{d^2 W}{dx dy} \right)^2 \right] \right] dx dy}{\frac{\rho h}{2} \iint W^2 dx dy}$

EI = Flexural Rigidity of Beam/Bridge T = Axial Force on Bridge ρ = Density
 D = Flexural Rigidity of Plate μ = Poisson's Ratio A = Cross-Sectional Area of Beam

Table 1. Resonant frequency of cantilever beam, bridge, and plate.

C. Acoustic Waves

An analog to Rayleigh's Method exists in the case of acoustic wave resonators, where it is possible to represent the resonant frequency of a non-piezoelectric resonator using variational methods as:

$$\omega^2 = \frac{\int_V \nabla_s \mathbf{w} : \mathbf{c} : \nabla_s \mathbf{w} dV}{\int_V \rho \mathbf{v} \cdot \mathbf{v} dV}$$

where the numerator is the strain energy and the denominator is the kinetic energy[6]. The velocity field distribution $\mathbf{w}(x,y,z)$ is analogous to the mode shape in the tensioned string example and is chosen to satisfy boundary conditions. Piezoelectric effects may be included by adding electrical potential energy terms. Perturbation methods are generally more tractable for calculating the effects of parameter variation on ω ; however, we will see in the next section that the energy method does yield a simple result for the mass change sensor.

VI. Resonant Sensors

A. Perturbations

Having determined the resonant frequency for some common microstructures, we now consider the use of resonant structures as transducing elements. In the following sections we consider the cases where the kinetic energy is perturbed by mass loading and the potential energy is perturbed by applying loads. For both cases we define a sensitivity to a parameter f as follows:

$$S = \frac{1}{\omega_0} \frac{d\omega}{df}$$

We write the resonant frequency as

$$\omega = \omega_0 \left[1 + \frac{dPE}{PE_0} \right]^{\frac{1}{2}} \quad \text{or} \quad \omega = \omega_0 \left[1 + \frac{dKE}{KE_0} \right]^{\frac{1}{2}}$$

for a small perturbation dPE or dKE , where KE_0 , PE_0 , and ω_0 are unperturbed quantities. Note that KE actually represents the kinetic energy divided by ω^2 . Substituting ω into the sensitivity expression, we obtain:

$$S = \frac{1}{2} \frac{1}{PE_0} \frac{dPE}{df} \quad \text{or} \quad -\frac{1}{2} \frac{1}{KE_0} \frac{dKE}{df}$$

The sensitivity to perturbation varies as the ratio of the change in energy (potential or kinetic) over the initial energy. We have assumed that the amplitude of vibration remains constant during perturbation. This assumption is superfluous for small amplitude linear vibrations such as the tensioned string or the bending beam since the resonant frequency is independent of amplitude. However, it is required for large deflections, in which stretching energy becomes important.

B. Mass Change Sensors

One class of resonant microsensors detects changes in kinetic energy due to mass loading by vapor sorption or material deposition. Examples include resonant-micro-bridge vapor sensors, bulk wave gas detectors, SAW vapor sensors, and acoustic-resonator film-thickness sensors.

We now evaluate the sensitivities of the resonant-microbridge[14] and SAW vapor sensors[9]. These devices detect the mass change that occurs when vapor is absorbed by a thin polymer film coating the resonating bridge or SAW. If we consider the sensitivity of the

resonant-microbridge to variations of film density ρ_0 due to changes in ambient vapor concentration dc , we find that

$$S = -\frac{1}{2} \left[\frac{\frac{d\rho}{dc} h}{\rho_0 h + \rho_1 d} \right]$$

where h and ρ_0 are the thickness and unperturbed density of the polymer and d and ρ_1 are the thickness and density of the bridge. For the SAW device we assume that the velocity components of the Rayleigh wave are constant through the thin polymer film. Consequently, the integral of the kinetic energy density reduces to $\rho h v^2$ with h being the film thickness:

$$S = -\frac{1}{2} \left[\frac{\frac{1}{2} \frac{d\rho}{dc} h (|v_x|^2 + |v_y|^2 + |v_z|^2)}{KE_0} \right]$$

The kinetic energy KE_0 is the unperturbed kinetic energy per unit surface area. The sensitivities of both vapor sensors are proportional to the kinetic energy in the sensitive film. Thus, it is desirable in the case of the microbridge to increase the ratio of film to bridge thickness, or in the case of the SAW to increase the film thickness to Rayleigh wave-length ratio. In pursuing this approach, the effects of the elastic properties of the film on the original resonant frequency and quality factor must be considered. The changes in elastic properties of the film as it interacts with the vapor may also affect the sensitivity.

C. Force/Pressure Sensors

The majority of resonant force and pressure sensors use perturbations of potential energy for sensing. We consider three general types; resonant-diaphragm pressure sensors, resonant-ribbon/quartz-microbeam force and pressure sensors, and SAW cantilever/diaphragm force and pressure sensors.

The resonant-diaphragm pressure sensor uses perturbations of the stretching energy term discussed in the previous section to measure pressure[25-27]. A static pressure induces a deflection of the diaphragm which introduces stretching. The vibrational potential energy of the diaphragm for a static deflection y (much greater than the vibration amplitude) is given by:

$$PE = k_1 + k_2 y^2$$

where k_1 and k_2 are constants[4]. Calculating the sensitivity of this structure to static deflection we find:

$$S = \frac{1}{2} \left[\frac{1}{PE_0} \right] 2k_2 y$$

The sensitivity is zero about the zero deflection point, because at very low deflections the stretching term does not affect resonant frequency. Thus, the sensitivity is a non-linear function of the displacement and requires a bias pressure.

An attractive approach to force or pressure measurement is to mechanically couple into the axial tension of a resonating element[15-18,29]. The sensitivity to variations in axial tension in a ribbon or microbeam is:

$$S = \frac{1}{2} \left[\frac{\frac{1}{2} \int_0^L Y^2(x) dx}{PE_0} \right]$$

The sensitivity is constant in the applied load. Examples of this type of sensor are the quartz microbeam/tuning fork devices.

A final example of potential energy change force

sensors are the SAW cantilever/diaphragm sensors[20-24]. The sensitivity is due to the third-order elastic coefficients which are functions of stress and strain in addition to strain induced geometry changes, and is typically analyzed using perturbation methods.

D. Other Resonant Sensors

Temperature sensors have been made using resonant structures[1,2]. These typically rely on the temperature sensitivity of a material property to alter the potential energy. It is also possible to make sensors which monitor the elastic property changes of materials. An example is the polymer glass-transition-temperature SAW sensor reported by Wohltjen[30].

V. Important Issues

In addition to ultimate sensitivity, there are many other materials, reliability and packaging issues that will dictate the applications of resonant microsensors.

The quality factor, both intrinsic and extrinsic, is important in determining performance. Quality factors of beams made of a variety of common microelectronic materials have been reported, and in general crystalline materials have substantially higher intrinsic Q than polycrystalline or amorphous films[33]. The extrinsic quality of resonance will depend strongly on geometry and packaging due to viscous damping. An example of this is a torsionally resonant silicon plate which has been reported to resonate with a Q of 10,000 in vacuums of 10^{-3} Torr but ceases to resonate above 1 Torr[28].

Many of the materials used in microfabrication have residual stresses which cause buckling and warpage[31,32]. Residual stresses can dominate the potential energy of vibration and the control of these stresses is critical to sensor performance. Both the quartz tuning fork and SAW devices have encountered substantial aging problems due to creep and fatigue of initially stressed structures. These problems motivated the development of the quartz microbeam resonator as a replacement for the tensioned string[15]. A microbeam does not require static tension in order to support vibration, thereby eliminating the potential for creep.

The method of driving and transducing resonance can substantially impact the reliability of a resonant sensor. As an example, stresses in deposited electrodes are critical in determining the aging of SAW delay lines and quartz resonators[35]. In general, excitation and detection mechanisms that do the least "damage" to the resonating structure are desirable.

As in all sensor applications, packaging poses special challenges. The way in which a resonating element is mounted can severely affect the quality factor because of poor rigidity. Dual tuning fork designs have been developed which eliminate this problem by canceling out any moments that would be imparted to the mount[18]. It is often desirable to keep the resonating element away from the environment being sensed. An example of this is the work by Greenwood which separates the resonating plate from the sensor diaphragm[28]. Finally, an example of a creative packaging scheme is the mounting of an axial-force-sensitive quartz beam in a metal package[34]. Axial forces induced by mismatch in thermal expansion coefficients cause the frequency to vary with temperature.

Acknowledgements

The authors would like to acknowledge S.D. Senturia who initially suggested that a comparison of sensitivities of resonant vapor sensors would be of interest.

References

1. R. M. Langdon, "Resonator Sensors - A Review", J. Phys. E., Sci. Instrum., 18, 1985, pp.103-115.
2. T. Gast, "Sensors with oscillating elements", J. Phys. E., Sci. Instrum., 18, 1985, pp.783-789.
3. J. P. Den Hartog, Mechanical Vibration, 4th Ed., McGraw-Hill, 1956.
4. S. Timoshenko and D. H. Young, Vibration Problems in Engineering, 3rd Ed., D. Van Nostrand, 1955.
5. C. M. Harris and C. E. Crede, Shock and Vibration Handbook, 2nd Ed., McGraw-Hill, 1976.
6. B. A. Auld, Acoustic Fields and Waves in Solids, Vol. 2, John Wiley, 1973.
7. M. C. Nathanson, W. E. Newell, R. A. Wickstrom, and J. R. Davis, Jr., "The Resonant Gate Transistor", IEEE Trans. on Elec. Dev., ED-14, March 1967, pp.117-133.
8. J. Hlavay and G. G. Guilbault, "Application of the Piezoelectric Crystal Detector in Analytical Chemistry", Anal. Chem., 49, November 1977, pp.1890-1898.
9. H. Wohltjen, "Mechanism of Operation and Design Considerations for Surface Acoustic Wave Device Vapour Sensors", Sensors and Actuators, 5, 1984, pp.307-325.
10. C. T. Chuang, R. M. White, and J. J. Bernstein, "A Thin-Membrane Surface-Acoustic-Wave Vapor-Sensing Device", IEEE Elec. Dev. Lett., EDL-3, June 1982, pp.145-148.
11. A. D'Amico, A. Palma, and E. Verona, "Surface Acoustic Wave Hydrogen Sensor", Sensors and Actuators, 3, 1982/83, pp.31-39.
12. S. J. Martin, K. S. Schweizer, A. J. Ricco, and T. E. Zipperian, "Gas Sensing with Surface Acoustic Wave Devices", Proc. 3rd Int. Conf. on Solid-state Sensors and Actuators, 1985, pp.71-73.
13. A. Bryant, M. Poirier, G. Riley, D. L. Lee, and J. F. Vetelino, "Gas Detection using Surface Acoustic Wave Delay Lines", Sensors and Actuators, 4, 1983, pp.105-111.
14. R. T. Howe and R. S. Muller, "Resonant-Microbridge Vapor Sensor", IEEE Trans. on Elec. Dev., ED-33, April 1986, pp.499-506.
15. J. M. Paros, "Precision Digital Pressure Transducer", ISA Trans., 12, 1973, pp.173-179.
16. E. P. EerNisse and J. M. Paros, "Practical Considerations for Miniature Quartz Resonator Force Transducers", Proc. 37th Ann. Symp. on Freq. Control, 1983, pp.255-260.
17. W. C. Albert, "Force Sensing Using Quartz Crystal Flexure Resonators", Proc. 38th Ann. Symp. on Freq. Control, 1984, pp.233-239.
18. S. S. Chuang, "Force Sensor Using Double-Ended Tuning Fork Quartz Crystals", Proc. 37th Ann. Symp. on Freq. Control, 1983, pp.248-254.
19. E. Karrer and R. Ward, "A Low-Range Quartz Resonator Pressure Transducer", ISA Trans., 16, 1977, pp.90-98.
20. D. E. Cullen and G. K. Montress, "Progress in the Development of SAW Resonator Pressure Transducers", IEEE Ultrasonics Symp. Proc., 1980, pp.696-701.
21. P. Das, C. Lanzl, and H. F. Tiersten, "A Pressure Sensing Acoustic Wave Resonator", IEEE Ultrasonics Symp. Proc., 1976, pp. 306-308.
22. D. Hauden, S. Kouiseau, J. J. Gagnepain, "Sensitivities of SAW Oscillators to Temperature, Force and Pressure: Application to Sensors", Proc. 34th Ann. Symp. on Freq. Control, 1980, pp.312-319.
23. J. F. Dias, H. E. Karrer, J. A. Kusters, and C. A. Adams, "Frequency/Stress Sensitivity of SAW Resonators", Elec. Lett., 12, 1976, pp.580-582.
24. P. Hartemann and P-L. Meunier, "Tensioned or Flexured SAW Accelerometers", IEEE Ultrasonics Symp. Proc., 1983, pp.291-294.
25. J. G. Smits, H. A. C. Tilmans, and T. S. J. Lammerink, "Pressure Dependence of Resonant Diaphragm Pressure Sensors", Proc. 3rd Int. Conf. on Solid-state Sensors and Actuators, 1985, pp.93-96.
26. T. S. J. Lammerink and W. Wlodarski, "Integrated Thermally Excited Resonant Diaphragm Pressure Sensor", Proc. 3rd Int. Conf. on Solid-state Sensors and Actuators, 1985, pp.97-100.
27. G. M. Schuster, "On the use of Resonant Diaphragms as FM Pressure Transducers", IEEE Trans. on Indst. Elec. and Cont. Instr., IECI-25, Feb. 1978, pp.29-38.
28. J. C. Greenwood, "Etched Silicon Vibrating Sensor", J. Phys. E., Sci. Inst., 17, 1984, pp.650-652.
29. P. M. Zavracky, "Piezoelectrically Driven Resonant Ribbons", Proc. 3rd Int. Conf. on Solid-state Sensors and Actuators, 1985, pp.109-112.
30. H. Wohltjen and R. Dessy, "Surface Acoustic Wave Probes for Chemical Analysis. III. Thermomechanical Polymer Analyzer", Anal. Chem., 51, August 1979, pp.1470-1475.
31. R. T. Howe, "Polycrystalline Silicon Microstructures", Micromachining and Micropackaging of Transducers, C. D. Fung, P. W. Cheung, W. H. Ko, and D. G. Fleming, Eds., Elsevier, 1985, pp.169-187.
32. H. Guckel, T. Randazzo, and D. W. Burns, "A Simple Technique for the Determination of Mechanical Strain in Thin Films with Application to Polysilicon", J. Appl. Phys., 57, March 1985, pp.1671-1675.
33. B. Hok, "Vibration Analysis of Micromechanical Elements", Proc. 3rd Int. Conf. on Solid-state Sensors and Actuators, 1985, pp.284-286.
34. J. M. Paros, U. S. Patent 4,448,546, "Digital Temperature Sensor".
35. E. P. EerNisse, "Quartz Resonator Frequency Shifts Arising from Electrode Stress", Proc. 29th Ann. Symp. on Freq. Control, 1975, pp.1-4.

SURFACE ACOUSTIC WAVE GAS SENSOR BASED ON FILM CONDUCTIVITY CHANGES

A. J. Ricco, S. J. Martin, and T. E. Zipperian

Sandia National Laboratories
Albuquerque, New Mexico 87185

The first surface acoustic wave (SAW) sensor which functions via changes in conductivity of a thin surface film has been constructed.¹ A lead phthalocyanine (PbPc) thin film is deposited by vacuum sublimation on the acoustic propagation path of a LiNbO_3 SAW delay line which serves as the feedback element of an oscillator circuit. Reaction with strongly oxidizing gases, in particular NO_2 , increases the conductivity of the PbPc film. Acousto-electric coupling of the traveling electric potential wave associated with the SAW to charge carriers in the PbPc film decreases the acoustic wave velocity, altering the oscillation frequency of the circuit. This sensor is about 1000 times more sensitive, in terms of the number of NO_2 molecules which can be detected (10^{16}

molecules/ cm^3 of PbPc film), than an identical SAW sensor functioning via mass loading would be. Sensitivity to a few ppm of NO_2 in N_2 has been demonstrated.

Surface acoustic wave (SAW) devices are currently being widely explored as sensors. In general, any change in a physical property of the SAW device surface or near-surface region which affects the acoustic wave velocity or attenuation can be exploited to construct a sensor. To sense a gas or gas phase constituent, molecules must be adsorbed and/or absorbed and must have a mechanism of interaction with the probing surface acoustic wave. Selectivity may rely on the properties of the material from which the SAW device is fabricated, or response may be altered or enhanced by coating the propagation path with a chemically selective material. Nearly all SAW gas/vapor sensors reported to date have relied on mass loading of the surface wave by sorbed species as the sensing mechanism. Variation of properties such as stiffness, conductivity, and dielectric coefficient have not yet been exploited in the fabrication of SAW chemical sensors.

We have fabricated a SAW device which uses changes in electrical conductivity of a thin surface film as a mechanism for chemical sensing. The device, Figure 1, is comprised of four interdigital transducers on a LiNbO_3 substrate forming two isolated acoustic delay lines. One delay line is used for sensing and the other for temperature and pressure compensation. The acoustic wave path of the sensing delay line is coated with a 1600 Å vacuum sublimed lead phthalocyanine film, the conductivity of which increases linearly with the gas phase concentration of NO_2 over a wide range.²

Changes in film conductivity result in a fractional velocity shift $\Delta v/v_0$ as well as attenuation (per wavenumber) of the acoustic wave α/k given by:^{1,3}

$$\frac{\Delta v}{v_0} = \frac{-K^2}{2} \frac{v_{sh}^2}{v_{sh}^2 + v_0^2 C_s^2}$$

$$\frac{\alpha}{k} = \frac{K^2}{2} \frac{v_0 C_s v_{sh}}{v_{sh}^2 + v_0^2 C_s^2}$$

The electromechanical coupling coefficient K^2 is a measure of the piezoelectric strength of the substrate; v_{sh} is the sheet conductivity of the film; C_s is the capacitance per unit length of the surface; v_0 is the unperturbed wave velocity and k is the wave vector.

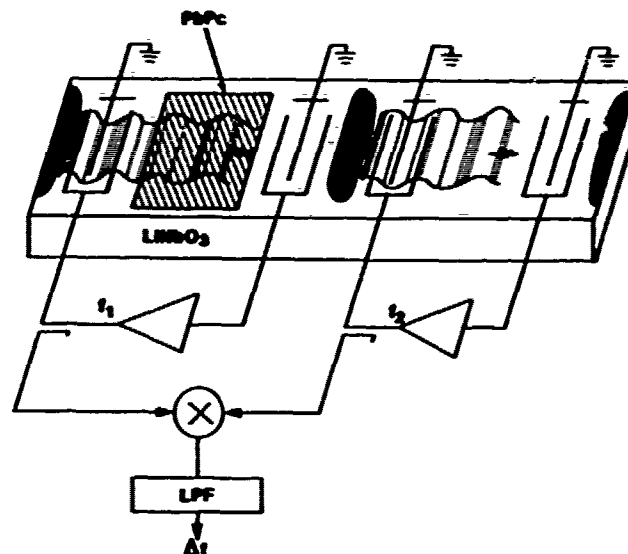


Figure 1 Dual delay line LiNbO_3 SAW device with PbPc film on left wave path. Acoustic waves propagate from left to right; silicone RTV beads (black) prevent acoustic coupling of waves and reflections at ends of crystal. Low pass filter (LPF) selects difference frequency from mixer for output to frequency counter.

Each delay line serves as the feedback element of an oscillator, the resonant frequency of which is thus a highly precise measure of the wave velocity in that delay line. The difference frequency of the sensing and reference delay lines, which is far less sensitive to variations in temperature or pressure than are the frequencies of the individual delay line oscillators, serves as the sensor signal.

Instead of temperature and pressure compensation, the pair of oscillators may be used to differentiate between two simultaneously occurring sensing mechanisms. In particular, the relative velocity perturbations due to mass loading and chemically induced conductivity changes can be separated from one another. As shown in Figure 2, one of the two delay lines is first coated with a thin film of a good conductor (Cr), then both delay lines are coated with identical PbPc films. The thin metal film underlying the PbPc film effectively decouples the SAW from charge carriers in the PbPc; the high conductivity of the metal eliminates the surface wave electrical potential. The response to surface mass loading, however, remains equivalent in the two delay lines. Figure 3 shows the response of each of the two delay lines

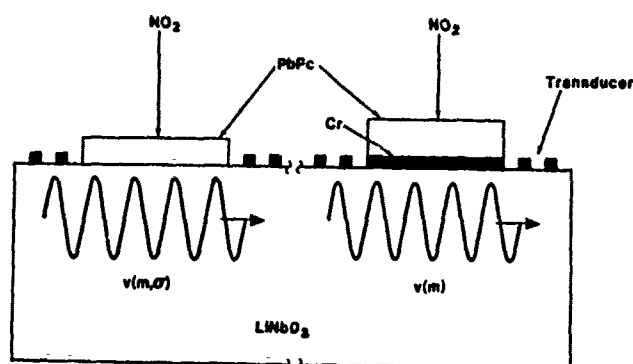


Figure 2 Dual delay line SAW device of Figure 1 altered so that velocity of left delay line is sensitive to conductivity, mass, and stiffness changes, while right delay line, with Cr layer between substrate and PbPc film, senses only mass and stiffness changes: σ is effectively decoupled.

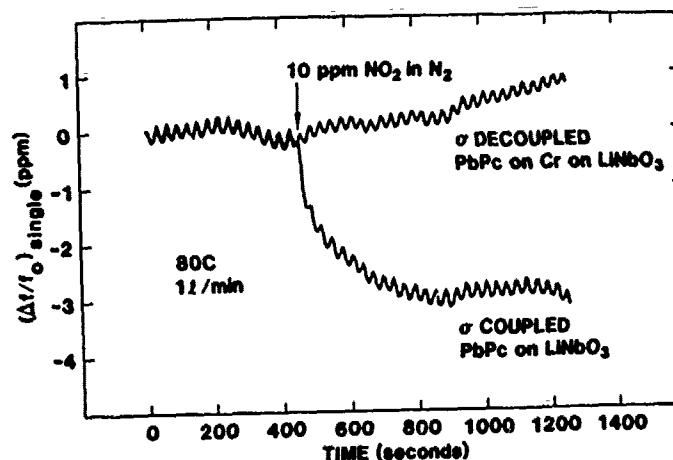


Figure 3 Frequency shift for each of the SAW delay lines of Figure 2 upon exposure to 10 ppm NO_2 in N_2 at 80 C. Decoupling of σ reveals negligible frequency shift due to mass loading; frequency shift of "σ coupled" oscillator is therefore due entirely to conductivity change.

of Figure 2 to the introduction of 10 ppm of NO_2 in N_2 at 80 C. Clearly, the effect of mass change is insignificant (curve labeled "σ decoupled") compared to the effect of conductivity change.

Advantages of a conductivity-based SAW sensor, as opposed to directly measuring the conductivity of a PbPc film, are chiefly a result of the fact that film continuity is unnecessary for the interaction of the SAW with charge carriers in the film. This allows use of a very thin discontinuous film which will equilibrate more rapidly with the gas of interest. It is also unnecessary for the conductivity change to extend all the way through the film, so that a rapid initial response should be obtained as soon as the conductivity of the film surface changes. A thinner film also allows lower operating temperatures, extending the life expectancy of the film.

Supported by the US DOE under contract DE-AC04-76DP00789.

1. A.J. Ricco, S.J. Martin, and T.E. Zipperian, "Surface Acoustic Wave Gas Sensor Based on Film Conductivity Changes", *Sensors and Actuators*, in press.
2. B. Bott and T.A. Jones, "A Highly Sensitive NO_2 Sensor Based on Electrical Conductivity Changes in Phthalocyanine Films," *Sensors and Actuators*, 5, 43-53, 1984.
3. S. Datta, *Surface Acoustic Wave Devices*, Prentice-Hall, Englewood Cliffs, NJ, 1985.

THIN-MEMBRANE LAMB-MODE ACOUSTIC OSCILLATORS FOR CHEMICAL DETECTION

Edward T. Zellers*, Stuart W. Wenzel, Richard M. White
and Peter J. Wicher

Department of Electrical Engineering and Computer Sciences,
University of California, Berkeley, CA 94720.

*Department of Biomedical and Environmental Health Sciences,
University of California, Berkeley, CA 94720.

ABSTRACT

Using computer simulation, we examined the response of polymer-coated acoustic-wave oscillators as chemical sensors. Two structures were studied for comparison: a thin-membrane ($\sim 2\mu\text{m}$) ZnO-on-Si oscillator, and a conventional surface acoustic wave (SAW) oscillator, both operating at a wavelength of $141\mu\text{m}$. For changes in the physical properties of the polymer coating, that might occur upon exposure to chemicals, the velocity sensitivity of the thin-membrane structure is typically an order of magnitude greater than that of the SAW structure. Approaches to the fabrication of these sensors are described.

INTRODUCTION

The sensitivity of SAW oscillators to surface perturbations has been used to advantage in making chemical sensors [1]. Development of composite ZnO-on-Si SAW devices allows consideration of integrating SAW chemical sensors with ancillary components such as amplifiers and signal processing electronics. However, realization of such sensor packages is complicated by the relatively high operating frequencies required for adequate sensitivity (greater than 30 MHz) and by the difficulty of protecting the supporting circuitry from the environment.

We are investigating the use of acoustic sensors that employ propagation of the lowest-order antisymmetric (AO) Lamb waves on composite ZnO-on-Si thin membranes. For membrane thicknesses that are small compared to the wavelength (e.g., on the order of 1-2% of the wavelength) the phase velocity, and hence operating frequency, of the AO-Lamb mode is about one-twentieth that of a Rayleigh mode of the same wavelength. Additionally, since wave energy is present on both the top and bottom surfaces of the membrane, detection of chemical analytes can be achieved by coating and exposing the bottom side while isolating the sensitive electronics on the top.

Figure 1 shows a cross section of the structure under consideration. Transducers placed on the membrane are used to launch and receive ultrasonic Lamb waves. Provided that the gain of the feedback amplifier is sufficient to account for losses in wave transmission and transduction, oscillation at radian frequency ω results, in accordance with Equation 1 [2].

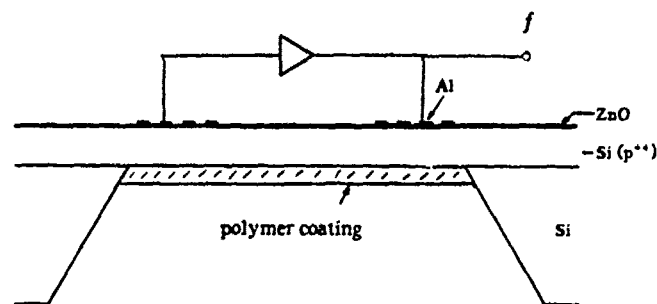


Fig. 1. Cross-section through ZnO-on-Si membrane oscillator structure.

$$\omega L / v_p + \phi_E = 2\pi N \quad (1)$$

This equation states that the total phase shift around the loop (consisting of the acoustic path having length L and phase velocity v_p , the transducers, and the amplifier having phase shift ϕ_E) is an integral number, N , times 2π radians. Since the phase shift of the amplifier is generally much smaller than that of the acoustic propagation path, any change of phase velocity results in a proportionate oscillator frequency change of opposite sign. It is this dependence of frequency upon v_p that is used in most SAW oscillator sensors since frequency can be measured accurately (typically, to better than 1 part in 10^7).

The sorption of a vapor by an organic polymer causes the polymer to swell, changing its thickness, density, and elastic stiffness. As a result, exposing a polymer-coated ultrasonic oscillator to a vapor changes the resonant frequency. Since the extent to which vapors are sorbed is a function of the "affinities" of the solvent and polymer for each other, at least partial selectivity in the response of coated oscillators to different solvent vapors is expected. We have computed the phase velocities of SAW and thin-membrane structures for three different polymers and several values of thickness, density, and stiffness.

RESULTS AND DISCUSSION

Computer Simulation

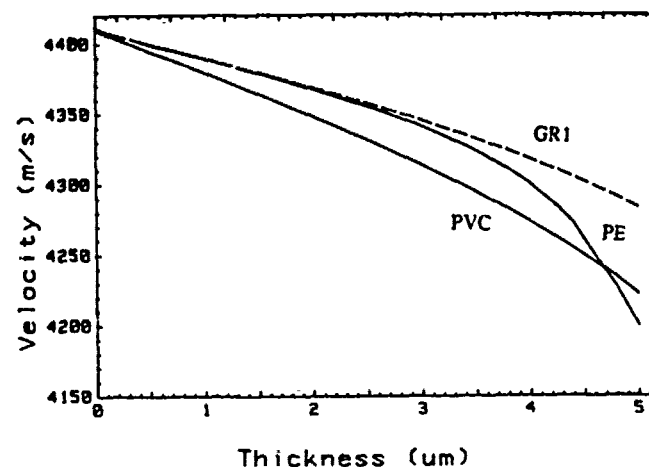
The results described below were obtained using a computer program written by Nassar and Adler [3].

Phase velocities were computed for the layered structures based on the physical and electrical constants of each material in the structure. We compared at a wavelength of $141\mu\text{m}$, a ZnO-on-Si SAW oscillator ($7.5\mu\text{m}$ ZnO) and a thin-membrane oscillator ($0.1\mu\text{m}$ ZnO, $2\mu\text{m}$ Si) coated with each of the following polymers; polyvinyl chloride (PVC, $\rho = 1390\text{ kg/m}^3$, $c_{11}=5.54$, $c_{12}=3.40$, and $c_{44}=1.07\times 10^9\text{ N/m}^2$ [4]), butyl rubber (GR1-soft vulcanizate, $\rho = 925\text{ kg/m}^3$, $c_{11}=3.30$, $c_{12}=1.70$, and $c_{44}=0.78\times 10^9\text{ N/m}^2$ [5,6]), and polyethylene (PE-"alkathene", $\rho = 915\text{ kg/m}^3$, $c_{11}=4.17$, $c_{12}=3.41$, and $c_{44}=0.38\times 10^9\text{ N/m}^2$ [7]) (ρ = density, c_{ij} = stiffness constants). The PVC is a highly crystalline polymer that is glassy at room temperature, while the PE is a rubbery polymer of low crystallinity, and the GR1 is a soft vulcanizate which is rubbery and amorphous.

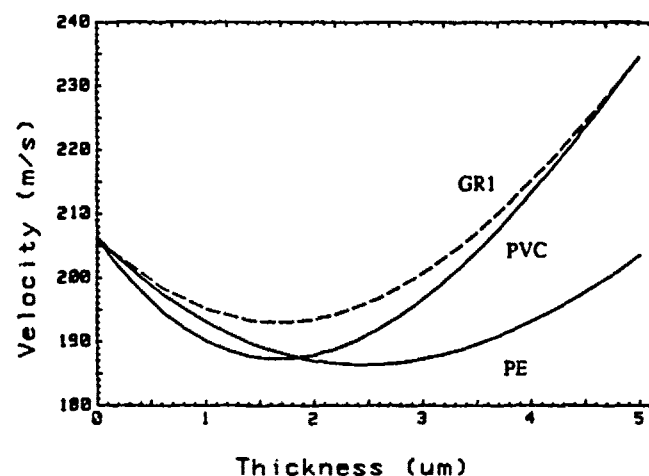
At this wavelength the uncoated SAW and membrane devices have resonant frequencies of 31 MHz and 1.46 MHz, and piezoelectric coupling strengths ($-\Delta v/v$) of 0.53% and 0.34%, respectively. Interestingly, the coupling of the membrane device increased to $\sim 0.6\%$ upon coating with the polymers.

Figure 2(a) shows the relationship between the SAW phase velocity and the thickness of each polymer. For thin polymer layers (less than $\sim 1\%$ of the wavelength) there is a linear dependence, with the slopes nearly proportional to the densities of the polymers. This agrees with experimental results reported by Wohltjen for other polymers on a quartz SAW oscillator [2]. As the layer thickness increases, the slopes also increase for all three polymers. The greater velocity decrease seen for PE may be due to its relatively low shear modulus, c_{44} . According to Wohltjen [2] the decrease of velocity (or frequency) due to mass loading of a SAW is mitigated by a stiffening effect in polymers having moderately high shear moduli. This effect would be stronger in the PVC and GR1 than in the PE.

The polymer-thickness dependence of the Lamb-mode oscillator phase velocity is shown in Figure 2(b). The velocity passes through a minimum near $1.7\mu\text{m}$ for PVC and GR1 and near $2.4\mu\text{m}$ for PE. Apparently, for thin layers the polymers load the Si membrane and consequently lower the velocity, but for film thicknesses that are comparable to or greater than that of the substrate, the structure starts to behave like a polymer membrane that is stiffened by the Si. As the polymer thickness increases, the AO-mode velocity increases and eventually approaches the Rayleigh-mode velocity for an infinitely-thick polymer substrate. The velocity of the PVC-coated device shows the strongest thickness dependence on both sides of its minimum, consistent with the high density and stiffness of the polymer. The PE and GR1 coated oscillators have similar slopes at very low thicknesses but the GR1 has a significantly steeper slope for the thicker layers. That the minimum velocity for PE occurs at a thicker coating layer and the slope of the curve is shallower beyond the velocity minimum may both be attributable to its relatively low shear modulus.



(a)



(b)

Fig 2. (a) Plot of phase velocity versus polymer thickness for SAW oscillator coated with PVC, GR1, and PE polymers. (b) Plot of phase velocity versus polymer thickness for membrane oscillator coated with the same polymers as above.

The sensitivities of each device to small changes in thickness, density, and stiffness are shown in Table I. Results were obtained by reducing the thickness (d) or density (ρ) by 1% or by reducing all of a polymer's stiffness constants (c) by 10%. Sensitivities are presented as the fractional velocity change divided by the fractional change in the parameter of interest. In all cases, the sensitivity of the AO-mode oscillator is greater than that of the SAW. The sensitivities of the AO-mode structures are from 3.2 times that of the SAW, for thickness changes in PE near $4\mu\text{m}$, to 86.5 for stiffness constant changes in PVC at $1\mu\text{m}$. For both structures the velocity decreases as the elastic stiffness decreases or as the density increases. The sign of the thickness dependence is, of course, a function of the initial thickness for the membrane oscillator but is always negative for the SAW device.

Table I: Sensitivities ($\times 10^2$) of AO-mode and SAW structures with given polymer coatings.

Polymer	t(μm)	$\frac{(\Delta v/v)}{(\Delta d/d)}$		$\frac{(\Delta v/v)}{(\Delta \rho/\rho)}$		$\frac{(\Delta v/v)}{(\Delta c/c)}$	
		AO	SAW	AO	SAW	AO	SAW
PVC	1	-4.66	-0.70	-10.6	-0.73	+3.46	+0.04
	3	+20.3	-2.55	-22.5	-2.50	+18.9	+0.35
GR1	1	-3.25	-0.46	-7.33	-0.47	+2.54	+0.03
	3	+16.6	-1.70	-17.0	-1.62	+15.4	+0.23
PE	1	-4.96	-0.47	-7.50	-0.48	+1.60	+0.02
	4	+17.0	-5.30	-20.9	-4.05	+17.2	+2.16

For a given polymer, the sensitivities of the SAW oscillator to changes of thickness and density are nearly equal, and are generally much greater than the sensitivity to stiffness changes (with the possible exception of PE at $4\mu\text{m}$). For a given polymer on the membrane device, changes of thickness, density or stiffness all produced comparable phase velocity changes.

When a polymer absorbs a vapor the polymer swells, softens, and usually undergoes a change in density. Therefore, in order to simulate more closely the response of the coated oscillators to chemical exposure, we calculated the fractional velocity change due to simultaneous changes in thickness, density, and stiffness. The results, shown in Table II, were obtained for polymers originally $1\mu\text{m}$ thick by increasing the polymer thickness by 10%, decreasing the density by 1%, and decreasing the stiffness constants by 10%. (Note that the density was reduced by only 1% since, in cases of swelling by organic solvent vapors having densities similar to the polymers, the net density change will be much smaller than thickness and stiffness changes). As shown, the sensitivity of the membrane structure is 10-13 times that of the SAW oscillator. We have shown recently that the fractional frequency shifts of the AO-mode oscillator will be twice the fractional changes of velocity, owing to the dispersion of this mode [8]. Thus, in terms of frequency, the sensitivity of the membrane structure should be 20-26 times that of the SAW.

Table II: Sensitivities ($\times 10^3$) of AO-mode and SAW structures, found by increasing polymer thickness 10%, decreasing density 1%, and decreasing stiffness 10% (for an original polymer thickness of $1\mu\text{m}$).

Polymer	$\frac{\Delta v}{v}$		Ratio
	AO	SAW	
PVC	-7.11	-0.66	10.7
GR1	-5.18	-0.45	11.6
PE	-5.79	-0.45	13.0

Membrane Fabrication

We have made square membranes up to 1.0cm on a side and from 0.9 to $3\mu\text{m}$ thick in (100)-Si wafers. The Si membranes are made by first diffusing boron to a high concentration ($> 7 \times 10^{19}\text{cm}^{-3}$) into the front surface of a wafer. A masking oxide is grown on the back side of the wafer, and square holes are etched in it to define the membrane area. The orientation-dependent etchant called EDP (ethylenediamine with pyrocatechol in water, plus a small amount of pyrazine [9]) is then used to etch the Si from the back side of the wafer. Etching stops once the less-heavily doped Si has etched away to expose the heavily boron-doped region.

Initially, when we deposited ZnO by rf planar magnetron sputtering the membranes buckled or broke owing to the compressive stresses that arise in the process. We found that the stress could be relieved substantially by depositing a 1000\AA -thick gold layer (deposited on top of a 250\AA -chromium layer for adhesion), before the ZnO sputtering. A number of initially buckled membranes left in the sputtering chamber for 12 h at 300°C flattened out sufficiently to permit us to form electrodes by photolithography. We have also made partially-coated membranes having flat central regions by sputtering ZnO through a silicon mask that exposes only the center of the membrane to ZnO.

Acknowledgements

This work was partially funded by Chevron Research Inc. and the California MICRO project.

REFERENCES

- [1] H. Wohltjen and R. Dessey, "Surface acoustic wave probe for chemical analysis", *Anal. Chem.*, vol. 51, pp.1458-1475, 1979.
- [2] H. Wohltjen, "Mechanism of operation and design considerations for surface acoustic wave device vapor sensors," *Sensors and Actuators*, vol. 5, pp. 307-325, June 1984.
- [3] A. A. Nassar and E. L. Adler, "Propagation and electromechanical coupling to plate modes in piezoelectric composite membranes," in *Proc. IEEE Ultrasonics Symp.*, 1983, pp. 369-372.

- [4] E. A. Collins, C. A. Daniels and C. E. Wilkes, in J. Brandrup and E. H. Immergut, eds., Polymer Handbook, John Wiley & Sons, Inc., New York, 1975, pp. v41-v50.
- [5] Y. Maeda, "Ultrasonic studies of high polymers," J. Polym. Sci., vol. 18, pp. 87-103, 1955.
- [6] L. A. Wood, in J. Brandrup and E. H. Immergut, eds., Polymer Handbook, John Wiley & Sons, Inc., New York, 1975, pp. v7-v12.
- [7] J. Schuyer, "Sound velocity in polyethylene," J. Polym. Sci., vol. 36, pp. 475-483, 1959.
- [8] P. J. Wicher, R. M. White, S. W. Wenzel and E. T. Zellers, "Plate-mode ultrasonic oscillator sensors," submitted to IEEE Trans. Sonics and Ultrasonics, March 1986.
- [9] A. Reisman et al., "The controlled etching of silicon in catalyzed ethylenediamine-pyrocatechol-water solutions," J. Electrochem. Soc., vol. 126, pp. 1406-1415, August 1979.

ZINC-OXIDE THIN FILMS FOR INTEGRATED-SENSOR APPLICATIONS

D.L. Polla and R.S. Muller

Department of Electrical Engineering and Computer Sciences
and the Electronics Research Laboratory
University of California, Berkeley, California 94720

ABSTRACT

Integrated sensors based on the piezoelectricity and pyroelectricity in zinc-oxide thin films have been fabricated compatibly with conventional NMOS technology. A study of material and electrical properties of the zinc-oxide films, prepared by planar magnetron sputtering, has been carried out. For 1- μm thick films, the measured piezoelectric coefficient is $d_{33} = 14.4 \times 10^{-12} \text{C/N}$ and the pyroelectric coefficient is $p^{\sigma} = 1.4 \times 10^{-9} \text{C/cm}^2 \text{K}^{-1}$. In practical integrated sensor designs, these films have yielded voltage responses of 5.2 mV/gm (piezoelectric effect) and 150 mV/K (pyroelectric effect).

INTRODUCTION

Thin films of zinc oxide have been combined with conventional silicon planar processing techniques to form integrated sensors in which a physical or chemical variable is sensed and transduced to an on-chip amplifier circuit. Integrated sensors using zinc-oxide thin films that have been fabricated and demonstrated to date in our laboratory include:

- (1) cantilever-beam accelerometer [1],
- (2) SAW convolver [2],
- (3) chemical vapor sensor [3],
- (4) anemometer [4],
- (5) infrared detector array [5],
- (6) chemical reaction sensor [6],
- (7) tactile sensor array [7], and
- (8) infrared charge-coupled device imager [8].

The operation of all sensors was based on the piezoelectric or pyroelectric effects in the zinc-oxide films.

This paper focuses on the material properties of zinc-oxide thin films and the basic design considerations for integrated-sensor applications such as those listed above.

ZINC-OXIDE THIN-FILM DEPOSITION

Techniques which have previously been used for zinc-oxide thin-film deposition include rf and dc sputtering [9,10], chemical-vapor deposition [11], ion plating [12], planar-magnetron sputtering [13], and reactive magnetron sputtering [14]. Our work has been based on films made using planar magnetron sputtering as the deposition technique. We chose this method because of its low film damage due to electron bombardment and high deposition rate.

Zinc-oxide thin-film crystallinity, obtained under varying sputtering conditions (substrate temperature, sputter power, thickness, ambient gas mixture), has been studied by x-ray diffraction and scanning electron microscopy. Highly-oriented zinc-oxide films have been deposited on SiO_2/Si and $\text{SiO}_2/\text{Poly-Si}/\text{Si}$ substrates. X-ray diffraction measurements indicate preferential c-axis orientation with a single diffraction peak at 33.8° in the best samples studied as shown in Fig. 1. Based on x-ray diffraction studies, we have found the best thin-film crystallinity to correspond to deposition conditions carried out at a forward sputtering power of 200 W with a 10 mTorr ambient gas mixture consisting of 50% oxygen and 50% argon. The substrate to target distance is 4 cm and the substrate temperature is maintained at 230°C during deposition.

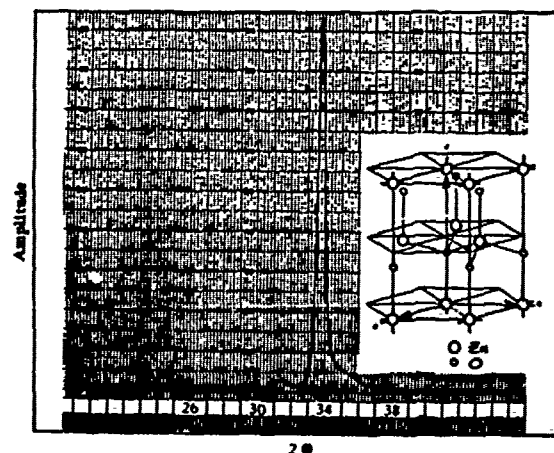


Fig. 1. Typical x-ray diffraction spectrum characterizing the preferential c-axis orientation in zinc-oxide thin films prepared by planar magnetron sputtering.

MATERIAL CHARACTERIZATION

Pyroelectric and piezoelectric properties have been measured by electrical techniques and correlated with the x-ray diffraction results. The measured pyroelectric coefficient at $T=300$ K is $p^{\sigma}=1.4 \times 10^{-9}$ $\text{Ccm}^{-2}\text{K}^{-1}$ and piezoelectric coefficient is $d_{33}=14.4 \times 10^{-12}$ CN^{-1} , in good agreement with the range of reported values in crystalline zinc oxide [15,16]. The temperature dependence of these coefficients is shown in Figs. 2 and 3. For typical sensor applications in $1 \mu\text{m}$ -thick films at $T=300$ K, these coefficients imply signal levels of 5.2 mV/gm (piezoelectric effect) and 150 mV/K (pyroelectric effect). Thin films that exhibit good piezoelectric properties were also found to exhibit good pyroelectric properties.

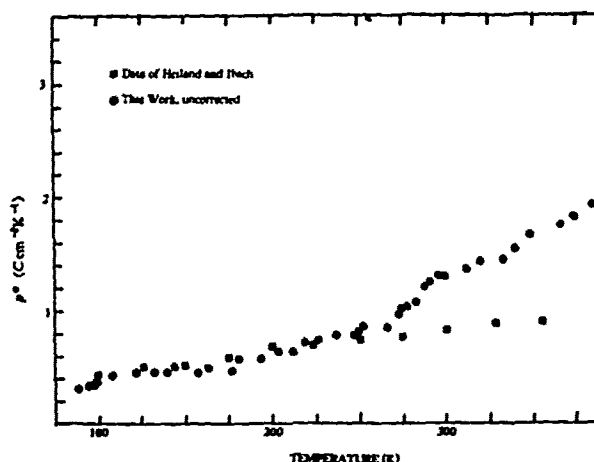


Fig. 2. Measurement of pyroelectric coefficient versus temperature in a $1.0\text{-}\mu\text{m}$ -thick zinc-oxide film.

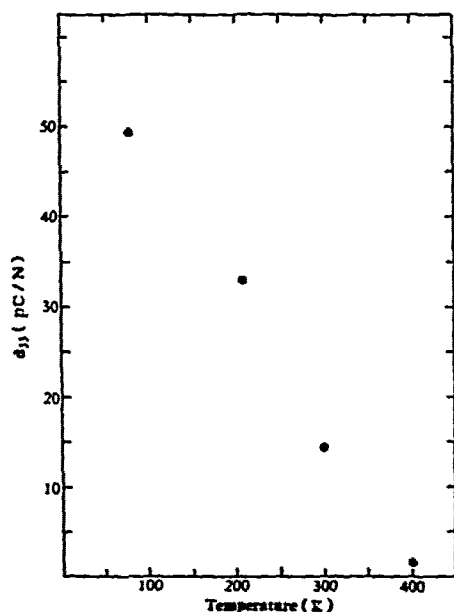


Fig. 3. Temperature dependence of the piezoelectric coefficient d_{33} .

The ability to fabricate sensors with a near dc response is based on the fact that typical film thicknesses ($1 \mu\text{m}$) are much thinner than a Debye length ($120 \mu\text{m}$). Static charge decay times (see Fig. 4) in excess of 32 days have been measured in these films when encapsulated by $0.4 \mu\text{m}$ -thick layers of SiO_2 . Thin-film resistivities of $3 \times 10^7 \Omega\text{-cm}$ and dielectric constants of $\epsilon_r=10.3$ have been characterized in these thin-films.

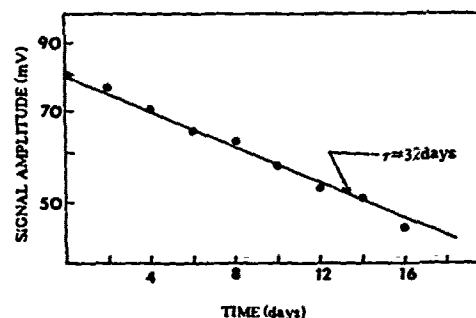


Fig. 4. Pyroelectric charge decay under conditions of constant infrared radiation. The indicated slope represents the characteristic charge retention time for zinc-oxide thin films encapsulated by silicon dioxide.

CONCLUSIONS

Zinc-oxide thin films with very useful piezoelectric and pyroelectric properties have been prepared by planar magnetron sputtering. The material and electrical properties characterized in these films have been utilized in the design and fabrication of diverse integrated sensors compatibly fabricated using NMOS technology. The performance of these sensors demonstrates: 1) the versatility of zinc-oxide thin-film technology for integrated-sensing applications based on either the piezoelectric or pyroelectric effect, and 2) the possibility of carrying out multifunction sensing on one integrated-circuit chip.

Acknowledgements

This work was supported in part by the National Science Foundation under Grant ECS 81-20562 and in part by the State of California MICRO program.

REFERENCES

- [1] P.-L. Chen, R.S. Muller, R.D. Jolly, G.L. Halac, R.M. White, A.P. Andrews, T.C. Lim, and M.E. Motamedi, "Integrated Silicon Microbeam PI-FET Accelerometer," *IEEE Electron Dev. ED-29*, 27-32 (1983).
- [2] A.E. Comer and R.S. Muller, "A New ZnO on Si Convolver Structure," *IEEE Electron Dev. Lett. EDL-3*, 118-120 (1982).

- [3] C.T. Chuang and R.M. White, "Sensors utilizing thin membrane SAW oscillators," *Proc. IEEE Ultrasonics Symposium*, Chicago, IL, 1981.
- [4] D.L. Polla, R.S. Muller, and R.M. White, "Monolithic Zinc-Oxide on Silicon Pyroelectric Anemometer," *IEEE International Electron Devices Meeting*, Washington, D.C. 1983.
- [5] D.L. Polla, R.S. Muller, and R.M. White, "Fully-Integrated ZnO on Silicon Infrared Detector Array," *IEEE International Electron Devices Meeting*, San Francisco, CA 1984.
- [6] D.L. Polla, R.M. White, and R.S. Muller, "Integrated Chemical-Reaction Sensor," *Third International Conference on Solid-State Sensors and Actuators*, Philadelphia, PA 1985.
- [7] D.L. Polla, W.T. Chang, R.S. Muller, and R.M. White, "Integrated Zinc Oxide-on-Silicon Tactile Sensor Array," *IEEE International Electron Devices Meeting*, Washington, D.C. 1985.
- [8] [18] D.L. Polla, R.M. White, and R.S. Muller, "Integrated Multi-Sensor Chip," *IEEE Electron Dev. Lett.*, (to be published in 1986).
- [9] H.W. Lehmann and R. Widmer, "RF Sputtering of ZnO Shear-Wave Transducers," *J. Appl. Phys.* 44, 3868-3879 (1973).
- [10] G.A. Rozgonyi and W.J. Polito, "Preparation of ZnO Thin Films by Sputtering of the Compound in Oxygen and Argon," *Appl. Phys. Lett.* 8, 220-221 (1966).
- [11] S.K. Tiku, C.K. Lau, and K.M. Lakin, "Chemical Vapor Deposition of ZnO Epitaxial Films on Sapphire," *Appl. Phys. Lett.* 36, 318-320 (1980).
- [12] M. Matsumoto, I. Kah, and Y. Murayama, *Tech. Group Ultrasonics US 78-47, 17 IECE Japan* (1979).
- [13] T. Yamamoto, T. Shiosaki, and A. Kawabata, "Characterization of ZnO Piezoelectric Films Prepared by RF Planar- Magnetron Sputtering," *J. Appl. Phys.* 51, 3113-3120 (1980).
- [14] B.T. Khuri-Yakub and J.G. Smits, "Reactive Magnetron Sputtering of ZnO," *J. Appl. Phys.* 52, 4772-4774 (1981).
- [15] G. Heiland and H. Ibach, "Pyroelectricity in Zinc Oxide," *Solid State Commun.* 4, 353 (1966).
- [16] Landolt-Bornstein Tables, Volume 15, edited by O. Madelung, H. Schulz, and H. Weiss, Springer-Verlag, Berlin, 1980.

TIN OXIDE MICROSENSORS ON THIN SILICON MEMBRANES

Shih-Chia Chang
David B. Hicks
Electronics Department
General Motors Research Laboratories
Warren, Michigan 48090-9056

Abstract

Tin oxide based microsensors with integrated polysilicon heaters were fabricated on thin silicon membranes (~2 μm thick) generated by anisotropic wet chemical etching using ethylene diamine-pyrocatechol (EDP) as the etchant. Good thermal isolation and lower power consumption were achieved. The sensing elements, tin oxide thin films, were prepared either by sputter-deposition or by metallo-organic deposition (MOD). The completed microsensors showed good response to alcohol vapor and good stability of the integrated polysilicon heaters.

Introduction

Semiconductor gas sensors generally have to be operated at elevated temperatures (150°C-700°C) to attain the speed and magnitude of response required for practical applications [1-3]. Consequently, for the development of portable gas sensors or integrated sensing systems with on-chip control/logic circuits, effective thermal isolation for the active sensing area becomes imperative in order to keep the power consumption low and to protect adjacent circuitry from extreme temperature generated by the sensor heater. One way of attaining low power consumption and good thermal isolation is by fabricating a sensing element with an integrated heater in thin film form on a suspended thin membrane. By doing this, both the heating mass and heat transport path are greatly reduced. Silicon membranes can be readily generated by an anisotropic wet chemical etching technique using either potassium hydroxide (KOH) or ethylene diamine-pyrocatechol (EDP) as the etchant [4,5]. Such a technique has been used to fabricate piezoresistive or piezocapacitive pressure transducers [6,7]. When using EDP, precise control of the membrane thickness can be achieved by using a heavily doped boron layer as the etch-stop.

The main purpose of this work is twofold: a) to fabricate tin oxide-based microsensors on micromachined thin membranes to attain good thermal isolation, and b) to evaluate sputter-deposited and metallo-organic deposited tin oxide thin films.

This paper describes the detailed processing procedures used to fabricate these microsensors and also presents the various sensor responses to reducing gaseous species (propylene, vapors of alcohol, ethyl ether, methoxyflurane and halothane).

Experimental

1. Device Fabrication

A five-mask process was used to fabricate tin oxide thin film microsensors on silicon membranes.

Most of the processing steps are similar to those used in our previous work [8]. The major additions and modifications adopted in the current fabrication process are described below:

a) The formation of a thin silicon membrane

A silicon membrane with a thickness of ~2 μm was formed by anisotropic chemical etching using EDP. EDP has a fast etch rate (~80 $\mu\text{m}/\text{h}$) in the Si <100> direction, a relatively slower etch rate (<10 $\mu\text{m}/\text{h}$) in the Si <111> direction, a very slow etch rate (<20 nm/h) for SiO_2 , and a close-to-zero etch rate for heavily boron doped silicon. Thus, a heavily boron doped layer (doping concentration $>5 \times 10^{19} \text{ cm}^{-3}$) generated by ion implantation (dosage $\sim 5 \times 10^{16} \text{ cm}^{-2}$, implant voltage ~200 keV) was used as the etch-stop.

b) The formation of the sensing element

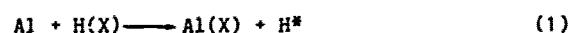
Tin oxide thin films were prepared either by sputter-deposition [3] or by metallo-organic deposition (MOD) [9]. For the sputter-deposited samples, the sensing element processing steps are the same as those used in our previous work. For the MOD technique, an ink was prepared by dissolving tin (II) 2-ethylhexanoate in xylene. The ink was spun onto a silicon wafer, fired to form a 100 nm to 200 nm tin oxide film, and subsequently patterned either by reactive ion etching or by wet chemical etching.

c) The formation of metal interconnects

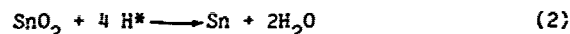
An aluminum (Al)/chromium (Cr) double layer with a thickness of 1 $\mu\text{m}/50 \text{ nm}$ was used to form metal interconnects for the tin oxide as well as the polysilicon heater. Chromium not only provides good ohmic contact for tin oxide, it also prevents electromigration of the interconnect metals at the heater contacts. Severe electromigration was observed if only Al was used as the contact metal, and would result in poor contact or premature contact failure. The processes used to form the MOD tin oxide metal interconnects had to be modified due to the high reactivity of the MOD films. The most commonly used process for metal interconnect fabrication consists of the following steps: a) Deposition of metal(s) on top of the material to be electroded, b) photolithographically defining the interconnect features into a photoresist layer, and c) transferring the defined feature into the underlying metal layer by wet chemical etching. However, when the above procedure is used, two problems are encountered:

(1) During wet chemical etching of Al, active hydrogen (H^*) is produced at the metal/MOD tin

oxide interface according to the following general equation:

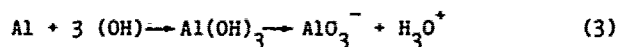


where $\text{H}(\text{X})$ is an etchant composed of H_3PO_4 , HNO_3 , and CH_3COOH . The MOD tin oxide is readily reduced to tin by H^* ,



and is removed by the etchant, resulting in a bad (or open) tin oxide contact.

(2) In photolithographic processes for the patterning of the metal interconnect feature, the weak chemical reaction between the hydroxide-based positive resist developer and Al produces active hydrogen



The reduction of SnO_2 by the active hydrogen as expressed by Eq. 2 at the metal/ SnO_2 interface degrades the metal contact of MOD tin oxide film.

Two approaches were used to overcome the MOD tin oxide/metal contact problems: a) by using a lift-off technique [10]; b) by using an inverse metallization technique. In the lift-off technique, the MOD tin oxide thin film sensing element was prepared as described in the previous section, an opposite contrast metal interconnect feature was defined in a positive photoresist layer and Al/Cr was then deposited. The metal on top of the photoresist layer was subsequently lifted off by acetone. In this process, the co-presence of positive photoresist developer, MOD tin oxide and metal was avoided, and wet chemical etching of the metal interconnect was eliminated. In the inverse metallization scheme, the Al/Cr metal interconnect was fabricated prior to the deposition of the MOD film. The Al layer at the metal/ SnO_2 area was etched off, exposing the underlying Cr layer. The MOD tin oxide sensing element was then fabricated as described before. In both cases, the chemical reaction expressed in Eq. 2 was avoided and a reliable metal/MOD tin oxide contact was obtained. The schematic diagrams of the cross-sectional views of the inverse metallization structure and conventional metallization structure are shown in Fig. 1. A complete microsensor structure is shown schematically in Fig. 2.

Figures 3a and 3b are the SEM pictures of a finished tin oxide microsensor on a Si membrane, showing the top and cross-sectional views, respectively. The dimensions of the sensing element (the sensing element was a sputter-deposited tin oxide, in this particular case) are $25 \mu\text{m} \times 25 \mu\text{m}$.

2. Results and Discussion

The electrical resistance of tin oxide film strongly depends on its stoichiometric composition and can be effected by fabrication processes. For instance, in the reactive ion etching (RIE) process, the sample was immersed in an intense plasma containing reactive reducing gaseous species such as chlorine radicals. A decrease in sample resistance was observed after the RIE process. (The sample resistance was restored after a proper heat treatment in air.) Oxygen plasma exposure, on the other hand, tends to increase the tin oxide resistance due to its

strong oxidation strength. Hence, in fabricating tin oxide microsensors as well as other transition metal oxide-based sensors, the effects of microfabrication processes on the properties of the sensing materials (intrinsic sample conductance as well as gas sensitivity) should be carefully investigated. From our work on tin oxide microsensors, we found that although the sensor resistance can be affected by the RIE and oxygen plasma treatments, no discernible, detrimental effect on the gas sensitivity by such treatments was observed. In this work, the exposure of tin oxide films to an oxygen plasma was kept to a minimum or totally avoided.

The responses of the MOD tin oxide thin film microsensors to propylene and to vapors of ethyl alcohol, ethyl ether, methoxyflurane and halothane in air are shown in Fig. 4. The relative sensitivities of the microsensor to the organic vapors tested are, in decreasing order, ethyl alcohol > ethyl ether > methoxyflurane > halothane. This is congruous with the relative chemical activeness of the respective molecular species. The alcohol vapor sensitivity of the current microsensor is about one third of that given by a similar sensor that has not been subjected to micromachining processes. This indicates that the protective black wax coating on top of the sensing device during the EDP cavity etching process has a detrimental effect on the alcohol sensitivity of the tin oxide sensor.

The integrated sensor heater was a boron doped polysilicon layer with a thickness of $\sim 5000 \text{ \AA}$. The sheet resistance of the heater versus temperature is shown in Fig. 5. In this experiment, a voltage of $\sim 3.6 \text{ V}$ and a current of $\sim 40 \text{ mA}$ were applied to the heater, which is equivalent to a power consumption of $\sim 0.15 \text{ watt}$. From the $R(T)$ curve of Fig. 5, the sensor temperature was estimated to be $\sim 250^\circ\text{C}$.

Summary

Microsensors with tin oxide sensing elements and integrated polysilicon heaters were fabricated on thin silicon membranes generated by anisotropic wet chemical etching using ethylene diamine-pyrocatechol (EDP) as the etchant. The fabricated microsensors had good thermal isolation and low power consumption, and showed good response to organic vapors such as ethyl alcohol and ethyl ether.

Acknowledgements

We would like to thank M. Putty, J. Biafora and C. Puzio for their assistance in microfabrication, R. Laugal and A. Micheli for providing metallo-organic inks and W. Lange for taking the SEM pictures.

References

- [1] S. R. Morrison, *Sensors and Actuators*, **2**, 329 (1982).
- [2] G. R. Heiland, *Sensors and Actuators*, **2**, 343 (1982).
- [3] S. C. Chang, *IEEE Trans. Electron Devices*, **ED-26**, 1875 (1979).
- [4] K. E. Petersen, *Proceedings of IEEE*, **70**, 420 (1982).

- [5] N. F. Raley, Y. Sugiyama, and T. V. Duzer, J. Electrochem. Soc. 131, 161 (1984).
- [6] S. K. Clark and K. D. Wise, IEEE Trans. Electron Devices, ED-26 1887, (1979).
- [7] C. S. Sander, J. W. Knutti, J. D. Meindl, IEEE Trans. Electron Devices ED-17, 927, (1980).
- [8] S. C. Chang and D. B. Hicks, CM Research Publication, GMR-4954, (1985).
- [9] S. C. Chang and A. L. Micheli, CM Research Publication GMR-5212, (1985).
- [10] M. Hatzakis, J. Electrochem. 116, 1033 (1969).

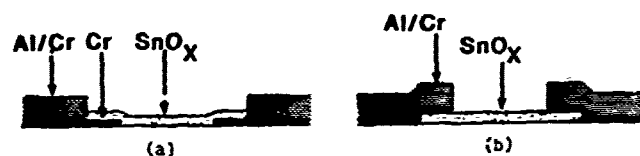


Fig. 1 Schematic diagrams of the cross-sectional view of the inverse metallization structure (a), and the conventional metallization structure (b).

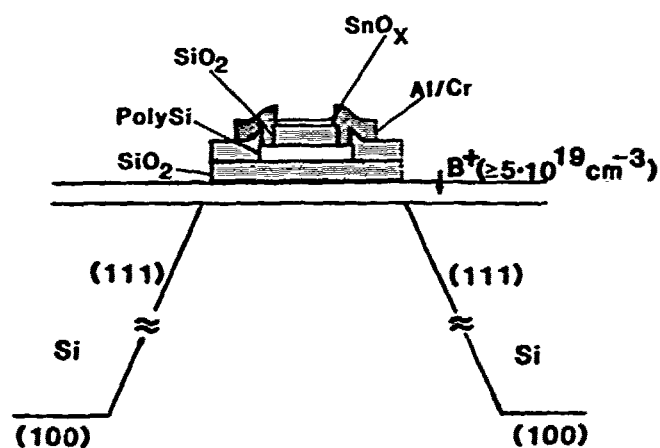
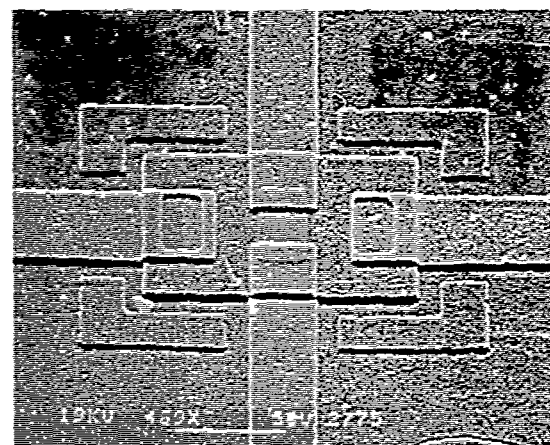
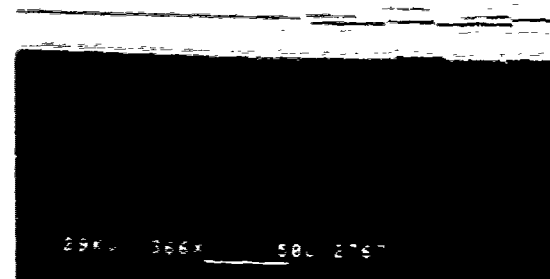


Fig. 2 Schematic diagram of a completed microsensor on a thin Si membrane. The Al/Cr metal contact on tin oxide is not shown.



(a)



(b)

Fig. 3 SEM pictures of a completed microsensor on a thin Si membrane (a) top view, (b) cross-sectional view.

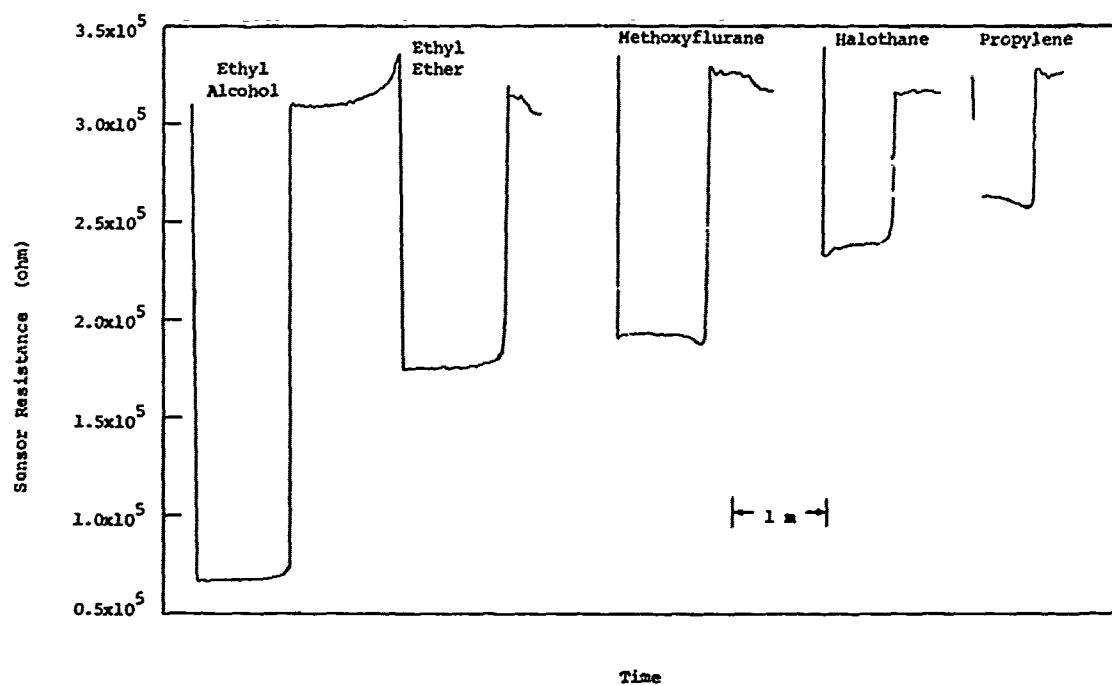


Fig. 4 Sensor responses to 200 ppm of ethyl alcohol, ethyl ether, methoxyflurane, halothane and propylene in air. Sensor material: MOD tin oxide, sensor temperature = -250°C .

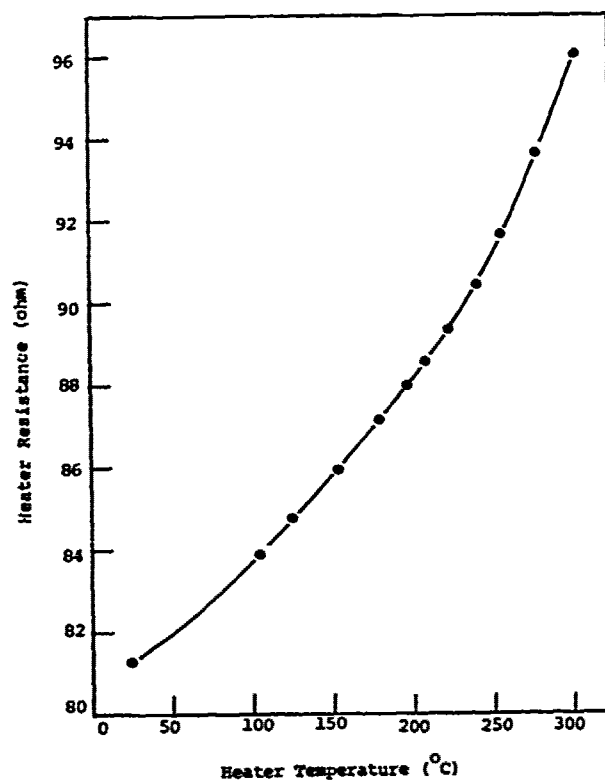


Fig. 5 Polysilicon heater resistance versus temperature.

DEPOSITION TECHNIQUES AND PROPERTIES OF STRAIN
COMPENSATED LPCVD SILICON NITRIDE FILMS

H. Guckel, D.K. Shovers, D.W. Burns, C.R. Rutigliano

Wisconsin Center for Applied Microelectronics
Department of Electrical and Computer Engineering
University of Wisconsin
1415 Johnson Drive
Madison, Wisconsin 53206

C.G. Nesler

Johnson Controls, Inc.
507 E. Michigan Street
Milwaukee, Wisconsin 53201

Our work on polysilicon transducers has shown that polysilicon resistors make acceptable strain sensors [1,2]. Since the devices can be deposited on a variety of substrates, transducer bodies from materials other than polysilicon become viable. Silicon nitride is particularly attractive because (1) it fits well into IC-processing, (2) is a good insulator and (3) the strain field in the material can be controlled by adjusting deposition conditions.

With a goal of developing masks for x-ray lithography, Sekimoto et al [3] describe experiments in which residual stress, optical index, optical transparency and hydrostatic strength of Low Pressure Chemical Vapor Deposited (LPCVD) silicon nitride were determined. The residual stress was determined using the bending plate method in which silicon nitride is deposited on a silicon substrate and changes in wafer deflection are measured.

Bromley et al [4] refined the measurement of intrinsic stress in LPCVD silicon nitride films using an interferometric apparatus to measure free-standing circular membrane deflection under applied pressures. A shortcoming of both these techniques is that an average or integrated strain measurement is made which provides little information about the local short order mechanical properties.

An alternate way to adjust the strain field is through ion-implantation of chemically vapor deposited silicon nitride [5]. A disadvantage of this technique is that subsequent annealing of the silicon nitride film reverses the strain compensation. The numerous reported studies involving silicon oxynitride [6] contribute little to the study of oxygen-free silicon nitride films.

Low pressure Chemical Vapor Deposited silicon nitride can be produced by reacting dichlorosilane with ammonia. Stoichiometric silicon nitride, Si_3N_4 , is produced using high ammonia/dichlorosilane volume ratios and is normally in strong tension. High dichlorosilane/ammonia gas ratios produce silicon-rich films, Si_xN_y , which exhibit compressive strain fields. The gas volume mixture can therefore be used to control the built-in strain field. In the experiment, the dichlorosilane/ammonia volume ratio was varied from 2.5 to 5.5 while maintaining a constant gas flow rate of 75 milliliters/minute and deposition temperature of 835°C. The tube pressure was maintained at 115 millitorr by injecting nitrogen at the pump inlet.

The fabrication of free-standing doubly supported and cantilever beams involved the low pressure chemical vapor deposition of 1.5 μm of polysilicon and .5 μm of silicon nitride over .5 μm of silicon dioxide grown on an n-type <100> silicon substrate. The silicon nitride test structures were defined using conventional photolithography and NF_3 reactive ion etching.

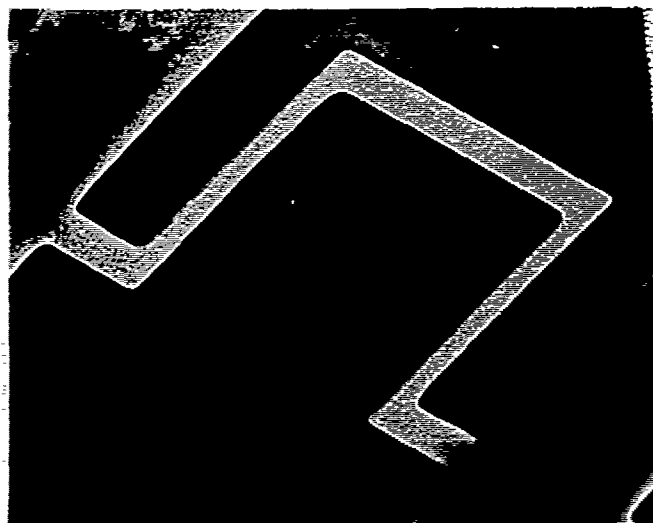
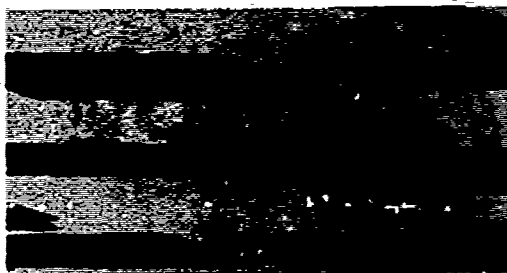
An aqueous KOH solution was used to remove the polysilicon under the beams thus making them free-standing. This process was used to fabricate 10 μm and 20 μm wide by .5 μm thick beams up to 320 μm long.

The fabrication of free-standing silicon nitride membranes involved depositing silicon nitride in the substrate and defining a number of windows on the back of the wafer using conventional photolithography and NF_3 reactive ion etching. An aqueous KOH solution was used to etch through the substrate leaving the nitride membranes exposed. Membranes which are 2 cm x 2 cm x .5 μm have been successfully fabricated using silicon nitride with a mild tensile built-in strain.

Optical index data was obtained using ellipsometry measurements of silicon nitride films deposited directly on silicon substrates. The index increases from 2.1 to 2.4 with increasing dichlorosilane to ammonia gas ratios of 2.5 to 5.5. The index of near-stoichiometric silicon nitride deposited at 800°C varied from 1.91 to 1.98 with dichlorosilane/ammonia ratios of .14 to .24. Optical transmission data was also obtained using the free-standing silicon nitride membranes.

Our technique of measuring compressive strain in polysilicon by beam buckling produces very good results [7]. While this technique is limited to films with compressive strain fields, a similar technique which (1) allows visual determination of the strain field and (2) gives information on local short order strain conditions is desired. Mechanical beams with built-in tensile strains will deform due to lateral buckling when subjected to a moment about the longitudinal axis. Lateral buckling causes twisting of the beam at a critical strain for a fixed geometry.

Mechanical structures which promote lateral buckling have been designed and are used to study the process-controlled strain field in silicon nitride. The figures show two views of the free-standing U-shaped beams used in our analysis. As reported, the strain field varies from highly tensile to compressive as the dichlorosilane/ammonia gas ratio increases. Processing conditions for films of a predetermined strain field and optical index have been determined.



The SEMs show two views of free-standing, U-shaped silicon nitride beams, 10 μm wide by .5 μm thick, which promote lateral buckling. Lateral buckling can be used to determine the built-in tensile strain fields in thin films.

- [1] H.Guckel and D.V.Burns, "Planar processed polysilicon sealed cavities for pressure transducer arrays," Technical Digest IEEE IEDM, pp.233, 1984.
- [2] H.Guckel and D.V.Burns, "Design and construction techniques for Planar Polysilicon pressure transducers with piezoresistive read-out," presented this workshop.
- [3] M.F. kimoto, H.Yoshirara and T.Ohkubo, "Silicon nitride single-layer x-ray mask," Journal of Vacuum Science Technology, vol.21, no.4, pp.1017-1021, Nov./Dec. 1982.
- [4] E.I.Browley, J.N.Randall, D.C.Flanders and R.W.Mountain, "A technique for the determination of stress in thin films," Journal of Vacuum Science Technology, vol.1, no.4, pp.1364-1366, Oct.- Dec. 1983.
- [5] E.P.EerNisse, "Stress in ion-implanted CVD Si_3N_4 films," Journal of Applied Physics, vol.48, no.8, pp.3337-3341, August 1977.
- [6] L.Csepregi and A. Heuberger, "Fabrication of silicon oxynitride masks for x-ray lithography," Journal of Vacuum Science Technology, vol.16, no.6, pp.1962-1364, Nov./Dec. 1979.
- [7] H.Guckel, T.Randazzo, and D.V.Burns, "A simple technique for the determination of mechanical strain in thin films with applications to polysilicon," Journal of Applied Physics, vol.57, no.5, pp.1671-1675, March 1985.

THE USE OF MICROMACHINED STRUCTURES FOR THE MEASUREMENT OF MECHANICAL PROPERTIES AND ADHESION OF THIN FILMS

Mehran Mehregany, Mark G. Allen, and Stephen D. Senturia

Microsystems Technology Laboratories
Massachusetts Institute of Technology
Cambridge, Massachusetts 02139

This paper reports the application of silicon micromachining to the measurement of mechanical properties of thin films such as intrinsic stress, Young's modulus, and adhesion. The measurement is based on the deflection and subsequent peeling of suspended membrane sections of the film. The original goal of the work was to make a quantitatively reproducible adhesion test by applying micromachining techniques to the blister peel test described by Hinkley [1]. Our initial measurements demonstrated the importance of residual stress in the films, which resulted in an expanded emphasis on the basic mechanical properties of the membrane as a prelude to accurate adhesion measurements. We will briefly discuss the process for micromachining suspended membranes, the theory leading to the determination of mechanical properties of the films, our results, and the present status of the adhesion work.

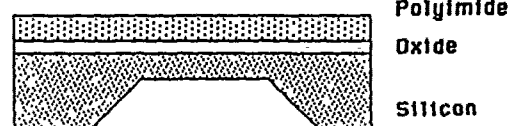
Square suspended membrane sites are fabricated using standard micromachining processes [2]. Figure 1 gives a schematic of the fabrication process. First, a p+ etch stop layer is formed by boron deposition from high temperature solid sources [3]. The deposition is at 1175 °C for 120 minutes in an environment of 90% nitrogen and 10% oxygen. A thermal oxide is grown at 990 °C for a total time of 75 minutes (15 minutes dry O₂, 45 minutes steam, 15 minutes dry O₂), giving a resulting oxide thickness of 3200 Å. Using standard photolithographic techniques, the test site pattern is defined on the back oxide while the front oxide is protected with photoresist. A 50/50 hydrazine/water solution [4] is used under reflux at 115 °C to form the silicon diaphragms, which are approximately 4.7 microns thick at this boron doping level. The polyimide (a BTDA-ODA/MPDA polymer obtained from Dupont) is spin cast on the wafer in multiple coats. After each coat, a prebake is done in air at 135 °C for 14 minutes. After the final coat, the film is cured in nitrogen at 400 °C for 45 minutes. Finally, the diaphragm supporting the film is etched away in a SF₆ plasma to form the free-standing polyimide membranes. Films ranging in thickness from 5 to 11 microns have been produced in this manner.

Theoretical analyses of the load-deflection behavior of elastic membranes have been done by many authors [5], [6], [7]. In this work, we have used the energy method described by Timoshenko [5]. Preliminary load-deflection results indicated that the intrinsic tensile stress in the film (due to shrink-

Basic test site



Apply PI



Etch away silicon membrane and oxide

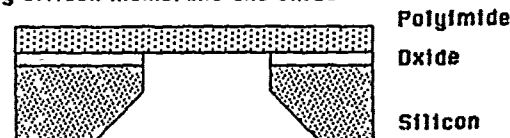


Figure 1. Process schematic

age during cure and/or thermal expansion coefficient mismatch between film and substrate) is not negligible, so the energy method was modified to include the contribution of this stress. In the energy method, which is necessarily approximate, functional forms for the displacements of the deflected surface are assumed. These functions contain several undetermined constants. The constants are found by minimizing the total system energy, leading to an expression for the deflected surface as a function of pressure and intrinsic stress.

Figure 2 shows the coordinate system for the deflected membrane. The origin is located in the plane of the oxide surface at the center of the square membrane. The functional forms we chose for the deflections are the lowest order components of the Fourier series expansion of the true solution:

$$u = c \sin\left(\frac{\pi x}{a}\right) \cos\left(\frac{\pi y}{2a}\right)$$

$$v = c \sin\left(\frac{\pi y}{a}\right) \cos\left(\frac{\pi x}{2a}\right)$$

$$w = w_0 \cos\left(\frac{\pi x}{2a}\right) \cos\left(\frac{\pi y}{2a}\right)$$

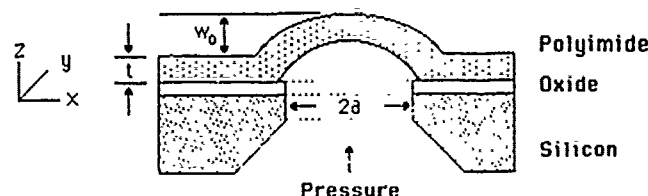


Figure 2. Definitions of blister parameters

where u , v , and w are the deflections along the x , y , and z axes respectively (see Fig. 2); w_0 and c are the two arbitrary constants to be determined; and a is the halflength of the square. These assumed functional forms satisfy the zero-strain boundary conditions at the edges of the membrane and lead to nearly hemispheric deflection near the membrane center. Performing the energy minimization leads to the following expressions for w_0 and c :

$$c = \frac{51\pi^2}{315\pi^2 + 320} \frac{w_0^2}{a}$$

$$E \left[\frac{w_0}{t} \right]^3 + 1.6649 \left[\frac{a}{t} \right]^2 \frac{N_0 w_0}{t} = 0.5469 \frac{p a^4}{t^4}$$

where N_0 is the intrinsic stress, E is Young's modulus, p is the differential pressure and t is the film thickness. The expression for w_0 , the deflection at the center of the film, is of particular interest since this is the quantity we measure. The expression predicts a linear dependence of deflection on pressure at low pressure due to intrinsic film stress, and a cubic dependence at higher pressure. What constitutes low and high pressure is determined by the magnitude of the intrinsic stress. The linear term depends only on residual stress and the cubic term depends only on elastic film constants (i.e., Young's modulus). In this model, therefore, the residual stress can be determined by the initial slope of the load-deflection curve, while Young's modulus can be determined by the curvature of this same curve. However, it must be recognized that more exact solutions for the membrane deflection may not separate so cleanly into two independent terms.

Load-deflection measurements of the suspended polyimide films are made by mounting the wafer in a specially designed chuck which seals the trapezoidal cavity in the wafer and permits the application of differential pressure by injecting volumes of air into that cavity with a microliter syringe. The cavity pressure is measured with a silicon pressure transducer which is built into the chuck. The deflection of the film at the center of the test site ($x=y=0$ in Fig. 2) is measured using an optical microscope. Typical data are shown in Figure 3 (circles), to which we have fit the model previously described (solid line). As can be seen, the data appear mostly linear with slight curvature. The almost linear behavior demonstrates the dominance of the intrinsic stress component of the deflection over the elastic component. Thus, we expect to be able to extract values for intrinsic film stress with greater precision than values for Young's modulus. This is indeed what is found.

Table I gives a summary of the data we have collected on various sized test sites. In this first study, each wafer contained only one test site at its center. Thus, each entry in the table represents a

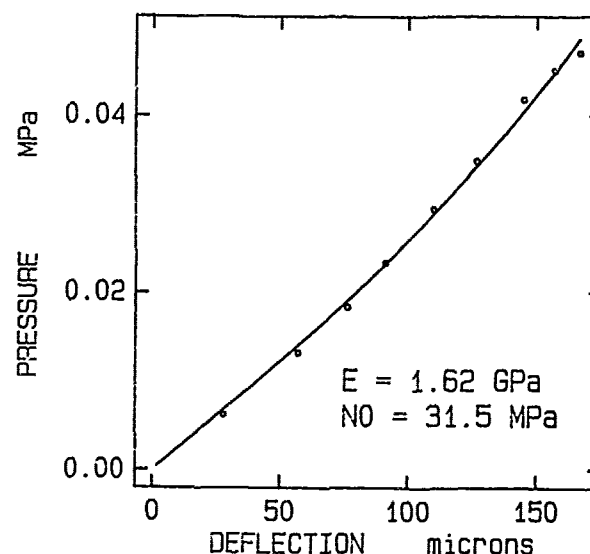


Figure 3. Model fitted to typical load-deflection data

different wafer. As can be seen, except for the 3x3 wafers, values for the intrinsic film stress agree rather well for various geometries. However, the values of Young's modulus obtained, although of the correct order of magnitude, vary substantially. We attribute this to poor resolution of the curvature measurement in such a residual stress dominated regime. This has led us to seek alternative approaches to determine Young's modulus. Note that the ratio of intrinsic stress to Young's modulus, which can be thought of as an 'intrinsic strain', is large, of the order of 1%. In general, the elastic component of the load-deflection behavior will be small until the elastic strain reaches 1%. This is dif-

SIZE (2a)	Thickness (microns)	E (GPa)	N_0 (MPa)
2	106	0.71	29.7
2	105	-	31.4
3	106	6.9	43.8
3	63	8.6	49.4
3	103	3.4	45.3
4	10	1.6	31.5
6	10	-	33.2
6	10	1.5	28.7

Table I. Intrinsic stress and modulus data

ficult to achieve in a membrane deflection. In other work which is being reported separately [8], we have developed an independent method which exploits this "intrinsic strain" in micromachined structures to determine the ratio of Young's modulus to intrinsic stress. With that ratio and with the value for the intrinsic stress determined by the method described here, a value for Young's modulus of these films can be determined with better precision than with the present measurements.

As mentioned above, the suspended membranes are also suited for measurement of the adhesion of a polymer film to a silicon wafer. By increasing the differential pressure on the test site, the film will peel off the substrate, forming a blister. Such a test has been reported by Hinkley [1], using test sites fabricated by a non-lithographic process. However, the test performed by Hinkley used a constant pressure source to peel the film. Since the critical pressure for peel (the pressure at which peel initiates) decreases with increasing radius, the constant pressure peel is inherently unstable. Once initiated, the blister either will peel to the edge of the wafer, or burst if the ultimate tensile stress of the film is exceeded. Our test chuck permits the use of controlled-volume peel. Since we are increasing pressure by injection of known volumes, the volume of the blister formed is constrained and controllable, both at peel initiation and incrementally thereafter. We have demonstrated that this method can be used to follow the peeling of polyimide on silicon. Quantitative measurements of adhesion using this technique are now under way.

ACKNOWLEDGEMENT

This work was supported in part by the Office of Naval Research and Dupont, and by 3M Corporation through fellowship of one of the authors (NM). Sample fabrication was carried out in the MIT Microsystems Technology Laboratories, and in the Microelectronics Central Facility of the Center for Materials Science and Engineering, which is supported in part by the National Science Foundation under contract DMR-81-19295. The authors acknowledge valued technical discussions with Martin Schmidt, and assistance in process development from Paul Maciel, Technical Director of the Microsystems Technology Laboratories.

REFERENCES

- [1] J.A. Hinkley, "Adhesion of Polymer Films to SiO_2 ", *Journal of Adhesion*, **16**, 115 (1983)
- [2] K. Peterson, "Silicon as a Mechanical Material" *Proceedings of the IEEE*, **70**, 420 (1982)
- [3] Boron+ solid sources, model GS-245
Owens-Illinois, Inc.
- [4] Silicon Anisotropic Etchant, PSE-100,
Transene Company, Inc.
- [5] S. Timoshenko, *Theory of Plates and Shells*
McGraw-Hill (1940) Ch. 8,9
- [6] S. Way, "Uniformly Loaded, Clamped, Rectangular Plates With Large Deflection", *Proceedings of the Fifth International Conference for Applied Mechanics*, Cambridge, Ma. 123 (1938)
- [7] J.G. Williams, *Fracture Mechanics of Polymers*
Holsted Press, 1984, Ch. 2
- [8] K. Mehregany, R. Howe, S. Senturia, "Novel Microstructures for the Study of Residual Stress in Polyimide Films", Paper submitted to the Electronic Materials Conference, Amherst, Ma. June, 1986